OSCILLATOR STRENGTHS FOR PHOTOABSORPTION AND PHOTOIONIZATION PROCESSES OF FREON AND NO_2 MOLECULES

By

Wenzhu Zhang

B. Sc. (Physics) Tsinghua University, Beijing, China, 1982

A THESIS SUBMITTED IN PARTIAL FULFILLMENT OF

THE REQUIREMENTS FOR THE DEGREE OF

DOCTOR OF PHILOSOPHY

in

THE FACULTY OF GRADUATE STUDIES

CHEMISTRY

We accept this thesis as conforming

to the required standard

THE UNIVERSITY OF BRITISH COLUMBIA

September 1991

In presenting this thesis in partial fulfilment of the requirements for an advanced degree at the University of British Columbia, I agree that the Library shall make it freely available for reference and study. I further agree that permission for extensive copying of this thesis for scholarly purposes may be granted by the head of my department or by his or her representatives. It is understood that copying or publication of this thesis for financial gain shall not be allowed without my written permission.

Department of Chemistry

The University of British Columbia
Vancouver, Canada

Date Sept 18, 1991

DE-6 (2/88)

Abstract

Absolute photoabsorption differential oscillator strengths (cross sections) for N 1*s* and O 1*s* inner shell excitation and ionization of NO_2 have been derived from the presently obtained high resolution electron energy loss spectra using dipole (e,e) spectroscopy. The NO_2 inner shell differential oscillator strength spectra are in good agreement with multi-channel quantum defect theory calculations in both excitation energies and (differential) oscillator strengths. The NO_2 spectra were interpreted with the aid of the calculations. A resonance present in both the NO_2 N 1*s* and O 1*s* ionization continua was identified as excitation to an unbound molecular orbital. A consideration of the present spectra for NO_2 and earlier spectra for other molecules showed that additional prominent structures observed in previously reported NO_2 inner shell photoabsorption spectra obtained using synchrotron radiation were due to the presence of impurities.

Absolute photoabsorption differential oscillator strengths for the valence shells of CF_4, CF_3Cl, CF_2Cl_2 and $CFCl_3$ have been measured in the equivalent photon energy range up to 200 eV using dipole (e,e) spectroscopy. The present results are in good agreement with earlier reported optical measurements and electron impact measurements. The photoionization efficiencies and also the photoion branching ratios have been determined for CF_4, CF_3Cl, CF_2Cl_2 and $CFCl_3$ from time of flight mass spectra using dipole (e,e+ion) coincidence spectroscopy at equivalent photon energies ranging up to 80 eV. Absolute partial differential oscillator strength spectra for the molecular and dissociative photoions have been derived. The natures of the dipole induced breakdown pathways of CF_4, CF_3Cl and CF_2Cl_2 were investigated by combining the present differential oscillator strength

measurements for molecular and dissociative photoionization with photoelectron data obtained in the present thesis work plus previously reported photoelectron branching ratios. On the basis of the present work, a revised set of absolute electronic state partial photoionization differential oscillator strengths for CF_4 are presented.

Absolute electronic state partial photoionization differential oscillator strength spectra for CF_3Cl, CF_2Cl_2 and $CFCl_3$ in the photon energy range 41—160 eV have been derived by combining total differential oscillator strength spectra obtained in the present thesis work with photoelectron branching ratios obtained from photoelectron spectra measured using synchrotron radiation.

Absolute photoabsorption differential oscillator strengths and for F $1s$, C $1s$, and Cl $2p, 2s$ inner shell excitation and ionization of freon molecules CF_4, CF_3Cl, CF_2Cl_2, $CFCl_3$ and CCl_4 have been derived from the presently obtained high resolution electron energy loss spectra plus previously reported. Tentative assignments of the spectra were obtained using the MO picture and the potential barrier model.

Table of Contents

List of Tables

List of Figures

List of Abbreviations

EELS	electron energy loss spectroscopy
EXAFS	extended X-ray absorption fine structure
FWHM	full width at half maximum
IP	ionization potential
ISEELS	inner shell electron energy loss spectroscopy
MCQD	multichannel quantum defect
MO	molecular orbital
MS-Xα	multiple scattering Xα method
OS	oscillator strength
PES	photoelectron spectroscopy
T	term value
TOF	time of flight
TRK	Thomas-Reiche-Kuhn
VUV	vacuum ultraviolet
XANES	X-ray absorption near edge structure
XPS	X-ray photoelectron spectroscopy

Acknowledgements

I should like to express my sincere thanks to Dr. C.E. Brion for his interest, assistance, encouragement and supervision throughout the course of my study. I appreciate having had the opportunity to work with him and other members in his research group. Special thanks are due to Dr. G. Cooper, who gave me a lot of help in my research, and also measured the freon photoelectron spectra, to Dr. H.K. Sze, who helped me in the early stages of my work, to Dr. X.M. Tong and Prof. J.M. Li, who performed the multichannel quantum defect calculation on the NO_2 molecule, to Dr. T. Ibuki, who helped to record the freon photoabsorption and photofragmentation data, to Prof. A.P. Hitchcock, who provided me with the background and Gaussian fitting programs, to Dr. J.H. Scofield, who supplied numerical data of calculated atomic photoionization cross sections, and to Dr. Y.H. Hong and G. Burton, who gave helpful comments and suggestions on the writing of my thesis.

For invaluable technical assistance, discussions of things I could not grasp on my own, for advice, for guidance and for a few good references, I am very grateful to: W.F. Chan, S. Clark, M. Coschizza, P. Duffy, B. Greene, X. Guo, B. Hollebone, N. Lermer, B. Todd, E. Zarate, and Y. Zheng.

I should also like to gratefully acknowledge a University of British Columbia Graduate Fellowship. The research work was also supported by operating grants from The National Sciences and Engineering Research Council of Canada.

Finally, I should like to thank my parents. This thesis is dedicated to them.

Chapter 1

Introduction

Absolute photoabsorption and photoionization differential oscillator strength (cross section) spectroscopies for molecular valence shell and inner shell excitation in the VUV and soft X-ray regions are of fundamental and applied interest. A quantitative knowledge of photoabsorption and photoionization processes is very important in understanding the interaction of molecules with electromagnetic radiation. Detailed information on the transition energies and (differential) oscillator strengths is urgently needed in a large number of scientific contexts, including studies in aeronomy [1], astrophysics [2], planetary sciences [3] and radiation chemistry, physics and biology [4]. However, until comparatively recently, only limited data were available from optical measurements using discharge lamps or X-ray tubes [5]. In the past decade, an increasing amount of quantitative spectral information over a wide energy range has been obtained with the increasing availability of tunable synchrotron radiation [6,7]. Alternatively, electron energy loss spectroscopy (EELS) can also be used to measure optical differential oscillator strengths by utilizing the virtual photon field created by a fast scattered electron at negligible momentum transfer. Under such conditions EELS techniques are often referred to as dipole electron impact experiments. A recent review of such techniques and measurements has been published by Gallagher *et al.* [8]. Electron energy loss techniques have been used to obtain most of the experimental results reported in the present work. In addition photoelectron branching ratios from synchrotron radiation measurements have

been used to determine some partial differential oscillator strengths.

Electron impact experiments are now widely recognized as providing physical information complementary to that obtained in photon impact experiments. In fact one of the earliest demonstrations of quantization was the classic Franck-Hertz experiment [9] in which electrons were used to probe atomic systems. Dipole electron impact techniques have been demonstrated in the past decade to provide a very suitable alternative to VUV and soft X-ray photoabsorption experiments for the measurement of optical quantities such as transition energies and dipole differential oscillator strengths or cross-sections for photoabsorption and photoionization processes [8]. The possibility of studying optical processes by electron impact was in fact pointed out as early as 1930 by Bethe [10]. The use of electron energy loss spectroscopy for optical differential oscillator strength measurements was pioneered by the early experiments of Lassettre [11], Geiger [12] and Van der Wiel [13,14,15]. In particular the direct techniques developed by Van der Wiel and co-workers [13,14,15] and more recent development here at The University of British Columbia have provided versatile methods for the measurement of absolute differential oscillator strengths for photoabsorption and photoionization processes for valence shell (for examples, see references [16,17,18]) and inner shell (for example, see reference [19]) processes. Some useful reviews on the electron energy loss spectroscopy studies and absolute optical differential oscillator strength measurements are to be found in references [8,20,21,22,23,24,25,26].

In the present work optical (differential) oscillator strengths and transition energies for photoabsorption and photoionization have been obtained for a variety of valence and inner shell processes in NO_2 (chapter 4) and the freon molecules CF_4, CF_3Cl, CF_2Cl_2 and $CFCl_3$ (chapters 5 and 7) using the EELS based techniques of dipole (e,e) and dipole (e,e+ion) spectroscopies. In addition partial optical differential oscillator strengths for valence

shell photoionization (electronic states) have been derived for CF_3Cl, CF_2Cl_2 and $CFCl_3$ (chapter 6) from synchrotron radiation PES measurements and the dipole (e,e) results. The NO_2 molecule and the freons were selected because of their fundamental interest and also because of the importance of their interaction with energetic electromagnetic radiation in a number of applications. For example NO_2 is a toxic gas which is an important link in the chain leading to the production of the atmospheric photochemical smog from air, sunlight, and automobile exhaust. Freons (in particular CF_2Cl_2 and $CFCl_3$) have been released to the atmosphere as a result of their widespread use in industry and daily life, for example as refrigerants, foam blowing agents and aerosol propellants. The release of these molecules into the atmosphere has caused major concern as to their role [27,28,29,30,31,32,33] in processes resulting in depletion of the ozone layer which protects us and our planet from the damaging effects of short wavelength solar radiation. Quantitative spectroscopic information for these molecules in the VUV and soft X-ray regions of the electromagnetic spectrum are thus needed due to the presence of such energetic solar radiation in the upper levels of the earth's atmosphere [34]. Prior to the present work very little quantitative spectroscopic information was available for NO_2 and the freons in the VUV and soft X-ray regions. The results of the work described in this thesis are to be found in the following publications:

- W. Zhang, K.H. Sze, C.E. Brion, X.M. Tong and J.M. Li, *Chem. Phys.* **140** (1990) 265.
- W. Zhang, G. Cooper, T. Ibuki and C.E. Brion, *Chem. Phys.* **137** (1989) 391.
- W. Zhang, G. Cooper, T. Ibuki and C.E. Brion, *Chem. Phys.* **151** (1991) 343.
- W. Zhang, G. Cooper, T. Ibuki and C.E. Brion, *Chem. Phys.* **151** (1991) 357.

- W. Zhang, G. Cooper, T. Ibuki and C.E. Brion, *Chem. Phys.* **153** (1991) 491.

- G. Cooper, W. Zhang, C.E. Brion and K.H. Tan, *Chem. Phys.* **145** (1990) 117.

Chapter 2

Photoabsorption and Electron Energy Loss Spectra

The spectroscopic properties of molecular systems can be studied by using either photons or electrons as probes. In a photoabsorption experiment, when a photon of energy $E = h\nu$ is resonantly absorbed by a target molecule, the process may be represented as

$$\begin{aligned} \text{Process}: \quad & h\nu \; + AB \longrightarrow AB^* \\ \text{Energy of photon}: \quad & E \end{aligned} \tag{2.1}$$

where AB is the molecule in its initial state and AB^* in its final (bound or continuum) state with an energy higher than the initial state by E. In an electron energy loss experiment with the same molecule, if an incident electron e transfers the same amount of energy E to the target molecule, the same final molecular state can be accessed. In this process

$$\begin{aligned} \text{Process}: \quad & e \; + \; AB \longrightarrow AB^* \; + \; e \\ \text{Energy of electron}: \quad & E_0 \qquad\qquad\qquad\quad E_0 - E, \end{aligned} \tag{2.2}$$

in which E_0 and $(E_0 - E)$ are the electron energies before and after the collision respectively. The energy loss E of the incident electron is analogous to the photon energy E in the photoabsorption experiment. Moreover, a quantitative relation exists between the target transition intensities in the two experiments when the electron impact experiment is performed under the condition that the momentum transfer to the target is negligibly

small. This parallel between photoabsorption and electron impact experiments is the basis of the major part of this thesis work.

2.1 Photoabsorption Cross Section and Differential Oscillator Strength

The probability that a photon of energy $E = h\nu$ will be absorbed in passing through a target is specified by a *cross section* $\sigma(E)$. $\sigma(E)$ has the dimensions of area and is often given a geometrical interpretation. Imagine that a circle of area $\sigma(E)$ is centered on each target molecule in the plane perpendicular to the incident photon beam. The circular area $\sigma(E)$ has the property that any photon of energy E entering $\sigma(E)$ is absorbed by the target [35]. Consider an incident photon flux N (N = number of photons per unit area per unit time) impinging on the target and passing through it with a path length dL. If no circles are hidden behind others within the distance dL, when viewed from the direction of the incident photon beam, the change in the photon flux is then

$$dN = -N\sigma(E)m\, dL \tag{2.3}$$

where m is the target density (i.e. the number of target molecules per unit volume). The corresponding attenuation of the incident light intensity ($I = Nh\nu$) is accordingly given by

$$dI = -I\sigma(E)m\, dL. \tag{2.4}$$

The condition corresponding to the requirement for the validity of the above linear relationships is

$$\sigma(E)m\, dL << 1, \tag{2.5}$$

in which the $\sigma(E)mdL$ is the total area of circles centered on molecules contained in a slab with thickness dL and *unit area* surface, on which the photon beam is incident.

This correspondence can be understood since, the smaller $\sigma(E)mdL$ is compared with one (unit area), the smaller the chance that the circles are hidden behind others. An equivalent of condition 2.5 is that the probability $(-dN/N)$ of a given photon being absorbed in passing a distance dL through the target is much smaller than one. In the language of electron scattering, this is also the condition for a single collision in an electron impact experiment (see the following section). In the situation where condition 2.5 is not valid for a path length L, equation 2.4 may be integrated over the path length and the *Lambert-Beer Law* is obtained, that is

$$I = I_0 \, e^{-\sigma(E)mL} \tag{2.6}$$

where I_0 and I are the light intensities before and after passing through the target.

The quantum mechanical expression for the cross section for a process in which a molecule having Z electrons with coordinates $\{\vec{r}_j\}$, whose components in the direction of the electric field of the electromagnetic radiation are $\{x_j\}$, undergoes a transition from an initial state u_0 to a bound, final state u_n, upon resonantly absorbing a photon of energy E, is (in atomic units)

$$\sigma(E) = \frac{2\pi^2}{c} \, f_n S(E) \tag{2.7}$$

with

$$\begin{aligned} f_n &= 2E \left| \int u_n^*(\vec{r}_1, \cdots, \vec{r}_Z) \sum_j x_j u_0(\vec{r}_1, \cdots, \vec{r}_Z) \, d\vec{r}_1 \cdots d\vec{r}_Z \right|^2 \\ &= 2E|(x)_n|^2 \end{aligned} \tag{2.8}$$

where c is the speed of light, $(x)_n$ is the dipole moment matrix element, f_n is the dimensionless photoabsorption (dipole) *oscillator strength*, and $S(E)$ is the lineshape function $(\int S(E)dE = 1)$ [36]. By integrating equation 2.7 on both sides over the linewidth, the

integrated cross section for the transition is obtained as

$$\sigma_n = \frac{2\pi^2}{c} f_n. \tag{2.9}$$

If the photon energy E is sufficiently large, ionization can occur and the cross section for a transition from an initial state u_0 to a continuum final state u_E is given by [25]

$$\sigma(E) = \frac{2\pi^2}{c} \frac{df}{dE} \tag{2.10}$$

and

$$\begin{aligned} \frac{df}{dE} &= 2E \left| \int u_E^*(\vec{r}_1, \cdots, \vec{r}_Z) \sum_j x_j u_0(\vec{r}_1, \cdots, \vec{r}_Z)\, d\vec{r}_1 \cdots d\vec{r}_Z \right|^2 \\ &= 2E|(x)_E|^2 \end{aligned} \tag{2.11}$$

where df/dE is the photoionization *differential oscillator strength.* df/dE has the dimensions of 1/energy.

The oscillator strength f_n and differential oscillator strength df/dE have a useful property known as the *Thomas-Reiche-Kuhn (TRK) sum rule* [25,37], namely

$$\sum_n f_n + \int \frac{df}{dE} dE = Z. \tag{2.12}$$

The TRK sum rule states that the sum of oscillator strengths over all possible transitions from an initial state to bound and continuum states is equal to Z, the total number of electrons in the target. This is a very general rule which rigorously holds for any atomic and molecular system [37]. In practice, an approximate *partial sum rule* has been used in spectral normalization. According to the partial sum rule, the sum of the oscillator strengths for transitions of a *single electron* (which is assumed to be in a fixed potential) from its initial state to all other states, which include both bound and continuous, occupied and unoccupied, is unity [38]. This approximation permits a separation of the valence and inner shell oscillator strengths (see section 2.3.8).

The transition probability for a photoionization process can be described by either the cross section or the differential oscillator strength. The relation between the values of these two quantities is given by $\sigma(\text{Mb}) = 109.75\, df/dE(\text{eV}^{-1})$ [25], where 1 Mb = 10^6 barn = 10^{-18} cm^2. When cross section is chosen to be the scale of the transition intensity in a photoabsorption spectrum, it is used for energy regions both below and above the ionization limit. In contrast, in the differential oscillator strength spectrum, the spectral intensity for transitions to ionization continua is df/dE, while the intensity of a feature which corresponds to a transition to a bound state is $f_n S(E)$, at a given photon energy E. To obtain the oscillator strength f_n for a discrete transition, the spectral intensity must be integrated over the linewidth of the spectral feature.

2.2 The Bethe-Born Theory of Fast Electron Impact

Consider a process in which a fast, but non-relativistic, electron collides with a target molecule. The influence of the incident electron on the molecule may be regarded as a sudden and small perturbation [26,39]. In the Born approximation, this perturbation could produce a sudden transfer of energy and momentum to target electrons [26] and the target molecule would undergo a transition from an initial state u_0 to a final state u_n, while the incident electron described by a plane wave would be deflected into a scattered wave which can also be approximated by a plane wave. The differential electron scattering cross section $d\sigma_n/d\Omega$ for such a process can be expressed as [26]

$$\frac{d\sigma_n}{d\Omega} = \frac{1}{4\pi^2}\frac{k'}{k}\left|\int e^{i\vec{K}\cdot\vec{r}}\, u_n^*(\vec{r}_1,\cdots,\vec{r}_Z) V u_0(\vec{r}_1,\cdots,\vec{r}_Z)\, d\vec{r}_1\cdots d\vec{r}_Z d\vec{r}\right|^2 \tag{2.13}$$

in which

$$\vec{K} = \vec{k} - \vec{k'} \tag{2.14}$$

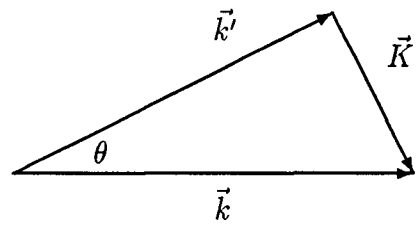

Figure 2.1: Schematic of scattering geometry. $\vec{k}$ and $\vec{k}'$ are the momenta of the electron before and after the collision, $\vec{K}$ is the momentum transfer and θ is the scattering angle.

as is shown in fig. 2.1, or

$$K^2 = k^2 + k'^2 - 2kk'cos\theta \tag{2.15}$$

where $\vec{r}$ is the position of the incident electron, $\vec{k}$ and $\vec{k}'$ are the momenta of the electron before and after the collision respectively, $\vec{K}$ is the momentum transfer from the incident electron to the target molecule, θ is the scattering angle, the u's are the wavefunctions in the coordinates $\{\vec{r}_j\}$ of the Z molecular electrons, and V is the Coulombic interaction between the incident electron and the target molecule, namely

$$V = -\sum_{p=1}^{M} \frac{z_p e^2}{|\vec{r} - \vec{R}_p|} + \sum_{j=1}^{Z} \frac{e^2}{|\vec{r} - \vec{r}_j|} \tag{2.16}$$

where M is the number of atoms associated with atomic number z_p.

Bethe showed [26] that equation 2.13 can be reduced to

$$\frac{d\sigma_n}{d\Omega} = 4\frac{k'}{k}\frac{1}{K^4}|\epsilon_n(K)|^2 \tag{2.17}$$

where $\epsilon_n(K)$ is a matrix element for the initial and final states,

$$\epsilon_n(K) = \int u_n^*(\vec{r}_1, \cdots, \vec{r}_Z) \sum_{j=1}^{Z} e^{i\vec{K}\cdot\vec{r}_j} u_0(\vec{r}_1, \cdots, \vec{r}_Z)\, d\vec{r}_1 \cdots d\vec{r}_Z. \tag{2.18}$$

The cross section expressed in equation 2.17, for a process in which a fast electron transfers a given amount of energy and momentum, consists of two distinct factors, namely $4(k'/k)(1/K^4)$ and $|\epsilon_n(K)|^2$. The quantity $4(k'/k)(1/K^4)$ may be evaluated from the measurable quantities k, k' and θ, which concern *the incoming and outgoing electrons only*, and it is therefore a purely *kinematic* factor. The second quantity $|\epsilon_n(K)|^2$, as shown in equation 2.18, is *target dependent* and it determines the conditional probability of a transition in the target from state u_0 to state u_n upon receiving a momentum transfer K. The conditional probability is because there is no unique correspondence between momentum transfer and energy transfer. The quantity $|\epsilon_n(K)|^2$ is referred to as a *dynamic* factor [26].

The differential cross section in equation 2.17 can be also written as

$$\frac{d\sigma_n}{d\Omega} = \frac{2}{E}\frac{k'}{k}\frac{1}{K^2}f_n(K) \tag{2.19}$$

where the *generalized oscillator strength*

$$f_n(K) = \frac{2E}{K^2}|\epsilon_n(K)|^2 \tag{2.20}$$

is introduced as a straightforward generalization of the optical oscillator strength defined in equation 2.8 [26].

The relationship between the electron scattering process, in which a small momentum is transferred, with the photoabsorption process can be revealed by considering the following: The term $e^{i\vec{K}\cdot\vec{r}_j}$ in equation 2.18 can be expanded in a power series of K

$$e^{i\vec{K}\cdot\vec{r}_j} = e^{iKx_j} = 1 + iKx_j + \frac{(iKx_j)^2}{2} + \cdots + \frac{(iKx_j)^t}{t!} + \cdots \tag{2.21}$$

assuming that the momentum transfer vector is in the x direction. With this expansion, and considering the orthogonality of the wavefunctions u_0 and u_n, equation 2.18 becomes

$$\epsilon_n(K) = (iK)e_1 + (iK)^2e_2 + \cdots + (iK)^te_t + \cdots \tag{2.22}$$

where the t^{th} order multipole matrix element e_t ($t = 1$ is electric dipole, $t = 2$ is electric quadrupole, etc) is given by

$$e_t = \frac{1}{t!} \int u_n^*(\vec{r}_1, \cdots, \vec{r}_Z) \sum_{j=1}^{Z} x_j^t u_0(\vec{r}_1, \cdots, \vec{r}_Z)\, d\vec{r}_1 \cdots d\vec{r}_Z. \tag{2.23}$$

The relationship between the optical and the generalized oscillator strength is obtained by combining equations 2.8 and 2.22, and is given by

$$\begin{aligned} f_n(K) &= 2E[e_1^2 + (e_2^2 - 2e_1e_3)K^2 + (e_3^2 + 2e_1e_5 - 2e_2e_4)K^4 + \cdots] \\ &= f_n + AK^2 + BK^4 + \cdots. \end{aligned} \tag{2.24}$$

Thus in the limit of zero momentum transfer, the generalized oscillator strength becomes equal to the optical oscillator strength, that is

$$\lim_{K^2 \longrightarrow 0} f_n(K) = f_n, \tag{2.25}$$

and therefore equation 2.19 becomes, in the limit of $K^2 \longrightarrow 0$,

$$\frac{d\sigma_n}{d\Omega} = \frac{2}{E}\frac{k'}{k}\frac{1}{K^2} f_n. \tag{2.26}$$

This is the *Bethe-Born equation* which gives the quantitative relationship between the process in which an electron is scattered at negligible momentum transfer and the photoabsorption process. This is the basis of dipole (e,e) and dipole (e,e+ion) spectroscopies.

For an ionization process in which the target molecule undergoes a transition from the initial state u_0 to a final continuum state u_E, the differential electron scattering cross section corresponding to equation 2.13 is

$$\frac{d^2\sigma}{d\Omega dE} = \frac{1}{4\pi^2}\frac{k'}{k}\left| \int e^{i\vec{K}\cdot\vec{r}} u_E^*(\vec{r}_1, \cdots, \vec{r}_Z) V u_0(\vec{r}_1, \cdots, \vec{r}_Z)\, d\vec{r}_1 \cdots d\vec{r}_Z d\vec{r} \right|^2 \tag{2.27}$$

and the parallel of equation 2.19 is

$$\frac{d^2\sigma}{d\Omega dE} = \frac{2}{E}\frac{k'}{k}\frac{1}{K^2}\frac{df(K)}{dE} \tag{2.28}$$

where the *generalized differential oscillator strength*

$$\frac{df(K)}{dE} = \frac{2E}{K^2}|\epsilon_E(K)|^2, \tag{2.29}$$

and

$$\epsilon_E(K) = \int u_E^*(\vec{r}_1, \cdots, \vec{r}_Z) \sum_{j=1}^{Z} e^{i\vec{K}\cdot\vec{r}_j} u_0(\vec{r}_1, \cdots, \vec{r}_Z)\, d\vec{r}_1 \cdots d\vec{r}_Z. \tag{2.30}$$

Similarly, in the limit of zero momentum transfer, the generalized differential oscillator strength is equal to the optical differential oscillator strength, that is

$$\lim_{K^2 \longrightarrow 0} \frac{df(K)}{dE} = \frac{df}{dE} \tag{2.31}$$

and the Bethe-Born equation which relates the differential electron scattering cross section and optical differential oscillator strength is

$$\frac{d^2\sigma}{d\Omega dE} = \frac{2}{E}\frac{k'}{k}\frac{1}{K^2}\frac{df}{dE}. \tag{2.32}$$

The fact that the molecule undergoes dipole transitions in response to the disturbance induced by a fast, negligibly deflected incident electron can be understood as follows [20,21,25]. Classically, when a fast electron passes at a large distance from a molecule (i.e. a large impact parameter), the molecule experiences an induced electric field which is rather uniform in space and sharply varying in time. If the field pulse is regarded as infinitely sharp in time (i.e. a delta function), its Fourier components of all frequencies have equal intensity. Thus the molecule experiences a *virtual photon field* which causes the molecule to undergo dipole allowed transitions. The large impact parameter corresponds to the small momentum transfer condition in the previous quantum

analysis. Therefore, at negligible momentum transfer the electron scattering differential cross section is quantitatively related to the optical (differential) oscillator strength by the kinematic Bethe-Born factor $(2/E)(k'/k)(1/K^2)$.

The Bethe-Born theory has been used in the past to evaluate optical oscillator strengths of atoms and molecules using electron impact experiments. To obtain the required experimental conditions under which momentum transfer is very small, K^2 can be expressed as a function of incident electron energy E_0, energy loss E, and scattering angle θ [20]. By substituting $k^2 = 2E_0$, $k'^2 = 2(E_0 - E)$ into equation 2.15,

$$\begin{aligned} K^2 &= 2E_0 + 2(E_0 - E) - 2\sqrt{2E_0}\sqrt{2(E_0 - E)}cos\theta \\ &= 2E_0(2 - \frac{E}{E_0} - 2\sqrt{1 - \frac{E}{E_0}}\, cos\theta). \end{aligned} \tag{2.33}$$

It can be proved, by using the above equation, that $K^2 \longrightarrow 0$ if and only if both E/E_0 and θ approach zero. Earlier electron impact experiments were based on the above considerations by measuring the generalized oscillator strength for a fixed transition as a function of K^2 and extrapolating to $K^2 = 0$ to obtain the optical oscillator strength. For example, Lassettre *et al.* [23,24,40] measured the generalized oscillator strength for a particular transition (fixed E) as a function of the scattering angle θ at a fixed impact energy E_0. Alternatively, Hertel and Ross [41,42] obtained the generalized oscillator strength for a particular transition (fixed E) at zero scattering angle, while varying the impact energy E_0. However, the extrapolating procedures used were tedious and involved considerable uncertainty in the resulting optical oscillator strength in some cases due to the long extrapolation needed under the experimental conditions employed. A more direct approach was employed by Geiger *et al.* [12] and by Van der Wiel *et al.* [13,14,15]. To this end, a very small K^2 in equation 2.33 can be approximated in terms of the first

order of $x^2 = (E/2E_0)^2$ and θ^2 as [20]

$$K^2 = 2E_0(x^2 + \theta^2). \tag{2.34}$$

With this expression for small K^2 and integrating equations 2.26 and 2.32 over the small scattering angle, it is found that

$$d\sigma_n = \left[\frac{\pi}{EE_0}\frac{k'}{k}\log_e\left(\frac{x^2+\theta_0^2}{x^2}\right)\right] f_n \tag{2.35}$$

and

$$d\left(\frac{d\sigma}{dE}\right) = \left[\frac{\pi}{EE_0}\frac{k'}{k}\log_e\left(\frac{x^2+\theta_0^2}{x^2}\right)\right]\frac{df}{dE} \tag{2.36}$$

where θ_0 is the half angle of acceptance of the scattered electrons [20]. Therefore, under experimental conditions of high impact energy (small x) and small scattering acceptance angle about zero degrees (small θ_0), the momentum transfer K is small, and therefore the electron scattering signal (which is proportional to the scattering cross section as discussed below) can be related to the optical oscillator strength through the Bethe-Born factor. This latter approach of direct measurements at negligible momentum transfer has been developed for a routine measurement procedure for oscillator strengths for various optical processes [8]. This direct method is preferable and has therefore been used in the present work. The scattered electron signal is recorded as a function of energy loss E and this electron energy loss spectrum is then converted to a relative optical spectrum by a Bethe-Born factor. An absolute optical differential oscillator strength scale is then established for the spectra by using a normalization method as described in section 2.3.8.

To convert an electron energy loss spectrum to a relative optical spectrum, the Bethe-Born factor in equations 2.35 and 2.36 can be evaluated from the scattering kinematics and the spectrometer geometry as has been done with the dipole (e,e+ion) spectrometer described in section 3.1. A simpler approach is to approximate equations 2.35 and 2.36

as [20,43]

$$d\sigma_n = aE^{-b}f_n \tag{2.37}$$

and

$$d\frac{d\sigma}{dE} = aE^{-b}\frac{df}{dE} \tag{2.38}$$

where a and b are constants depending on the values of the impact energy of the incident electrons and the acceptance angle of the scattering electrons. In an actual experimental situation, it is found that $2 \leq b \leq 3$ [44]. The above equations are useful for Bethe-Born conversion over a limited energy range, and have been used to obtain approximate optical differential oscillator strength spectra in section 5.3 and chapter 7 using the high resolution dipole (e,e) spectrometer which is described in section 3.2.

In the presently described electron energy loss experiments the gas pressure in the collision chamber is adjusted so that the length of chamber is much smaller than the mean free path of the molecules to ensure that only single collision events occur when the incident electrons pass through the gas sample. This can be checked by estimating the value of the mean free path in the present experiments, and also by seeing that peaks corresponding to multiple scattering processes are absent in the spectra obtained in the lower electron energy loss region (i.e. in valence shell spectra). Under this condition, which in fact corresponds to condition 2.5 (since $\sigma ml = 1$ [45], where σ and l are the cross section and the mean free path for the forward scattering, and m is the target density), a linear relationship exists between the electron scattering signal and the corresponding electron scattering cross section, similar to that for light intensity attenuation given in equation 2.4. Therefore, the intensity of the electron energy loss spectrum is related to the photoabsorption differential oscillator strength as indicated in equations 2.35 and 2.36 or in the approximate equations 2.37 and 2.38. For this reason, the scattered electron

signal in a dipole electron scattering experiment drops off $\sim E^{-b}$ times as quickly as does the corresponding photoabsorption intensity.

2.3 Spectral Analysis

The profile and features of a photoabsorption differential oscillator strength spectrum are determined by the molecular wavefunctions before and after the transition as shown in equations 2.8 and 2.11. To assign these features to particular transitions accurately, reliable theoretical calculations of both transition energies and oscillator strengths are needed. In chapter 4, such a high quality calculation for NO_2 based on multichannel quantum defect theory [46] has been used to provide the spectral assignments. However, such calculations are often not available, especially for larger polyatomic molecules, due to computational difficulties and the cost of computation. Therefore it is necessary to have an alternative method to analyze spectra with the aid of simple qualitative and semi-quantitative principles without involving extensive calculations. The qualitative principles concern general characteristic of various molecular orbitals, and of corresponding transition processes. Regarding the semi-quantitative analysis, term values and quantum defects have proved to be useful concepts for providing tentative spectral assignments in electron energy loss and photoabsorption studies [47,48,49]. In addition, relatively simple calculations such as GAUSSIAN 76 [50] are sometimes also helpful for spectral assignment.

2.3.1 Occupied and Unoccupied Molecular Orbitals

In the molecular orbital (MO) theory, the state of an electron in the molecule is described by a one-electron wavefunction, which is also referred to as a molecular orbital. The molecular orbitals can be conveniently classified into occupied inner shell (core) orbitals,

occupied valence orbitals, unoccupied (virtual) valence orbitals and unoccupied Rydberg orbitals [47]. An inner shell orbital closely surrounds a particular atomic site and orbital character is therefore dominantly atomic-like and non-bonding. The ionization energy of an inner shell electron (or binding energy of inner shell orbital) is close to the corresponding value for the isolated atom, differing only by a small chemical shift which is due to molecular effects. In contrast, occupied and unoccupied valence shell orbitals extend over the molecular framework, and they can be bonding, anti-bonding, or non-bonding. These molecular orbitals are therefore responsible for the formation and chemical properties of the molecule. The ionization energies of electrons in occupied valence orbitals are generally in the energy range $\sim$ 10–45 eV. As for Rydberg orbitals, they are large and diffuse, extending well beyond the spatial bounds of the ground state molecule. If an electron is excited to a Rydberg orbital, it does not distinguish the detailed spatial charge distribution of the molecular ion core and sees the ion core essentially as a point charge. A Rydberg orbital is therefore atomic-like and non-bonding. In addition to the bound states involving the above types of orbitals, the molecule may alteratively be in an ionized (continuum) state in which case the electron is unbound.

The present study provides an examination of the differential oscillator strength spectrum resulting from excitations of electrons from the occupied valence shell or inner shell orbitals in the ground state molecule to the unoccupied Rydberg and virtual valence orbitals as well as for ionization to continuum states. The *term value* T is a useful quantity in the spectral analysis. For a particular transition feature in the spectrum, T is defined as [47]

$$T = IP - E \tag{2.39}$$

where IP is the ionization potential of the electron in the initial state and E is the transition energy between the initial and final states. T can therefore be thought of as the

ionization energy of the excited, final state. The term values corresponding to the same final state, but different initial states, have been found to be related. In particular, since an electron in a Rydberg state is mostly located far away from the molecular ion core, the hole location has little effect on its orbital energy. Therefore, Rydberg transitions associated with the same final state have similar term values. This is often referred to by saying that the Rydberg term value is transferable. In contrast, virtual valence orbitals are normally delocalized over the framework of the molecule and their energies are sensitive to the hole location. Hence the virtual valence term value is not expected to be transferable [51,52,53]. In addition to the term value of a feature, its transition intensity is another important consideration in spectral analysis. The intensity of a transition induced by photons (or electrons under the conditions of negligible momentum transfer) depends on the dipole moment matrix element for the initial and final states as shown in equation 2.8. Such transitions which obey dipole selection rules are called dipole allowed transitions. Given a dipole allowed transition, another necessary condition for appreciable transition probability is that the two wavefunctions involved have significant spatial overlap. In the absence of a detailed oscillator strength calculation for a molecule a qualitative argument which is often used is that the intensity of a transition is expected to increase with the degree of spatial overlap.

2.3.2 Transitions to Rydberg Orbitals

Since Rydberg orbitals in a molecule are atomic-like, the term values for Rydberg transitions can be fitted into the Rydberg formula [47]

$$T = \frac{R}{(n - \delta_l)^2} \tag{2.40}$$

where R is the Rydberg energy (13.605 eV), n is a quantum number, and δ_l is the dimensionless *quantum defect* of the *s, p, d* etc. type of Rydberg orbital labeled according to the angular momentum quantum number l. The quantum defect reflects the degree of penetration of the Rydberg orbital into the molecular ion core. The deeper the penetration, the larger the δ_l value (i.e. larger T). For molecules containing second and third row atoms, the typical range of quantum defects δ_l is 0.8–1.3 for s Rydberg series, 0.4–0.8 for p Rydberg series and 0–0.2 for d Rydberg series [47]. The typical magnitudes of term values for the lowest members of Rydberg series are in the range 2.8–5.0 eV for the lowest ns member, 2.0–2.8 for the lowest np member and 1.5–1.8 for the lowest nd member [47].

Since both the inner shell orbitals and Rydberg orbitals are essentially non-bonding, the excitation of an inner shell electron to a Rydberg state does not cause any appreciable change in internuclear distance. At room temperature the ground state molecules are populated mostly in the lowest vibrational level, and the Franck-Condon region [54] of the transition will mainly contain the lowest vibrational level of the Rydberg state. Therefore Rydberg features in inner shell spectra are generally expected to be *sharper* than those features associated with transitions to the virtual valence orbitals which are mostly anti-bonding. Since Rydberg orbitals are large and have low probability density in the molecular ion core region, where the inner shell orbital resides, the intensities of Rydberg transitions are usually weak compared to transitions to virtual valence orbitals. As the quantum number n increases, the higher Rydberg orbitals have even less spatial overlap with the initial state orbital, and the transition intensities become smaller [55]. These properties of shape and intensity are useful for identifying Rydberg transition features in inner shell spectra.

2.3.3 Transitions to Virtual Valence Orbitals

The orbitals which have spatial distributions most delocalized over the framework of molecule are valence orbitals and may be occupied or unoccupied by electrons. The virtual valence (unoccupied) states can either be located below ($T > 0$) or above ($T < 0$) the ionization limit. The latter situation is due to potential barrier effects (see section 2.3.6 below). Since the initial orbital generally has better spatial overlap with virtual valence orbitals than with Rydberg orbitals, transitions to virtual valence states are expected to have larger intensities than those to Rydberg states. Unlike Rydberg orbitals, which are essentially non-bonding, virtual valence orbitals are mostly antibonding in character, and the excitation of an electron to these virtual valence orbitals will lead to a significant change in internuclear distance. According to the Franck-Condon principle, the features for transition to these states are expected to be vibrationally broadened, particularly in inner shell spectra. Thus the virtual valence features in inner shell spectra are usually more intense and broader than those features associated with Rydberg states.

2.3.4 Transitions to Ionization Continua

For the hydrogen atom, the photoionization differential oscillator strength is a maximum at ionization threshold and monotonically decreases at higher energies [25,56]. Such a hydrogenic profile in the atomic photoionization differential oscillator strength is also observed for many-electron atoms when an electron in a sufficiently deep inner shell is ionized [25,57]. Centrifugal effects and molecular field effects have been observed in the photoionization differential oscillator strength spectra of molecules, and such effects lead to the various types of non-hydrogenic spectral behavior discussed below.

2.3.4.1 Delayed Onsets of Ionization Continua

A delayed onset in the spectral distribution occurs when the photoionization intensity is depressed near the ionization threshold and then increases to a maximum at an energy above the threshold. This phenomenon, which may be explained in terms of centrifugal effects [25,56], has been observed for some photoionization processes in many-electron atoms and molecules, for example the $2p \longrightarrow \epsilon d$ transition in Ne (ϵ represents a continuum state), the $3d \longrightarrow \epsilon f$ transition in Kr [25] and the Cl $2p$ continua in the freon molecules studied in the present work (see figure 7.47). When an electron is ionized to a continuum state of higher angular momentum the centrifugal repulsion prevents the ionized electron from approaching close to the ion core and thereby reduces its wavefunction overlap with the initial state. Hence the photoabsorption is depressed near the ionization threshold by centrifugal effects which become more significant with increasing angular momentum. An absorption maximum occurs when the photoelectron energy has increased sufficiently to overcome centrifugal effects.

2.3.4.2 XANES and EXAFS

Inner shell photoionization spectra are also called "above edge X-ray absorption spectra". The spectra can be divided into two regions. The spectral structures in the high photoelectron energy region are referred to as extended X-ray absorption fine structure (EXAFS) and this has been interpreted as being due to scattering processes where the high kinetic energy photoelectron emitted by an atom is weakly scattered by *only one neighboring atom* in a *single* scattering process [58]. In contrast, the X-ray absorption near edge structure (XANES) located in the low photoelectron energy region is explained in terms of *multiple* scattering of the low kinetic energy photoelectron by *neighboring*

atoms in the molecule [58]. The shape resonances (see section 2.3.6 below) in the inner shell spectra are actually special cases of XANES [58]. A photoelectron energy of ~40 eV has been used, somewhat arbitrarily, to divide the spectra XANES and EXAFS [58].

2.3.4.3 Atomic and Molecular Photoionization at High Photoelectron Energies

A theoretical study of the N 1*s* photoionization of N_2 molecule by Dehmer and Dill [59] showed that in the high energy continuum the total molecular ionization cross section is close to twice the atomic cross section in magnitude. This is because the initial core state has an atomic-like charge distribution and also because the escape of the energetic photoelectron is not significantly altered relative to the free atom case (i.e. the final orbital is also atomic-like). Thus, to a first approximation, the molecular inner shell photoionization differential oscillator strength for high photoelectron energies is equal to the sum of the corresponding differential oscillator strengths for the constituent atoms. Molecular effects, including EXAFS discussed in the previous section 2.3.4.2, are weak modulations on the sum of the atomic differential oscillator strengths. This relationship between molecular and atomic photoionization is the basis for the inner shell spectral normalization procedures used in the present study (see section 2.3.8) and also by others [44,60].

2.3.5 Photoelectron Spectroscopy and Dipole (e,e+ion) Spectroscopy

When a photon excites a molecule to a state above its first ionization threshold, ionization may occur where an electron is ejected, but this need not occur 100% of the time [56]. The ratio of the number of photo-ejected electrons to the number of photons absorbed is the *photoionization efficiency* [8].

In a photoionization process where a particular electron in an orbital is ejected, the molecular ion is left in a corresponding electronic ion state. Subsequently the molecular ion relaxes and may remain as a stable molecular ion or dissociate into fragments (charged and/or neutral). The photoelectron spectrum indicates the intensity of the ejected photoelectrons at a given photon energy as a function of electron kinetic energy. By using Einstein's photoelectric equation, the scale can be converted from electron kinetic energy into orbital binding energy. In this spectrum, to a first approximation, each peak corresponds to the ejection of an electron from a particular orbital or more precisely, to the production of the molecular ion in a particular electronic state. The probability for a molecule to produce a molecular ion in a particular electronic state upon absorbing a photon can be expressed by the *electronic state branching ratio* which is the ratio of the corresponding peak area to the area of all peaks in the photoelectron spectrum. Accurate branching ratios are only obtained in an experiment if the variation of the analyzer transmission efficiency with electron kinetic energy is taken into account.

The photofragmentation processes following the electron photo-ejection can be studied by photoionization mass spectrometry or the equivalent electron impact technique of dipole (e,e+ion) coincidence spectroscopy [8]. In the dipole (e,e+ion) experiment, the photoions are detected in coincidence with the energy loss electrons as a function of mass-to-charge ratio. Similar to the electronic state branching ratio, the *photoion branching ratio* is obtained as the ratio of the area of one ion peak to the area of all ion peaks in the mass spectrum.

The partial photoionization differential oscillator strengths for production of the electronic states and photoions can be obtained by taking the triple product of the total photoabsorption differential oscillator strengths and the photoionization efficiencies with the branching ratios for producing the electronic states and the photoions, respectively.

Furthermore, the dipole induced breakdown pathways can be investigated by appropriate combination of the two kinds of partial photoionization differential oscillator strengths (see chapter 5).

2.3.6 Potential Barrier Effects

Originally studied for many-electron atoms where potential barriers are formed due to the presence of centrifugal potentials [25], potential barrier effects have also been investigated for many molecules (for examples, see references [59,61,62,63,64]). Such effects have been found to occur in the inner shell spectra of NO_2 (chapter 4) and the freon molecules (chapter 7). The potential barrier effects are manifested in inner shell photoabsorption and electron energy loss spectra by intense resonance features (*shape resonances*) accompanied by a suppressed ionization continuum and/or Rydberg structures. The mechanism of the effects has been studied earlier [61,62,65]. Briefly, if a double well potential exists in a molecule, with a potential barrier on the perimeter of the molecule, it is possible that the spatial distribution of a particular wavefunction is mostly within the inner well or the outer well. An inner well wavefunction, which can be at an energy either above or below the ionization energy of the molecule, has a large spatial overlap with the initial state wavefunction which resides mainly in the inner well and this results in strongly enhanced spectral features [65]. In contrast, the outer well wavefunctions have small amplitudes in the inner well region, and this leads to very low intensities for transitions to the outer well states [65]. Rydberg states belong to the outer well manifold of states [65]. The causes of potential barriers have been studied theoretically and experimentally. For example, centrifugal effects have been assigned as the cause of the shape resonances in the inner shell spectra of the N_2 molecule [59]. The presence of electronegative ligands surrounding a central atom in a molecule is also believed to cause a potential barrier.

Such an explanation was used to account for the inner shell spectra of molecules such as SF_6, SeF_6, TeF_6 and ClF_3 [62,63,64].

2.3.7 The Equivalent Core $(Z+1)$ Analogy

Inner shell spectra can also be analyzed using the $(Z+1)$ *equivalent core model* [66,67]. Consider an inner shell electron, bound to a particular atomic site with atomic number Z, which is excited to an unoccupied virtual valence or Rydberg orbital. Since, in the final state, there is one less electron in the core to shield the nucleus, the promoted electron will see the atom as having an effective atomic number of $(Z+1)$ so that the term values for the inner shell transitions will be approximated by those for valence excitations in the $(Z+1)$ core analogous species. For example, the term values for the NO_2 N $1s$ transitions are expected to be comparable with those for the valence transitions for the $(Z+1)$ core analogous species O_3 as discussed in chapter 4.

2.3.8 The Absolute Differential Oscillator Strength Scale

Since in general only relative intensities are obtained for both photoabsorption and Bethe-Born converted EELS spectra, calibration (normalization) procedures are required in order to establish an absolute differential oscillator strength scale. Normalization may be achieved using several different approaches:

1. Normalization at a single photon energy to a published absolute measurement or calculation for the molecule.

2. Normalization using the partial TRK sum rule. For example, in chapter 5, the partial TRK sum rule (see section 2.1) has been used to normalize valence shell Bethe-Born converted EELS spectra so that the area under the normalized valence

shell differential oscillator strength spectrum, as a function of photon energy (eV), is equal to the number of valence shell electrons plus a small correction corresponding to Pauli excluded transitions [38]. Similarly, in chapter 7 the partial TRK sum rule has been used to verify the differential oscillator strength scale established using atomic differential oscillator strengths (see method 3 below).

3. Normalization of inner shell spectra in the high photoelectron energy region to atomic differential oscillator strengths (see section 2.3.4.3). The atomic differential oscillator strengths (cross sections) can be obtained either from calculations [57, 68,69] or from recommended semi-empirical values [70]. This approach has been used in the normalization of inner shell Bethe-Born converted EELS spectra in section 5.3 and chapter 7.

Chapter 3

Experimental Methods

The results reported in this thesis were obtained using dipole (e,e+ion) and dipole (e,e) spectroscopies. The dipole (e,e+ion) spectrometer was used to obtain the valence shell photoabsorption, photoionization and photofragmentation differential oscillator strength spectra and photoionization mass spectra for the freon molecules discussed in chapters 5. The inner shell photoabsorption and photoionization differential oscillator strength spectra for NO_2 in chapter 4 and for the freon molecules in chapter 7 were derived from electron energy loss spectra measured using the high resolution dipole (e,e) spectrometer. The photoelectron branching ratios and partial electronic state photoionization differential oscillator strengths for the freon molecules discussed in chapter 6 were obtained from photoelectron spectroscopy measurements made at the Canadian Synchrotron Radiation Facility at the University of Wisconsin by Dr. G. Cooper.

3.1 The Dipole (e,e+ion) Spectrometer

The dipole (e,e+ion) spectrometer was originally built and operated at the FOM institute in Amsterdam [13,14,15,71,72,73,74,75]. In 1980 this instrument was moved to the University of British Columbia where it has been modified [76,77]. Details of the construction of the apparatus and its operation have been described in references [13,14,15, 71,72,73,74,75,76,77]. The form of the spectrometer as used for the work discussed in this thesis is shown in figure 3.2.

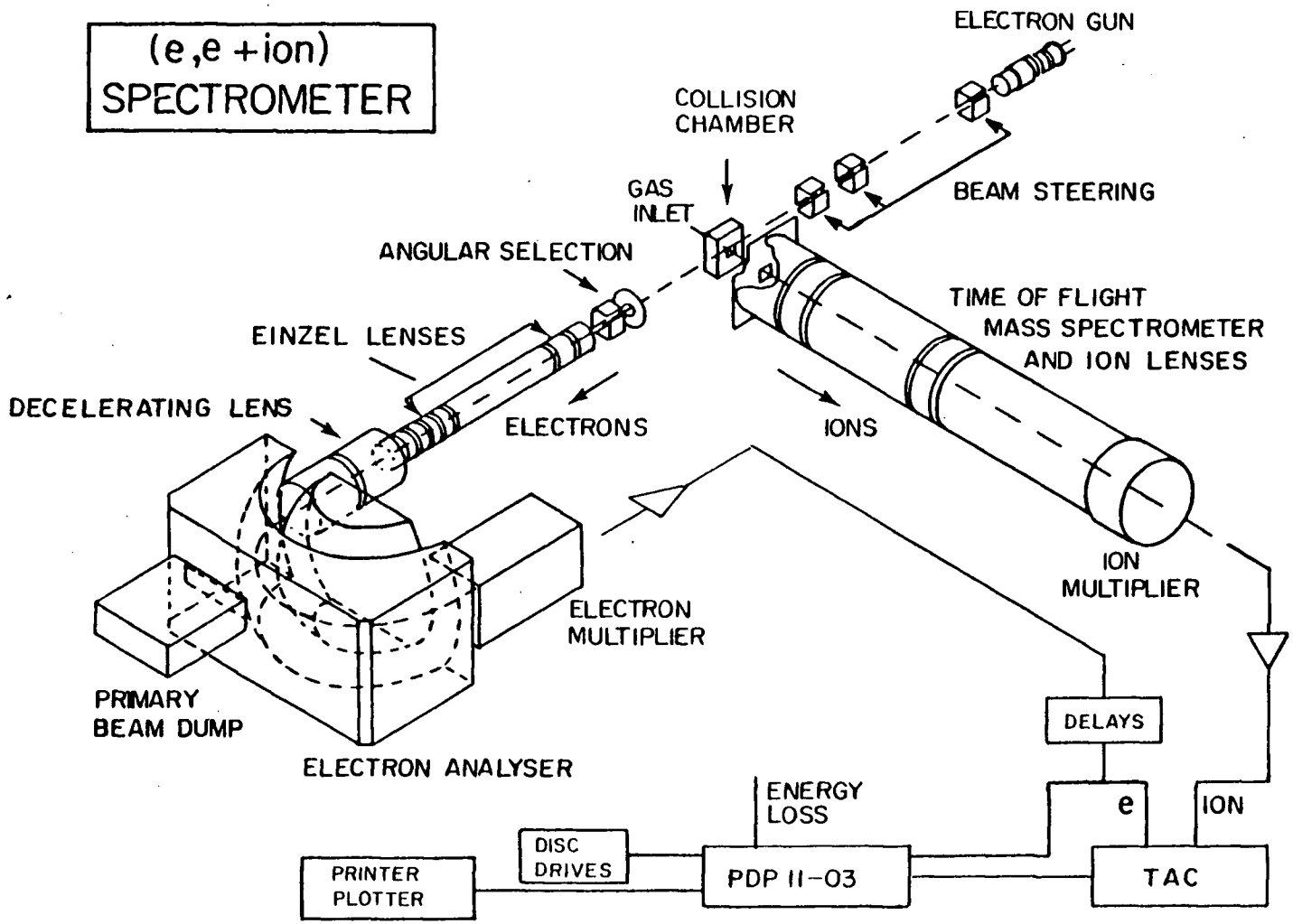

Figure 3.2: Schematic of the dipole (e,e+ion) spectrometer. Legend:
TAC—time to amplitude convertor PDP 11-03—computer

A narrow (1 mm diameter) beam of fast electrons (8 keV) is produced from a black and white television electron gun with an indirectly heated oxide cathode (Philips 6AW59). The incident electrons interact with target molecules in the collision chamber. In the scattered channel the electrons in a small cone of 1.4×10^{-4} steradians about the zero scattering angle pass through an angular selection aperture and are transported and decelerated by the Einzel lenses and the decelerating lens as shown in figure 3.2. The electrons then are energy analyzed by the hemispherical electron analyzer ($\sim$1 eV FWHM resolution) and are detected by a channel electron multiplier (Mullard B419AL). The positive ions produced in the collision chamber are extracted at 90 degrees to the incident electron beam into the time-of-flight (TOF) drift tube and are then detected by the ion multiplier (Johnston MM1-1SG). A homogeneous electric field (400 Vcm^{-1}) across the collision chamber and an accelerating lens system ensure uniform collection of ions with up to $\sim$20 eV excess kinetic energy of fragmentation, independent of the initial direction of dissociation [73,74,77]. The length of the drift tube and the final ion kinetic energy are such that mass spectra with a mass resolving power ($m/\Delta m$) of 50 can be obtained from a time-of-flight analysis. Magnetic shielding is achieved with Helmholtz coils and high permeability mumetal shields. The spectrometer is evacuated with turbo molecular pumps to provide the clean vacuum environment desirable for quantitative ion and electron spectroscopy.

Two modes of operation of the spectrometer are possible:

1. *Photoabsorption differential oscillator strengths.*

   According to the Bethe-Born theory discussed in section 2.2, the small momentum transfer (K) condition is to be satisfied to ensure that the collected scattered electrons are associated with dipole transitions in the target molecule. In the present

studies for which the energy loss $E < 200$ eV, this condition is met by choosing the scattering kinematics of the spectrometer: high electron impact energy ($E_0 = 8$ keV) and small half scattering acceptance angle ($\theta_0 = 6.7 \times 10^{-3}$ radians) about zero degrees. The electron energy loss spectrum can be converted to a relative optical spectrum by using equations 2.35 and 2.36 through a Bethe-Born factor which can be readily obtained from the E, E_0, θ_0 values. The absolute differential oscillator strength scale for the optical spectrum can then be established using the partial TRK sum-rule (section 2.12).

2. *Time of flight mass spectra and ionic photofragmentation differential oscillator strengths.*

TOF mass spectra at a fixed energy loss (i.e. photon energy) can be obtained in an electron-ion coincidence measurement with the aid of a time to amplitude converter (TAC). The TAC is started by a pulse signal from an electron of a given energy loss and stopped by a pulse from the ion signal. The TAC generates an output pulse with an amplitude proportional to the time between the start and stop pulses. This time is proportional to $\sqrt{m/e}$, a characteristic quantity for a specific ion which has mass m and positive charge e. A TOF mass spectrum is then constituted from the pulse height distribution measured using a PDP-11/03 computer via an analogue to digital converter and software routines. As has been discussed in section 2.3.5, the ionic photofragmentation branching ratios at a fixed energy loss for a particular ion are obtained from the ratio of the area under the corresponding peak to the area under all ion peaks. The photoionization efficiency is measured as the number of ions produced by each energy loss electron. The photofragmentation differential oscillator strength for a particular ion can then be obtained by taking the triple

product of the absolute photoabsorption differential oscillator strength (derived from the non-coincident energy loss measurement described in the measurement mode above), the photofragmentation branching ratio, and the photoionization efficiency.

3.2 The High Resolution Dipole (e,e) Spectrometer

The high resolution dipole (e,e) spectrometer was built in this laboratory in the early 1980s. Fig. 3.3 shows a schematic diagram of the instrument. The design and constructional details have been described in detail in reference [78] and hence only a brief description will be given here.

Electrons are produced from a direct current heated thoriated tungsten filament located within an externally adjustable mount in an oscilloscope electron gun body (Cliftronics CE5AH). The voltage for the filament cathode (C), grid (G), anode (A) and the second element of the focussing Einzel lens F are all floated at the negative of the impact energy (typically in the range 2–3.7 keV in the present work) with respect to the grounded first and third elements of the focusing lens F. The electron gun provides a narrow (1 mm diameter) electron beam. The beam is then retarded by the two element lens L_1 at the monochromator entrance to the required pass energy of the monochromator, which is a hemispherical electron energy analyzer. The monochromated beam then exits through a virtual slit formed by the accelerating lens L_2 (ratio 1:20) and is brought into focus at the entrance (P_4) of the stainless steel reaction chamber after passing through a second accelerating lens L_3 (ratio 1:5). The beam is then transported to the collision chamber (CC) by the Einzel lens L_4 to collide with the molecules under study. The exiting main beam and scattered electron beam then pass through a zoom (energy-add on) lens L_5, retarding lenses L_6 (ratio 5:1) and L_7 (ratio 20:1) to a virtual slit formed

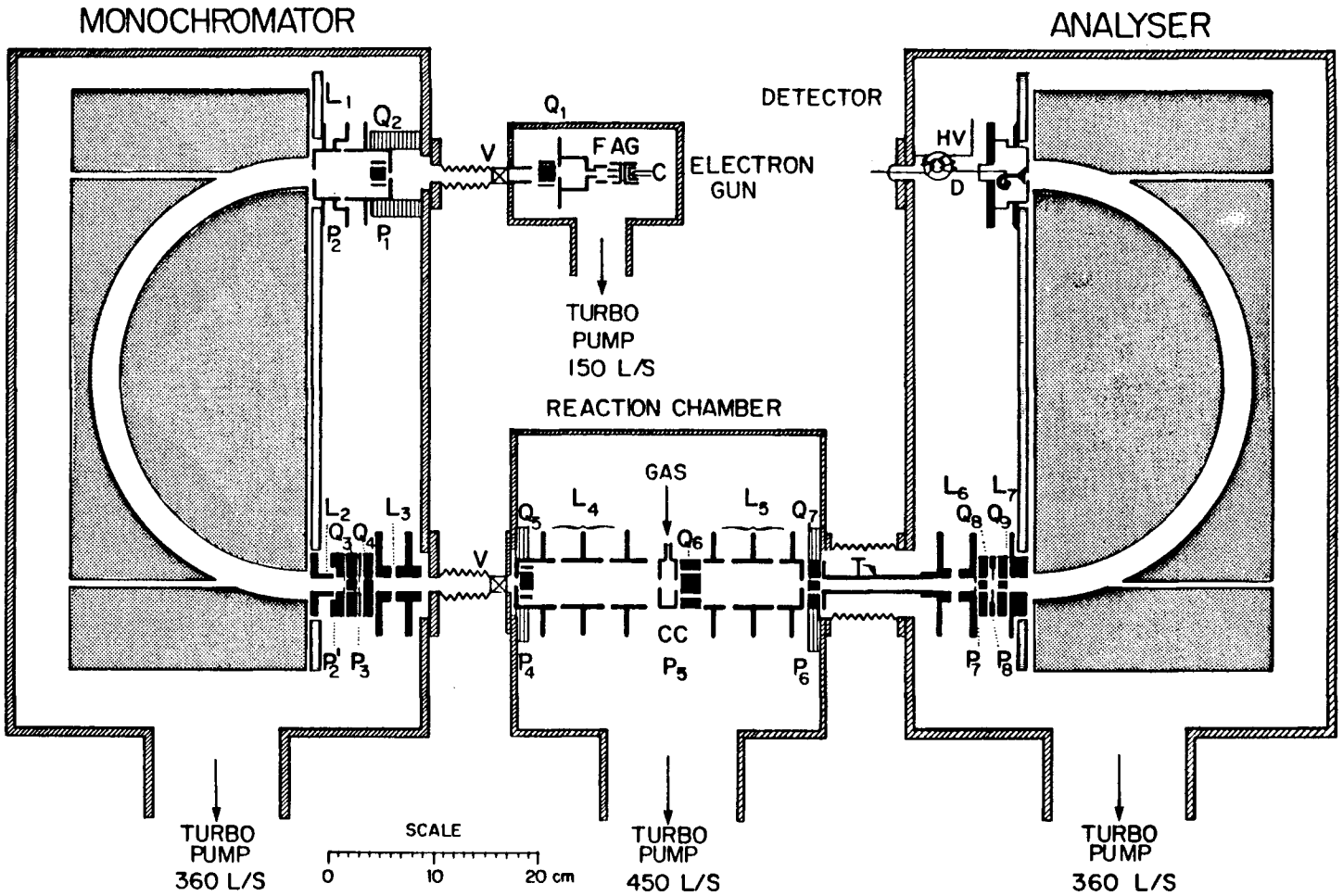

Figure 3.3: Schematic of the high resolution dipole (e,e) spectrometer. Legend:

A	anode	G	grid	P_1–P_8	apertures
C	cathode	GAS	gas inlet	Q_1–Q_9	deflectors
CC	collision chamber	HV	high voltage	T	tube
D	decoupling transformer	L_1–L_7	lenses	V	valve
F	forcusing lens	L/S	liter per second		

at the analyzer entrance. The half angle of acceptance (θ_0) of the scattered electrons is 3.0×10^{-3} radians about zero degrees. Following energy analysis, the scattered electrons are detected by a channeltron electron multiplier (Mullard B419AL) mounted behind the analyzer exit aperture. The channeltron is operated at high voltage of 3.5 keV and the signal is decoupled using a ferrite core transformer. Magnetic shielding of the various regions of the spectrometer is provided by hydrogen-annealed mumetal enclosures, exterior to the vacuum housing. Turbo molecular pumps are used to provide a clean vacuum environment.

High resolution, high sensitivity, and high stability are achieved by this spectrometer due to the following features [78]:

1. Separate differential pumping of the four vacuum chambers of the spectrometer has alleviated the problems of surface contamination, retuning and frequent cleaning that occur with single chamber instruments. This ensures long term stability and maintains high sensitivity and good resolution. In addition, thermal stability of the hot filament is not affected when the sample is introduced into the spectrometer.

2. The advanced electron optics allow transmission of large beam currents and also minimize the effects of scattering of the beam from slit edges and the surfaces of the analyzer into the detector. This design also permits operation at zero degree scattering angle since the main (unscattered) primary electron bean is strongly suppressed due to the high energy selectivity of the zoom lenses.

3. The large hemispherical electron energy analyzers (mean radius $R_0 = 19$ cm $= 7.5$ in) chosen provide high transmission and high resolution for a relatively high pass energy. This also permits a high impact energy, which is necessary for optical differential oscillator strength measurements, while still retaining reasonable lens

ratios.

The primary (unscattered) electron beam is used to tune up the spectrometer by steering the beam with analyzer deflection voltages, lens voltages and the deflectors (Q_1 to Q_9). Each of the deflectors consist of two pairs of electrostatic plates. The collimation and direction of the electron beam can be monitored with electrometers connected to the apertures (P_1 to P_8) and to the cone of the channeltron. The small currents on the channeltron cone are measured with a floated vibrating reed electrometer (Cary, model 401). To obtain an energy loss spectrum, a voltage equal to the energy loss corresponding to the inelastic scattering is added on top of the voltages already applied to the analyzer system, from the lens L_5 onward. Thus by regaining their energy loss, the scattered electrons are transmitted through the analyzer system to the channeltron and an energy loss spectrum is obtained by using a suitable offset energy loss voltage and scanning the energy loss region of interest.

The channeltron signals are processed by high gain pre-amplifier and amplifier-/discriminator units (PRA models 1762 and 1763 respectively). The spectrum is recorded by using a PDP 11/023 computer, and/or a Nicolet 1071 signal averager operated in a multichannel scaling mode where the channel address is stepped synchronously with the voltage on L_5 and the analyzer. The spectrum is monitored on-line via a VT105 graphics terminal.

The energy resolution, which can be defined as the full width at half maximum height (FWHM) of the electron beam at the analyzer exit, depends on the pass energies selected for the monochromator (E_M) and analyzer (E_A). The theoretical resolution for this spectrometer has been derived to be [78]

$$\Delta E_{FWHM} = 0.003\sqrt{E_M^2 + E_A^2}.$$

In practice, the experimental resolution achieved is slightly better than the above theoretical value. The energy resolutions specified in the spectra reported in the present work were obtained by measuring the profile of the primary electron beam, and were within the range 0.030—0.3 eV FWHM. The choice of the resolution to be used is determined by the spectral region of interest as well as natural linewidth considerations. For example, when structures in the pre-ionization edge region of a molecule are to be examined, high resolution is chosen; when a spectrum over a long energy range, including both pre-ionization edge and continuum regions, is to be scanned, a lower energy resolution is used. The length of time need to collect an inner shell spectrum ranges from a few hours to several days, depending on the primary beam current and the intensities of the transitions involved.

3.3 Energy Calibration

To calibrate the energy loss scale of the electron energy loss spectrum measured using the high resolution dipole (e,e) spectrometer, the sample and a suitable reference gas were introduced simultaneously into the spectrometer, and the spectrum of the mixture was measured to avoid any problems of chemical-dependent energy shifts and contact potentials. The absolute energy scale was then established by calibrating a prominent spectral feature due to the sample with respect to a known feature of the reference gas. Sodhi and Brion have carefully measured the energy of a number of selected inner shell atomic and molecular transitions for calibrating energy loss spectra [51]. The particular calibration energies used in this work are listed in table 3.1. The calibration corrections have been found to be very small (<0.03 eV) due to the efficient differential pumping of the different regions of the spectrometer (see section 3.2). The energies of the various spectral features were visually determined with the aid of computer software.

The energy loss scale for the dipole (e,e+ion) spectrometer has been calibrated using one of the following methods:

1. Using a prominent feature of known energy from previously published high resolution spectrum of the sample molecule.

2. Using the reported appearance potential for production of a particular ion in the mass spectrum of the sample molecule.

3.4 Sample Handling

The samples studied were introduced to the reaction chambers of the respective spectrometers through gas inlet systems including Granville-Phillips series 203 stainless steel leak valves. Appropriate gas regulators were used for the respective gaseous samples depending on the type of gas in the gas cylinder. In case of $CFCl_3$ the liquid sample was degassed by freeze, pump and thaw cycles before the sample was allowed to evaporate into the spectrometer via the leak valve. Cylinders of commercially available NO_2 were found to contain various amounts of NO impurity. The NO was removed by cooling and pumping the cylinder prior to use. No dimers (i.e. N_2O_4) were expected to be present [79] at the low pressures employed in the presently reported experiment.

Table 3.1: Reference energies for inner shell spectra[a]

Inner shell transition		Transition energy [b] (eV)
SF_6	S $2p_{1/2} \longrightarrow t_{2g}$	184.54(5)
N_2	N $1s \longrightarrow \pi^*(v=1)$	401.10(2)
CO	C $1s \longrightarrow \pi^*(v=0)$	287.40(2)

[a] Reference energies are taken from ref. [51].
[b] Uncertainties are shown in brackets, e.g. 184.54(5) means 184.54 ± 0.05 eV.

All the samples studied in the work presented in this thesis were obtained commercially and their stated purities are listed in table 3.2.

Table 3.2: Source and purity of samples

Sample	Source	Purity(%)
NO_2	Matheson	99.5
CF_4	Matheson	99.7
CF_3Cl	Matheson	99.0
CF_2Cl_2	Matheson	99.0
$CFCl_3$	PCR	99.0

Chapter 4

Inner Shell Electron Energy Loss Spectra of NO_2 at High Resolution: Comparison with Multichannel Quantum Defect Calculations of Dipole Oscillator Strengths and Transition Energies

The NO_2 inner shell EELS spectra reported in this chapter were measured using the high resolution dipole (e,e) spectrometer described in section 3.2.

4.1 Calculations

The multichannel quantum defect (MCQD) theory calculations were carried out by Tong and Li [80] and the details of the calculations are similar to those reported earlier for SO_2 [53]. Fig. 4.4 shows the calculated quantum defects for a_1, b_1, b_2 and a_2 symmetries. The calculated term values (IP-E) are obtained from the (state-dependent) quantum defects. The calculated (electronic) oscillator strengths f's for discrete transitions are represented (see figs. 4.5a and 4.9a below) as f/Δ, where the width Δ (FWHM) is estimated from the experimental spectra ($\sim$0.9 eV for the $6a_1$, $2b_1$, and $7a_1$ final states, 3 eV for $5b_2$ and $\sim$0.5 eV for the lower Rydberg states). The representation of oscillator strength in the discrete transition region has been discussed in section 2.1. Oscillator strengths for the higher Rydberg states and in the ionization continuum are represented as differential oscillator strengths, df/dE.

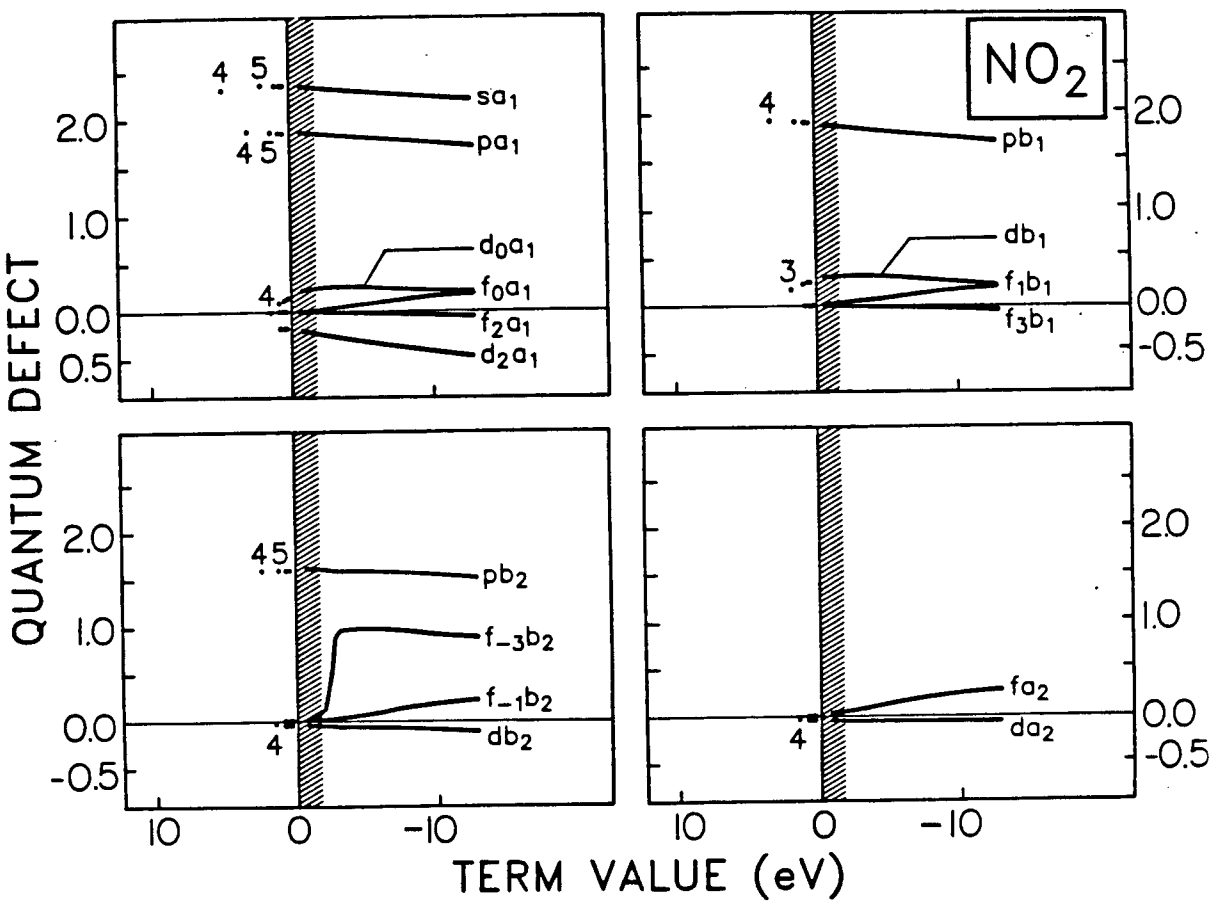

Figure 4.4: Calculated quantum defects for excitations of NO_2.

4.2 Results and Discussion

The NO_2 molecule is of C_{2v} symmetry, and the ground state, independent particle, electron configuration, including the unoccupied (virtual) valence orbitals, may be written as [81,82,83]

$$\underbrace{(1b_2)^2(1a_1)^2}_{\text{O } 1s}\underbrace{(2a_1)^2}_{\text{N } 1s}\underbrace{(3a_1)^2(2b_2)^2(4a_1)^2(5a_1)^2(3b_2)^2(1b_1)^2(1a_2)^2(4b_2)^2(6a_1)^1}_{\text{valence orbitals}}$$

$$\underbrace{(2b_1)^0(7a_1)^0(5b_2)^0}_{\text{unoccupied (virtual) valence orbitals}} \quad ; \ {}^2\mathrm{A}_1.$$

As a result of the unpaired electron in the half-filled $6a_1$ valence orbital, any transition from the core orbitals to any other final orbital results in a pair of doublet final excited states, depending on the coupling of electron spins [82]. Similarly, core ionization leads to the $^3\mathrm{A}_1$ and $^1\mathrm{A}_1$ states of NO_2^+ [84,85]. The splitting caused by interaction between the two O $1s$ orbitals ($1b_2$ and $1a_1$) is expected to be negligibly small due to their essentially atomic-like nature. The dipole-allowed transitions for NO_2 are shown in table 4.3.

Fig. 4.5 shows the measured low-resolution (0.14 eV FWHM) ISEELS and MCQD calculated N $1s$ excitation spectra of NO_2 in the discrete (pre-ionization edge) and ionization continuum regions. The absolute differential oscillator strength scale was established using procedures described below. The NO_2 sample was purified as explained in section 3.4 above (see also further discussion below), but a very small amount of residual NO is still present. Fig. 4.6 shows the high-resolution (0.090 eV FWHM) N $1s$ ISEELS spectrum of the pre-ionization edge region for an NO_2 sample of higher purity, together with the MCQD calculation. The MCQD calculated oscillator strengths are presented in the discrete and continuum transition regions, as discussed in section 4.1. The measured energies and oscillator strengths together with the calculated oscillator strengths and

Table 4.3: Dipole-allowed transitions in NO_2 from the $^2A_1$ ground state for C_{2v} symmetry

Final configuration		Dipole-allowed
core hole orbital	occupied virtual MO	final state
a_1	a_1	$1^2A_1, 2^2A_1$ [a]
a_1	b_1	$1^2B_1, 2^2B_1$ [a]
a_1	b_2	$1^2B_2, 2^2B_2$ [a]
a_2	b_1	$1^2B_2, 2^2B_2$
a_2	b_2	$1^2B_1, 2^2B_1$
b_1	a_1	$1^2B_1, 2^2B_1$ [a]
b_1	b_1	$1^2A_1, 2^2A_1$
b_2	a_1	$1^2B_2, 2^2B_2$ [a]
b_2	b_2	$1^2A_1, 2^2A_1$
a_1	continuum	$^3A_1, ^1A_1$
a_2	continuum	$^3A_2, ^1A_2$
b_1	continuum	$^3B_1, ^1B_1$
b_2	continuum	$^3B_2, ^1B_2$

[a] Only one doublet state will result from transitions to final states in which the $6a_1$ orbital is doubly occupied or empty.

term values are shown in table 4.4. Also shown are the assignments based on a consideration of the MCQD calculations. The energies of the $^3A_1$ and $^1A_1$ N 1*s* ionization edges are assigned according to XPS measurements [84,85,86] using the triplet-singlet splitting of 0.70 eV reported by Davis *et al.* [84]. The energies of features 1 and 2 are close to the values reported for the two largest peaks in the N 1*s* photoabsorption spectrum (see fig. 4.8b below) of NO_2 from ref. [82], but peak 1 is much less intense relative to peak 2 in the ISEELS spectrum. The small peak, just below 400 eV, barely visible in fig. 4.5b but present to a much larger extent in the photoabsorption spectrum [82], is clearly due to the presence of a small amount of an NO impurity (see discussion below) which has

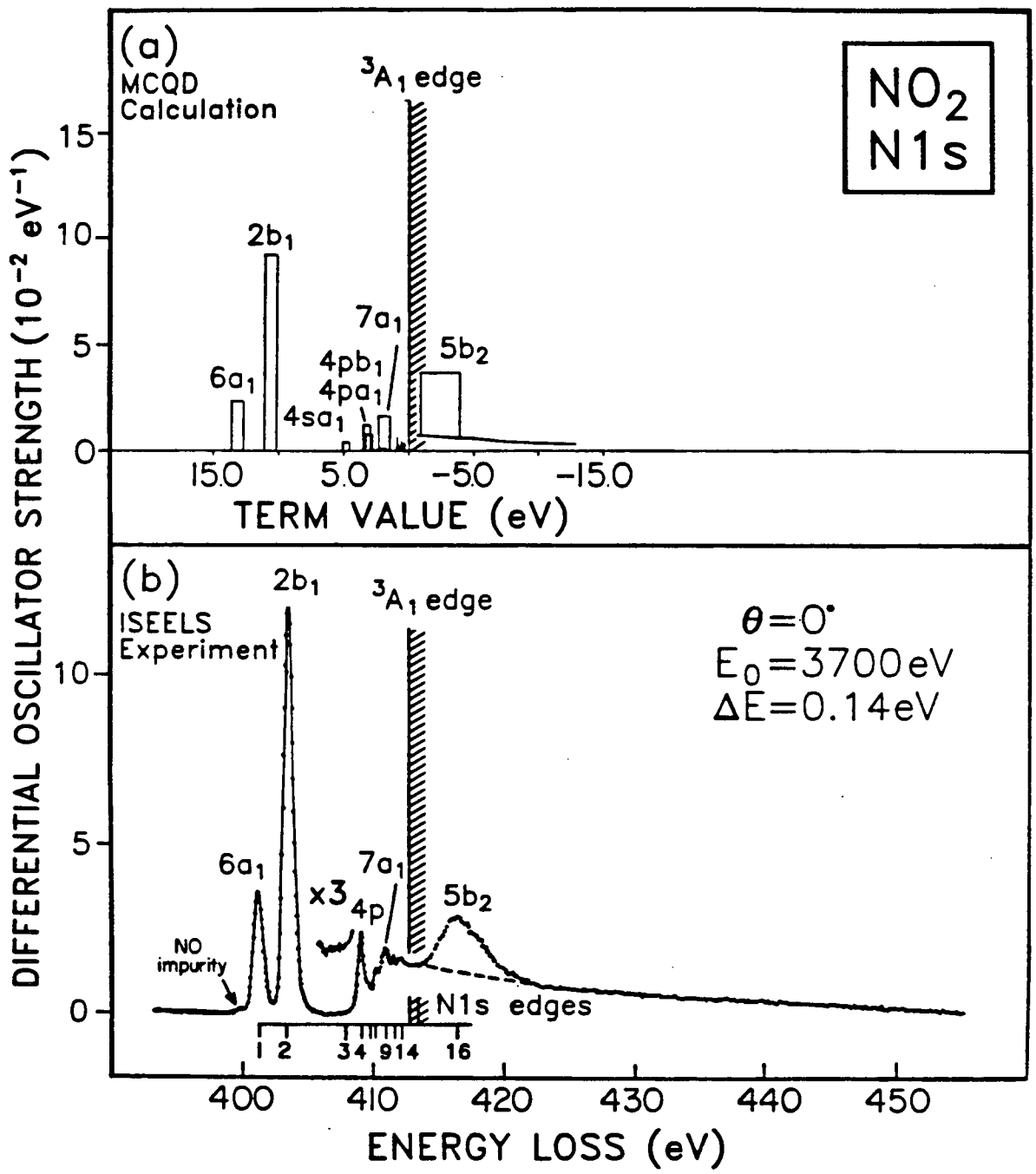

Figure 4.5: (a) MCQD calculation and (b) low-resolution N 1*s* ISEELS spectrum of NO_2 in the discrete and continuum regions. Spectrum (b) as shown is not Bethe-Born corrected.

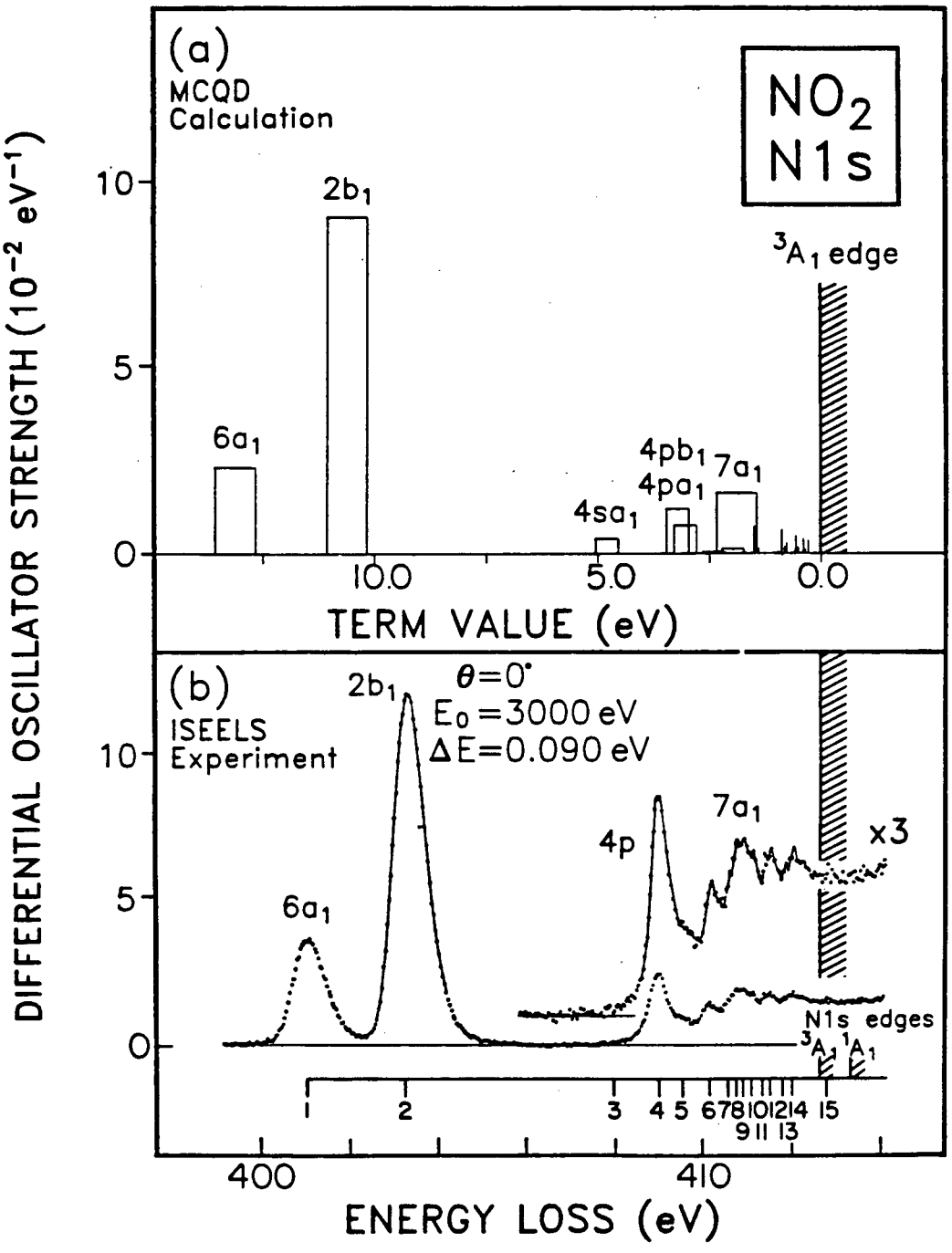

Figure 4.6: (a) MCQD calculation and (b) high-resolution N 1*s* ISEELS spectrum of NO_2 in the pre-ionization edge region. Spectrum (b) as shown is not Bethe-Born corrected.

Table 4.4: Experimental and calculated data[a] for N 1*s* excitation of NO_2

Experimental [this work]					MCQD calculation		
feature	energy (eV)	term value		oscillator[b] strength ($\times 10^{-2}$)	term value[c] (eV)	oscillator strength ($\times 10^{-2}$)	assignment final orbital (to $^3A_1$ limit)[d]
		$^3A_1$	$^1A_1$[d]				
1	401.04	11.56		2.7	13.12	2.10	$6a_1$
2	403.28	9.32		8.9	10.62	8.26	$2b_1(b_1^*)$
3	$\sim$ 408	$\sim$ 5			4.80	0.20	$4sa_1$
4	408.92	3.68			3.22	0.60	$4pb_1$
5	409.48	3.12	(3.82)		3.05	0.38	$4pa_1$
6	410.08	2.52	(3.22)		2.40	0.02	$4pb_2$
7	410.48	2.12	(2.82)		1.98	0.06	$5sa_1$
8	410.68	1.92	(2.62)		1.89	1.46	$7a_1(a_1^*)$
9	410.84	1.76	(2.46)		1.70	0.04	$3db_1$
10	411.04	1.56	(2.26)		1.50	0.72	$3d_2a_1$
					1.44	0.18	$5pb_1$
11	411.28	1.32	(2.02)		1.39	0.14	$5pa_1$
12	411.52	1.08	(1.78)		0.96	0.02	$4db_1$
					0.89	0.30	$4d_0a_1$
13	411.76	0.84	(1.54)		0.82	0.08	$6pb_1$
					0.80	0.06	$6pa_1$
					0.78	0.10	$4d_2a_1$
					0.60	0.02	$5db_1$
14	411.96	0.64	(1.34)		0.57	0.12	$5d_0a_1$
					0.53	0.04	$7pb_1$
					0.52	0.02	$7pa_1$
					0.51	0.02	$5d_2a_1$
					0.40	0.06	$6d_0a_1$
					0.36	0.02	$6d_2a_1$
					0.29	0.04	$7d_0a_1$
IP($^3A_1$)	412.6[e]	0			0	—	∞
15	412.72		(0.58)				
IP($^1A_1$)	413.30[e]		0				
16	416.16	-3.56		7.3	-2.45	9	$5b_2(b_2^*)$

[a] See fig. 4.5 and 4.6.
[b] A kinematic Bethe-Born conversion of $E^{2.5}$ has been applied.
[c] With respect to the $^3A_1$ limit.
[d] Note assignment for $^1A_1$ term value must be interpolated since MCQD calculation is shown for $^3A_1$ terms only.
[e] $^3A_1$,$^1A_1$, IPs from XPS [84,85,86].

an intense N $1s \rightarrow \pi^*$ band at 399.7 eV [51,87,88,89]. Much larger contributions from NO were found in spectra produced from gas samples taken directly from commercially supplied gas bottles of NO_2 without any further purification. The NO contribution in the NO_2 could be diminished to an almost negligible level (as shown in figs. 4.6b and 4.7a) by repeated freezing, pumping and thawing cycles of the gas cylinder.

The presence of impurities may be the reason for the significant differences between the spectral features observed in the present ISEELS N $1s$ and O $1s$ spectra of NO_2 and those shown in the previously published photoabsorption results [82]. Therefore a careful study has been made of spectra obtained from commercial cylinders of NO_2 before and after fractionation. In addition, comparisons are made with the known ISEELS spectra of possible impurities. The results of these investigations are shown in fig. 4.7.

The peak at 399.5 eV observed in fig. 4.5b is clearly shown to be due to an NO impurity by the vibrational structure present in a high-resolution (0.068 eV FWHM) ISEELS spectrum obtained using a sample from an unfractionated commercial NO_2 cylinder (fig. 4.7b). This vibrational structure is identical in profile and energy position to that observed in an earlier reported high-resolution ISEELS spectrum of NO [88], which is shown as an insert in fig. 4.7b. A further possible impurity that could complicate NO_2 N $1s$ spectra is N_2, since peak 1 (N $1s \rightarrow 6a_1$) of the N $1s$ spectrum of NO_2 (see fig. 4.5b and table 4.4) is at 401.04 eV, whereas the intense $1s \rightarrow \pi^*(v = 1)$ peak of N_2 is known to be at 401.10 eV [51]. This is clearly shown by the spectra in fig. 4.7c. in which comparable amounts of N_2 and NO_2 were admitted simultaneously (see comparison of spectra 4.7c and 4.7d with 4.7a). The familiar pattern [21,51,89,90] of the vibrationally resolved N $1s \rightarrow \pi^*$ transition of N_2 can clearly be seen, superimposed on the NO_2 (N $1s \rightarrow 6a_1$) band at ~401 eV. Fig. 4.7d shows the spectrum when the relative contribution of N_2 is greatly increased. Fig. 4.7a shows the same spectral region for an NO_2 sample

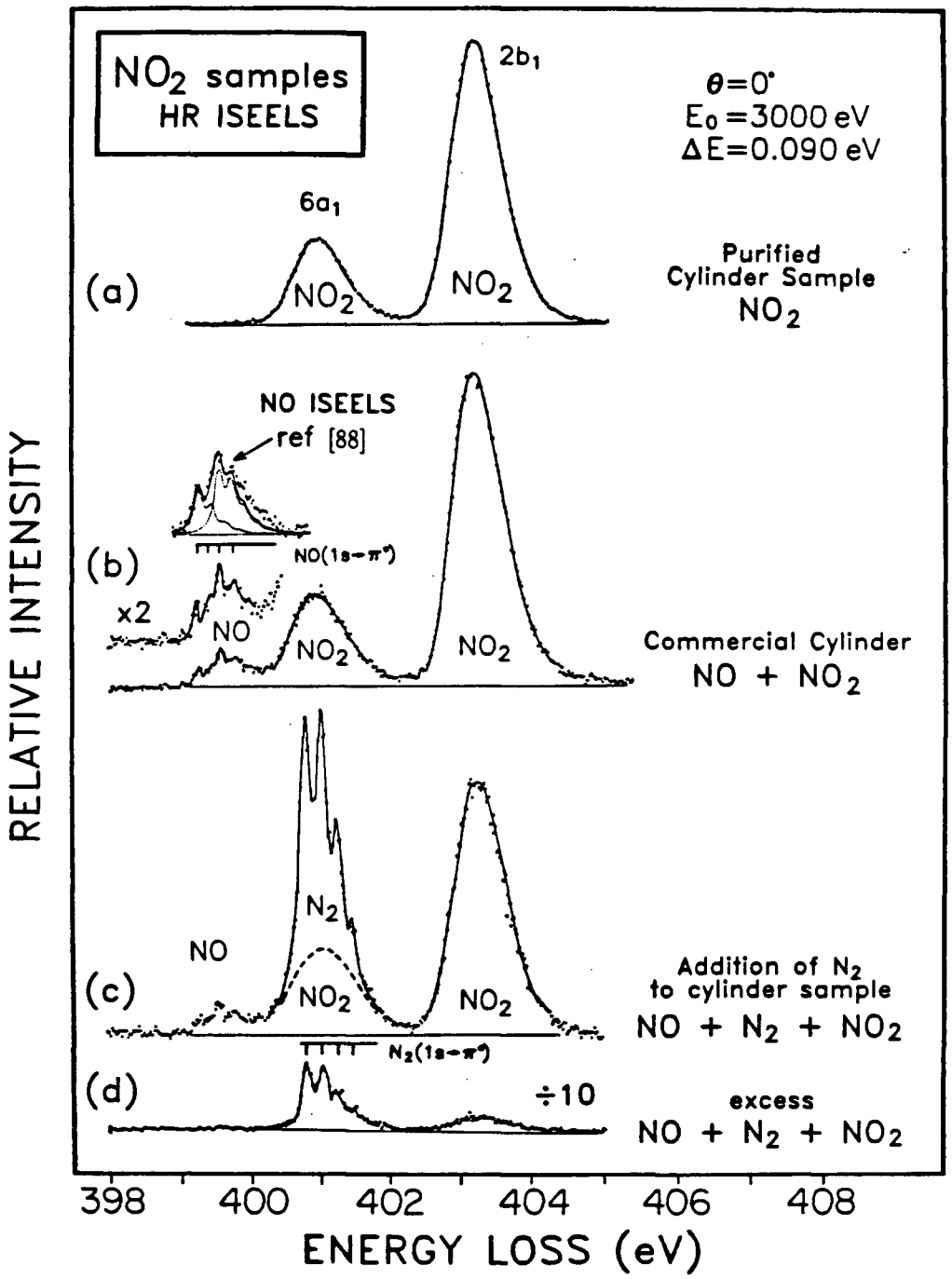

Figure 4.7: Investigation of sample purity in NO_2 cylinders by high resolution ISEELS measurements in the N 1*s* region: (a) purified NO_2; (b cylinder NO_2 (unpurified) showing NO impurity and the high resolution NO spectrum of Tronic *et al.* [88]; (c) Addition of N_2 to cylinder NO_2; (d) same as (c) but with excess N_2.

that has been purified by repeated freezing, pumping and thawing of the cylinder.

The earlier published photoabsorption results [82] show a prominent peak at ~400 eV in the N 1*s* spectrum and also a number of other significant differences from the present N 1*s* (figs. 4.5 and 4.6) and O 1*s* (see figs. 4.9 and 4.10 below) ISEELS spectra of NO_2. We have therefore digitized the previously published N 1*s* and O 1*s* photoabsorption spectra attributed to NO_2 [82] and transposed them from a wavelength (Å) to an energy scale (eV). The respective photoabsorption results (figs. 4.8b and 4.8f) are compared on the same energy scales with similar resolution N 1*s* ISEELS spectra of pure NO_2 (this work), N_2 [89], and NO [87] in figs. 4.8a–4.8d, and with O 1*s* ISEELS spectra of NO_2 (this work), O_2 [89], NO [87], and H_2O [91] in figs. 4.8e–4.8i. It should be noted that some differences in relative intensities may occur since the photoabsorption spectral intensities were presumably derived [82] from a photoplate. It can be concluded from a consideration of the data in figs. 4.7 and 4.8 that both the discrete and continuum regions of the inner-shell photoabsorption spectra [1] of ref. [82] contain appreciable contributions from impurities that probably include NO and N_2 in the case of N 1*s*, and O_2, NO, and H_2O in the case of O 1*s*. This implies that peaks attributed to double excitation in the photoabsorption spectra [82] are in fact due to impurity gases. In view of these considerations, no further comparison between the present ISEELS measurements and the experimental photoabsorption results of ref. [82] will be made for either the N 1*s* or O 1*s* spectra.

That the experimental N 1*s* ISEELS spectra obtained in the present work are of the NO molecule and contain no significant contributions from impurities is further confirmed by the MCQD calculations, which predict features that correspond extremely well with

[1] In comparing the various spectra, it should be noted that the uncertainties in the energy (wavelength) scales of the photoabsorption spectra [82] were stated to be to ± 0.4 eV (N 1*s* and ± 1 eV (O 1*s*). In the present ISEELS work the energy scales are considered to have an uncertainty of ± 0.02 eV.

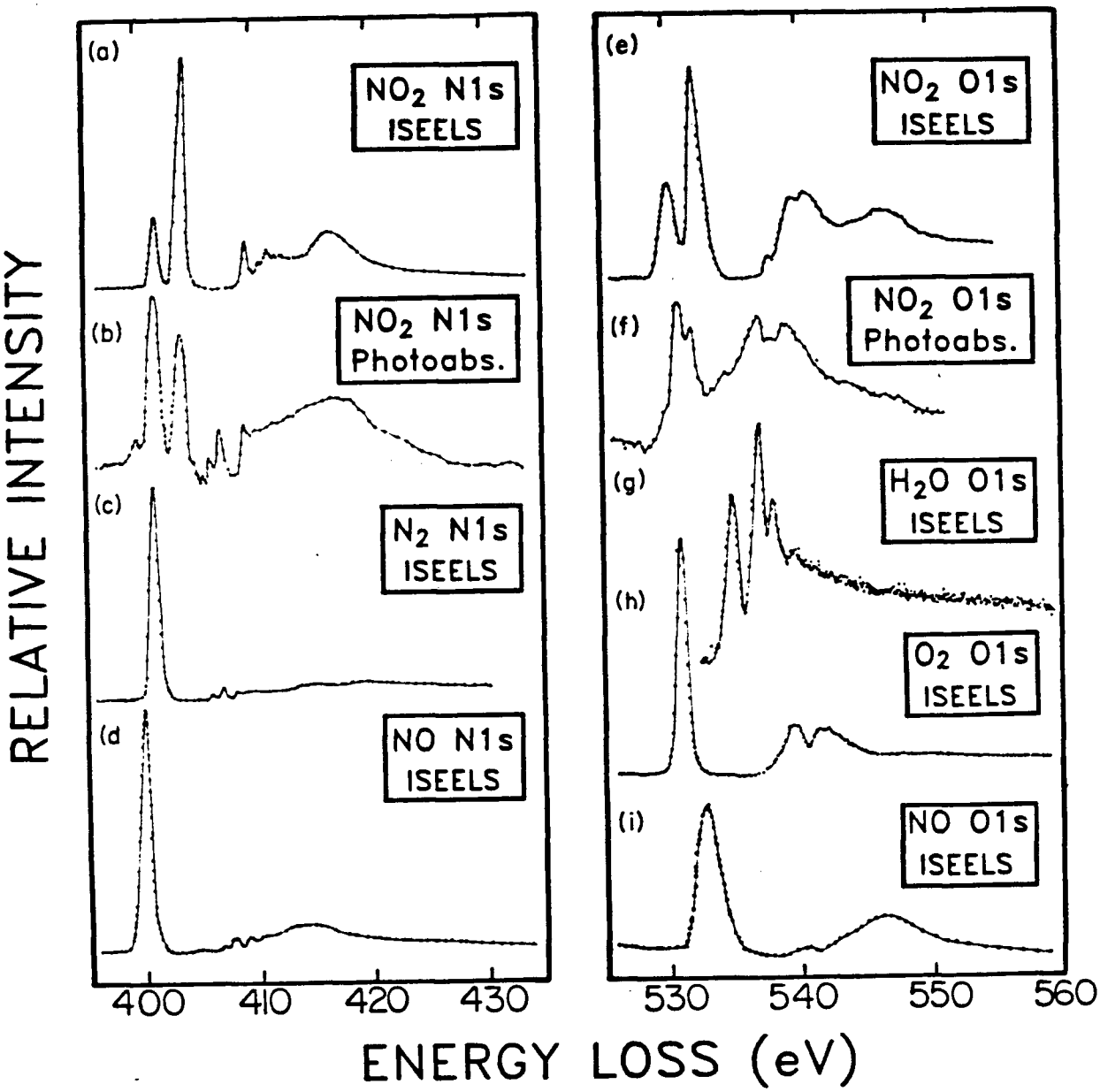

Figure 4.8: Comparison of N 1*s* and O 1*s* ISEELS spectra of NO_2 (a) and (e) with photoabsorption measurements (b) and (f) from ref. [82]. Also shown ((c) and (d)) are N 1*s* ISEELS spectra of N_2 [89] and NO [87], as well as O 1*s* ISEELS spectra of H_2O [91], O_2 [89] and NO [87] ((g) and (i), respectively).

the present experiment (but not the photoabsorption spectra [82]) with regard to both transition energies and relative intensities (see table 4.4 and figs. 4.5 and 4.6). The MCQD calculations are therefore used for the spectral assignments (see table 4.4 and figs. 4.5 and 4.6). There is a small difference between experimental and calculated energies for the N 1*s* to $6a_1$ and N 1*s* to $2b_1$ virtual-valence excitations, but agreement is quite good for the higher valence ($7a_1(a_1^*)$ and $5b_2(b_2^*)$) and Rydberg excitations. It should be noted that the $7a_1$ peak is both predicted and observed in the discrete portion of the spectrum. This is contrary to the conclusions of Schwarz *et al.* [82].

When an inner-shell electron in the open-shell molecule NO_2 is excited to an orbital above the (singly occupied) $6a_1$ orbital there will be three unpaired electrons and the final states accessible according to dipole selection rules are in two doublet series (1^2B_1, and 2^2B_1, for example [82]). Following Slater's treatment of three unpaired electrons [92,93], the wavefunctions of the two doublet states can be represented as linear combinations of the Slater determinants for the spin degenerate states. The coefficient of the linear combinations are determined by the interactions (exchange integrals) among the electrons and the relative intensities for the transitions to the two doublet states can be calculated accordingly. Two situations involving different couplings can be envisaged. In the first case, if one electron is far away from the other two electrons (i.e. the situation for higher Rydbergs or ionization) the two doublet states would result from weak coupling of the remote Rydberg (or ionized) electron with the two more strongly coupled electrons (in the core and $6a_1$ orbitals, respectively) and these states would be associated with the $^3A_1$ and $^1A_1$ ionization limits. In this situation the relative intensities of the doublet states would be [94] approximately 3 : 1, as observed in XPS measurements [84]. The second type of situation occurs when the three electrons are much closer together and this corresponds to excitation to the normally unoccupied virtual valence orbitals, which are of course quite

localized. In this situation all interactions between the three electrons are important and a consideration of the various couplings leads to relative intensities for transitions to the two doublet states leading to the $^3A_1$ and $^1A_1$ ion states of $p : 1$ (where $1 \leq p \leq 3$, depending on the interactions) with the lower-lying doublet state being the more intense. The unsymmetrical profiles of peaks 2 and 16 in the N 1*s* spectra (figs. 4.5b and 4.6b) and peaks 2 and 10 in the O 1*s* spectra (figs. 4.9b and 4.10b) of NO_2 are consistent with these considerations. Thus two doublet series are expected throughout the ISEELS spectra. However, the linewidths and densities of states, together with the lower relative intensity expected for those states leading to the higher energy $^1A_1$ limit, result in only the lower energy, higher intensity doublet series being clearly identifiable in the present work. The asymmetry of peaks 16 (N 1*s*, fig. 4.5) and 10 (O 1*s*, fig. 4.9) may alternatively be due to the inherent nature of continuum resonance line shapes, as discussed in refs. [96,97].

The MCQD calculation (table 4.4) predicts a relatively low intensity for the $4s(a_1)$ Rydberg state, which is at best rather weak (feature 3) on the low-energy side of feature 4 (see also the discussion below for the situation in the O 1*s* spectrum) in the measured spectrum (figs. 4.5b and 4.6b), in keeping with the fact that on the basis of a purely atomic-like selection rule a $1s \rightarrow 4s$ transition would be formally dipole forbidden. Such atomic-like selection rules have generally been found to be a reasonable guide for interpreting intensities of core-to-Rydberg molecular transitions, given the essential atomic-like character of both the initial and final orbitals [20]. In general, the predicted overall distribution of Rydberg intensity compares quite favorably with the high-resolution experimental spectrum (fig. 4.6). In the continuum (fig. 4.5) the position and intensity of the N 1*s* to $5b_2(b_2^*)$ resonance is fairly accurately predicted (table 4.4), as is the intensity of the underlying continuum relative to the discrete structure below the ionization edge (see fig. 4.5). A width of 3 eV has been assigned to the b_2^* resonance,

as indicated by the measured spectrum.

The presently obtained N 1*s* and O 1*s* inner-shell excitation spectra of NO_2 (see figs. 4.5b, 4.6b, 4.9b and 4.10b) have each been placed on an approximate absolute dipole (i.e. optical) differential oscillator strength scale, according to the normalization principles discussed in sections 2.3.4.3 and 2.3.8. The normalization procedures used were as follows. Firstly a straight-line extrapolation of the pre-ionization edge region below the respective $6a_1$ excited states was used to estimate a baseline for the respective inner-shell spectra. The lower resolution N 1*s* (fig. 4.5b) and O 1*s* (fig. 4.9b) spectra were then respectively normalized to the known atomic nitrogen 1*s* and twice the atomic oxygen 1*s* photoionization differential oscillator strengths [57,68,70], at 25 eV above the respective ionization edges. No kinematic Bethe-Born conversions (equations 2.35 and 2.36) were applied to the spectra shown in figs. 4.5b, 4.6b, 4.9b and 4.10b. While such conversions are of the order of $\sim E^b$ $(3 > b > 2)$ as approximated in equations 2.37 and 2.37, their effect in the N 1*s* and O 1*s* inner-shell region will be small (only about 20% and 15% variation, respectively) over the energy loss (E) ranges of the spectra shown in figs. 4.5b and 4.9b. The slightly higher resolution spectra (figs. 4.6b and 4.10b) were then normalized to the respective lower resolution spectra (figs. 4.6b and 4.9b). Despite the approximations and uncertainties in the procedure outlined above, it can be seen (figs. 4.5, 4.6, 4.9 and 4.10) that quite good agreement exists between the differential oscillator strength spectra obtained for the normalized experimental spectra and those derived from the MCQD calculations. The experimental optical oscillator strengths for transitions to the $6a_1$, $2b_1$ and $5b_2$ orbitals as shown in table 4.4 have been obtained by integrating the respective peak areas in figs. 4.5 and 4.6 and then applying an estimated Bethe-Born conversion factor of $E^{2.5}$. Good quantitative agreement exists between the measured and calculated values.

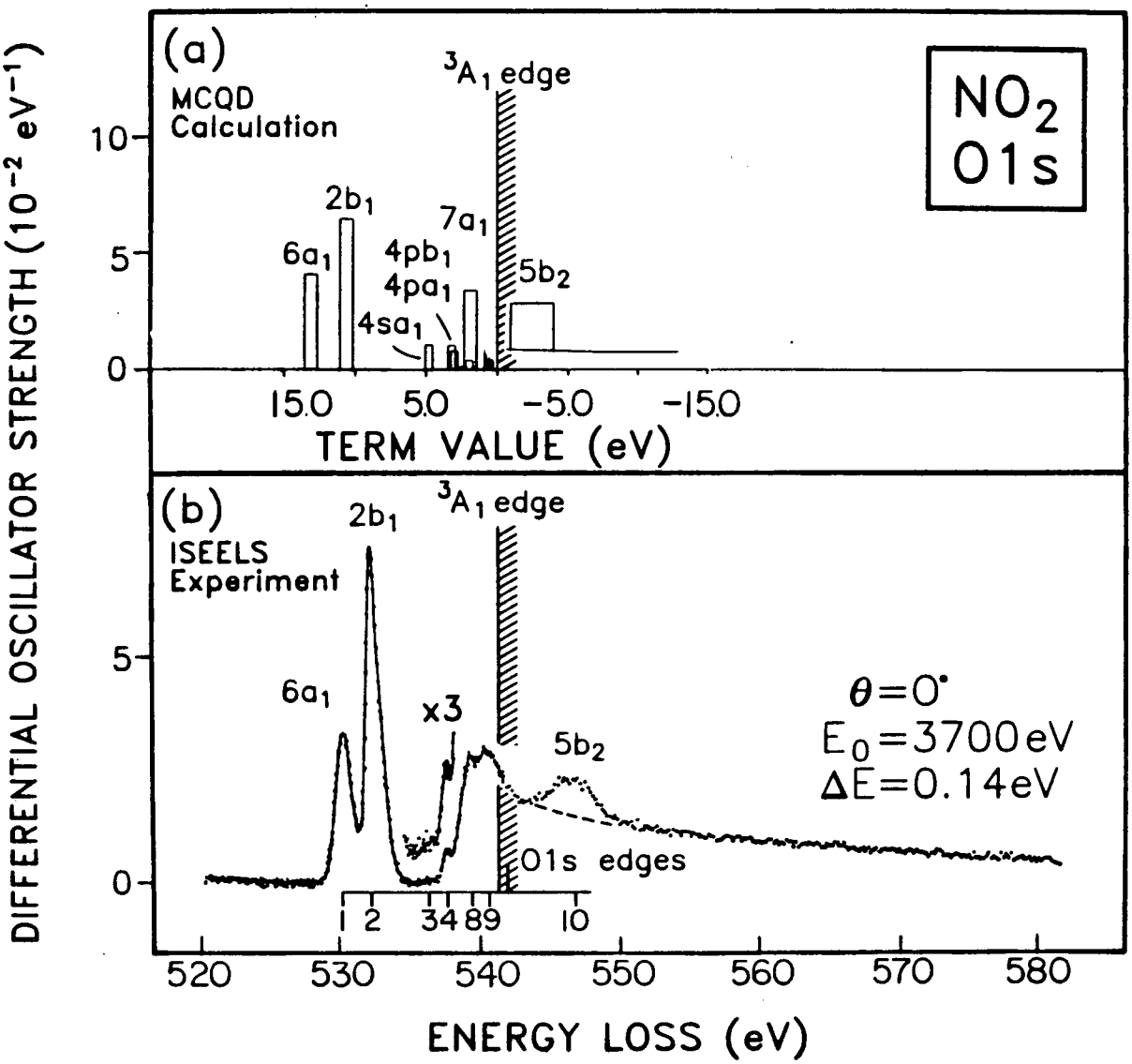

Figure 4.9: (a) MCQD calculation and (b) low-resolution O 1*s* ISEELS spectrum of NO_2 in the discrete and continuum regions. Spectrum (b) as shown is not Bethe-Born corrected.

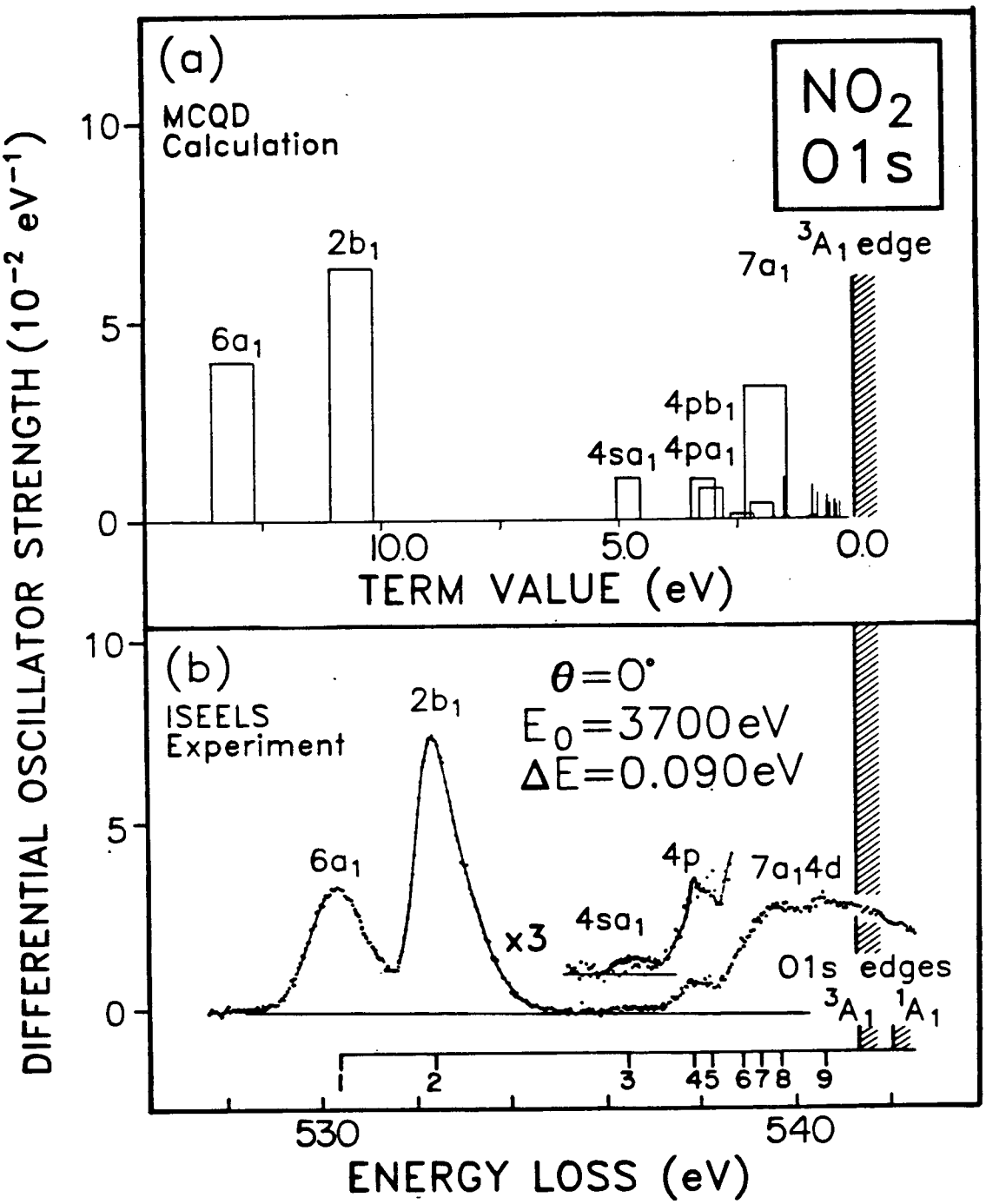

Figure 4.10: (a) MCQD calculation and (b) high-resolution O 1*s* ISEELS spectrum of NO_2 in the discrete region. Spectrum (b) as shown is not Bethe-Born corrected.

Table 4.5: Experimental and calculated data[a] for O 1*s* excitation of NO_2

Experimental [this work]					MCQD calculation		
feature	energy (eV)	term value		oscillator[b] strength	term value[c]	oscillator strength	assignment final orbital
		$^3A_1$	$^1A_1$[d]	($\times 10^{-2}$)	(eV)	($\times 10^{-2}$)	(to $^3A_1$ limit)[d]
1	530.32	10.98		4.1	13.12	3.68	$6a_1$
2	532.36	8.94		8.1	10.62	5.84	$2b_1(b_1^*)$
3	536.34	4.96			4.80	0.54	$4sa_1$
4	537.76	3.54	(4.21)		3.22	0.52	$4pb_1$
5	538.20	3.10	(3.77)		3.05	0.40	$4pa_1$
6	538.82	2.48	(3.15)		2.40	0.06	$4pb_2$
7	539.18	2.12	(2.79)		1.98	0.20	$5sa_1$
8	539.6	1.7	(2.37)		1.89	3.06	$7a_1(a_1^*)$
					1.70	0.08	$3db_1$
					1.50	1.06	$3d_2a_1$
					1.49	0.06	$3db_2$
					1.48	0.06	$3da_2$
					1.44	0.08	$5pb_1$
					1.39	0.06	$5pa_1$
					0.96	0.02	$4db_1$
9	540.52	0.78	(1.45)		0.89	0.40	$4d_0a_1$
					0.84	0.04	$4db_2$
					0.83	0.04	$4da_2$
					0.82	0.02	$6pb_1$
					0.80	0.02	$6pa_1$
					0.78	0.24	$4d_2a_1$
					0.60	0.02	$5db_1$
					0.57	0.14	$5d_0a_1$
					0.54	0.02	$5db_2$
					0.53	0.02	$5da_2$
					0.52	0.02	$7pb_1$
					0.52	0.02	$7pa_1$
					0.51	0.08	$5d_2a_1$
					0.40	0.06	$6d_0a_1$
					0.37	0.02	$6db_2$
					0.37	0.02	$6da_2$
					0.36	0.04	$6d_2a_1$
					0.29	0.04	$7d_0a_1$
IP($^3A_1$)	541.3[e]	0			0	—	∞
IP($^1A_1$)	541.97[e]		0				
10	547.18	-5.88		4.3	-2.45	6	$5b_2(b_2^*)$

[a] See fig. 4.9 and 4.10.

[b] A kinematic Bethe-Born conversion of $E^{2.5}$ has been applied.

[c] With respect to the $^3A_1$ limit.

[d] Note assignment for $^1A_1$ term value must be interpolated since MCQD calculation is shown for $^3A_1$ terms only.

[e] $^3A_1$, $^1A_1$, IPs from XPS [84,85,86].

Figs. 4.9a and 4.9b show the measured ISEELS O 1*s* spectra of NO_2 at low resolution (0.14 eV FWHM), together with the MCQD calculation. Fig. 4.10 shows the high-resolution experimental O 1*s* spectrum and the MCQD calculation in the below-edge region in somewhat greater detail. The approximate differential oscillator strength scale for the experimental spectra as shown in figs. 4.9 and 4.10 was established as described above. The measured energies and oscillator strengths together with calculated oscillator strengths and term values, are shown in table 4.5. Also shown are the assignments based on a consideration of the MCQD calculations. The values of the experimental oscillator strengths for transitions to the $6a_1$, $2b_1$ and $5b_2$ orbitals reported in table 4.5 include application of an estimated Bethe-Born conversion of $E^{2.5}$ to the peak areas in the spectra. The energies of the O 1*s* $^3A_1$ and $^1A_1$ ionization edges are assigned according to XPS measurements [84,85,86] using the singlet-triplet splitting of 0.67 eV reported by Davis *et al.* [84]. As has already been discussed with reference to fig. 4.8 the earlier reported O 1*s* photoabsorption spectrum of NO_2 contains major contributions from impurities, and thus no effective comparison with the present work can be made. While the MCQD calculation is in quite good quantitative agreement with respect to the transition energies and also the relative intensities observed in the present ISEELS work the differences with experiment are greater than in the case of the N 1*s* excitation (compare figs. 4.5 and 4.6 with figs. 4.9 and 4.10). These differences, particularly noticeable for the $6a_1$ and $2b_1$ states probably arise from the fact that the present calculations use C_{2v} symmetry for the O 1*s* excited and ionized states of NO_2 and thus do not take account of the broken symmetry caused by a localized 1*s* hole in one of the O atoms. It can be seen that the $4sa_1$ Rydberg state is clearly visible (feature 3) in figs. 4.9b and 4.10b in contrast to the situation in the N 1*s* spectrum where the corresponding transition is extremely weak. The greater intensity of the $4sa_1$ peak in the O 1*s* spectrum reflects a further relaxation

Table 4.6: Term values for N 1*s* and O 1*s* excitation of NO_2

Transition	Measured term value (eV) [a]		Estimated term value (eV) [b]
	$^3A_1$ limit	$^1A_1$ limit	from $(Z+1)$ analogue
N $1s \longrightarrow 6a_1$	11.6	12.3	11.4
N $1s \longrightarrow 2b_1$	9.3	10.0	8.7
N $1s \longrightarrow 7a_1$	1.9	2.6	4
N $1s \longrightarrow 5b_2$	-3.6	-2.9	–
O $1s \longrightarrow 6a_1$	11.0	11.7	–
O $1s \longrightarrow 2b_1$	8.9	9.6	–
O $1s \longrightarrow 7a_1$	1.7	2.4	–
O $1s \longrightarrow 5b_2$	-5.9	-5.2	–

[a] This work, from NO_2 ISEELS; see tables 4.4 and 4.5
[b] from data for valence-shell excitation of O_3 using geometry and exchange correction—see ref. [82].

of the atomic-like ($s \rightarrow s$) selection rule due to the broken symmetry. The below-edge $7a_1$ (a_1^*) final state (peak 8) is quite prominent, as is the above-edge b_2 (b_2^*) resonance. The MCQD calculation reproduces these features as well as the rest of the spectrum, quite well both for transition energies and oscillator strengths.

In accord with the equivalent core model discussed in section 2.3.7, the term values of the N 1*s* core excitations in NO_2 would be expected to be similar to those for the corresponding valence-shell excitations of the $(Z+1)$ analogue, O_3, if geometry and exchange corrections are taken into account [82]. This situation for core-excited NO_2 and valence-excited O_3 has been discussed in some detail by Schwarz *et al.* [82]. The term values of the O_3 valence excitation obtained from extensive CI calculations were adapted [82] to the NO_2 geometry and allowance was made for exchange effects (since core-excited NO_2 is open-shell). Table 4.6 shows the adapted O_3 valence-shell term values [82] in comparison with the presently measured N 1*s* term values for several transitions. A quite reasonable correspondence exists, given the various approximations

involved [82] in obtaining the estimated term values of O_3 valence excitation. In a similar fashion the term values for the O 1*s* excitations of NO (see table 4.6) could be used to obtain estimates of the valence-shell excitation energies of the species NOF.

A consideration of the data in tables 4.4–4.6 shows that the term values for given core-to-virtual-valence transitions show systematic differences, with the O 1*s* values being consistently lower than those for N 1*s*. In contrast, and as expected (see discussed in section 2.3.1), the term values for Rydberg transitions to the same final orbitals are almost identical for N 1*s* and O 1*s* excitation.

In conclusion, the present work demonstrates the use of high quality MCQD calculations of transition energies and oscillator strengths to provide definitive interpretations of high resolution inner-shell electronic excitation spectra for the NO_2 molecule.

Chapter 5

Absolute Differential Oscillator Strengths for the Photoabsorption and the Ionic Photofragmentation of CF_4, CF_3Cl, CF_2Cl_2 and $CFCl_3$

The relative photoabsorption spectra and time of flight (TOF) mass spectra used to derive absolute differential oscillator strengths (total and partial) for CF_4, CF_3Cl, CF_2Cl_2 and $CFCl_3$ were obtained using the dipole (e,e+ion) spectrometer described in section 3.1.

5.1 Electronic Structures

The point group symmetries for CF_4, CF_3Cl and $CFCl_3$, and CF_2Cl_2 are T_d, C_{3v} and C_{2v} respectively. The electronic state configurations of the ground states of CF_4, CF_3Cl, CF_2Cl_2 and $CFCl_3$ are shown in table 5.7. The electronic states produced by ionizing corresponding outer and inner valence orbitals of corresponding vertical ionization energies are summarized in tables 5.8–5.11. In addition, the carbon K and fluorine K-edges of CF_4 have been measured to be at 301.8 eV and 695.2 eV respectively by X-ray photoelectron spectroscopy [86].

5.2 Photoabsorption Differential Oscillator Strengths for the Valence Shells

The absolute photoabsorption differential oscillator strengths obtained in the present work for the valence shells of CF_4, CF_3Cl, CF_2Cl_2 and $CFCl_3$ are presented respectively in tables 5.12, 5.13, 5.14 and 5.15. They are shown diagrammatically in fig. 5.11a (12–100 eV), fig. 5.11b (70–200 eV) and (on an expanded scale) in fig. 5.11c (12–25 eV)

Table 5.7: Valence electronic configurations for the CF_4, CF_3Cl, CF_2Cl_2 and $CFCl_3$

Molecule	Inner valence orbitals	Outer valence orbitals
CF_4	$1a_1^2\ 1t_2^6$	$2a_1^2\ 2t_2^6\ 1e^4\ 3t_2^6\ 1t_1^6$
CF_3Cl	$1a_1^2\ 1e^4\ 2a_1^2$	$3a_1^2\ 2e^4\ 4a_1^2\ 3e^4\ 4e^4\ 1a_2^2\ 5a_1^2\ 5e^4$
CF_2Cl_2	$1a_1^2\ 1b_1^2\ 2a_1^2\ 1b_2^2$	$3a_1^2\ 2b_2^2\ 4a_1^2\ 2b_1^2\ 5a_1^2\ 1a_2^2\ 3b_1^2\ 3b_2^2\ 6a_1^2\ 2a_2^2\ 4b_1^2\ 4b_2^2$
$CFCl_3$	$1a_1^2\ 2a_1^2\ 1e^4$	$3a_1^2\ 4a_1^2\ 2e^4\ 3e^4\ 5a_1^2\ 4e^4\ 5e^4\ 1a_2^2$

Table 5.8: Electronic ion states produced by photoionizing valence electrons from the CF_4 ground state ($^1A_1$)

Electronic ion states	$\tilde{X}^2T_1$	$\tilde{A}^2T_2$	$\tilde{B}^2E$	$\tilde{C}^2T_2$	$\tilde{D}^2A_1$
Outer valence orbitals	$1t_1$	$3t_2$	$1e$	$2t_2$	$2a_1$
Vertical IPs (eV)[a]	16.20	17.40	18.50	22.12	25.12
Electronic ion states	$\tilde{E}^2T_2$	$\tilde{F}^2A_2$			
Inner valence orbitals	$1t_2$	$1a_1$			
Vertical IPs (eV)[b]	40.3	43.3			

[a]IPs of outer valence are from He I and He II PES measurement [99].
[b]IPs of inner valence are from PES measurement [86].

Table 5.9: Electronic ion states produced by photoionizing valence electrons from the CF_3Cl ground state ($^1A_1$)

Electronic ion states	$\tilde{X}^2E$	$\tilde{A}^2A_1$	$\tilde{B}^2A_2$	$\tilde{C}^2E$	$\tilde{D}^2E$	$\tilde{E}^2A_1$	$\tilde{F}^2E$	$\tilde{G}^2A_1$
Outer valence orbitals	$5e$	$5a_1$	$1a_2$	$4e$	$3e$	$4a_1$	$2e$	$3a_1$
Vertical IPs (eV)[a]	13.08	15.20	15.80	16.72	17.71	20.20	21.8	23.8
Electronic ion states	$\tilde{H}^2A_1$	$\tilde{I}^2E$	$\tilde{J}^2A_1$					
Inner valence orbitals	$2a_1$	$1e$	$1a_1$					
Vertical IPs (eV)[b]	26.9	40.0	42.5					

[a]IPs of outer valence are from He I and He II PES measurement [100].
[b]IPs of inner valence are from PES measurement presented in chapter 6.

Table 5.10: Electronic ion states produced by photoionizing valence electrons from the CF_2Cl_2 ground state ($^1A_1$)

Electronic ion states	$\tilde{X}^2B_2$	$\tilde{A}^2B_1$	$\tilde{B}^2A_2$	$\tilde{C}^2A_1$	$\tilde{D}^2B_1$	$\tilde{E}^2B_1$
Outer valence orbitals	$4b_2$	$4b_1$	$2a_2$	$6a_1$	$3b_2$	$3b_1$
Vertical IPs (eV)[a]	12.26	12.53	13.11	13.45	14.36	15.9
Electronic ion states	$\tilde{F}^2A_2$	$\tilde{G}^2A_1$	$\tilde{H}^2B_1 + \tilde{I}^2A_1$	$\tilde{J}^2B_2$	$\tilde{K}^2A_1$	
Outer valence orbitals	$1a_2$	$5a_1$	$2b_1, 4a_1$	$2b_2$	$3a_1$	
Vertical IPs (eV)[a]	16.30	16.9	19.3	20.4	22.4	
Electronic ion states	$\tilde{L}^2B_1 + \tilde{M}^2A_1$	$\tilde{N}^2B_1$	$\tilde{O}^2A_1$			
Inner valence orbitals	$1b_2, 2a_1$	$1b_1$	$1a_1$			
Vertical IPs (eV)[b]	27.2	38.6	41.1			

[a]IPs of outer valence are from He I and He II PES measurement [100].
[b]IPs of inner valence are from PES measurement presented in chapter 6.

Table 5.11: Electronic ion states produced by photoionizing valence electrons from the $CFCl_3$ ground state ($^1A_1$)

Electronic ion states	$\tilde{X}^2A_1$	$\tilde{A}^2E$	$\tilde{B}^2E$	$\tilde{C}^2A_1$	$\tilde{D}^2E$	$\tilde{E}^2E$	$\tilde{F}^2A_1$	$\tilde{G}^2A_1$
Outer valence orbitals	$1a_2$	$5e$	$4e$	$5a_1$	$3e$	$2e$	$4a_1$	$3a_1$
Vertical IPs (eV)[a]	11.73	12.13	12.97	13.45	15.05	18.0	18.4	21.5
Electronic ion states	$\tilde{H}^2E$	$\tilde{I}^2A_1$	$\tilde{J}^2A_1$					
Inner valence orbitals	$1e$	$2a_1$	$1a_1$					
Vertical IPs (eV)[b]	25.3	27.6	40.0					

[a]IPs of outer valence are from He I and He II PES measurement [100].
[b]IPs of inner valence are from PES measurement presented in chapter 6.

Table 5.12: Absolute differential oscillator strengths for the total photoabsorption and the dissociative photoionization of CF_4

Photon energy (eV)	Differential oscillator strength ($10^{-2}eV^{-1}$) [a]							Ionization efficiency η_i
	Photo-absorption	CF_3^+	CF_2^+	CF^+	F^+	C^+	CF_2^{2+}	
12.0	0.91							
12.5	2.38							
13.0	10.50							
13.5	22.25							
14.0	21.38							
14.5	13.83							
15.0	14.58							
15.5	23.92	0.81						0.03
16.0	26.28	3.64						0.14
16.5	27.95	7.80						0.28
17.0	29.99	14.95						0.50
17.5	32.89	22.47						0.68
18.0	35.57	29.85						0.84
18.5	36.69	34.22						0.93
19.0	39.64	37.48						0.95
19.5	40.89	39.69						0.97
20.0	42.11	42.11						1.00 [b]
20.5	45.70	45.64	0.06					
21.0	48.61	48.49	0.12					
21.5	50.61	49.86	0.75					
22.0	52.36	50.19	2.17					
22.5	52.27	48.13	4.14					
23.0	51.39	46.24	5.15					
23.5	49.15	43.83	5.31					
24.0	48.17	42.95	5.22					
24.5	46.91	42.18	4.73					
25.0	45.11	41.01	4.11					

continued on next page

[a] $\sigma(\mathrm{Mb}) = 1.0975 \times 10^2 (\mathrm{d}f/\mathrm{d}E)(\mathrm{eV}^{-1})$.

[b] The photoionization efficiency is constant and therefore assumed to be unity above 20.0 eV, see section 5.4 and the insert to fig. 5.11a for details.

Table 5.12: (continued)

Photon energy (eV)	Differential oscillator strength (10^{-2}eV^{-1}) [a]							Ionization efficiency η_i
	Photo-absorption	CF_3^+	CF_2^+	CF^+	F^+	C^+	CF_2^{2+}	
25.5	42.37	38.72	3.65					
26.0	40.83	37.82	3.01					
26.5	40.19	37.60	3.59					
27.0	39.57	37.19	2.38					
27.5	39.02	37.00	2.02					
28.0	39.03	37.25	1.78					
28.5	38.71	37.00	1.71					
29.0	38.91	37.29	1.62					
29.5	38.95	37.24	1.64	0.07				
30.0	38.91	37.15	1.65	0.12				
31.0	38.78	36.86	1.67	0.26				
32.0	38.59	36.30	1.73	0.56				
33.0	39.42	36.63	1.90	0.89				
34.0	39.79	36.56	1.98	1.24				
35.0	39.55	35.58	2.14	1.70	0.07	0.06		
36.0	39.42	34.95	2.13	1.99	0.15	0.21		
37.0	38.76	33.68	2.15	2.19	0.28	0.45		
38.0	39.39	33.59	2.22	2.34	0.46	0.78		
39.0	39.21	32.61	2.27	2.49	0.65	1.20		
40.0	38.99	31.77	2.37	2.34	0.86	1.66		
41.0	38.65	31.09	2.37	2.04	1.12	2.03		
42.0	37.08	30.07	2.24	1.81	1.15	1.82		
43.0	35.24	28.59	2.24	1.50	1.23	1.68		
44.0	33.38	27.10	2.12	1.27	1.23	1.61	0.05	
45.0	31.37	25.61	2.07	1.14	1.24	1.27	0.04	
46.0	30.01	24.64	1.92	1.09	1.14	1.12	0.09	
47.0	29.05	23.75	1.91	1.01	1.21	1.06	0.12	
48.0	27.99	22.96	1.78	0.99	1.16	0.99	0.12	
49.0	27.07	22.00	1.69	1.01	1.15	1.05	0.17	
50.0	26.37	21.48	1.54	0.94	1.26	1.02	0.13	
55.0	23.92	18.39	1.48	1.07	1.60	1.22	0.15	

continued on next page

[a] $\sigma(\text{Mb}) = 1.0975 \times 10^2 (df/dE)(\text{eV}^{-1})$.

Table 5.12: (continued)

Photon energy (eV)	Differential oscillator strength (10^{-2}eV^{-1}) [a]							Ionization efficiency η_i
	Photo-absorption	CF_3^+	CF_2^+	CF^+	F^+	C^+	CF_2^{2+}	
60.0	22.45	16.69	1.43	1.13	1.79	1.17	0.23	
65.0	19.83	14.40	1.34	1.08	1.79	1.02	0.20	
70.0	18.09	12.84	1.24	0.98	1.89	0.94	0.20	
75.0	16.39	11.33	1.07	1.00	1.88	0.93	0.19	
80.0	15.02	10.11	0.96	0.97	1.88	0.93	0.17	
85.0	13.71							
86.0	13.23							
87.0	13.28							
88.0	12.73							
89.0	12.58							
90.0	12.56							
91.0	12.02							
92.0	11.76							
93.0	11.57							
94.0	11.55							
95.0	11.27							
96.0	11.08							
97.0	10.89							
98.0	10.73							
99.0	10.59							
100.0	10.39							
110.0	8.93							
120.0	7.63							
130.0	6.53							
140.0	5.63							
150.0	4.88							
160.0	4.39							
170.0	3.64							
180.0	3.12							
190.0	3.18							
200.0	2.61							

[a] $\sigma(\mathrm{Mb}) = 1.0975 \times 10^2 (\mathrm{d}f/\mathrm{d}E)(\mathrm{eV}^{-1})$.

Table 5.13: Absolute differential oscillator strengths for the total photoabsorption and the dissociative photoionization of CF_3Cl

Photon	Differential oscillator strength $(10^{-2}eV^{-1})^a$												Ionization
energy (eV)	Photo-absorption	CF_3Cl^+	CF_2Cl^+	CF_3^+	$CFCl^+$	CF_2^+	CCl^+	Cl^+	CF^+	F^+	C^+	CF_2Cl^{2+}	efficiency η_i
7.5	0.44												
8.0	0.34												
8.5	0.40												
9.0	4.42												
9.5	9.93												
10.0	9.35												
10.5	11.14												
11.0	20.75												
11.5	28.45												
12.0	30.60												
12.5	36.14	0.25		2.99									0.09
13.0	42.04	0.35		14.73									0.36
13.5	42.16	0.39		21.45									0.52
14.0	40.71	0.47		23.57	0.07								0.59
14.5	37.25	0.34	0.23	21.37	0.09								0.59
15.0	36.41	0.28	0.65	19.44	0.05								0.56
15.5	39.91	0.24	2.16	21.96	0.04								0.61
16.0	47.21	0.31	5.51	28.38	0.03								0.72
16.5	50.72	0.26	10.30	30.66	0.06								0.81
17.0	53.06	0.26	14.48	32.61	0.07								0.89
17.5	54.26	0.32	17.25	32.30	0.08								0.92
18.0	56.10	0.30	19.16	33.72	0.10								0.95
18.5	57.44	0.24	20.35	34.53	0.09								0.96
19.0	57.30	0.34	21.16	35.10	0.06	0.24							0.99
19.5	56.29	0.19	20.63	32.88	0.08	0.72		0.39					0.98
20.0	56.15	0.18	18.97	30.92	0.05	1.29		1.20					0.94
20.5	56.50	0.30	18.21	30.87	0.10	2.45		2.34					0.96
21.0	56.48	0.21	16.20	28.43	0.09	5.09		3.78					0.95
21.5	56.38	0.24	15.04	26.78	0.17	6.88		4.14					0.94
22.0	57.39	0.24	15.78	27.18	0.24	8.15		4.69					0.98
22.5	57.04	0.22	16.18	26.92	0.30	8.72		4.70					1.00

continued on next page

[a] $\sigma(\text{Mb}) = 1.0975 \times 10^2 (df/dE)(eV^{-1})$.

Table 5.13: (continued)

Photon	Differential oscillator strength $(10^{-2}eV^{-1})^a$												Ionization
energy (eV)	Photo-absorption	CF_3Cl^+	CF_2Cl^+	CF_3^+	$CFCl^+$	CF_2^+	CCl^+	Cl^+	CF^+	F^+	C^+	CF_2Cl^{2+}	efficiency η_i
23.0	55.58	0.24	16.03	25.49	0.30	8.42		4.47	0.35				0.99
23.5	55.12	0.22	16.27	25.35	0.30	8.36		4.22	0.41				1.00[b]
24.0	53.38	0.14	16.25	24.09	0.28	7.95		4.21	0.46				
24.5	51.02	0.14	15.74	22.84	0.25	7.40		4.01	0.64				
25.0	49.98	0.21	15.81	21.76	0.27	7.11		4.05	0.77				
25.5	48.77	0.18	15.86	20.98	0.23	6.60		3.97	0.94				
26.0	47.07	0.20	15.50	19.86	0.21	6.13		4.05	1.11				
26.5	45.64	0.10	15.37	18.93	0.20	5.79		3.91	1.33				
27.0	44.39	0.13	15.40	17.96	0.16	5.47		3.80	1.48				
27.5	42.25	0.11	14.83	16.92	0.14	5.12		3.50	1.64				
28.0	40.95	0.06	14.72	15.80	0.16	4.90	0.03	3.64	1.64				
28.5	40.04	0.12	14.55	15.15	0.16	4.74	0.07	3.47	1.78				
29.0	39.36	0.08	14.64	14.40	0.12	4.62	0.09	3.51	1.89				
29.5	38.37	0.08	14.23	13.67	0.12	4.52	0.13	3.61	2.01				
30.0	37.66	0.06	14.22	13.09	0.13	4.46	0.15	3.57	1.98				
31.0	35.06	0.06	13.61	11.68	0.12	4.21	0.24	3.24	1.88				
32.0	33.67	0.04	13.33	10.57	0.08	4.08	0.29	3.32	1.96				
33.0	31.84	0.02	12.98	9.39	0.10	3.86	0.31	3.30	1.85		0.03		
34.0	31.59	0.02	12.83	8.70	0.09	4.10	0.43	3.36	1.86	0.06	0.15		
35.0	30.28	0.02	12.40	7.80	0.09	4.08	0.43	3.38	1.80	0.07	0.22		
36.0	29.35	0.02	11.95	7.14	0.12	4.05	0.46	3.47	1.71	0.10	0.33		
37.0	29.57	0.00	11.64	6.93	0.10	4.27	0.47	3.75	1.75	0.19	0.48		
38.0	29.44	0.00	11.47	6.47	0.10	4.35	0.52	3.88	1.73	0.24	0.62	0.05	
39.0	29.55	0.00	11.29	6.31	0.11	4.55	0.47	4.08	1.66	0.28	0.70	0.07	
40.0	28.70	0.00	10.62	6.05	0.10	4.55	0.42	4.23	1.56	0.32	0.75	0.09	

continued on next page

[a] $\sigma(\mathrm{Mb}) = 1.0975 \times 10^2 (df/dE)(\mathrm{eV}^{-1})$.

[b] The photoionization efficiency is constant and therefore assumed to be unity above 23.5 eV, see section 5.4 and the insert to fig. 5.12a for details.

Table 5.13: (continued)

Photon energy (eV)	Photo-absorption	Differential oscillator strength (10^{-2}eV^{-1})[a] CF_3Cl^+	CF_2Cl^+	CF_3^+	$CFCl^+$	CF_2^+	CCl^+	Cl^+	CF^+	F^+	C^+	CF_2Cl^{2+}	Ionization efficiency η_i
41.0	28.00	0.00	10.25	5.78	0.10	4.46	0.37	4.39	1.48	0.34	0.74	0.08	
42.0	26.54	0.00	9.59	5.51	0.10	4.31	0.32	4.09	1.44	0.37	0.71	0.08	
43.0	25.71	0.00	9.30	5.31	0.08	4.20	0.30	4.07	1.42	0.36	0.58	0.09	
44.0	24.48	0.00	8.81	5.11	0.11	3.96	0.25	3.88	1.36	0.36	0.56	0.09	
45.0	23.44	0.00	8.29	4.94	0.09	3.82	0.21	3.86	1.35	0.33	0.47	0.08	
46.0	22.17	0.00	7.89	4.75	0.08	3.59	0.20	3.54	1.29	0.32	0.41	0.10	
47.0	22.07	0.00	7.76	4.67	0.08	3.51	0.21	3.59	1.36	0.34	0.45	0.10	
48.0	20.98	0.00	7.33	4.50	0.07	3.27	0.20	3.40	1.32	0.35	0.44	0.09	
49.0	20.73	0.00	7.18	4.40	0.06	3.22	0.21	3.46	1.36	0.35	0.41	0.08	
50.0	19.95	0.00	6.92	4.21	0.07	3.02	0.19	3.32	1.36	0.37	0.40	0.08	
55.0	17.83	0.00	5.61	3.94	0.06	2.83	0.16	2.93	1.38	0.40	0.40	0.11	
60.0	16.28	0.00	4.95	3.36	0.02	2.59	0.15	2.81	1.37	0.49	0.45	0.08	
65.0	14.59	0.00	4.29	2.94	0.03	2.27	0.14	2.65	1.24	0.50	0.45	0.08	
70.0	13.19	0.00	3.85	2.64	0.05	2.07	0.12	2.32	1.11	0.50	0.43	0.09	
75.0	11.89	0.00	3.35	2.29	0.03	1.90	0.11	2.18	1.00	0.54	0.43	0.05	
80.0	11.03	0.00	3.06	2.10	0.02	1.64	0.11	2.08	0.95	0.59	0.41	0.07	
85.0	10.23												
90.0	8.96												
95.0	8.24												
100.0	7.95												
110.0	6.55												
120.0	5.63												
130.0	5.04												
140.0	4.29												
150.0	3.82												
160.0	3.55												
170.0	3.15												
180.0	2.82												
190.0	2.70												
200.0	2.55												

[a] $\sigma(\mathrm{Mb}) = 1.0975 \times 10^2 (\mathrm{d}f/\mathrm{d}E)(\mathrm{eV}^{-1})$.

Table 5.14: Absolute differential oscillator strengths for the total photoabsorption and the dissociative photoionization of CF_2Cl_2

Photon	Differential oscillator strength $(10^{-2}eV^{-1})^a$											Ionization
energy (eV)	Photo-absorption	$CFCl_2^+$	CF_2Cl^+	CCl_2^+	$CFCl^+$	CF_2^+	CCl^+	Cl^+	CF^+	F^+	C^+	CF_2Cl^{2+}	efficiency η_i
8.5	0.17												
9.0	6.08												
9.5	19.22												
10.0	26.20												
10.5	30.45												
11.0	38.00												
11.5	42.48		8.33										0.20
12.0	46.44		20.84										0.45
12.5	52.02		32.09										0.62
13.0	55.32		39.06										0.71
13.5	53.68		39.32										0.73
14.0	56.98	0.14	49.20										0.87
14.5	63.48	0.62	55.84										0.89
15.0	66.49	1.05	59.70										0.91
15.5	68.95	2.47	62.66										0.94
16.0	71.20	4.81	65.83										0.99
16.5	72.36	6.66	64.16										0.98
17.0	72.47	7.98	63.80										0.99
17.5	74.37	8.93	65.12			0.32							1.0 [b]
18.0	76.63	10.10	65.52			1.01							
18.5	79.73	10.32	66.72		0.34	2.36							
19.0	81.06	10.19	65.39		0.88	4.59							
19.5	81.55	9.82	63.33		1.47	6.93							
20.0	80.31	9.41	59.31		2.33	8.50		0.31	0.45				

continued on next page

[a] $\sigma(\text{Mb}) = 1.0975 \times 10^2 (df/dE)(eV^{-1})$.

[b] The photoionization efficiency is constant and therefore assumed to be unity above 17.5 eV, see section 5.2.3 and the insert to fig. 5.13a for details.

Table 5.14: (continued)

Photon energy (eV)	Photo-absorption	Differential oscillator strength (10^{-2}eV^{-1})[a]											Ionization efficiency η_i
		$CFCl_2^+$	CF_2Cl^+	CCl_2^+	$CFCl^+$	CF_2^+	CCl^+	Cl^+	CF^+	F^+	C^+	CF_2Cl^{2+}	
20.5	77.94	8.67	56.46	2.87	8.72		0.44	0.79					
21.0	75.44	8.18	53.74	3.16	8.69		0.70	0.97					
21.5	73.03	8.16	50.78	3.36	8.90		0.69	1.14					
22.0	71.08	7.82	48.02	3.67	8.90		0.95	1.72					
22.5	69.58	7.44	46.18	3.73	8.84		1.08	2.32					
23.0	68.21	7.14	44.43	3.84	9.16		0.95	2.68					
23.5	66.63	6.94	42.18	4.01	9.04		1.09	3.37					
24.0	65.08	6.79	40.07	4.00	8.85	0.21	1.33	3.82					
24.5	63.23	6.52	38.45	3.99	8.64	0.20	1.25	4.19					
25.0	61.86	6.64	37.02	3.53	8.35	0.35	1.15	4.82					
25.5	59.95	6.61	35.53	3.27	7.94	0.50	1.35	4.75					
26.0	57.02	6.60	33.23	2.95	7.53	0.64	1.45	4.61					
26.5	54.65	6.68	31.42	2.79	7.14	0.63	1.58	4.42					
27.0	52.10	6.41	29.48	2.55	6.89	0.78	1.66	4.32					
27.5	49.61	6.34	27.50	2.45	6.42	0.86	1.81	4.24					
28.0	47.39	6.30	25.92	2.20	6.61	0.91	1.97	3.97					
28.5	45.25	6.36	24.09	2.20	5.72	0.93	2.10	3.87					
29.0	43.28	6.21	22.54	2.04	5.72	1.05	2.08	3.64					
29.5	40.16	5.93	20.49	1.83	5.32	1.00	2.15	3.44					
30.0	39.60	6.06	19.81	1.85	5.21	1.01	2.18	3.49					
31.0	35.26	5.82	16.55	1.77	4.79	1.05	2.17	3.02			0.09		
32.0	32.82	5.54	14.74	1.61	4.58	1.05	2.24	2.83			0.23		
33.0	29.71	5.34	12.62	1.49	4.30	1.03	2.26	2.45			0.24		
34.0	27.11	4.99	10.71	1.53	3.99	0.89	2.34	2.30			0.36		
35.0	25.86	4.85	9.63	1.49	3.88	0.85	2.54	2.21			0.40		
36.0	24.68	4.61	8.71	1.42	3.73	0.83	2.70	2.09	0.15	0.45			
37.0	24.81	4.58	8.23	1.59	3.77	0.80	3.03	2.17	0.14	0.51			
38.0	23.71	4.42	7.49	1.54	3.60	0.71	3.10	2.07	0.16	0.57	0.05		

continued on next page

[a] $\sigma(\text{Mb}) = 1.0975 \times 10^2 (\mathrm{d}f/\mathrm{d}E)(\text{eV}^{-1})$.

Table 5.14: (continued)

Photon energy (eV)	Photo-absorption	Differential oscillator strength (10^{-2}eV^{-1})[a]											Ionization efficiency η_i
		$CFCl_2^+$	CF_2Cl^+	CCl_2^+	$CFCl^+$	CF_2^+	CCl^+	Cl^+	CF^+	F^+	C^+	CF_2Cl^{2+}	
39.0	22.84	4.30	7.03		1.50	3.51	0.70	3.16	1.96	0.14	0.51	0.04	
40.0	22.27	4.04	6.59		1.62	3.43	0.59	3.26	2.01	0.17	0.47	0.08	
42.0	21.20	3.78	6.07		1.56	3.23	0.56	3.21	2.14	0.19	0.37	0.09	
44.0	19.84	3.38	5.49		1.48	3.06	0.55	3.15	2.14	0.18	0.33	0.09	
46.0	18.49	3.04	5.12	0.02	1.35	2.77	0.52	3.00	2.10	0.17	0.30	0.09	
48.0	17.36	2.81	4.79	0.00	1.25	2.62	0.52	2.84	1.99	0.18	0.25	0.10	
50.0	16.73	2.63	4.66	0.02	1.19	2.54	0.55	2.74	1.87	0.20	0.26	0.08	
55.0	14.91	2.21	4.00	0.01	0.93	2.21	0.53	2.69	1.69	0.21	0.34	0.09	
60.0	13.83	1.85	3.69	0.02	0.90	2.04	0.50	2.73	1.52	0.23	0.30	0.05	
65.0	12.97	1.71	3.31	0.02	0.80	1.91	0.46	2.67	1.39	0.28	0.36	0.06	
70.0	11.75	1.54	2.95	0.02	0.72	1.66	0.44	2.42	1.25	0.31	0.34	0.09	
75.0	10.51												
80.0	9.94												
85.0	8.92												
90.0	8.32												
95.0	7.71												
100.0	6.91												
110.0	6.22												
120.0	5.41												
130.0	4.70												
140.0	4.07												
150.0	3.60												
160.0	3.25												
170.0	2.76												
180.0	2.63												
190.0	2.32												
200.0	4.08												

[a] $\sigma(\mathrm{Mb}) = 1.0975 \times 10^2 (\mathrm{d}f/\mathrm{d}E)(\mathrm{eV}^{-1})$.

Table 5.15: Absolute differential oscillator strengths for the total photoabsorption and the dissociative photoionization of $CFCl_3$

Photon energy (eV)	Photo-absorption	Differential oscillator strength $(10^{-2}eV^{-1})^a$									Ionization efficiency η_i
		CCl_3^+	$CFCl_2^+$	CCl_2^+	$CFCl^+$	CCl^+	Cl^+	CF^+	F^+	C^+	
6.0	0.39										
6.5	0.57										
7.0	1.14										
7.5	1.60										
8.0	3.03										
8.5	8.05										
9.0	25.57										
9.5	42.97										
10.0	48.32										
10.5	47.07										
11.0	48.04										
11.5	49.81		3.14								0.06
12.0	52.49		17.81								0.34
12.5	57.03		31.61								0.55
13.0	65.10		50.73								0.78
13.5	74.42		65.98								0.89
14.0	83.81	0.44	82.96								0.99
14.5	93.08	1.11	91.97								1.0[b]
15.0	93.57	1.51	92.06								
15.5	93.74	2.10	91.64								
16.0	90.87	2.31	88.57								
16.5	93.26	2.71	90.00		0.55						
17.0	95.39	3.00	91.23		1.16						
17.5	95.88	2.22	89.83	0.44	3.39						
18.0	94.85	1.76	85.35	1.06	6.21			0.47			
18.5	93.93	1.90	79.72	2.01	9.55		0.21	0.53			

continued on next page

[a] $\sigma(\mathrm{Mb}) = 1.0975 \times 10^2 (df/dE)(eV^{-1})$.

[b] The photoionization efficiency is constant and therefore assumed to be unity above 14.5 eV, see section 5.4 and the insert to fig. 5.14a for details.

Table 5.15: (continued)

Photon energy (eV)	Differential oscillator strength (10^{-2}eV^{-1})[a]										Ionization efficiency η_i
	Photo-absorption	CCl_3^+	$CFCl_2^+$	CCl_2^+	$CFCl^+$	CCl^+	Cl^+	CF^+	F^+	C^+	
19.0	92.48	1.59	75.05	2.75	11.62		0.33	1.13			
19.5	90.09	1.72	71.27	3.09	12.06		0.36	1.58			
20.0	90.26	1.45	69.77	3.37	12.62		0.53	2.52			
20.5	89.08	1.45	68.42	3.43	12.19		0.51	3.08			
21.0	88.64	1.27	66.78	3.75	12.38	0.24	0.47	3.74			
21.5	87.65	1.45	65.06	3.70	12.02	0.77	0.39	4.25			
22.0	86.05	1.40	63.14	3.74	11.73	1.17	0.63	4.23			
22.5	84.75	1.32	61.33	3.98	11.06	1.64	0.67	4.75			
23.0	78.88	1.23	55.55	3.65	10.34	2.48	0.69	4.94			
23.5	78.07	1.28	54.47	3.14	10.12	2.99	0.97	5.11			
24.0	73.61	1.14	51.16	3.20	8.80	3.42	1.09	4.80			
24.5	71.98	1.26	49.10	2.95	8.51	4.04	1.36	4.75			
25.0	68.33	1.14	46.14	2.73	7.92	4.24	1.87	4.30			
25.5	64.11	1.10	42.47	2.44	7.49	4.30	2.15	4.16			
26.0	61.75	1.02	40.91	2.23	7.25	4.37	2.33	3.64			
26.5	58.31	1.01	37.62	2.36	6.51	4.75	2.64	3.43			
27.0	55.14	0.98	35.11	2.00	6.39	4.59	2.79	3.28			
27.5	51.82	1.01	32.20	2.21	6.07	4.31	2.79	3.23			
28.0	50.19	0.96	30.48	2.16	6.07	4.46	2.88	3.19			
28.5	46.80	0.97	28.20	1.92	5.83	4.16	2.92	2.79			
29.0	43.74	0.85	25.81	1.90	5.48	3.91	2.80	2.80		0.19	
29.5	41.30	0.85	23.86	1.96	5.61	3.63	2.70	2.48		0.22	
30.0	37.54	0.83	21.37	1.77	4.87	3.25	2.84	2.32		0.29	
31.0	33.75	0.70	16.82	1.66	4.98	3.14	3.71	2.24		0.50	
32.0	29.07	0.68	13.79	1.53	4.49	2.64	3.60	1.80		0.53	
33.0	25.69	0.57	11.52	1.39	4.01	2.35	3.51	1.81		0.54	
34.0	22.12	0.44	9.51	1.27	3.59	2.01	3.24	1.57		0.47	
35.0	19.92	0.45	8.32	1.13	3.29	1.81	3.16	1.40		0.36	

continued on next page

[a] $\sigma(\text{Mb}) = 1.0975 \times 10^2 (\mathrm{d}f/\mathrm{d}E)(\text{eV}^{-1})$.

Table 5.15: (continued)

Photon energy (eV)	Differential oscillator strength (10^{-2}eV^{-1})[a]										Ionization efficiency η_i
	Photo-absorption	CCl_3^+	$CFCl_2^+$	CCl_2^+	$CFCl^+$	CCl^+	Cl^+	CF^+	F^+	C^+	
36.0	17.53	0.37	6.68	1.00	3.13	1.49	3.14	1.31		0.40	
37.0	17.57	0.38	6.25	1.22	3.23	1.48	3.28	1.39		0.35	
38.0	15.69	0.34	5.38	0.94	2.99	1.37	3.11	1.24	0.01	0.31	
39.0	15.09	0.32	5.14	1.03	2.75	1.34	2.99	1.18	0.03	0.30	
40.0	14.72	0.30	4.89	0.99	2.55	1.28	3.07	1.35	0.03	0.27	
41.0	14.22	0.31	4.52	0.98	2.60	1.28	2.97	1.26	0.03	0.26	
43.0	13.52	0.30	4.08	0.90	2.49	1.31	2.89	1.29	0.04	0.23	
45.0	12.92	0.26	3.83	0.85	2.27	1.29	2.90	1.26	0.04	0.23	
47.0	12.44	0.25	3.66	0.82	2.16	1.28	2.83	1.19	0.04	0.20	
49.0	11.59	0.21	3.46	0.73	1.93	1.20	2.70	1.11	0.03	0.20	
50.0	11.77										
52.0	11.19										
54.0	10.96										
56.0	10.93										
58.0	10.33										
60.0	10.17										
62.0	9.91										
64.0	9.60										
66.0	9.95										
68.0	9.47										
70.0	9.27										
72.0	8.83										
74.0	8.47										
76.0	8.16										
78.0	7.71										
80.0	7.75										
82.0	7.33										
84.0	7.54										

continued on next page

[a] $\sigma(\text{Mb}) = 1.0975 \times 10^2 (df/dE)(\text{eV}^{-1})$.

Table 5.15: (continued)

Photon energy (eV)	Differential oscillator strength (10^{-2}eV^{-1})[a]										Ionization efficiency η_i
	Photo-absorption	CCl_3^+	$CFCl_2^+$	CCl_2^+	$CFCl^+$	CCl^+	Cl^+	CF^+	F^+	C^+	
86.0	7.10										
88.0	7.08										
90.0	6.98										
92.0	6.17										
94.0	6.02										
96.0	6.10										
98.0	6.10										
100.0	6.02										
105.0	5.62										
110.0	5.13										
115.0	4.98										
120.0	4.65										
125.0	4.34										
130.0	4.07										
135.0	3.77										
140.0	3.54										
145.0	3.34										
150.0	3.10										
155.0	3.01										
160.0	2.79										
165.0	2.73										
170.0	2.57										
175.0	2.46										
180.0	2.37										
185.0	2.21										
190.0	2.04										
195.0	2.16										
200.0	3.31										

[a] $\sigma(\mathrm{Mb}) = 1.0975 \times 10^2 (\mathrm{d}f/\mathrm{d}E)(\mathrm{eV}^{-1})$.

for CF_4; in fig. 5.12a (7.5–100 eV), fig. 5.12b (70–200 eV) and fig. 5.12c (7.5–35 eV) for CF_3Cl; in fig. 5.13a (8.5–100 eV), fig. 5.13b (70–200 eV) and fig. 5.13c (8.5–36 eV) for CF_2Cl_2; and in fig. 5.14a (6–100 eV), fig. 5.14b (65–200 eV) and fig. 5.14c (6–38 eV) for $CFCl_3$.

The absolute photoabsorption values for CF_4, CF_3Cl, CF_2Cl_2 and $CFCl_3$ were obtained in the present work using the partial TRK sum-rule as discussed in sections 2.1 and 2.3.8. The total areas under the relative photoabsorption spectra (i.e. the Bethe-Born converted electron energy loss spectra) were normalized to total integrated oscillator strengths of 33.18, 33.18, 33.17 and 33.17 respectively. These sums correspond to 32 valence electrons for each of the four molecules CF_4, CF_3Cl, CF_2Cl_2 and $CFCl_3$ plus estimated contributions of 1.18, 1.18, 1.17 and 1.17 respectively for the Pauli excluded transitions from the inner shells to the already occupied valence shell orbitals [112]. The fractions of the areas above 200 eV for CF_4 and CF_3Cl, and above 190 eV and 195 eV for CF_2Cl_2 and $CFCl_3$ respectively were estimated from extrapolation by fitting a curve of the form:

$$\frac{df}{dE} = AE^{-1.5} + BE^{-2.5} + CE^{-3.5} \tag{5.41}$$

to the experimental data over the energy ranges 70–200 eV for CF_4 and CF_3Cl, 70–190 eV for CF_2Cl_2 and 65–195 eV for $CFCl_3$, and then integrating the respective equations from the upper energy limit of the above fitting ranges to infinity (df/dE is the differential oscillator strength, E is the excitation energy and A, B and C are constants). A similar approach has been used by Dillon and Inokuti to fit an analytical function to measured differential oscillator strengths [113]. The presently used procedure has been found to provide a very good fit to experimental data in a series of other measurements [16,114, 115]. The best fit (see figs. 5.11b, 5.12b, 5.13b and 5.14b) was determined by the method of least squares using a computer program written by Dr. G. Cooper for the purpose.

Table 5.16: The coefficients of the extrapolating formula (equation 5.41) for CF_4, CF_3Cl, CF_2Cl_2 and $CFCl_3$

Molecules	Fitting coefficients		
	A	B	C
CF_4	18.439	1.4625×10^4	-5.9640×10^5
CF_3Cl	49.004	4.7303×10^3	-1.9156×10^5
CF_2Cl_2	38.348	5.9654×10^3	-2.6863×10^5
$CFCl_3$	43.662	3.6390×10^3	-2.1182×10^5

For the present data the so obtained best fit coefficients A, B and C for each of CF_4, CF_3Cl, CF_2Cl_2 and $CFCl_3$ are summarized in table 5.16. The extrapolated portions of oscillator strength with respect to the total oscillator strengths are 17.0% and 23.8% respectively for CF_4 and CF_3Cl from 200 eV to infinity, 20.7% for CF_2Cl_2 from 190 eV to infinity, and 21.0% for $CFCl_3$ from 195 eV to infinity. The accuracy of the absolute differential oscillator strength scales is estimated to be better than $\pm 5\%$. An indication of the random errors is given by the smoothness of the data in various continuum regions.

When comparing the present results with other work in the following sections, it should be noted that the dipole (e,e) technique has constant energy resolution (1 eV FWHM) at all photon energies, whereas the photoabsorption techniques have an energy resolution (i.e. $\Delta\lambda/\lambda^2$) which becomes broader with increasing photon energy [20,75]. Another feature of the present work that should be remembered in comparing and assessing the various data sets is that the present dipole (e,e) measurements, unlike the other determinations, have the advantage of an absolute scale determined by the partial TRK sum rule and thus they are further constrained by the requirements of the total oscillator strength sum.

5.2.1 The CF_4 Photoabsorption Differential Oscillator Strengths

The presently reported measurements on CF_4 are compared with previously reported photoabsorption [101,102] as well as photoionization data (sum of $(\tilde{X}+\tilde{A}+\tilde{B}+\tilde{C}+\tilde{D})$ states only, without including the inner valence states $\tilde{E}$ and $\tilde{F}$) [105] obtained using tunable light sources in fig. 5.11a. In fig. 5.11c, photoabsorption data obtained in the low photon energy region with the Hopfield He II continuum as a radiation source [103] and also data derived from small momentum transfer electron impact measurements [104] are shown on an expanded scale.

The only pre-ionization edge structure clearly observed is a peak at 13.5 eV which has been assigned as the Rydberg transition $1t_1 \rightarrow 3p$ [116], while the other Rydberg transitions heavily overlap each other. A maximum at 22 eV and a broad feature at ~40 eV are observed. The data of Lee *et al.* [101] shows the same maximum and broad feature. In the region 33–69 eV, the agreement between our data and that of Lee *et al.* [101] is quite good. However, in the 16–36 eV energy region, the data of Lee *et al.* is higher than the present results. Similar discrepancies in this same energy region (16–24 eV) have also been observed in the comparisons between our results (figs. 5.12 and 5.13) and those of Lee *et al.* [101] and Wu *et al.* [110] for the molecules CF_3Cl and CF_2Cl_2. We note that in the experiments of refs. [101,110] photoabsorption cross sections were measured with a Sn film in the region 16–24 eV and an Al film in the region 24–71 eV to separate the absorption cell from the high vacuum of the electron storage ring. Therefore the differences between the present results and those reported by Lee *et al.* [101] in the energy region 16–24 eV are most likely due to a systematic error in the use of the Sn film in the latter work. Also for the data of Lee *et al.*, in the 23.8–36 eV region second order light had a significant effect and the experimental error in this region was reported to be as

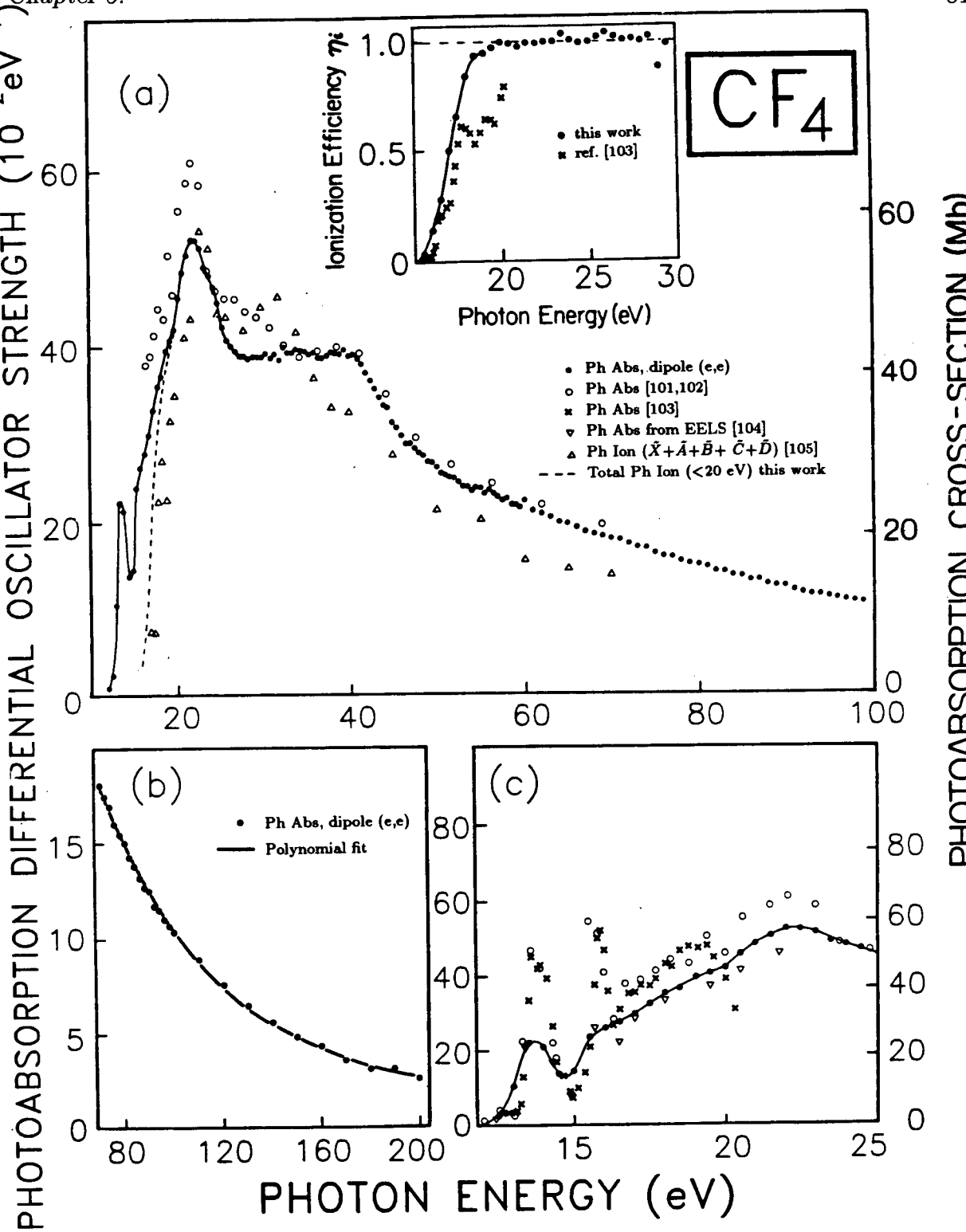

Figure 5.11: Absolute photoabsorption differential oscillator strengths for the valence shell of CF_4. a) 10–100 eV (insert shows ionization efficiency). b) 70–200 eV. c) 10–30 eV (expanded scale).

much as 20%. This may well account for the disagreement between the present work and the data of Lee *et al.* in the region of 25–33 eV. The photoionization data of Carlson *et al.* [105], which is the sum of the electronic state partial differential oscillator strengths for the production of the ion states $\tilde{X}$, $\tilde{A}$, $\tilde{B}$, $\tilde{C}$ and $\tilde{D}$, are also shown in fig. 5.11a. In the region above 34 eV, where the $\tilde{E}$ state starts to be produced [117], the data of Carlson *et al.* (i.e. the sum of the electronic state partial photoionization differential oscillator strengths $\tilde{X}+\tilde{A}+\tilde{B}+\tilde{C}+\tilde{D}$) are therefore understandably lower than the total photoabsorption. Below 22 eV, the data of Carlson *et al.* are lower than the presently reported total photoionization differential oscillator strengths (i.e. the photoabsorption differential oscillator strengths multiplied by the photoionization efficiency) which are shown by the dashed line on fig. 5.11a. It is noteworthy that in the 25–34 eV region, the data of Carlson *et al.* are significantly higher than the present work. The cause of this discrepancy is probably either the presence of higher order radiation (as in ref. [101]) or the method used for determining the absolute cross-section scale in the optical measurements [105]. In the latter work, the absolute values were obtained by calibrating the apparatus with noble gases and measuring the gas pressure. Such procedures are extremely difficult and can lead to large errors as has been discussed earlier [115,118].

A broad feature (fig. 5.11a) centered at $\sim$ 40 eV is observed in the present photoabsorption measurements for CF_4 and is also seen in the work of Lee *et al.* [101]. Similar but weaker features are also seen in the spectra of CF_3Cl (fig. 5.12a), CF_2Cl_2 (fig. 5.13a) and $CFCl_3$ (fig. 5.14a) at photon energies $\sim$ 40 eV, $\sim$ 40 eV and $\sim$ 37 eV respectively. This feature may be associated with inner valence ionization or possibly scattering (diffraction) of the outgoing (outer valence) photoelectrons by the neighboring atoms in the molecules [121,122,123,124,125], as discussed for CF_3Cl in section 5.2.2.

5.2.2 The CF_3Cl Photoabsorption Differential Oscillator Strengths

The presently reported measurements on CF_3Cl are compared with earlier photoabsorption measurements [101,109] obtained using synchrotron radiation light sources in figs. 5.12a and 5.12b. In fig. 5.12c the present photoabsorption data are also compared in the low energy region (7.5–35 eV) with previously reported results obtained using synchrotron radiation [101,107] and the helium Hopfield continuum [106] as light sources. The photoabsorption data derived from earlier small momentum transfer electron impact measurements [104] which were originally reported in the form of integrated oscillator strengths have been converted to average differential oscillator strengths (i.e. the integrated oscillator strengths divided by the corresponding energy intervals) and are also shown in fig. 5.12c.

The different energy resolution characteristics of the present dipole (e,e) techniques and optical methods (i.e. the large differences in energy resolution and the fact that the energy resolution changes with photon energy in optical experiments—see section 5.2) complicates comparison of the various data sets at lower energies, particularly in the region of discrete excitation. In particular meaningful comparisons of such data are not possible below 11 eV and such higher resolution data from refs. [106,107] are omitted from fig. 5.12c. The present photoabsorption spectrum is similar in shape to those reported in refs. [101,104,107] in the low energy region below 23 eV. However, the magnitudes of the reported cross-sections [101,104,106,107] vary considerably. Rydberg transitions have been assigned to the various features in the low energy region below 25 eV. In particular, the peak at 9.5 eV has been attributed to the $5e \rightarrow 4s$ Rydberg transition [104,119]. Similarly, Rydberg transitions ($5e \rightarrow 5s$ and/or $5e \rightarrow 3d$), ($4e \rightarrow 4s$ and/or $1a_2 \rightarrow 4p$) and $4a_1 \rightarrow 4s$ are the assignments for the features at 11.5 eV, 13.5 eV and 16.5 eV

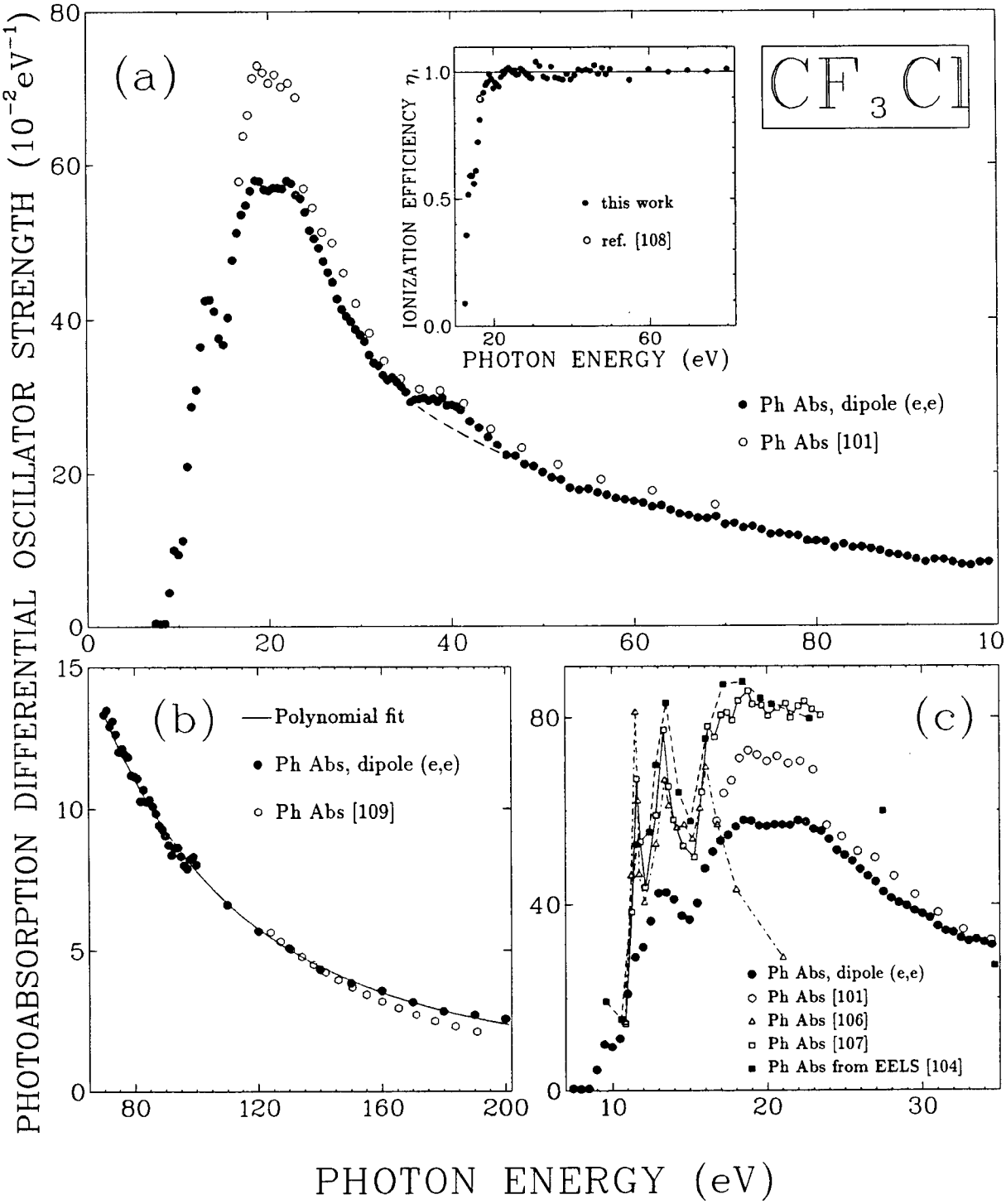

Figure 5.12: Absolute photoabsorption differential oscillator strengths for the valence shell of CF_3Cl. a) 7.5–100 eV (insert shows ionization efficiency). b) 70–200 eV. c) 7.5–35 eV (expanded scale).

[104,119]. The two maxima in the 18–24 eV region have been recently assigned to the Rydberg transitions ($4a_1 \rightarrow 5s$ and/or $2e \rightarrow 4p$) and $2a_1 \rightarrow 3s$ [119].

A broad feature (fig. 5.12a) centered at ~40 eV is observed in the present photoabsorption measurement for CF_3Cl and is also seen in the work of Lee *et al.* [101]. A similar but even more prominent broad feature at ~40 eV is also present in the photoabsorption differential oscillator strength spectrum of CF_4 (fig. 5.11a). Similar but weaker features are also seen in the photoabsorption differential oscillator strength spectra of CF_2Cl_2 (fig. 5.13a) and $CFCl_3$ (fig. 5.14a) at photon energies ~40 eV and ~37 eV respectively. The amplitudes of these structures decrease as the number of F atoms decreases. In this regard it is noteworthy that these structures occur close to the region of the onsets of ionization of the inner valence (F $2s$) orbitals (see chapter 6 and ref. [120]) and it is possible that they are associated with the cross sections for these processes. However it should be noted that MS-Xα calculations and PES partial cross section measurements of CF_3Cl indicate a maximum in some of the outer valence partial photoionization channels in a similar energy range [121]. The authors [121] pointed out that these predicted and observed outer valence structures are not due to shape resonances but are probably associated with scattering (diffraction) of the photoelectrons by the neighboring atoms in the molecule (see also refs. [122,123,124,125]).

Above a photon energy of 24 eV the present results agree with those reported by Lee *et al.* [101] to better than 10%. However in the 16–24 eV region the cross sections reported by Lee *et al.* [101] are ~20 % higher than the present results (figs. 5.12a and 5.12c). Similar discrepancies in this same energy region (16–24 eV) have also been observed in the comparisons between our results (figs. 5.11 and 5.13) and those of Lee *et al.* [101] and Wu *et al.* [110] for the molecules CF_4 and CF_2Cl_2. As discussed in section 5.2.1, the differences between the present results and those reported by Lee *et al.* [101] and Wu *et*

al. [110] in the energy region 16–24 eV are most likely due to a systematic error in the use of the Sn film in the latter work. The data of Jochims *et al.* [107] were single point normalized to the photoabsorption measurement reported by Rebbert and Ausloos [108] whereas the data of King and McConkey [104] were put on an absolute scale at a single point to an average of the photoabsorption measurements reported by Jochims *et al.* [107] and the electron impact measurement reported by Huebner *et al.* [126]. The previously reported single point normalized results [104,107] are of the same overall shape but are considerably higher than the present results below 23 eV (fig. 5.12c). Above 23 eV the data of King and McConkey [104] approach the present data with increasing photon energy. Our data are also lower than the photoabsorption measurements of Gilbert *et al.* [106] below 17 eV, whereas at higher energy their data diverge rather drastically from all other measurements (fig. 5.12c). The absolute photoabsorption cross sections of CF_3Cl from 124–270 eV have been measured by Cole and Dexter [109] using synchrotron radiation. Agreement with the present work is good below 160 eV but the measurements diverge at the higher energies and exhibit a 20% difference at 190 eV (fig. 5.12b).

5.2.3 The CF_2Cl_2 Photoabsorption Differential Oscillator Strengths

The presently reported measurements on CF_2Cl_2 are compared with earlier photoabsorption measurements [109,110] obtained using synchrotron radiation light sources in figs. 5.12a and 5.13b. In fig. 5.13c the present photoabsorption data are also compared in the low energy region (8.5–36 eV) with previously reported results obtained using synchrotron radiation [107,110] and the helium Hopfield continuum [106] as light sources. The previous photoabsorption data derived from small momentum transfer electron impact measurements [104] have been digitized from the reported diagram and are also shown in fig. 5.13c.

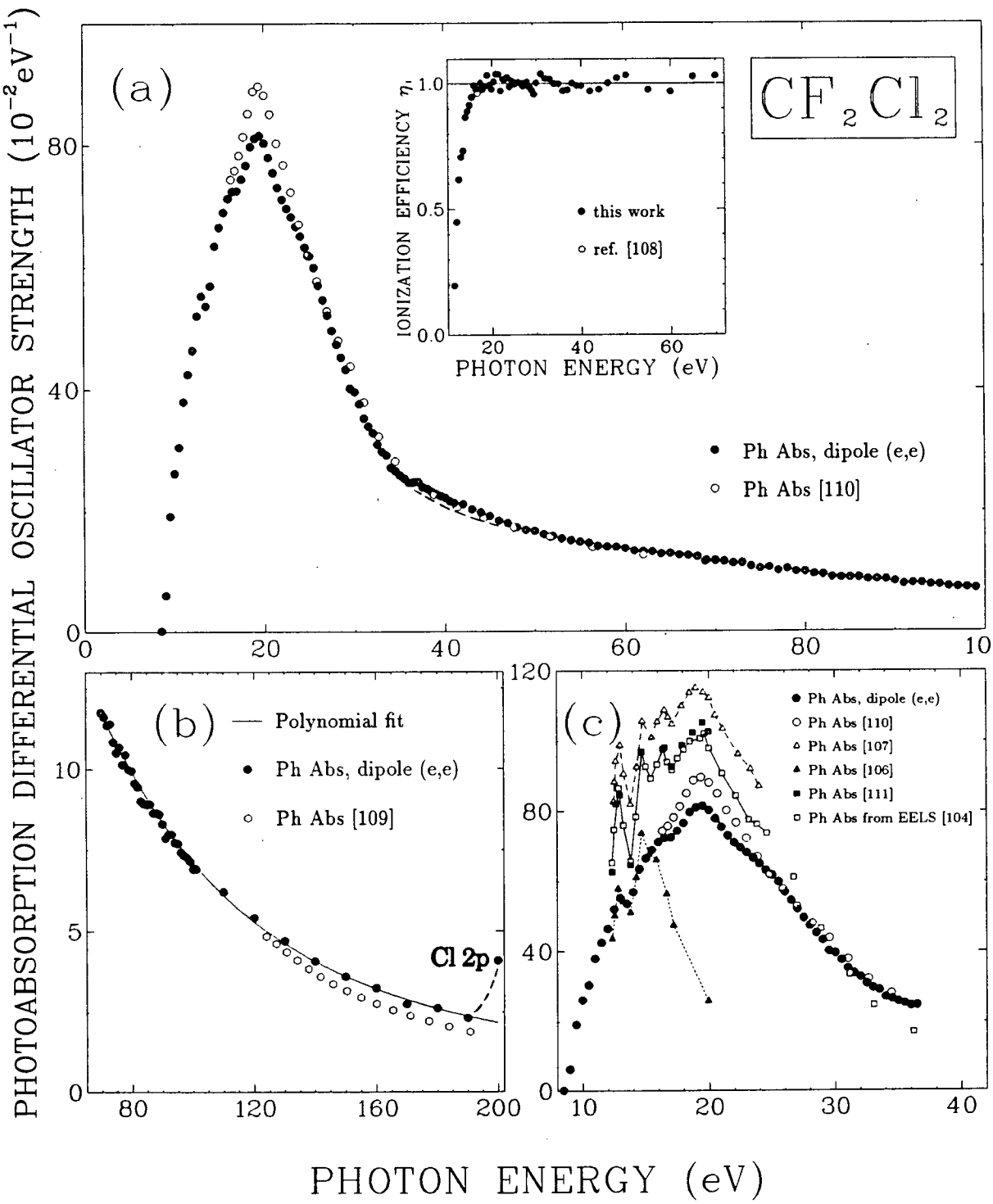

Figure 5.13: Absolute photoabsorption differential oscillator strengths for the valence shell of CF_2Cl_2. a) 8.5–100 eV (insert shows ionization efficiency). b) 70–200 eV. c) 8.5–36 eV (expanded scale).

The different energy resolution characteristics of the present dipole (e,e) techniques and optical methods (i.e. the large differences in energy resolution and the fact that the energy resolution changes with photon energy in optical experiments—see section 5.2) complicates comparison of the various data sets at lower energies, particularly in the region of discrete excitation. A similar difficulty exists in comparing the present results at 1 eV FWHM resolution in the discrete excitation region with the data [104] derived from intermediate impact energy EELS at ~0.05 eV resolution. In particular, meaningful comparisons of such data with the present work are not possible below 12.5 eV and the higher resolution data from references [104,106,107] are omitted from fig. 5.13c in this region. The shape of the presently reported photoabsorption spectrum in the energy region below 25 eV (fig. 5.13c) is similar to the shapes of the spectra reported in refs. [110, 104,107]. However considerable variations exist in the absolute magnitudes of the various data sets. In the structured low energy region below 15 eV Rydberg transitions have been assigned to the various features. In particular, the peak at 13 eV just discernible in the present low resolution work has been attributed to the Rydberg transitions $4b_2 \rightarrow 3d$ and/or $3a_2 \rightarrow 4s$ [49,104,119]. The Rydberg transitions $3a_2 \rightarrow 3d$ and/or $6b_1 \rightarrow 5p$ and $(2a_2+5b_1) \rightarrow 4s$ are the assignments for the structures in the 15–17 eV region [104,119] (unresolved in the present work). The maximum at 19.5 eV has been assigned to the $7a_1 \rightarrow 4s$ Rydberg transition [49,104,119], while the broad shoulder at ~24.5 eV has been suggested by Robin [49] to be due to a Rydberg transition originating from the carbon $2s$ orbitals. A term value of ~3 eV can be derived for this transition from the ionization potential of the C $2s$ orbitals $(2a_1+1b_2)$ of CF_2Cl_2 presented in chapter 6. The magnitude of this term value is consistent with the assignment $(2a_1, 1b_2) \rightarrow 3s$ or $(2a_1, 1b_2) \rightarrow 3p$, since the typical magnitudes of Rydberg term values are in the range 2.8–5.0 eV for the lowest s orbital and 2.0–2.8 for the lowest p orbital [47]. It should be noted that the

Rydberg transition assigned to a particular structure depends largely on the ionization energies taken from PES measurements (i.e. different ionization energies give rise to different term values (see sections 2.3.1 and 2.3.2) for the same structure and therefore the assignment of the particular structure can be different in utilizing ionization energies from different PES measurements). The rise in photoabsorption differential oscillator strength at 200 eV in fig. 5.13b is caused by excitation of Cl $2p$ inner shell electrons [119].

Above a photon energy of 24 eV the present results are in excellent quantitative agreement with those reported by Wu *et al.* [110]. However in the 16–24 eV region the cross-sections reported by Wu *et al.* [110] are ~10% higher than the present work (figs. 5.12a and 5.13c). Similar discrepancies in this energy region have been observed in earlier comparisons between our results (figs. 5.11 and 5.12) and those of Lee *et al.* [101] for the molecules CF_4 and CF_3Cl. As pointed out in section 5.2.1, the discrepancies in the 16–24 eV energy region are most likely due to a systematic error in the use of a Sn film in the work of Wu *et al.* [110] and Lee *et al.* [101]. The data of King and McConkey [104] and of Jochims *et al.* [107], which were single point normalized to the photoabsorption measurements reported by Person *et al.* [111] and Rebbert and Ausloos [108] respectively, are of similar shape but proportionally higher than the present results below 24 eV (fig. 5.13c). In the 24–30 eV energy region the data of King and McConkey [104] approach the present data with increasing photon energy, however, above 30 eV their data fall below ours. The agreement between the present results and those of Gilbert *et al.* [106] is good in the region 12–16 eV, but above 16 eV their data diverge rather drastically from all other measurements (fig. 5.13c). The absolute photoabsorption cross sections of CF_2Cl_2 from 124 eV to 270 eV have been measured by Cole and Dexter [109] using synchrotron radiation. Agreement with the present work is good below 130 eV but the measurements diverge at the higher energies and exhibit a 20% difference at 190 eV (fig. 5.13b).

A broad feature of low intensity (fig. 5.12a) centered at ~40 eV is observed. Similar but more prominent broad features were also seen in the photoabsorption differential oscillator strength spectra of CF_4 (fig. 5.11a) and CF_3Cl (fig. 5.12a). They were interpreted (section 5.2.2) as being associated with inner valence ionization or possibly scattering (diffraction) of the outgoing (outer valence) photoelectrons by the neighboring atoms in the molecules [121,122,123,124,125]. The presently observed feature (fig. 5.12a) probably also has similar origins. Final assignment must await detailed PES experiments and theoretical calculations. A even weaker feature at ~37 eV is also present in the photoabsorption differential oscillator strength spectra of $CFCl_3$ (fig. 5.14a)

5.2.4 The $CFCl_3$ Photoabsorption Differential Oscillator Strengths

The presently reported measurements are compared with earlier photoabsorption measurements [109] obtained using synchrotron radiation as the light source in fig. 5.14b. In fig. 5.14c the present photoabsorption data are also compared in the low photon energy region with previously reported results obtained using synchrotron radiation [107] and the helium Hopfield continuum [106] as light sources. The photoabsorption data (~0.05 eV FWHM resolution) derived from small momentum transfer electron impact measurements [104] were reported both in the form of integrated oscillator strengths (in a table) and differential oscillator strengths (in a diagram). In fig. 5.14c in order to make meaningful comparisons with the present results, which were obtained with lower resolution (1 eV FWHM), below 12.5 eV the results from ref. [104] are shown as average differential oscillator strengths (i.e. the integrated oscillator strengths divided by the corresponding energy intervals). This has been done in order to smooth away sharp structures in the discrete region. Above 12.5 eV the results are shown as differential oscillator strengths digitized from the reported diagram [104].

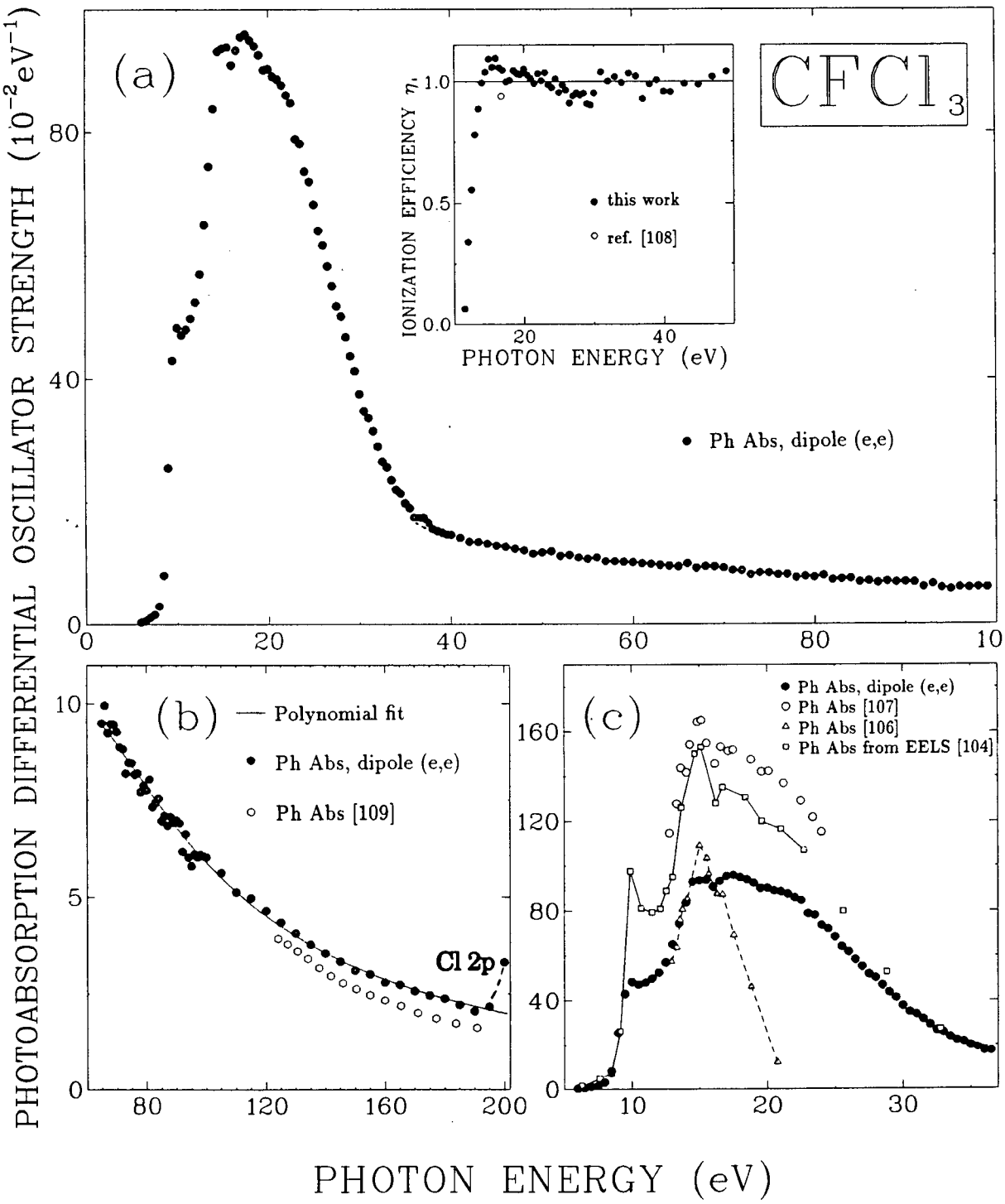

Figure 5.14: Absolute photoabsorption differential oscillator strengths for the valence shell of $CFCl_3$. a) 6–100 eV (insert shows ionization efficiency). b) 65–200 eV. c) 6–38 eV (expanded scale).

The different energy resolution characteristics of the present dipole (e,e) techniques and optical methods (i.e. the large differences in energy resolution and the fact that the energy resolution changes with photon energy in optical experiments—see section 5.2) complicates comparison of the various data sets at lower energies, particularly in the region of discrete excitation. In particular meaningful comparisons of such data with the present work are not possible below 12.5 eV for $CFCl_3$, and therefore the higher resolution data from refs. [106,107] are omitted from fig. 5.14c in this region. The presently reported photoabsorption spectrum is similar in shape to those reported in refs. [104,107] in the energy region below 24 eV (fig. 5.14c). The absolute magnitudes of the photoabsorption cross-sections, however, exhibit considerable variations between the various data sets. Rydberg transitions have been assigned to the features in the low energy region below 24 eV. In particular, the peak at 10 eV just discernible in the present low resolution work has been assigned to the Rydberg transition $4e \rightarrow 4s$ [104,119]. Similarly the broad structure at ~15 eV has been attributed to the Rydberg transitions $2e \rightarrow 4s$ and $4a_1 \rightarrow 4s$ [104,119]. The maximum at ~17.5 eV and the shoulder at ~22 eV have been recently assigned to the Rydberg transitions $3a_1 \rightarrow 4s$ and $1e \rightarrow 4s$ [119]. A feature only just discernible at ~37 eV is similar to progressively less intense features observed in CF_4 (fig. 5.11a), CF_3Cl (fig. 5.12a) and CF_2Cl_2 (fig. 5.13a). As discussed earlier (section 5.2.2) such features are perhaps due to the onsets of inner valence (i.e. F $2s$) ionization processes or possibly scattering (diffraction) of the outgoing (outer valence) photoelectrons by the neighboring atoms in the molecule [121,122,123,124,125]. A more definite assignment of this feature must await more detailed PES partial cross section experiments and theoretical calculations. The rise of differential oscillator strength at ~200 eV (fig. 5.14b) is due to excitation of the Cl $2p$ inner shell [119].

The electron impact measurements of King and McConkey [104] and the photoabsorption measurements of Jochims *et al.* [107] are considerably higher than the present work below 24 eV. Above 24 eV the data of King and McConkey [104] approach the present results with increasing photon energy. The agreement between the present results and those of Gilbert *et al.* [106] is good in the region 13–16 eV, but above 16 eV their data diverge rather drastically from all other measurements. The absolute photoabsorption cross sections of $CFCl_3$ from 124 eV to 270 eV have been measured by Cole and Dexter [109] using synchrotron radiation and at 124 eV these results agree with the present work within 10%. However the measurements diverge at the higher energies and exhibit a 25% difference at 190 eV (fig. 5.14b).

5.2.5 Comparison of the Photoabsorption Differential Oscillator Strengths of CF_4, CF_3Cl, CF_2Cl_2 and $CFCl_3$

Although the total integrated oscillator strengths for the four freons all have similar values (i.e. $\sim$ 33, see section 5.2), the shapes of the photoabsorption differential oscillator strength spectra vary considerably in going through the series CF_4, CF_3Cl, CF_2Cl_2 and $CFCl_3$, with the oscillator strength becoming progressively more concentrated in the low photon energy region as the number of Cl atoms increases. With increasing number of Cl atoms in the freon molecules, the photoabsorption differential oscillator strength decreases more rapidly in the 20–40 eV region, while above $\sim$40 eV the rate of decrease becomes smaller. For example, at energies $\sim$35 eV above the photoabsorption onsets of the respective spectra the differential oscillator strengths for CF_4, CF_3Cl, CF_2Cl_2 and $CFCl_3$ are 0.29, 0.26, 0.20 and 0.14 eV^{-1} respectively, whereas at $\sim$100 eV above the onsets the values are 0.09, 0.07, 0.06, 0.06 eV^{-1} respectively. These differences between the differential oscillator strengths for CF_4, CF_3Cl, CF_2Cl_2 and $CFCl_3$ occur because an increasing

number of molecular orbitals with predominantly Cl $3p$ atomic character contribute to the differential oscillator strengths. This effect is due to the Cooper minimum [25,127] in the Cl $3p$ atomic orbital photoionization cross-sections at ~35–40 eV [68].

5.3 The CF_4 Photoabsorption Differential Oscillator Strengths for the C $1s$ and F $1s$ Inner Shells and the Valence Shell Extrapolation

In this section the extrapolated CF_4 differential oscillator strengths for valence excitations obtained using formula 5.41 and also the differential oscillator strengths for CF_4 C $1s$ and F $1s$ excitations obtained from normalization of Bethe-Born converted EELS spectra are compared with the reported results from direct X-ray absorption measurements. The absolute differential oscillator strengths of inner shell excitations for other freon molecules will be reported in chapter 7.

As discussed in section 5.2 above, an analytical function was fitted to the valence shell experimental data for CF_4 from 70 to 200 eV and was used to estimate the differential oscillator strength for valence shell photoabsorption from 200 eV to infinity. This estimated valence shell contribution is shown by the dashed lines in figs. 5.15a (valence shell), 5.15b (C $1s$ region) and 5.15c (F $1s$ region) in the photon energy regions 200–250, 270–350 and 670–740 eV respectively. For the comparison to be made below, we have digitized literature results of C $1s$ and F $1s$ inner shell photoabsorption measurements [128,129] and they are also shown in fig. 5.15b and 5.15c by the solid and dash-dot lines respectively. In the region below the C $1s$ IP (i.e. the K edge), there is excellent agreement between our valence shell estimation of the absolute differential oscillator strengths using the analytical function and the direct photoabsorption measurements obtained using X-ray characteristic lines at 248.0 eV (fig. 5.15a) and 277.4 eV (fig. 5.15b).

In the present work, we have also converted the earlier reported relative inner shell

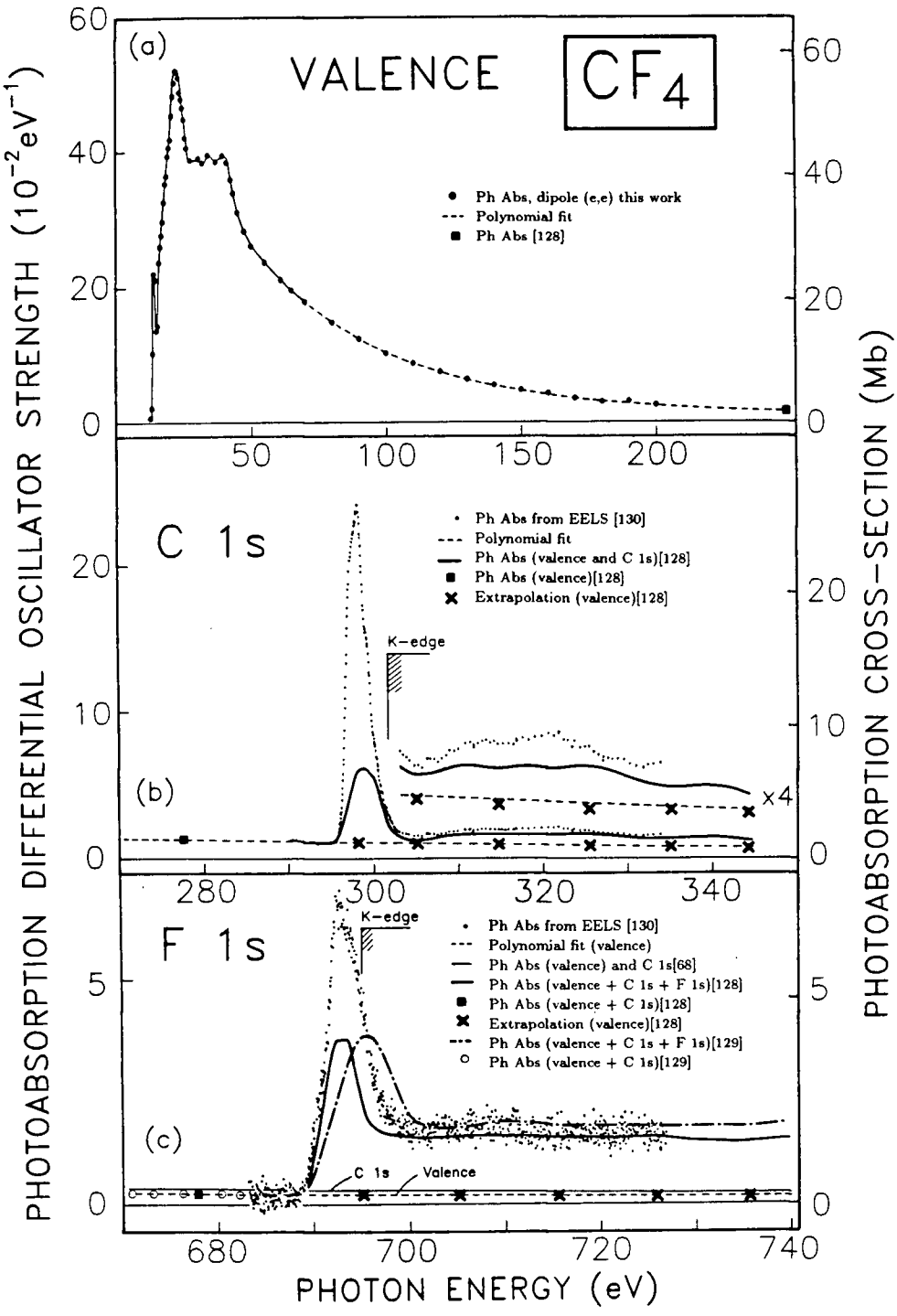

Figure 5.15: Absolute photoabsorption differential oscillator strengths for (a) the Valence-shell, (b) the C 1*s* region and (c) the F1s region of CF_4. In each spectrum the dashed line represents the fitted (valence shell, 70–200 eV) and extrapolated valence shell contribution. See text for details.

electron energy loss spectra (ISEELS) of CF_4 [130] to absolute photoabsorption differential oscillator strengths by using known absolute atomic photoionization differential oscillator strengths, according to the normalization principles discussed in sections 2.3.4.3 and 2.3.8. The procedures used were as follows. Firstly, the estimated background and valence shell continuum contributions were subtracted from the raw ISEELS data [130] by straight line extrapolation of the pre-ionization edge spectral intensity. (A modified subtraction procedure is used in chapter 7.) The resulting spectrum due to inner shell excitation alone was then converted to an approximate relative optical spectrum by using equations 2.35 and 2.36 where the estimated kinematic (Bethe-Born) factor was taken to be proportional to $E^{2.5}$. The absolute photoabsorption differential oscillator strengths were then obtained by normalizing the relative optical spectrum at a reasonably high photoelectron energy (i.e. ~25–30 eV above the 1*s* edge) to the sum of corresponding atomic 1*s* cross-sections for the respective constituent atoms [57,70,68]. The carbon 1*s* atomic cross-section at 30 eV above the ionization potential was used to place the C 1*s* spectrum of CF_4 on the absolute differential oscillator strength scale (fig. 5.15b). Similarly, four times the fluorine 1*s* atomic photoionization cross-section at 25 eV above the F 1*s* ionization potential was taken for the normalization of the CF_4 F 1*s* spectrum. The so obtained C 1*s* inner shell absolute photoabsorption differential oscillator strength spectrum of CF_4 was then added to the valence continuum contribution determined by the present analytical function to give the total photoabsorption differential oscillator strengths in the C 1*s* region as shown in fig. 5.15b. Similar procedures were used for the F 1*s* spectrum shown in fig. 5.15c. Our results are compared to those obtained by direct photoabsorption measurements [128,129]. In the C 1*s* region, the presently converted ISEELS results are higher than the optical measurements [128], especially in the discrete region. This could be due to the uncertainty involved in the background subtraction

procedure. It should be noted that the differential oscillator strengths for CF_4 C 1*s* is re-derived in chapter 7 using a modified background subtraction procedure. However, even after the re-derivation, the differential oscillator strength as obtained in chapter 7 is still higher than the optical results in the discrete transition region. This discrepancy may partly be due to a systematic error in the present normalization method, since for highly fluorinated molecules such as CF_4 [44] the presence of potential barriers may depress the photoabsorption cross-section corresponding to the central atom in the region of the continuum immediately above the IP. As for the F 1*s* spectra, the converted ISEELS spectra are in good agreement with the optical measurements [128,129] in the continuum region within statistical error. The differences between the photon measurements and the converted ISEELS spectra in the discrete regions of the C 1*s* and also the F 1*s* spectra might be due to line saturation (bandwidth) effects which can seriously perturb the intensities of discrete transitions in photoabsorption measurements [26,131]. Since electron impact excitation is non-resonant, such bandwidth effects do not occur in electron energy loss spectra [8,26]. The photoabsorption spectrum of ref. [129] shows an energy shift which is probably due to energy calibration errors.

5.4 Molecular and Dissociative Photoionization of CF_4, CF_3Cl, CF_2Cl_2 and $CFCl_3$

Time of flight mass spectra have been measured using the dipole (e,e+ion) spectrometer described in section 3.1 in the equivalent photon energy ranges 15.5–80 eV, 12.5–80 eV, 11.5–70 eV and 11.5–49 eV respectively for CF_4, CF_3Cl, CF_2Cl_2 and $CFCl_3$. Typical TOF mass spectra are shown in figs. 5.16, 5.17, 5.18 and 5.19, obtained respectively at 80 eV for CF_4, at 45 eV for CF_3Cl, at 50 eV for CF_2Cl_2, and at 49 eV for $CFCl_3$. The positive ions detected in the TOF mass spectra of CF_4 were CF_3^+, CF_2^+, CF^+, C^+, F^+

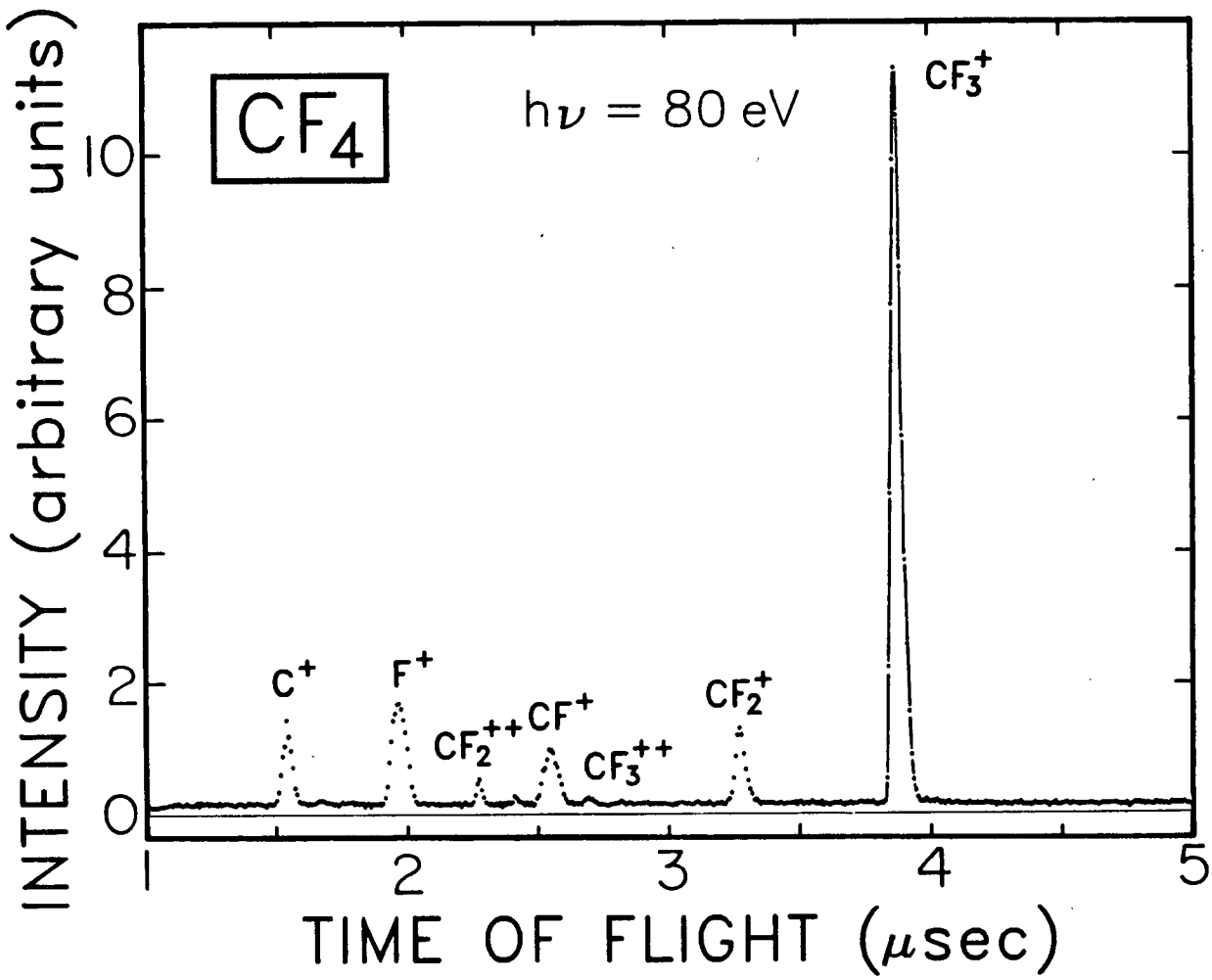

Figure 5.16: Time of flight mass spectrum of CF_4 at 80 eV equivalent photon energy.

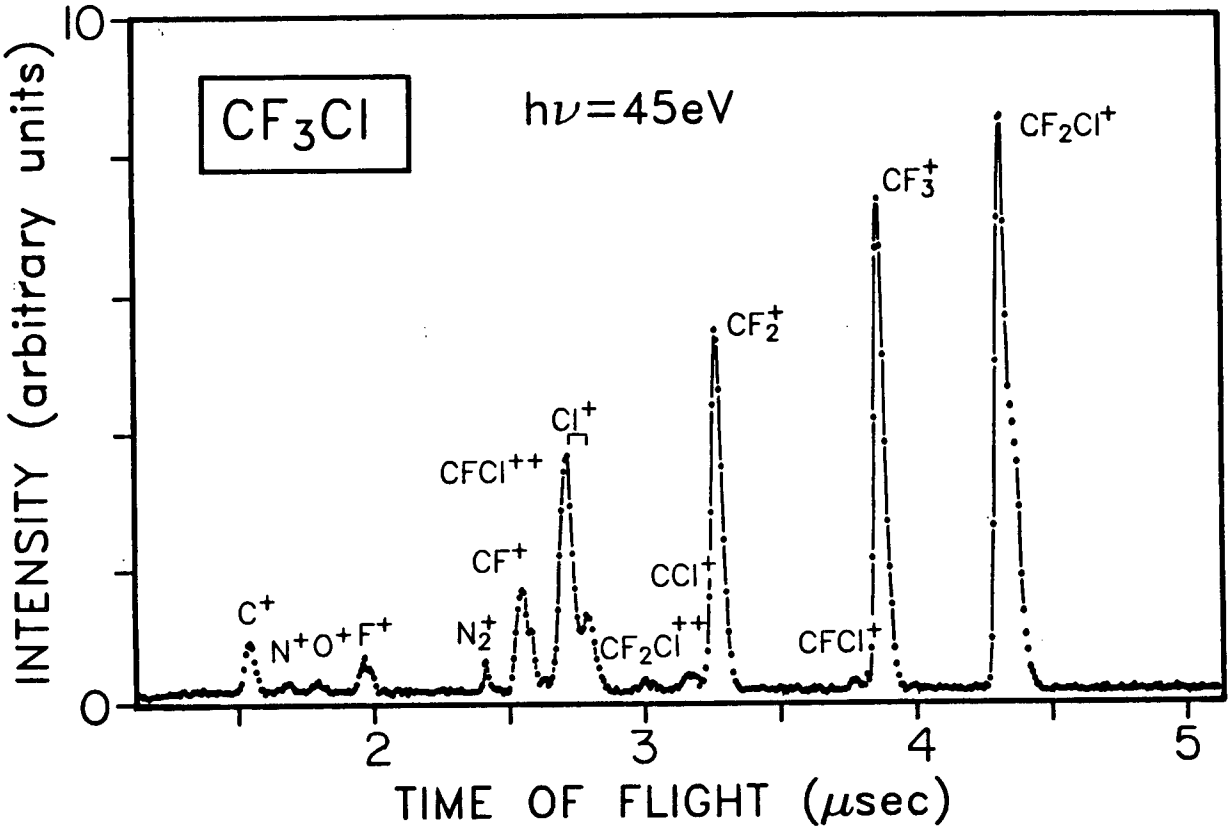

Figure 5.17: Time of flight mass spectrum of CF_3Cl at 45 eV equivalent photon energy.

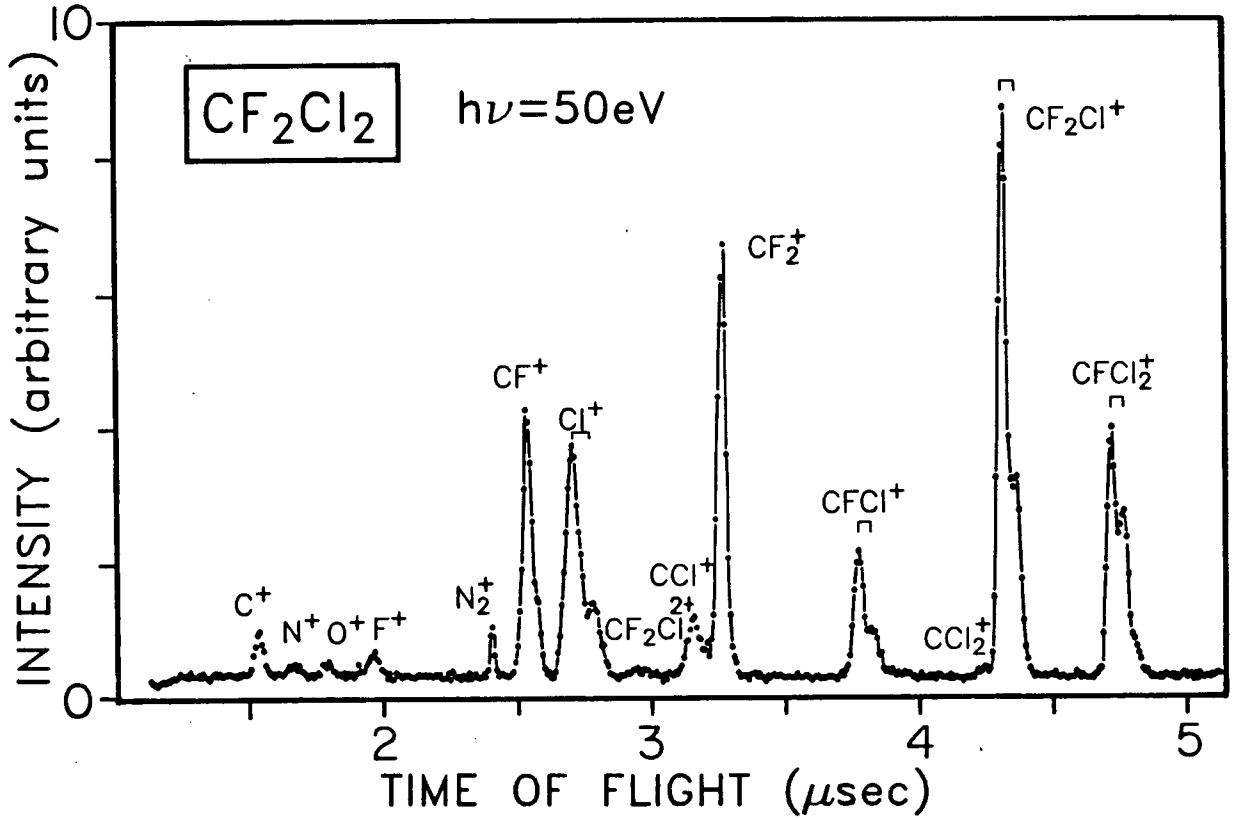

Figure 5.18: Time of flight mass spectrum of CF_2Cl_2 at 50 eV equivalent photon energy.

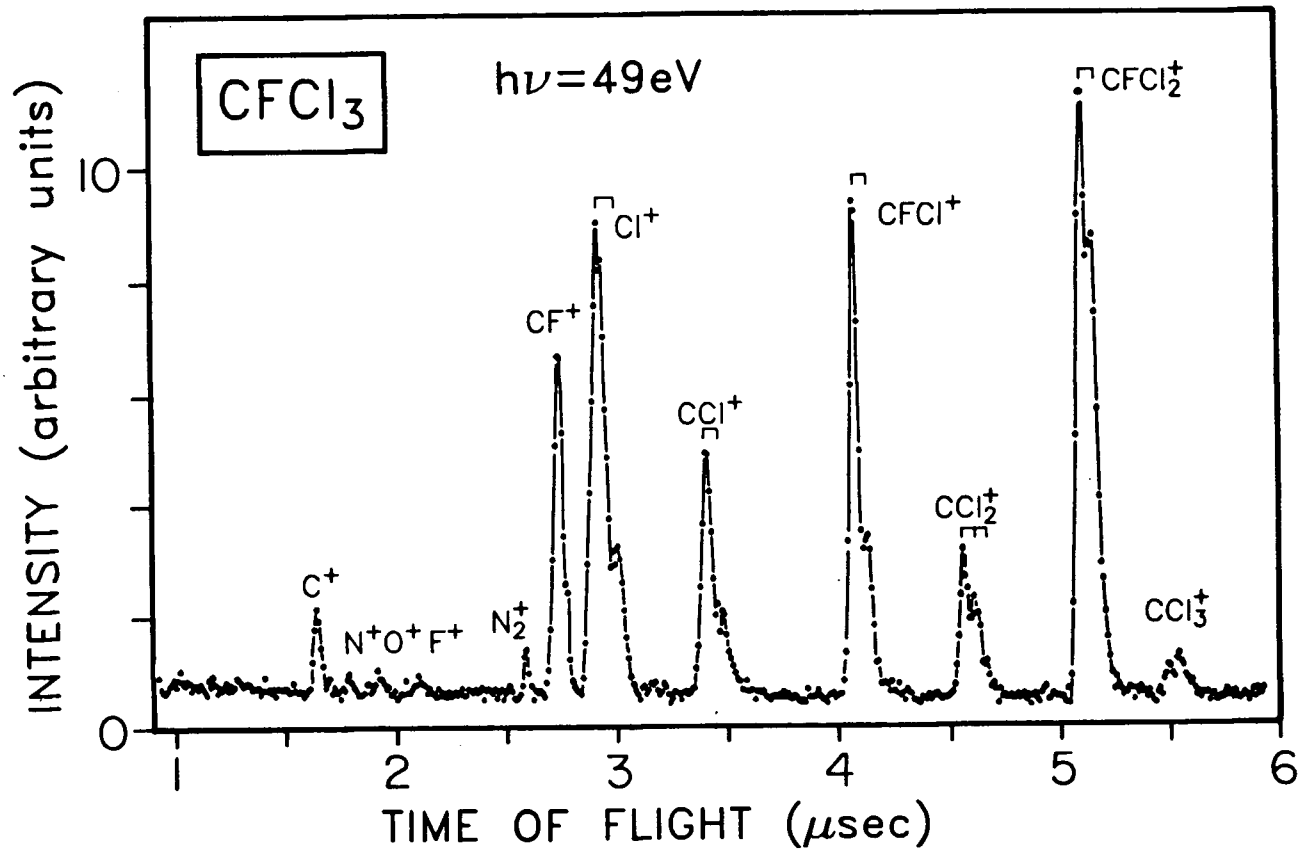

Figure 5.19: Time of flight mass spectrum of $CFCl_3$ at 49 eV equivalent photon energy.

and the doubly charged ion CF^{2+}. The CF_4^+ molecular ion was not found, in accord with previous work [132]. For CF_3Cl, the molecular ion CF_3Cl^+ and the fragment (dissociative) ions CF_2Cl^+, CF_3^+, $CFCl^+$, CF_2^+, CCl^+, Cl^+, CF^+, F^+, C^+ as well as the doubly charged ions CF_2Cl^{2+} and $CFCl^{2+}$ were detected. The positive fragment (dissociative) ions $CFCl_2^+$, CF_2Cl^+, CCl_2^+, $CFCl^+$, CF_2^+, CCl^+, Cl^+, CF^+, F^+, C^+ and the doubly charged ion CF_2Cl^{2+} were detected for CF_2Cl_2. The molecular ion $CF_2Cl_2^+$ was not observed in contrast to the situation for CF_3Cl. In the TOF spectra of $CFCl_3$, the positive fragment ions CCl_3^+, $CFCl_2^+$, CCl_2^+, $CFCl^+$, CCl^+, Cl^+, CF^+, F^+ and C^+ were detected. Unlike the situation for CF_3Cl, the molecular ion ($CFCl_3^+$) was not detected. Also no doubly charged ions were observed for $CFCl_3$ in contrast to the other freons. Photoion branching ratios determined by integrating the mass peaks in the TOF spectra are reported diagrammatically in figs. 5.20, 5.21, 5.22 and 5.23 for CF_4, CF_3Cl, CF_2Cl_2 and $CFCl_3$ respectively, and also numerically in respective tables 5.17, 5.18, 5.19 and 5.20. It can be seen that the dominant ion produced from CF_4 by ionizing radiation in the region 15.5–80 eV is CF_3^+ (see table 5.17 and fig. 5.20) and the molecular ion CF_3Cl^+ is only observed with any appreciable intensity below 30 eV (see table 5.18 and fig. 5.21).

In comparing the branching ratios of various photoion fragments produced by photoionization of CF_3Cl, CF_2Cl_2 and $CFCl_3$, it is found that the excited molecular ions favor fragmentation processes involving loss of one or more Cl atoms over loss of an F atom. For example the molecules CF_3Cl, CF_2Cl_2 and $CFCl_3$ have a larger yield of the CF_3^+, CF_2Cl^+ and $CFCl_2^+$ ions (per C-Cl bond) resulting from loss of a Cl atom than of the CF_2Cl^+, $CFCl_2^+$ and CCl_3^+ ions (per C-F bond) from lose of an F atom respectively. These phenomena are all consistent with the fact that the bond strength of a C-Cl bond (3.58 eV) is weaker than that of a C-F bond (4.84 eV). It is also observed that the intensities of the ion fragments C^+ and F^+ are highest for the photoionization of CF_4

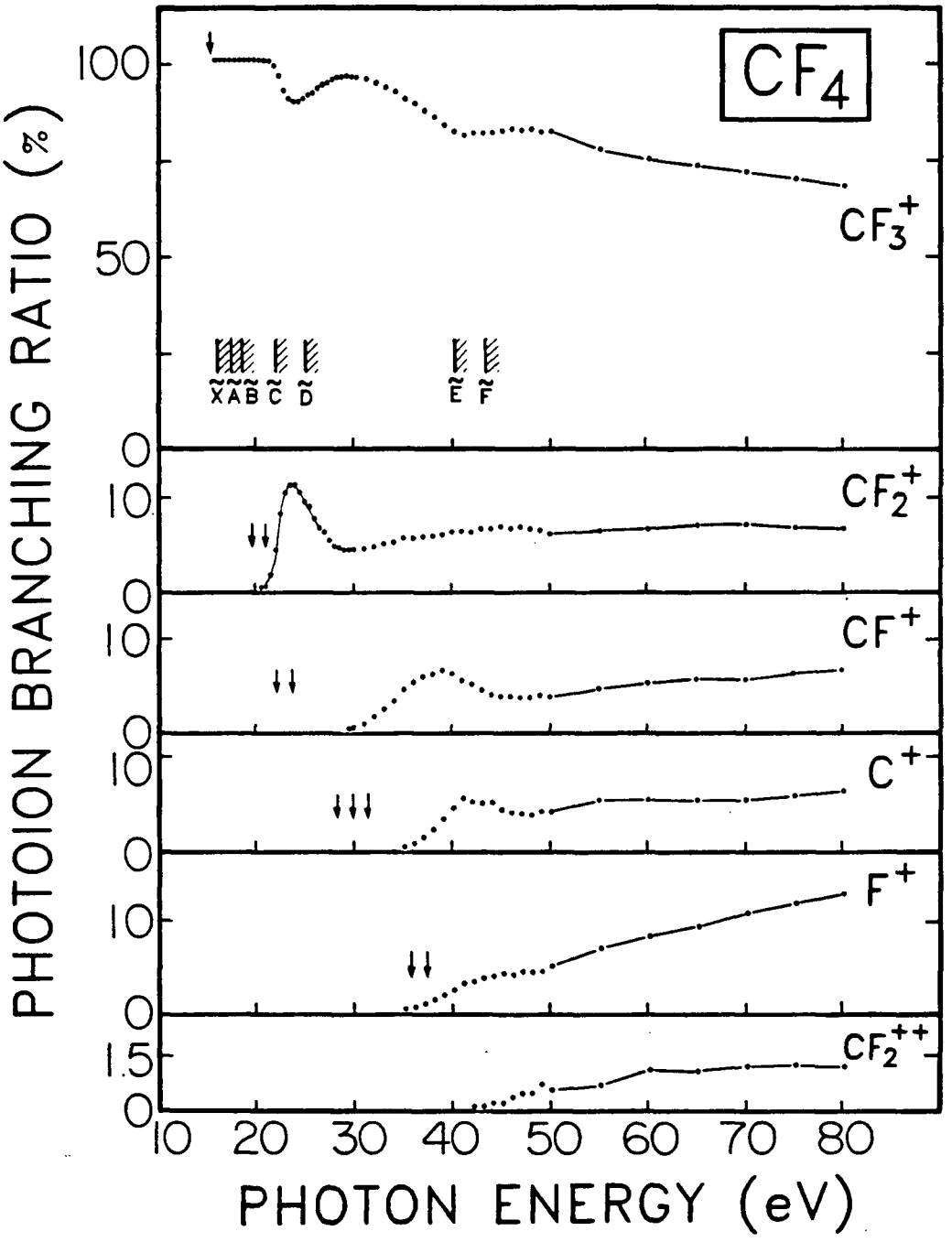

Figure 5.20: Branching ratios for dissociative photoionization of CF_4. The vertical arrows represent expected thermodynamic appearance potentials (see table 5.21) and the hatched lines indicate the vertical ionization energies [99,98] for production of the electronic states of CF_4^+.

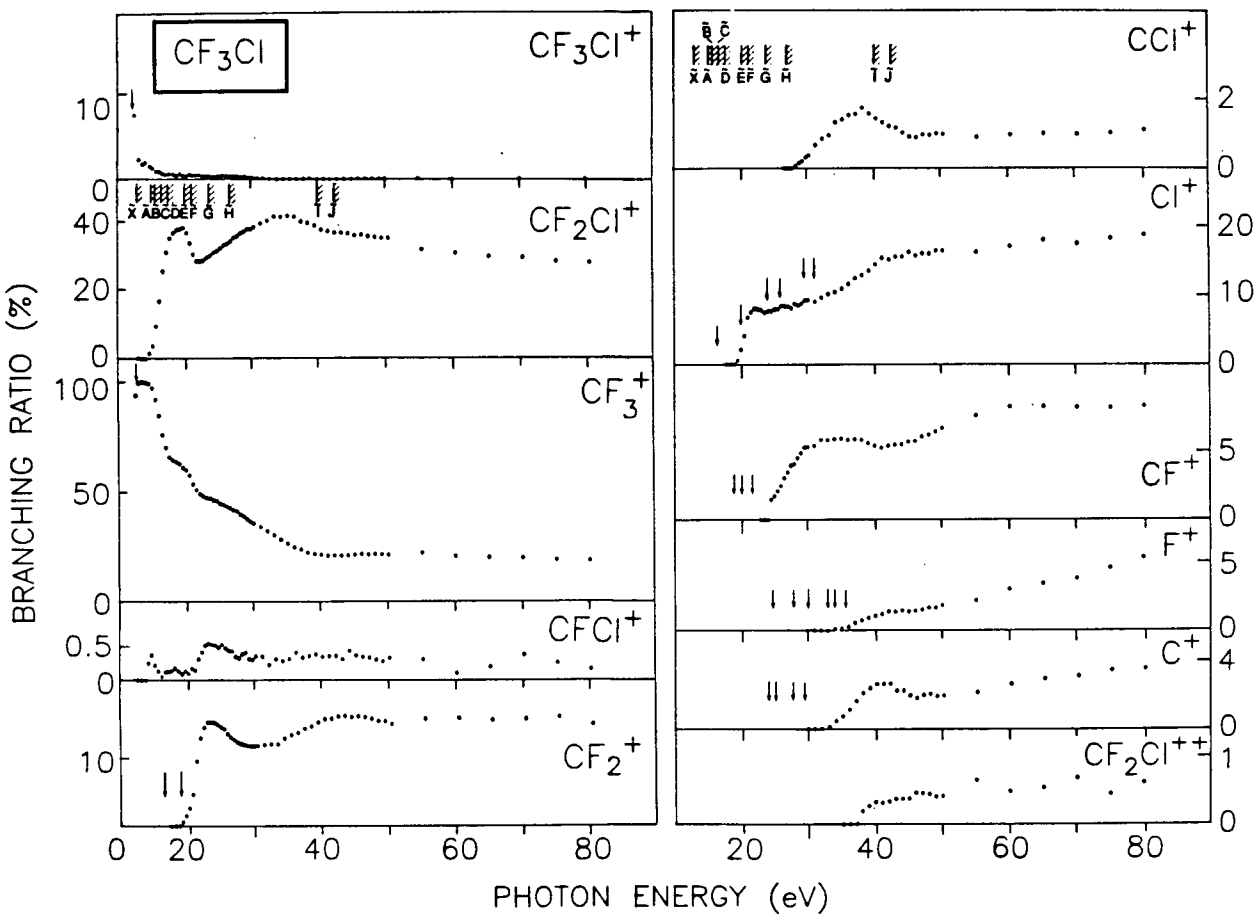

Figure 5.21: Branching ratios for dissociative photoionization of CF_3Cl. The vertical arrows represent expected thermodynamic appearance potentials (see table 5.22) and the hatched lines indicate the vertical ionization energies presented in chapter 6 and reported in ref. [100] for production of the electronic states of CF_3Cl^+.

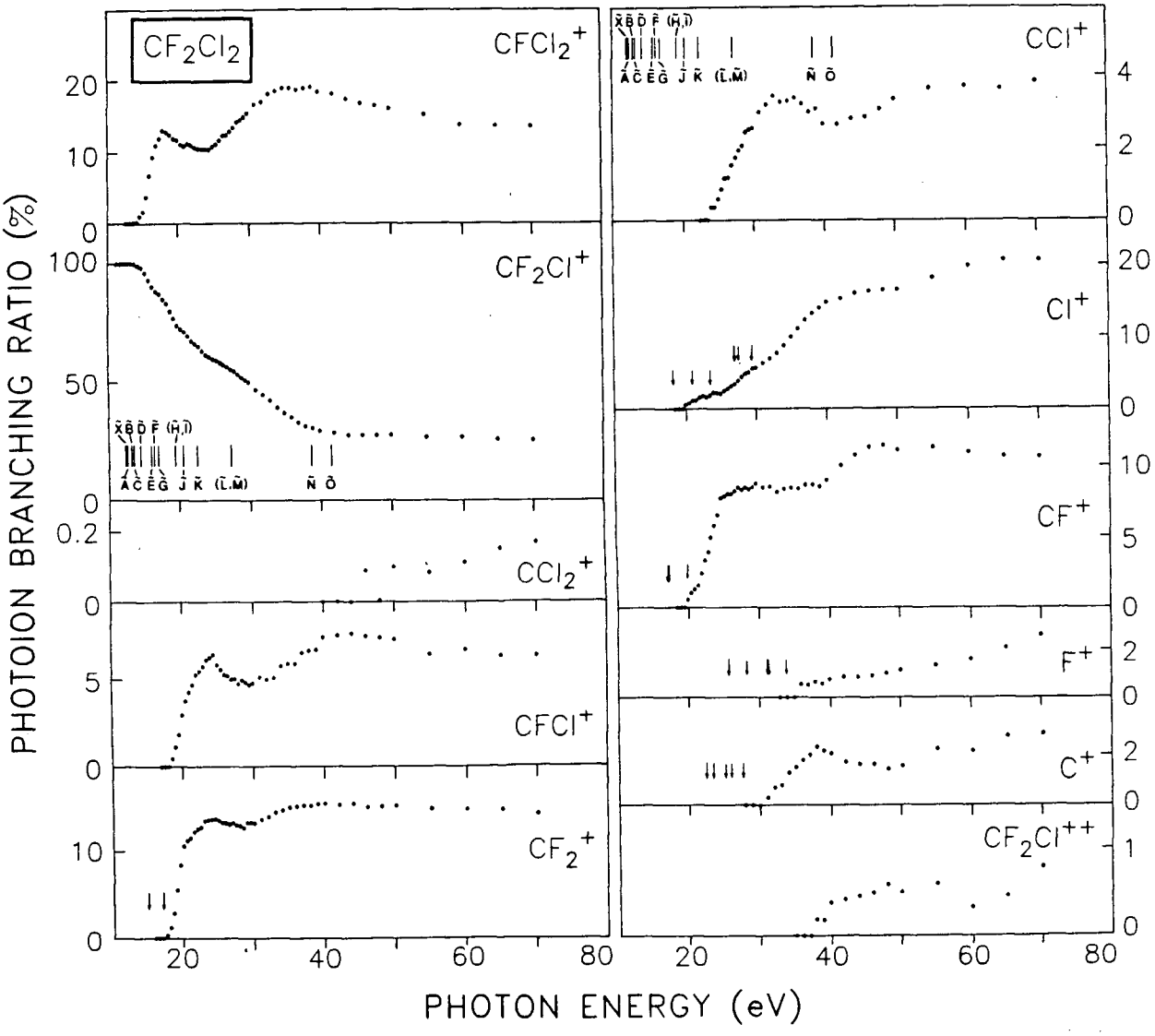

Figure 5.22: Branching ratios for dissociative photoionization of CF_2Cl_2. The vertical arrows represent expected thermodynamic appearance potentials (see table 5.23) and the vertical lines indicate the vertical ionization energies presented in chapter 6 and reported in ref. [100] for production of the electronic states of $CF_2Cl_2^+$.

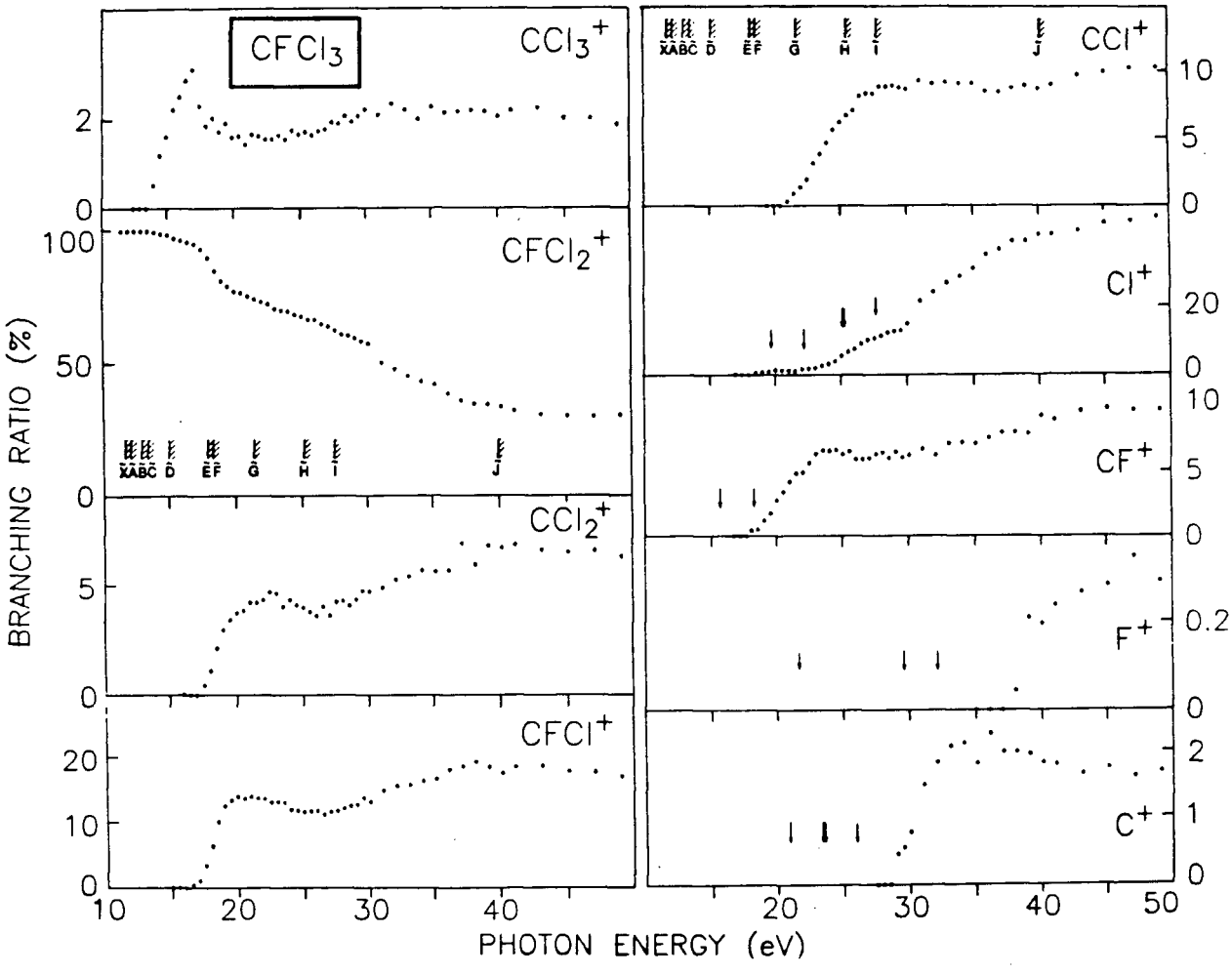

Figure 5.23: Branching ratios for dissociative photoionization of $CFCl_3$. The vertical arrows represent expected thermodynamic appearance potentials (see table 5.24) and the hatched lines indicate the vertical ionization energies presented in chapter 6 and reported in ref. [100] for production of the electronic states of $CFCl_3^+$.

Table 5.17: Photoion branching ratios of CF_4

Photon energy	Branching ratio (%)					
(eV)	CF_3^+	CF_2^+	CF^+	F^+	C^+	CF_2^{2+}
15.5	100.00					
16.0	100.00					
16.5	100.00					
17.0	100.00					
17.5	100.00					
18.0	100.00					
18.5	100.00					
19.0	100.00					
19.5	100.00					
20.0	100.00					
20.5	99.86	0.14				
21.0	99.74	0.26				
21.5	98.52	1.48				
22.0	95.86	4.14				
22.5	92.08	7.92				
23.0	89.98	10.02				
23.5	89.19	10.81				
24.0	89.17	10.83				
24.5	89.91	10.09				
25.0	90.90	9.10				
25.5	91.39	8.61				
26.0	92.63	7.37				
26.5	93.54	6.46				
27.0	93.99	6.01				
27.5	94.83	5.17				
28.0	94.44	4.56				
28.5	95.58	4.42				
29.0	95.83	4.17				

continued on next page

Table 5.17: (continued)

Photon energy	Branching ratio (%)					
(eV)	CF_3^+	CF_2^+	CF^+	F^+	C^+	CF_2^{2+}
29.5	95.62	4.20	0.18			
30.0	95.47	4.23	0.30			
31.0	95.03	4.31	0.66			
32.0	94.06	4.49	1.46			
33.0	92.91	4.83	2.27			
34.0	91.90	4.99	3.11			
35.0	89.97	5.42	4.29	0.17	0.15	
36.0	88.64	5.40	5.05	0.38	0.53	
37.0	86.90	5.56	5.65	0.73	1.16	
38.0	85.28	5.64	5.94	1.17	1.97	
39.0	83.17	5.78	6.34	1.65	3.06	
40.0	81.49	6.07	5.99	2.20	4.25	
41.0	80.44	6.12	5.27	2.91	5.26	
42.0	81.10	6.04	4.87	3.10	4.90	
43.0	81.12	6.37	4.27	3.48	4.77	
44.0	81.19	6.36	3.79	3.69	4.82	0.14
45.0	81.62	6.61	3.62	3.96	4.05	0.14
46.0	82.11	6.41	3.63	3.81	3.75	0.29
47.0	81.74	6.58	3.49	4.15	3.64	0.40
48.0	82.02	6.37	3.52	4.14	3.53	0.41
49.0	81.25	6.23	3.73	4.25	3.88	0.64
50.0	81.45	5.85	3.56	4.78	3.87	0.49
55.0	76.90	6.20	4.48	6.70	5.10	0.63
60.0	74.35	6.39	5.05	7.97	5.22	1.03
65.0	72.61	6.77	5.46	9.01	5.15	1.00
70.0	70.96	6.85	5.42	10.46	5.19	1.13
75.0	69.08	6.52	6.09	11.48	5.65	1.17
80.0	67.29	6.42	6.45	12.52	6.18	1.14

Table 5.18: Photoion branching ratio for CF_3Cl

Photon energy (eV)	Branching ratio (%)									
	CF_3Cl^+	CF_2Cl^+	CF_3^+	$CFCl^+$	CF_2^+	CCl^+	Cl^+	CF^+	F^+	C^+	CF_2Cl^{2+}
12.5	7.83		92.17								
13.0	2.32		97.68								
13.5	1.80		98.20								
14.0	1.94		97.77	0.29							
14.5	1.54	1.06	97.00	0.40							
15.0	1.39	3.19	95.17	0.25							
15.5	0.97	8.84	90.03	0.16							
16.0	0.90	16.10	82.93	0.07							
16.5	0.64	24.95	74.27	0.14							
17.0	0.55	30.53	68.78	0.14							
17.5	0.65	34.54	64.66	0.15							
18.0	0.57	35.97	63.28	0.19							
18.5	0.44	36.87	62.54	0.16							
19.0	0.59	37.19	61.70	0.10	0.42						
19.5	0.34	37.58	59.90	0.15	1.31		0.72				
20.0	0.34	36.06	58.76	0.10	2.45		2.29				
20.5	0.56	33.55	56.87	0.19	4.51		4.32				
21.0	0.40	30.11	52.85	0.16	9.46		7.02				
21.5	0.45	28.23	50.29	0.32	12.92		7.78				
22.0	0.42	28.04	48.30	0.42	14.49		8.33				
22.5	0.38	28.37	47.20	0.52	15.29		8.23				
23.0	0.44	28.99	46.09	0.55	15.22		8.09	0.62			
23.5	0.40	29.51	45.99	0.54	15.17		7.65	0.74			
24.0	0.27	30.44	45.13	0.52	14.90		7.88	0.86			
24.5	0.27	30.85	44.77	0.49	14.51		7.85	1.26			
25.0	0.41	31.64	43.53	0.53	14.23		8.11	1.54			
25.5	0.37	32.52	43.02	0.48	13.54		8.14	1.93			
26.0	0.43	32.94	42.20	0.44	13.03		8.61	2.35			
26.5	0.23	33.67	41.49	0.43	12.69		8.58	2.92			
27.0	0.29	34.68	40.46	0.35	12.32		8.56	3.34			
27.5	0.26	35.10	40.05	0.33	12.12		8.28	3.87			

continued on next page

Table 5.18: (continued)

Photon energy (eV)	Branching ratio (%)										
	CF_3Cl^+	CF_2Cl^+	CF_3^+	$CFCl^+$	CF_2^+	CCl^+	Cl^+	CF^+	F^+	C^+	CF_2Cl^{2+}
28.0	0.14	35.95	38.58	0.38	11.96	0.08	8.89	4.01			
28.5	0.30	36.34	37.84	0.41	11.83	0.17	8.66	4.45			
29.0	0.21	37.20	36.60	0.32	11.74	0.22	8.91	4.81			
29.5	0.20	37.09	35.64	0.30	11.79	0.33	9.42	5.32			
30.0	0.16	37.76	34.75	0.36	11.84	0.39	9.48	5.26			
31.0	0.19	38.81	33.32	0.35	12.02	0.70	9.24	5.38			
32.0	0.12	39.60	31.40	0.23	12.12	0.87	9.85	5.82			
33.0	0.06	40.77	29.49	0.31	12.13	0.97	10.37	5.83		0.08	
34.0	0.05	40.62	27.55	0.28	12.97	1.35	10.63	5.90	0.20	0.46	
35.0	0.06	40.93	25.77	0.31	13.47	1.43	11.15	5.94	0.22	0.74	
36.0	0.07	40.70	24.32	0.40	13.81	1.55	11.83	5.84	0.36	1.13	
37.0	0.00	39.36	23.42	0.33	14.43	1.58	12.70	5.91	0.63	1.63	
38.0	0.00	38.98	21.98	0.35	14.79	1.76	13.17	5.87	0.81	2.10	0.17
39.0	0.00	38.21	21.38	0.38	15.39	1.60	13.82	5.63	0.96	2.38	0.25
40.0	0.00	37.02	21.10	0.34	15.86	1.45	14.75	5.45	1.10	2.62	0.31
41.0	0.00	36.61	20.65	0.35	15.93	1.33	15.66	5.30	1.22	2.64	0.30
42.0	0.00	36.14	20.78	0.36	16.23	1.22	15.44	5.44	1.41	2.66	0.32
43.0	0.00	36.17	20.66	0.31	16.32	1.17	15.82	5.53	1.40	2.27	0.36
44.0	0.00	35.98	20.88	0.43	16.17	1.03	15.83	5.56	1.48	2.28	0.35
45.0	0.00	35.37	21.06	0.37	16.28	0.91	16.47	5.77	1.40	2.01	0.36
46.0	0.00	35.62	21.45	0.35	16.18	0.88	15.95	5.81	1.45	1.86	0.44
47.0	0.00	35.18	21.15	0.34	15.92	0.96	16.28	6.15	1.54	2.04	0.44
48.0	0.00	34.96	21.44	0.31	15.61	0.95	16.21	6.30	1.68	2.11	0.43
49.0	0.00	34.65	21.25	0.29	15.56	0.99	16.68	6.54	1.67	1.98	0.39
50.0	0.00	34.70	21.10	0.34	15.15	0.97	16.66	6.81	1.84	2.03	0.40
55.0	0.00	31.48	22.11	0.32	15.88	0.87	16.46	7.76	2.22	2.25	0.64
60.0	0.00	30.34	20.63	0.13	15.93	0.93	17.28	8.44	3.01	2.73	0.48
65.0	0.00	29.43	20.15	0.23	15.59	0.97	18.17	8.48	3.41	3.06	0.53
70.0	0.00	29.19	20.02	0.41	15.70	0.94	17.60	8.44	3.79	3.24	0.68
75.0	0.00	28.14	19.27	0.29	15.96	0.97	18.33	8.43	4.58	3.60	0.44
80.0	0.00	27.74	19.07	0.20	14.86	1.04	18.82	8.57	5.37	3.72	0.61

Table 5.19: Photoion branching ratio for CF_2Cl_2

Photon energy (eV)	Branching ratio (%)										
	$CFCl_2^+$	CF_2Cl^+	CCl_2^+	$CFCl^+$	CF_2^+	CCl^+	Cl^+	CF^+	F^+	C^+	CF_2Cl^{2+}
11.5		100.00									
12.0		100.00									
12.5		100.00									
13.0		100.00									
13.5		100.00									
14.0	0.28	99.72									
14.5	1.11	98.89									
15.0	1.73	98.27									
15.5	3.79	96.21									
16.0	6.81	93.19									
16.5	9.40	90.60									
17.0	11.12	88.88									
17.5	12.01	87.56			0.44						
18.0	13.18	85.50			1.31						
18.5	12.94	83.67		0.42	2.96						
19.0	12.57	80.67		1.09	5.67						
19.5	12.04	77.66		1.80	8.49						
20.0	11.72	73.84		2.90	10.58		0.39	0.56			
20.5	11.12	72.44		3.68	11.19		0.56	1.02			
21.0	10.85	71.23		4.19	11.52		0.93	1.28			
21.5	11.18	69.53		4.60	12.18		0.95	1.56			
22.0	11.00	67.56		5.16	12.52		1.33	2.42			
22.5	10.69	66.37		5.35	12.71		1.55	3.33			
23.0	10.47	65.13		5.63	13.44		1.39	3.93			
23.5	10.42	63.31		6.01	13.57		1.64	5.05			
24.0	10.43	61.58		6.15	13.60	0.32	2.04	5.87			
24.5	10.31	60.80		6.31	13.66	0.32	1.98	6.62			
25.0	10.73	59.84		5.71	13.50	0.56	1.87	7.80			
25.5	11.03	59.26		5.45	13.24	0.83	2.25	7.93			

continued on next page

Table 5.19: (continued)

Photon energy (eV)	Branching ratio (%)										
	$CFCl_2^+$	CF_2Cl^+	CCl_2^+	$CFCl^+$	CF_2^+	CCl^+	Cl^+	CF^+	F^+	C^+	CF_2Cl^{2+}
26.0	11.58	58.29		5.17	13.20	1.13	2.54	8.09			
26.5	12.23	57.49		5.10	13.06	1.15	2.88	8.09			
27.0	12.31	56.57		4.90	13.23	1.50	3.19	8.29			
27.5	12.78	55.43		4.93	12.94	1.72	3.65	8.55			
28.0	13.30	54.70		4.64	12.90	1.93	4.16	8.37			
28.5	14.05	53.23		4.85	12.63	2.05	4.64	8.55			
29.0	14.34	52.07		4.72	13.23	2.43	4.81	8.41			
29.5	14.76	51.02		4.57	13.24	2.50	5.35	8.56			
30.0	15.29	50.03		4.67	13.15	2.54	5.50	8.81			
31.0	16.50	46.94		5.01	13.58	2.99	6.16	8.56		0.26	
32.0	16.88	44.91		4.89	13.96	3.21	6.82	8.63		0.69	
33.0	17.98	42.47		5.00	14.46	3.45	7.59	8.26		0.79	
34.0	18.41	39.49		5.66	14.72	3.28	8.65	8.48		1.31	
35.0	18.74	37.26		5.78	15.01	3.30	9.83	8.54		1.54	
36.0	18.67	35.29		5.75	15.10	3.36	10.93	8.46	0.60	1.83	
37.0	18.46	33.15		6.41	15.20	3.21	12.21	8.73	0.57	2.07	
38.0	18.66	31.59		6.51	15.16	2.98	13.09	8.73	0.69	2.40	0.19
39.0	18.80	30.77		6.55	15.36	3.06	13.83	8.60	0.61	2.23	0.18
40.0	18.13	29.61		7.26	15.40	2.64	14.65	9.04	0.78	2.11	0.38
42.0	17.83	28.64		7.37	15.25	2.62	15.14	10.08	0.90	1.75	0.42
44.0	17.05	27.67		7.44	15.40	2.78	15.87	10.80	0.89	1.64	0.46
46.0	16.46	27.70	0.09	7.31	15.00	2.81	16.20	11.35	0.94	1.64	0.49
48.0	16.16	27.62	0.00	7.22	15.07	3.02	16.37	11.47	1.05	1.43	0.59
50.0	15.73	27.82	0.10	7.12	15.18	3.29	16.39	11.15	1.17	1.55	0.51
55.0	14.85	26.80	0.08	6.27	14.80	3.58	18.04	11.33	1.39	2.26	0.60
60.0	13.39	26.70	0.11	6.53	14.74	3.62	19.75	11.00	1.65	2.17	0.33
65.0	13.20	25.54	0.15	6.18	14.69	3.56	20.60	10.70	2.13	2.80	0.47
70.0	13.10	25.13	0.17	6.14	14.13	3.75	20.59	10.65	2.67	2.88	0.79

Table 5.20: Photoion branching ratio for $CFCl_3$

Photon energy (eV)	Branching ratio (%)								
	CCl_3^+	$CFCl_2^+$	CCl_2^+	$CFCl^+$	CCl^+	Cl^+	CF^+	F^+	C^+
11.5		100.00							
12.0		100.00							
12.5		100.00							
13.0		100.00							
13.5		100.00							
14.0	0.53	99.47							
14.5	1.19	98.81							
15.0	1.61	98.39							
15.5	2.24	97.76							
16.0	2.54	97.46							
16.5	2.90	96.51		0.59					
17.0	3.15	95.63		1.22					
17.5	2.32	93.69	0.46	3.54					
18.0	1.86	89.98	1.12	6.55			0.49		
18.5	2.02	84.87	2.14	10.17		0.23	0.57		
19.0	1.72	81.16	2.97	12.57		0.36	1.22		
19.5	1.91	79.11	3.43	13.38		0.40	1.75		
20.0	1.60	77.30	3.74	13.99		0.58	2.79		
20.5	1.63	76.81	3.85	13.68		0.57	3.46		
21.0	1.43	75.34	4.23	13.97	0.28	0.53	4.22		
21.5	1.66	74.23	4.22	13.72	0.88	0.45	4.85		
22.0	1.63	73.38	4.35	13.63	1.36	0.73	4.92		
22.5	1.55	72.36	4.70	13.05	1.93	0.80	5.61		
23.0	1.56	70.43	4.63	13.11	3.14	0.87	6.26		
23.5	1.64	69.77	4.02	12.96	3.83	1.24	6.54		

continued on next page

Table 5.20: (continued)

Photon energy (eV)	Branching ratio (%)								
	CCl_3^+	$CFCl_2^+$	CCl_2^+	$CFCl^+$	CCl^+	Cl^+	CF^+	F^+	C^+
24.0	1.55	69.50	4.34	11.95	4.65	1.48	6.52		
24.5	1.75	68.22	4.10	11.83	5.61	1.89	6.60		
25.0	1.67	67.53	3.99	11.59	6.21	2.74	6.29		
25.5	1.71	66.25	3.80	11.69	6.71	3.35	6.49		
26.0	1.64	66.24	3.61	11.75	7.08	3.78	5.89		
26.5	1.73	64.51	4.04	11.16	8.15	4.54	5.88		
27.0	1.77	63.68	3.63	11.58	8.32	5.06	5.95		
27.5	1.94	62.15	4.26	11.72	8.32	5.38	6.24		
28.0	1.91	60.72	4.31	12.10	8.88	5.73	6.36		
28.5	2.08	60.27	4.11	12.47	8.89	6.24	5.96		
29.0	1.94	59.00	4.35	12.53	8.93	6.40	6.39		0.44
29.5	2.06	57.76	4.75	13.58	8.78	6.53	6.00		0.54
30.0	2.20	56.92	4.73	12.97	8.65	7.56	6.19		0.78
31.0	2.09	49.82	4.91	14.74	9.32	10.98	6.65		1.49
32.0	2.34	47.44	5.28	15.44	9.09	12.37	6.20		1.84
33.0	2.20	44.84	5.42	15.59	9.16	13.67	7.03		2.09
34.0	2.00	43.00	5.72	16.25	9.11	14.66	7.12		2.14
35.0	2.27	41.75	5.67	16.50	9.10	15.86	7.03		1.83
36.0	2.13	38.12	5.73	17.84	8.49	17.92	7.49		2.28
37.0	2.15	35.56	6.93	18.37	8.42	18.67	7.89		2.00
38.0	2.18	34.26	5.98	19.06	8.72	19.85	7.91	0.04	2.00
39.0	2.15	34.07	6.82	18.22	8.89	19.85	7.81	0.21	1.97
40.0	2.05	33.22	6.75	17.29	8.66	20.83	9.16	0.20	1.84
41.0	2.18	31.79	6.90	18.29	9.02	20.89	8.88	0.24	1.82
43.0	2.23	30.21	6.64	18.39	9.71	21.37	9.51	0.27	1.67
45.0	2.01	29.68	6.54	17.55	9.96	22.48	9.72	0.29	1.77
47.0	2.00	29.41	6.63	17.40	10.27	22.72	9.59	0.35	1.63
49.0	1.85	29.87	6.34	16.67	10.32	23.33	9.61	0.30	1.71

and decrease in the order of $CF_4 > CF_3Cl > CF_2Cl_2 > CFCl_3$.

In the dipole (e, e+ion) experiments the ratio of the total coincident ion signal to the forward scattered energy loss signal at each energy loss gives the relative photoionization efficiency as defined in section 2.3.5. Our data show 20 eV , 23.5 eV, 17.5 eV and 14.5 eV to be the lowest photon energies at which the photoionization efficiencies (η_i) for CF_4, CF_3Cl, CF_2Cl_2 and $CFCl_3$ reach approximately respective constant values. Making the reasonable assumption that the photoionization efficiency is unity at high energy [8,20,114], we therefore obtain the result that η_i for CF_4, CF_3Cl, CF_2Cl_2 and $CFCl_3$ reach 1.0 respectively at ~20 eV, 23.5 eV, 17.5 eV and 14.5 eV. The photoionization efficiency curves for CF_4, CF_3Cl, CF_2Cl_2 and $CFCl_3$ are shown as inserts to respective figs. 5.11a, 5.12a, 5.13a and 5.14a, and values of η_i are listed in respective tables 5.12, 5.13, 5.14 and 5.15. Compared to previously reported work [103], our CF_4 ionization efficiency curve is higher and has less structure (insert to fig. 5.11a), probably due to lower energy resolution. The previously reported photoionization efficiencies [108] of CF_3Cl, CF_2Cl_2 and $CFCl_3$ determined using neon resonance lamp radiation at ~16.75 eV are in generally good agreement with the present results (inserts to figs. 5.12a, 5.13a and 5.14a).

Absolute differential oscillator strengths for production of the fragment (dissociative) ions are obtained by taking the triple product of the photoabsorption, the photoionization efficiency and the photoion branching ratio at each photon energy. The absolute partial differential oscillator strengths for production of the molecular and fragment ions are shown in fig. 5.24 and table 5.12 for CF_4, in fig. 5.25 and table 5.13 for CF_3Cl, in fig. 5.26 and table 5.14 for CF_2Cl_2, and in fig. 5.27 and table 5.15 for $CFCl_3$.

Tables 5.21, 5.22, 5.23 and 5.24 present the appearance potentials ($\pm$ 1 eV) for the production of ion species respectively from CF_4, CF_3Cl, CF_2Cl_2 and $CFCl_3$ measured in

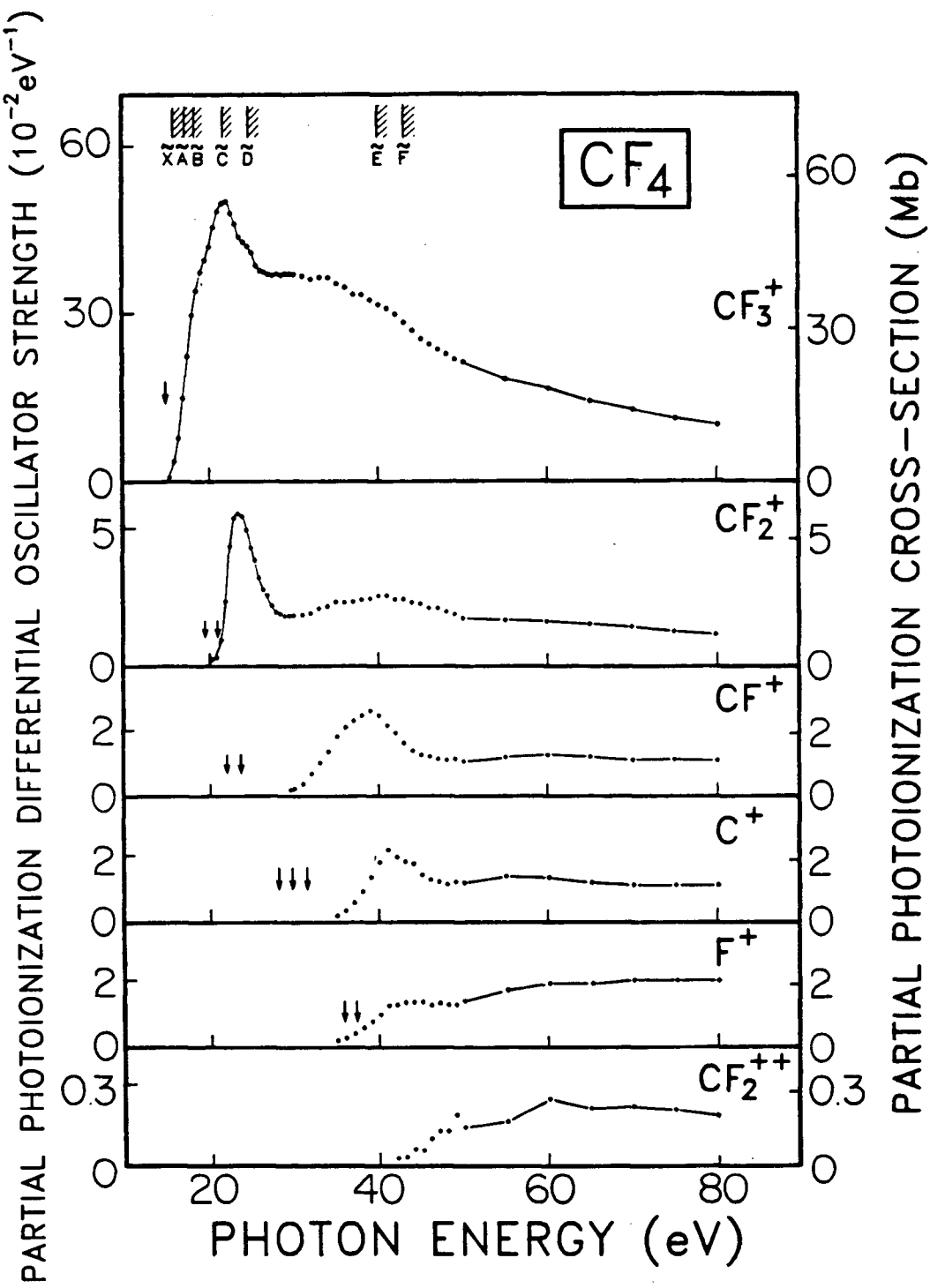

Figure 5.24: Absolute differential oscillator strengths for dissociative photoionization of CF_4. The vertical arrows represent expected thermodynamic appearance potentials (see table 5.21) and the hatched lines indicate the vertical ionization energies [99,98] for production of the electronic states of CF_4^+.

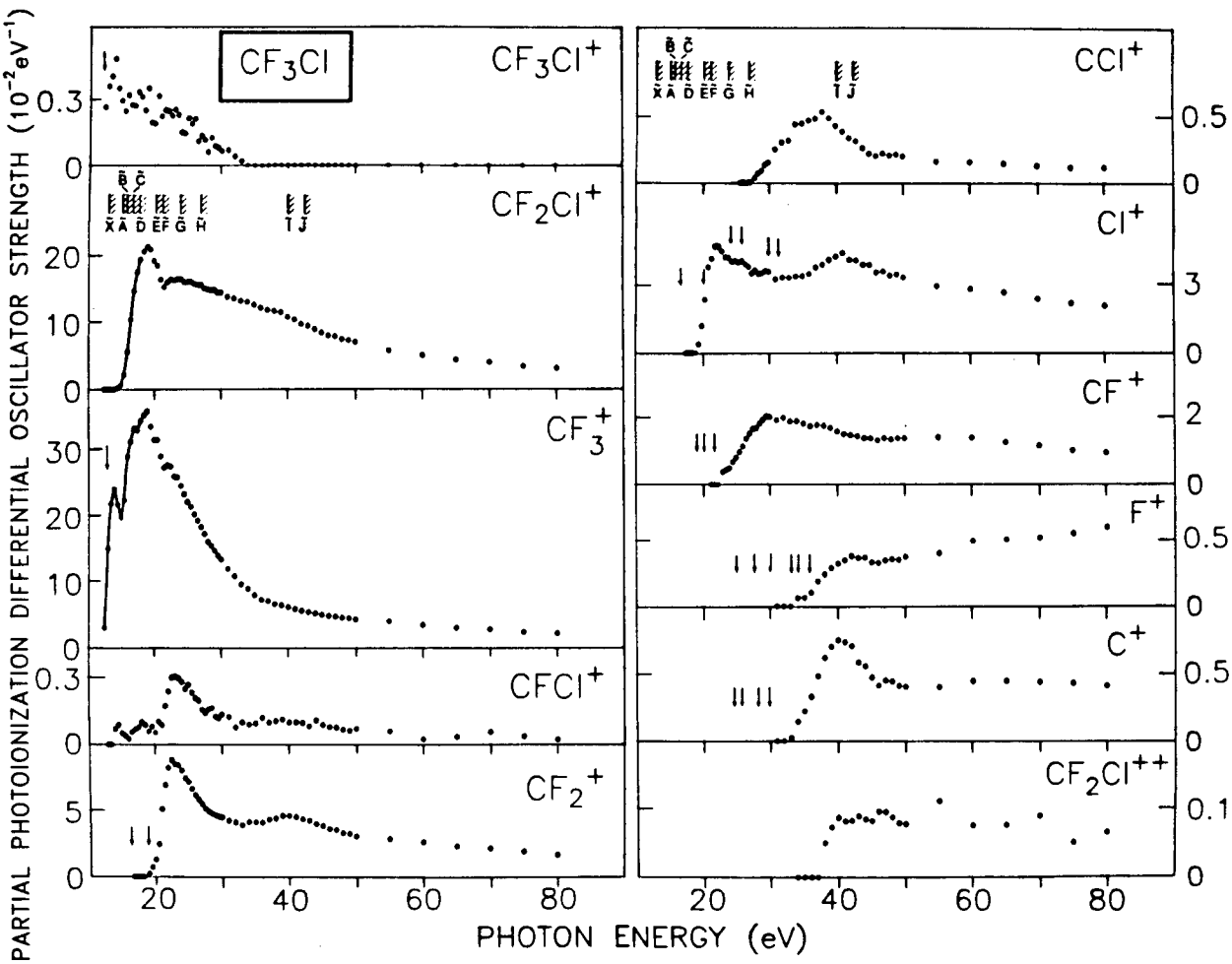

Figure 5.25: Absolute differential oscillator strengths for molecular and dissociative photoionization of CF_3Cl. The vertical arrows represent expected thermodynamic appearance potentials (see table 5.22) and the hatched lines indicate the vertical ionization energies presented in chapter 6 and reported in ref. [100] for production of the electronic states of CF_3Cl^+.

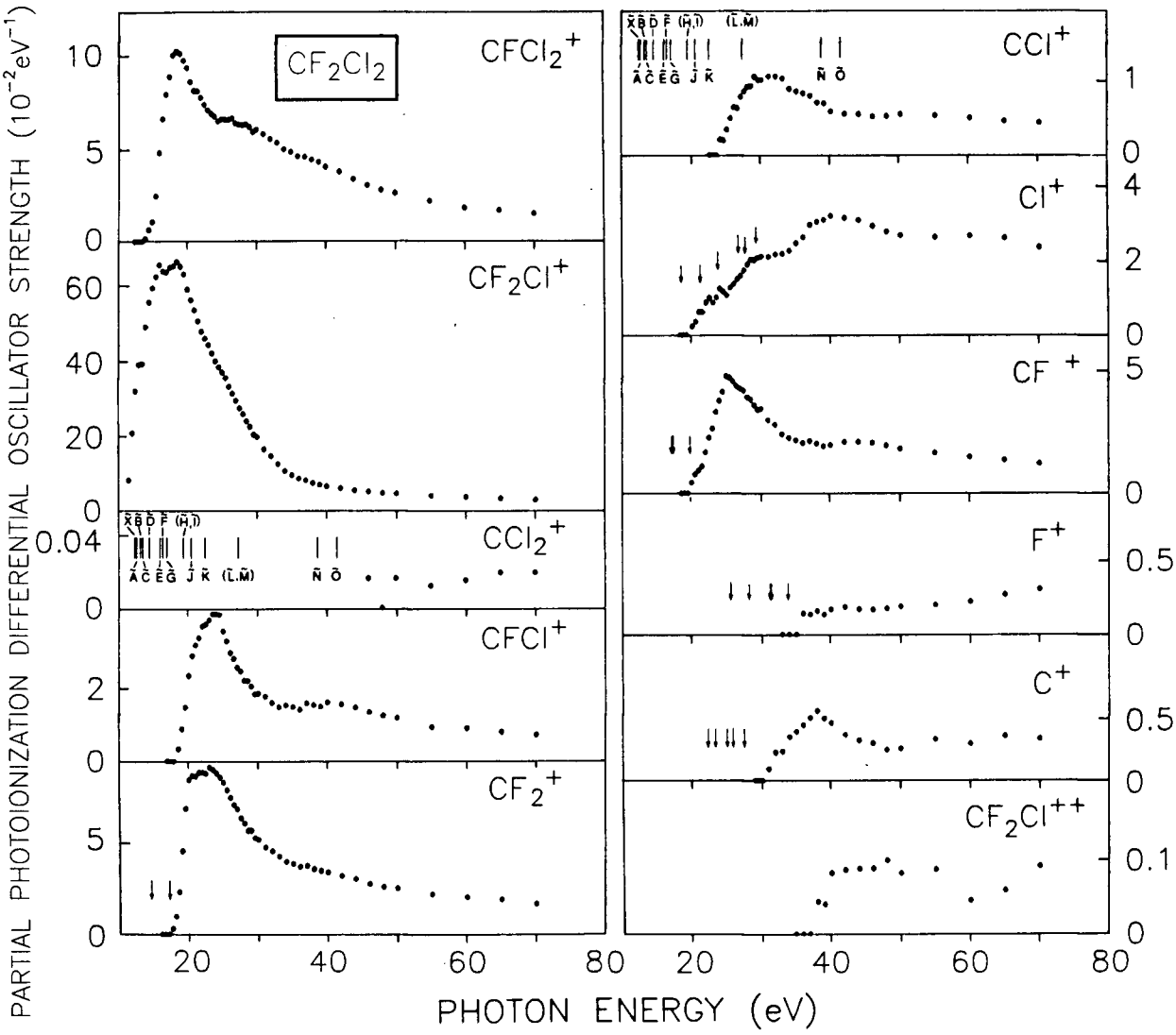

Figure 5.26: Absolute differential oscillator strengths for dissociative photoionization of CF_2Cl_2. The vertical arrows represent expected thermodynamic appearance potentials (see table 5.23) and the vertical lines indicate the vertical ionization energies presented in chapter 6 and reported in ref. [100] for production of the electronic states of $CF_2Cl_2^+$.

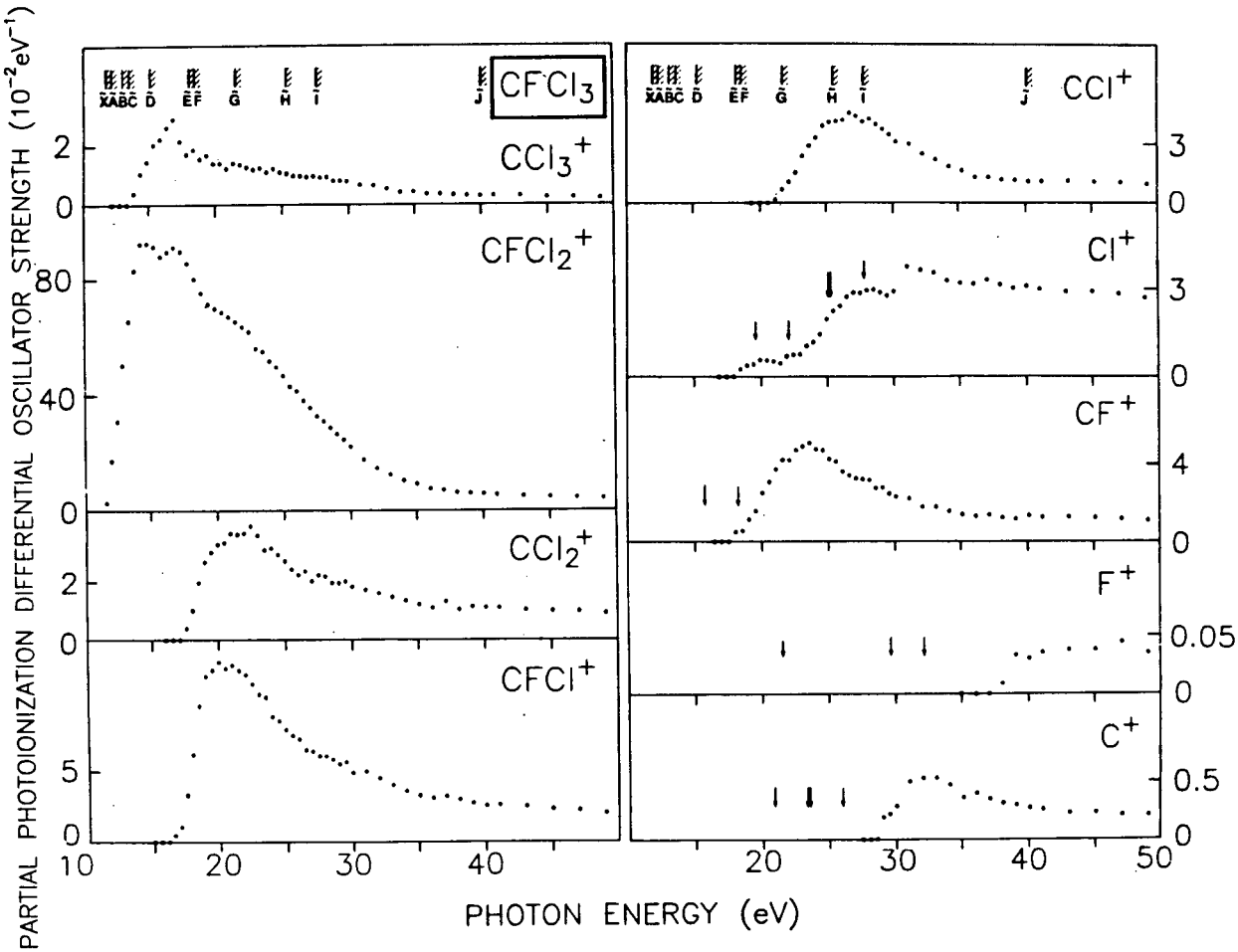

Figure 5.27: Absolute differential oscillator strengths for dissociative photoionization of $CFCl_3$. The vertical arrows represent expected thermodynamic appearance potentials (see table 5.24) and the hatched lines indicate the vertical ionization energies presented in chapter 6 and reported in ref. [100] for production of the electronic states of $CFCl_3^+$.

Table 5.21: Calculated and measured appearance potentials for production of charged species from CF_4

Process	Appearance potential (eV)								
	calcu-	experimental[ref.]							
	lated[a]	this work [b]	[135]	[136]	[137]	[138]	[139]	[103]	[140]
(1) CF_3^++F	14.74	16	15.9	15.4	16.0	16.2	15.35	15.56	15.52
(2) CF_2^++F_2	19.32	21	22.45	22.33	20.3	22.2			
(3) CF_2^++2F	20.92								
(4) CF^++F_2+F	22.07								
(5) CF^++3F	23.66	30	22.85	27.32	22.6				
(6) C^++2F_2	28.23								
(7) C^++F_2+2F	29.82								
(8) C^++4F	31.42	35		29.5	31.5				
(9) F^++F_2+F+C	35.99	35	24.0		36				
(10)F^++3F+C	37.58								
(11) CF_2^{2+}+?	44	44.3							
(12) CF_3^{2+}+?	42.7								

[a]Using thermochemical data from ref. [132], assuming zero kinetic energy of fragmentation.
[b]±1 eV.

Table 5.22: Calculated and measured appearance potentials for the production of charged species from CF_3Cl

Process	Appearance potential (eV)											
	Calculated[a]	Experimental [ref.]										
		This work[b]	[137]	[141]	[107]	[142]	[140]	[143]	[144]	[145]	[146]	[147]
(1) CF_3Cl^+	12.6	12.5	13	12.8	12.45	12.39	12.43	12.91			12.6	
(2) CF_2Cl^+		14.5	15.0	15.5	14.25				16.15			
(3) CF_3^++Cl	12.7	12.5	12.7	12.95	12.55	12.65	12.57			13.06		
(4) $CFCl^+$		14.5										20.45
(5) CF_2^++FCl	16.5											
(6) CF_2^++F+Cl	19.1	19	20	21.0	18.85	18.84						18.85
(7) CCl^+		28										
(8) Cl^++CF_3	16.8											
(9) Cl^++CF_2+F	20.4	19.5	21	21.0								
(10) Cl^++CF+F_2	24.1											
(11) Cl^++CF+2F	25.7											
(12) Cl^++C+F+F_2	29.7											
(13) Cl^++C+3F	31.3											
(14) CF^++F+FCl	19.3											
(15) CF^++F_2+Cl	20.2											20.28
(16) CF^++2F+Cl	21.8	23.5	22.6	25.0								22.00
(17) F^++CF_2+Cl	24.9											
(18) F^++CF+FCl	27.6											
(19) F^++CF+F+Cl	30.1		31									
(20) F^++C+FCl+F	33.2											
(21) F^++C+F_2+Cl	34.1	34										
(22) F^++C+2F+Cl	35.7			35.0								
(23) C^++F_3Cl	24.3											
(24) C^++F_2+FCl	25.4											
(25) C^++F_2+F+Cl	28.0											
(26) C^++3F+Cl	29.6	33	31									
(27) CF_2Cl^{2+}+??		38										
(28) $CFCl^{2+}$+??		40										

[a]Using thermochemical data from refs. [133,132,134] assuming zero kinetic energy of fragmentation.
[b]± 1 eV.

Table 5.23: Calculated and measured appearance potentials for the production of charged species from CF_2Cl_2

Process	Appearance Potential (eV)							
	Calculated[a]	Experimental [ref.]						
		This work[b]	[107]	[142]	[143]	[144]	[146]	[147]
(1) $CF_2Cl_2^+$	11.8		11.75	11.75	12.31		11.87	
(2) $CFCl_2^+$		14.0	14.15	13.81				13.30
(3) CF_2Cl^+		11.5	12.10	11.99		12.55		11.96
(4) CCl_2^+		46						
(5) $CFCl^+$		18.5		17.76				18.60
(6) $CF_2^+ + Cl_2$	14.6							14.90
(7) $CF_2^+ + 2Cl$	17.1	17.5	17.22	16.98				
(8) CCl^+		24						21.60
(9) $Cl^+ + CF_2 + Cl$	18.5							18.76
(10) $Cl^+ + CF + FCl$	21.2	20						
(11) $Cl^+ + CF + F + Cl$	23.8							
(12) $Cl^+ + C + FCl + F$	26.8							
(13) $Cl^+ + C + F_2 + Cl$	27.7							
(14) $Cl^+ + C + 2F + Cl$	29.3							
(15) $CF^+ + FCl + Cl$	17.3							
(16) $CF^+ + F + Cl_2$	17.4		17.65					17.35
(17) $CF^+ + F + 2Cl$	19.9	20	20.20					19.84
(18) $F^+ + CF + Cl_2$	25.7							
(19) $F^+ + CF + 2Cl$	28.2							
(20) $F^+ + C + FCl + Cl$	31.2							
(21) $F^+ + C + F + Cl_2$	31.3							
(22) $F^+ + C + F + 2Cl$	33.8	36						
(23) $C^+ + 2FCl$	20.5							
(24) $C^+ + F_2 + Cl_2$	23.5							
(25) $C^+ + FCl + F + Cl$	25.1							
(26) $C^+ + 2F + Cl_2$	25.1							
(27) $C^+ + F_2 + 2Cl$	26.0							
(28) $C^+ + 2F + 2Cl$	27.6	31						
(29) $CF_2Cl^{2+} + ??$		38						

[a] Using thermochemical data from refs. [133,132,134] assuming zero kinetic energy of fragmentation.
[b] $\pm$ 1 eV.

Table 5.24: Calculated and measured appearance potentials for the production of charged species from $CFCl_3$

Process	Appearance potential (eV)							
	calculated[a]	Experimental [ref.]						
		this work[b]	[107]	[142]	[148]	[147]	[146]	[141]
(1) $CFCl_3^+$	11.8						11.46	
(2) CCl_3^+		14	13.50	13.25	12.77			13.8
(3) $CFCl_2^+$		11.5	11.65	11.57	11.97			
(4) CCl_2^+		17.5	17.0	17.12				
(5) $CFCl^+$		16.5	16.0	16.02	17.41	16.95		
(6) CCl^+		21	20.5			20.00		
(7) Cl^++CF+Cl_2	19.6	18.5						
(8) Cl^++CF+2Cl	22.0							
(9)Cl^++C+FCl+Cl	25.0							
(10)Cl^++C+F+Cl_2	25.1							
(11)Cl^++C+F+2Cl	27.6							
(12)CF^++Cl+Cl_2	15.7		15.7					
(13) CF^++3Cl	18.2	18	18.35			18.10		
(14) F^++CCl_3	21.6							
(15)F^++C+Cl+Cl_2	29.6							
(16) F^++C+3Cl	32.0	38						
(17) C^++FCl+Cl_2	20.8							
(18) C^++FCl+2Cl	23.3							
(19)C^++F+Cl+Cl_2	23.4							
(20) C^++F+3Cl	25.9	29						

[a]Using thermochemical data from refs. [133,132,134] assuming zero kinetic energy of fragmentation.
[b]± 1 eV.

the present work and appearance potentials for the various processes calculated from thermodynamic data [132,133,134], assuming zero kinetic energy of fragmentation. Previously reported values are also shown in tables 5.21, 5.22, 5.23 and 5.24 for comparison. The calculated thresholds are denoted by arrows on figs. 5.20, 5.24, 5.21, 5.25, 5.22, 5.26, 5.23 and 5.27, together with the vertical ionization energies for production of the electronic ion states of respective molecules (see section 5.1).

5.5 Absolute Electronic State Partial Photoionization Differential Oscillator Strengths for CF_4

In this section the electronic state partial differential oscillator strengths for CF_4 have been re-derived based on the earlier reported results and the new information available from the present investigations. Those for other freon molecules will be reported in chapter 6.

Electronic state partial photoionization cross sections have been reported for CF_4 [105] for production of the $\tilde{X}$, $\tilde{A}$, $\tilde{B}$, $\tilde{C}$ and $\tilde{D}$ ion states up to 70 eV photon energy. Yates *et al.* [149] have reported PES branching ratio measurements for CF_4 consistent with the cross-section data of Carlson *et al.* [105]. However, as discussed in section 5.2.1 above, the reported absolute values of the electronic state partial cross-sections for the $\tilde{X}$, $\tilde{A}$, $\tilde{B}$, $\tilde{C}$ and $\tilde{D}$ states [105] may be incorrect due to the method used for the absolute measurement and/or the effects of higher order radiation (see section 5.2.1). It should be noted that the $\tilde{E}$ ion state has an adiabatic ionization potential of ~34 eV [117], while the appearance potentials of C^+ and F^+ are ~35 eV in the present work (see table 5.21). Therefore, we can tentatively set the sum of the differential oscillator strengths for production of the $\tilde{E}$ and $\tilde{F}$ ion states to be equal to the sum of those for producing C^+ and F^+. With these considerations in mind, we have re-analyzed the PES data for CF_4 reported by Carlson

et al. [105] as follows:

1. In the energy region below the adiabatic ionization energy of the $\tilde{E}$ state (~34 eV), photoelectron branching ratios were calculated from the previously reported experimental partial cross-sections [105]. These were then combined with the presently reported photoabsorption and photoionization efficiency results (table 5.12) to obtain improved estimates of the electronic state partial photoionization differential oscillator strengths of the $\tilde{X}$, $\tilde{A}$, $\tilde{B}$, $\tilde{C}$ and $\tilde{D}$ states of CF_4.

2. At higher photon energies up to 70 eV, the originally reported relative intensities for the $\tilde{X}$, $\tilde{A}$, $\tilde{B}$, $\tilde{C}$ and $\tilde{D}$ ion states [105] were used to partition a differential oscillator strength equal to the present total photoabsorption (table 5.12) minus an appropriate allowance for the combined ($\tilde{E}$+$\tilde{F}$) state differential oscillator strengths. Since there are no direct experimental measurements, the combined ($\tilde{E}$+$\tilde{F}$) state differential oscillator strengths have been equated to the sum of the measured differential oscillator strengths for the production of the C^+ and F^+ ions (this work) for the reasons described above.

These revised electronic state partial differential oscillator strengths are presented numerically in table 5.25 and are shown together with the MS-Xα calculations [150] and previous PES data [105] in fig. 5.28. The revised values show only small differences from the original PES data [105] for the $\tilde{B}$, $\tilde{C}$ and $\tilde{D}$ states. Somewhat larger differences exist for the (<20 and 25–35 eV) and (<23 eV) state partial cross-sections. In general, the (resolutionless) MS-Xα calculations give a reasonable semi-quantitative description of the trends in the measured partial cross-sections. The presently estimated differential oscillator strengths for the combined ($\tilde{E}$+$\tilde{F}$) states are comparable with the calculation in terms of shape and magnitude. It is noteworthy that for the $\tilde{X}$ state, the presently

Table 5.25: Electronic state partial differential oscillator strengths for the photoionization of CF_4 [a]

Photon energy (eV)	Electronic state differential oscillator strength ($10^{-2}eV^{-1}$)					
	$\tilde{X}$	$\tilde{A}$	$\tilde{B}$	$\tilde{C}$	$\tilde{D}$	$\tilde{E}+\tilde{F}$ [b]
15.5	0.81					
16.0	3.64					
16.5	7.80					
17.0	14.95					
17.5	22.47					
18.0	9.58	20.26				
18.5	12.21	22.00				
19.0	14.65	22.82				
19.5	10.99	25.72	2.97			
20.0	11.58	22.82	7.71			
21.0	14.56	24.60	9.45			
22.0	18.43	21.47	12.46			
23.0	16.34	15.62	8.33	11.10		
24.0	16.76	12.57	6.84	11.99		
25.0	18.31	11.05	6.36	9.38		
26.0	17.97	9.92	6.17	6.78		
28.0	18.62	8.70	5.93	5.35	0.42	
30.0	19.22	8.72	5.33	4.94	0.72	
32.0	17.98	8.76	5.83	5.06	0.92	
34.0	16.31	10.42	5.73	6.01	1.31	
36.0	14.06	10.62	5.59	6.76	2.05	0.36
38.0	12.52	10.61	5.34	7.36	2.31	1.24
40.0	11.52	10.39	5.11	7.33	2.12	2.52
45.0	9.38	8.60	4.16	5.02	1.70	2.51
50.0	7.78	7.37	3.69	3.40	1.85	2.28
55.0	6.44	6.16	3.21	3.69	1.61	2.82
60.0	5.48	5.81	3.20	3.76	1.25	2.96
65.0	4.58	4.58	3.30	3.28	1.28	2.81
70.0	4.21	4.01	2.81	3.11	1.11	2.83

[a] Based on branching ratios calculated from previously published PES measurements [105] combined with the present photoabsorption and photoionization efficiency data (table 5.12) and using values of the ($\tilde{E}+\tilde{F}$) state partial differential oscillator strengths estimated from the partial photoionization differential oscillator strength sum ($C^+ + F^+$). See text for details.

[b] The electronic state differential oscillator strength sum ($\tilde{E}+\tilde{F}$) was set equal to the partial photoionization differential oscillator strengths ($C^+ + F^+$). See text for details.

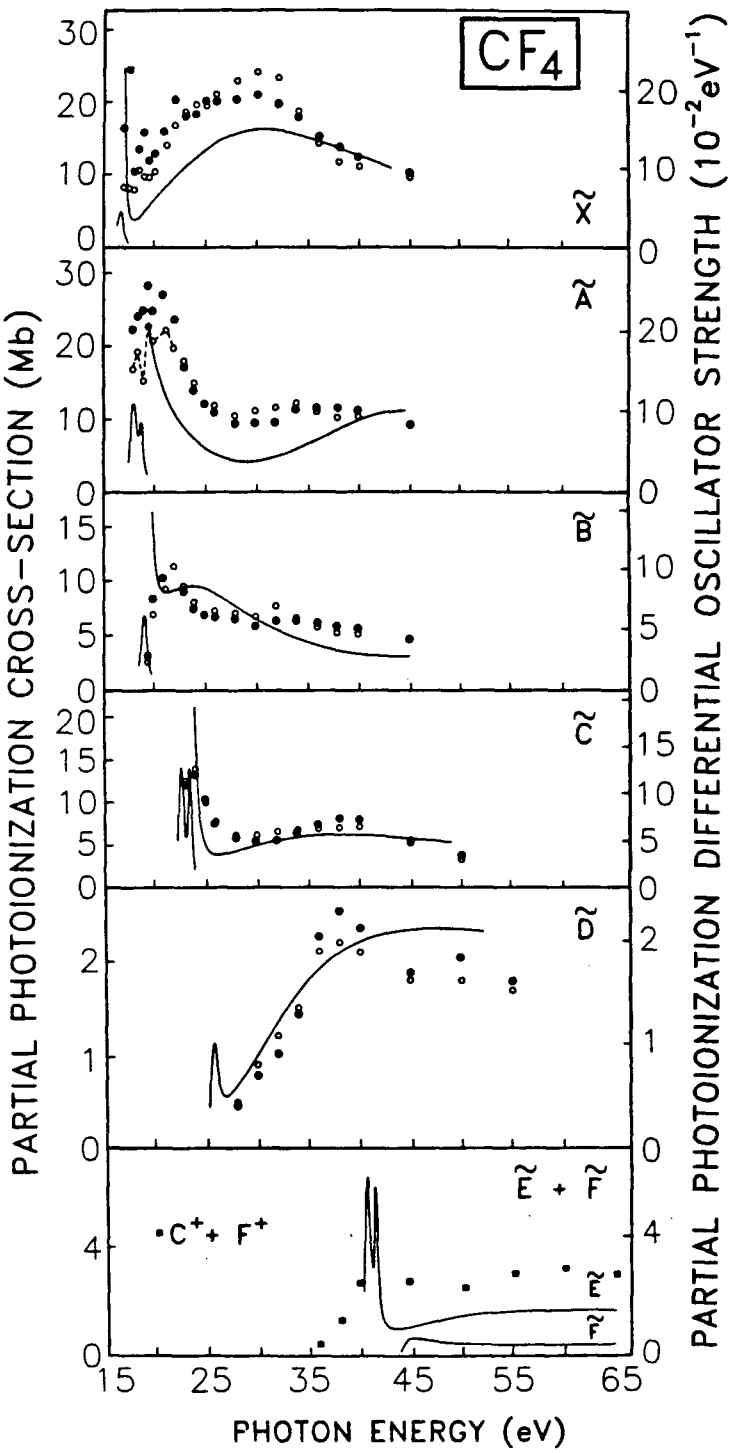

Figure 5.28: Electronic state partial photoionization differential oscillator strengths of CF_4. Open circles—previously reported partial photoionization cross—section (electronic states) measurements obtained by PES [105] (see text). Solid circles—revised values obtained by combining the present photoabsorption and photoionization data with PES branching ratios derived from reference [105]. See section 5.5 for details. Solid lines—MS-Xα calculations [150]. Squares—summed (C^++F^+) partial differential oscillator strengths. See text for details.

revised PES cross-sections show a resonance at ~17.5 eV which is predicted by the calculation but not exhibited in the PES data as originally presented [105].

5.6 The Dipole Induced Breakdown

In photoionization once the photon energy exceeds the upper limit of the Franck-Condon region, the internal energy of the molecular ion is independent of the photon energy for a given electronic state and the remainder of the energy is carried by the photoelectron according to Einstein's photoelectric equation. On the assumption that fragmentation ratios for dissociative ionization from each electronic state of the ion are constant when the photon energy is above the Franck-Condon region [77], the partial differential oscillator strengths for the production of the singly charged molecular or any stable dissociative (fragment) ion should be a fixed linear combination of electronic state partial photoionization differential oscillator strengths at all photon energies. This general approach and possible exceptions such as autoionization, internal conversion to other electronic ion states and multiple ionization have been discussed in ref. [77]. The dipole induced breakdown patterns of many small molecules have been investigated with considerable success by this type of analysis, for example, see refs. [77,114]. The dipole induced breakdown schemes for CF_4, CF_3Cl and CF_2Cl_2 discussed below have been obtained using the presently reported absolute differential oscillator strengths for molecular and dissociative photoionization. The electronic state partial photoionization differential oscillator strengths for CF_4 are as reported in section 5.5, while those for CF_3Cl and CF_2Cl_2 are obtained from the triple product of the presently measured total photoabsorption differential oscillator strengths (section 5.2.2), the photoionization efficiencies (section 5.4) and the electronic state branching ratios obtained from synchrotron radiation PES measurements reported in section 6.2 and ref. [121,151] (see details below). The dipole induced

breakdown of $CFCl_3$ is not reported since insufficient PES data is available.

5.6.1 The Dipole Induced Breakdown of CF_4

Since stable CF_4^+ is not observed on the time scale of the TOF mass spectrometer and because CF_3^+ is the only ion produced below the state ionization potential (adiabatic IP = 21.7 eV [99])–see table 5.21, the $\tilde{X}$, $\tilde{A}$ and $\tilde{B}$ electronic states of singly ionized CF_4 must exclusively lead to production of CF_3^+. A consideration of the Franck-Condon width of the $\tilde{C}$ state and the appearance potential of CF_2^+ (~21 eV) indicates that CF_2^+ can be formed from the $\tilde{C}$ state. Similarly the smaller fragments can only be formed from the $\tilde{D}$ and/or higher states. In the region below ~40 eV, CF^+ can only be formed from the $\tilde{D}$ state. With these considerations in mind the following relationships between the differential oscillator strengths for formation of CF_3^+, CF_2^+, CF^+, C^+ and F^+, and those for production of the $\tilde{X}$, $\tilde{A}$, $\tilde{B}$, $\tilde{C}$, $\tilde{D}$, $\tilde{E}$ and $\tilde{F}$ ion states are found to provide a reasonably consistent rationalization of the breakdown:

$$\frac{df}{dE}(CF_3^+) = \frac{df}{dE}(\tilde{X} + \tilde{A} + \tilde{B} + 0.62\tilde{C}) \tag{5.42}$$

$$\frac{df}{dE}(CF_2^+) = \frac{df}{dE}(0.38\tilde{C}) \tag{5.43}$$

$$\frac{df}{dE}(CF^+) = \frac{df}{dE}(\tilde{D}) \tag{5.44}$$

$$\frac{df}{dE}(C^+ + F^+) = \frac{df}{dE}(\tilde{E} + \tilde{F}). \tag{5.45}$$

Fig. 5.29 shows the breakdown relationship as a function of photon energy. In scheme I, the originally presented PES data [105] have been used. The agreement is quite good considering that the PES data and the ion photofragment differential oscillator strengths are from independent measurements using different techniques with independent means of establishing the absolute scales. However, as discussed in section 5.2.1, we have some reservations concerning the absolute values reported in the original PES study [105] and,

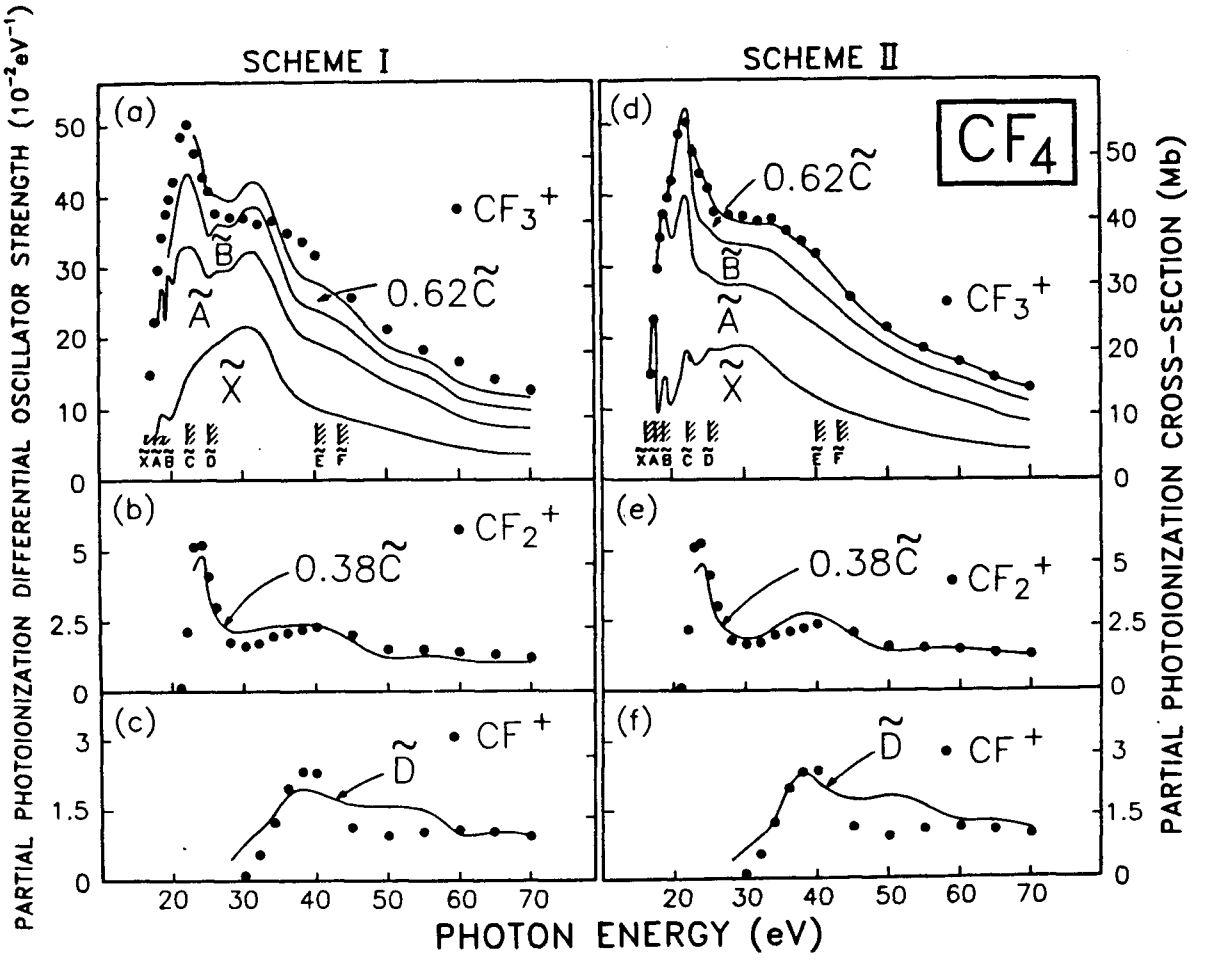

Figure 5.29: Absolute differential oscillator strengths for the proposed dipole induced breakdown scheme of CF_4. Solid circles—present dipole (e, e+ion) experimental data, solid lines—sums of electronic state partial differential oscillator strengths (scheme I using original PES data [105]; scheme II using revised PES data). See text for details. (a,d) Photofragmentation to CF_3^+. (b,e) Photofragmentation to CF_2^+. (c,f) Photofragmentation to CF^+.

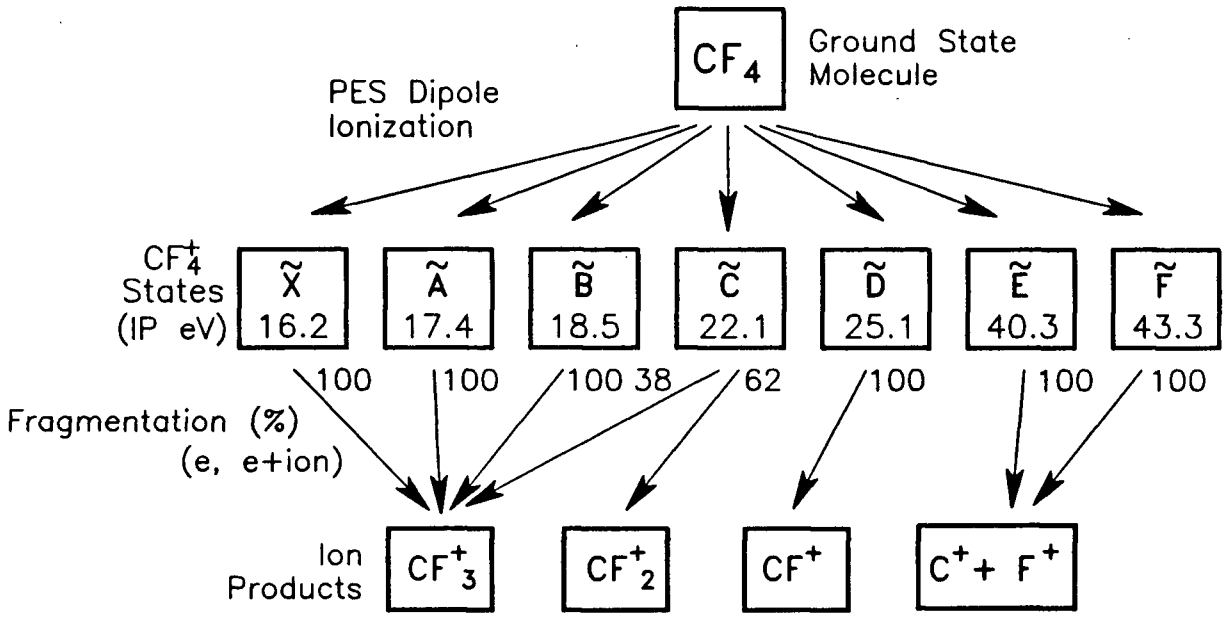

Figure 5.30: Proposed dipole induced breakdown scheme for the ionic photoionization of CF_4. See text for details.

therefore, have considered a set of revised PES data as discussed in section 5.5. The revised electronic state cross-sections are used in scheme II of fig. 5.29. Scheme II shows a somewhat better overall fit to the ion data. However it should be remembered that localized variations of the overall breakdown pattern might be expected at lower energies due to the autoionization levels preceding the various ionization limits. Nevertheless the general consistency of the fits for CF_3^+, CF_2^+ and CF^+ over the entire energy range up to 70 eV in both schemes lends confidence to the essential correctness of the breakdown scheme as proposed above. Fig. 5.30 shows in diagrammatic form the main features of the proposed dipole induced breakdown scheme for CF_4. Further details of the breakdown pattern of CF_4 must await detailed photoelectron-photoion coincidence studies as a function of photon energy.

5.6.2 The Dipole Induced Breakdown of CF_3Cl

Since the molecular ion CF_3Cl^+ and the ion CF_3^+ are the ions produced from CF_3Cl (see table 5.22) below the $\tilde{A}$ state ionization potential [100], the $\tilde{X}$ state must lead to production of CF_3Cl^+ and CF_3^+. Considering the Franck-Condon region of the $\tilde{A}$ state [100] and the appearance potentials of CF_2Cl^+ and $CFCl^+$, it appears that the ions CF_2Cl^+ and $CFCl^+$ are the fragments produced from the dipole induced breakdown of the $\tilde{A}$ state. By taking account of the present energy resolution (1 eV FWHM), the Franck-Condon width and the ionization energy of the $\tilde{D}$ state [100] and the appearance potential of CF_2^+, it is suggested that the CF_2^+ ion is formed from the $\tilde{D}$ electronic state of the molecular ion. Similarly, the ions Cl^+, CF^+ and CCl^+ can be formed from the $\tilde{F}$, $\tilde{G}$ and $\tilde{H}$ states (ref. [100] and chapter 6) respectively and the ions F^+ and C^+ from the $\tilde{I}$ state (chapter 6). With these considerations in mind the following relationships between the partial differential oscillator strengths for formation of CF_3Cl^+, CF_2Cl^+,CF_3^+,

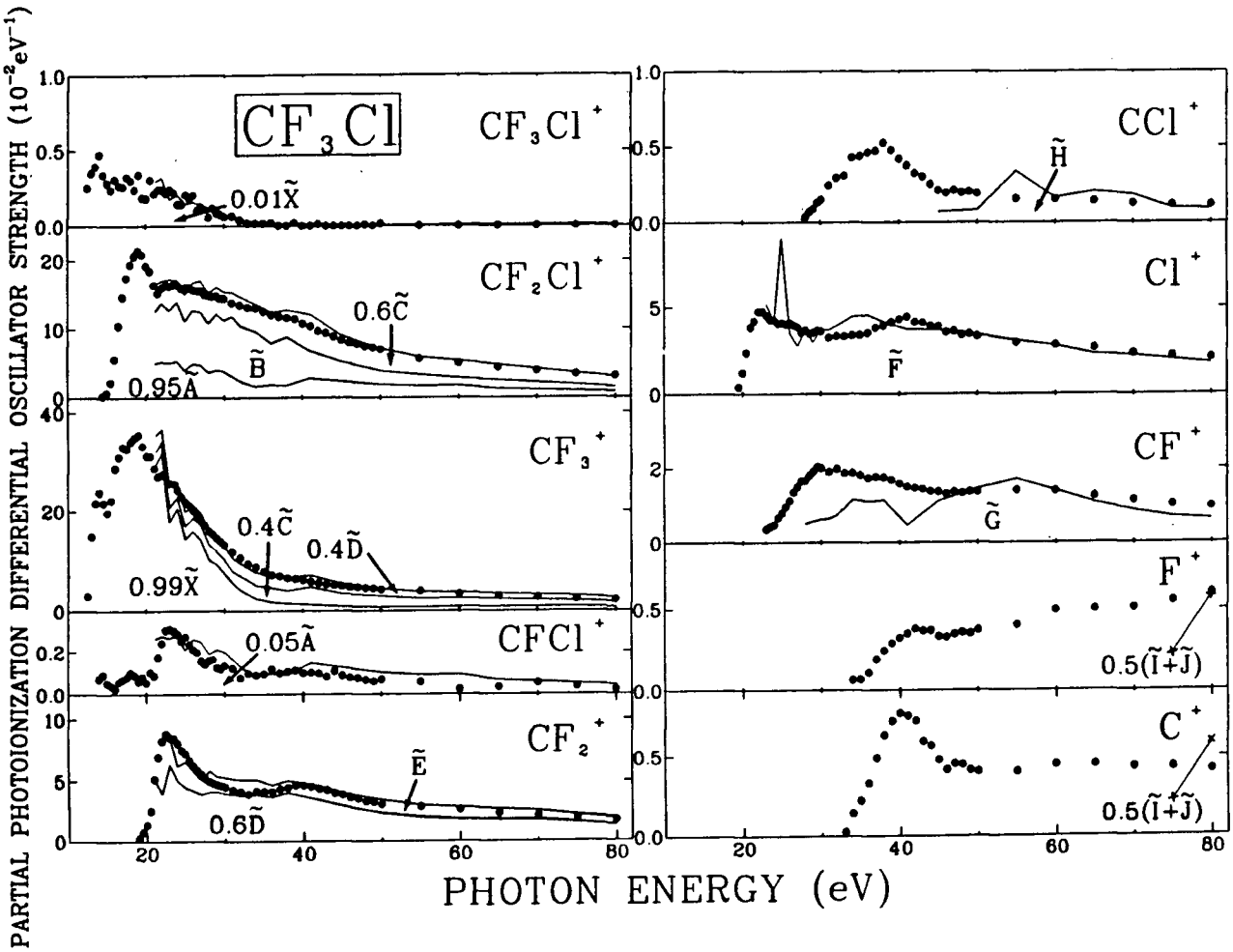

Figure 5.31: Absolute differential oscillator strengths for the proposed dipole induced breakdown scheme of CF_3Cl. Solid circles—present dipole (e,e+ion) experimental data. Solid lines—sums of the electronic state partial differential oscillator strengths obtained using the presently determined photoabsorption differential oscillator strengths and PES branching ratio data in the 21–41 eV [121] and 41-80 eV (chapter 6) regions. See text section 5.6.2 for details. Crosses—$(df/dE)[0.5(\tilde{I}+\tilde{J})]$ obtained the same way as the solid lines using PES data presented in chapter 6.

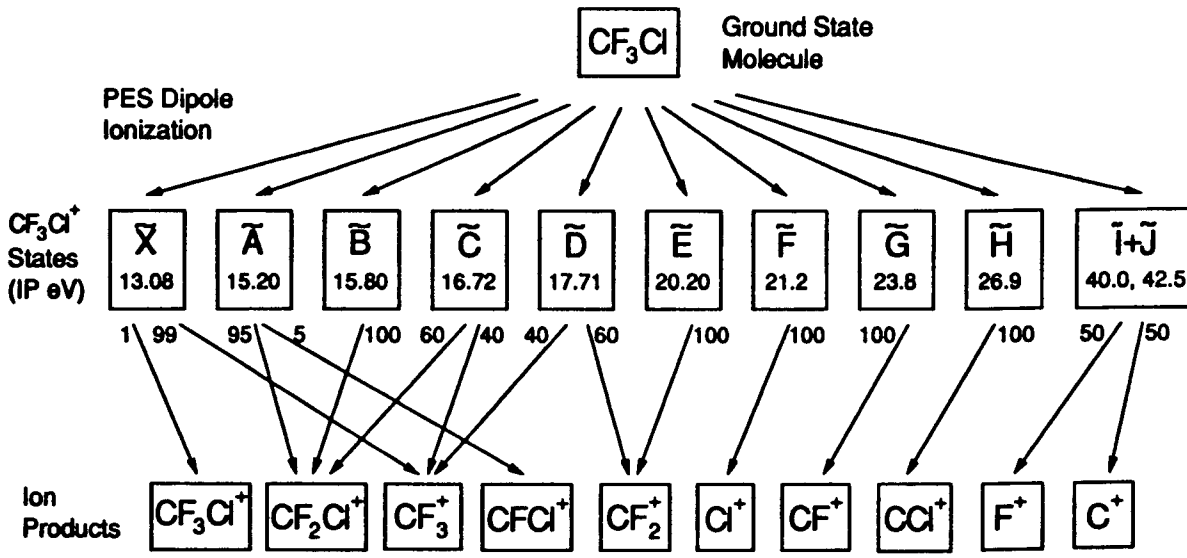

Figure 5.32: Proposed dipole induced breakdown scheme for the ionic photoionization of CF_3Cl. See text for details.

$CFCl^+$, CF_2^+, CCl^+, Cl^+, CF^+, F^+ and C^+, and those for production of the $\tilde{X}$, $\tilde{A}$, $\tilde{B}$, $\tilde{C}$, $\tilde{D}$, $\tilde{E}$, $\tilde{F}$, $\tilde{G}$, $\tilde{H}$ and $(\tilde{I}+\tilde{J})$ electronic states are found to provide a reasonably consistent rationalization of the dipole induced breakdown of CF_3Cl within the energy range of the present data:

$$\frac{df}{dE}(CF_3Cl^+) = \frac{df}{dE}(0.01\tilde{X}) \tag{5.46}$$

$$\frac{df}{dE}(CF_2Cl^+) = \frac{df}{dE}(0.95\tilde{A} + \tilde{B} + 0.6\tilde{C}) \tag{5.47}$$

$$\frac{df}{dE}(CF_3^+) = \frac{df}{dE}(0.99\tilde{X} + 0.4\tilde{C} + 0.4\tilde{D}) \tag{5.48}$$

$$\frac{df}{dE}(CFCl^+) = \frac{df}{dE}(0.05\tilde{A}) \tag{5.49}$$

$$\frac{df}{dE}(CF_2^+) = \frac{df}{dE}(0.6\tilde{D} + \tilde{E}) \tag{5.50}$$

$$\frac{df}{dE}(CCl^+) = \frac{df}{dE}(\tilde{H}) \tag{5.51}$$

$$\frac{df}{dE}(Cl^+) = \frac{df}{dE}(\tilde{F}) \tag{5.52}$$

$$\frac{df}{dE}(CF^+) = \frac{df}{dE}(\tilde{G}) \tag{5.53}$$

$$\frac{df}{dE}(F^+) = \frac{df}{dE}[0.5(\tilde{I} + \tilde{J})] \tag{5.54}$$

$$\frac{df}{dE}(C^+) = \frac{df}{dE}[(0.5(\tilde{I} + \tilde{J})]. \tag{5.55}$$

Fig. 5.31 shows these breakdown relationships as a function of photon energy. The electronic state partial differential oscillator strengths used in fig. 5.31 were obtained from the triple product of the presently measured total photoabsorption differential oscillator strengths (section 5.2.2), the photoionization efficiencies (section 5.4) and the electronic state branching ratios obtained from PES measurements in the 21–41 eV [121] and 41–80 eV (chapter 6) regions. The measurement in chapter 6 includes the inner-valence photoelectron bands. Since only the sum of the branching ratios for the $\tilde{I}$ and $\tilde{J}$ states could be reported (chapter 6), the partial differential oscillator strengths for the production of the $\tilde{I}$ and $\tilde{J}$ states are represented in the form of a sum in the above breakdown

relationships. As can be seen from fig. 5.31 the relationships are reasonably successful in reproducing both the shapes and magnitudes of the photoion partial differential oscillator strengths. Fig. 5.32 shows the presently proposed overall dipole induced breakdown scheme for CF_3Cl. A more detailed investigation of the breakdown patterns of CF_3Cl must await photoelectron-photoion coincidence studies as a function of photon energy.

5.6.3 The Dipole Induced Breakdown of CF_2Cl_2

Since the molecular ion $CF_2Cl_2^+$ is not observed on the time scale of the TOF mass spectrometer and because CF_2Cl^+ is the only ion detected (see table 5.23) below the $\tilde{D}$ state ionization potential of CF_2Cl_2 [100], the $\tilde{X}$, $\tilde{A}$, $\tilde{B}$ and $\tilde{C}$ electronic states of the molecular ion must exclusively lead to production of the CF_2Cl^+ ion. Considering the Franck-Condon region of the $\tilde{D}$ state [100] and the appearance potential of $CFCl_2^+$, it appears that $CFCl_2^+$ is the fragment ion produced from the $\tilde{D}$ electronic state of the molecular ion. Similarly the fragment ions CCl_2^+, CF_2^+, CCl^+, Cl^+, F^+ and C^+ can be formed from the $(\tilde{N}+\tilde{O})$, $\tilde{G}$, $\tilde{K}$, $\tilde{J}$, $\tilde{N}$ and $(\tilde{L}+\tilde{M})$ electronic states (ref. [100] and chapter 6) respectively, and the ions $CFCl^+$ and CF^+ from the $(\tilde{H}+\tilde{I})$ states [100]. With these consideration in mind the following relationships between the partial differential oscillator strengths for the formation of $CFCl_2^+$, CF_2Cl^+, CCl_2^+, $CFCl^+$, CF_2^+, CCl^+, Cl^+, CF^+, F^+ and C^+, and those for the production of the $(\tilde{X}+\tilde{A})$, $(\tilde{B}+\tilde{C})$, $\tilde{D}$, $(\tilde{E}+\tilde{F}+\tilde{G})$, $(\tilde{H}+\tilde{I})$, $\tilde{J}$, $\tilde{K}$, $(\tilde{L}+\tilde{M})$ and $(\tilde{N}+\tilde{O})$ electronic states are found to provide a reasonably consistent rationalization of the dipole induced breakdown of CF_2Cl_2 within the energy range of the present data:

$$\frac{df}{dE}(CFCl_2^+) = \frac{df}{dE}[\tilde{D} + 0.15(\tilde{E} + \tilde{F} + \tilde{G}] \tag{5.56}$$

$$\frac{df}{dE}(CF_2Cl^+) = \frac{df}{dE}[(\tilde{X} + \tilde{A}) + (\tilde{B} + \tilde{C}) + 0.47(\tilde{E} + \tilde{F} + \tilde{G}] \tag{5.57}$$

$$\frac{df}{dE}(CCl_2^+) = \frac{df}{dE}[0.015(\tilde{N} + \tilde{O})] \tag{5.58}$$

$$\frac{df}{dE}(CFCl^+) = \frac{df}{dE}[0.38(\tilde{H} + \tilde{I})] \tag{5.59}$$

$$\frac{df}{dE}(CF_2^+) = \frac{df}{dE}[0.38(\tilde{E} + \tilde{F} + \tilde{G})] \tag{5.60}$$

$$\frac{df}{dE}(CCl^+) = \frac{df}{dE}(0.36\tilde{K}) \tag{5.61}$$

$$\frac{df}{dE}(Cl^+) = \frac{df}{dE}[\tilde{J} + 0.64\tilde{K} + 0.485(\tilde{N} + \tilde{O})] \tag{5.62}$$

$$\frac{df}{dE}(CF^+) = \frac{df}{dE}[0.62(\tilde{H} + \tilde{I}) + 0.2(\tilde{N} + \tilde{O})] \tag{5.63}$$

$$\frac{df}{dE}(F^+) = \frac{df}{dE}[0.2(\tilde{N} + \tilde{O})] \tag{5.64}$$

$$\frac{df}{dE}(C^+) = \frac{df}{dE}[(\tilde{L} + \tilde{M}) + 0.1(\tilde{N} + \tilde{O})]. \tag{5.65}$$

Fig. 5.33 shows these breakdown relationships as a function of photon energy. The electronic state partial differential oscillator strengths used in fig. 5.33 were obtained from the products of the presently measured total photoabsorption differential oscillator strengths (section 5.2.3) and the electronic state branching ratios obtained from PES measurements in the 27–41 eV [151] and 41–70 eV (chapter 6) regions. The measurements in chapter 6 includes the inner-valence photoelectron bands. Due to the unresolvability of certain features in the photoelectron spectra reported in chapter 6 and in ref. [151], the branching ratios for the production of the relevant states were reported as sums, i.e. ($\tilde{X}$+$\tilde{A}$), ($\tilde{B}$+$\tilde{C}$), ($\tilde{E}$+$\tilde{F}$+$\tilde{G}$), ($\tilde{H}$+$\tilde{I}$), ($\tilde{L}$+$\tilde{M}$) and ($\tilde{N}$+$\tilde{O}$), therefore the corresponding partial differential oscillator strengths are presented in similar form in the above breakdown relationships. In spite of the uncertainties involved in such a simple rationale the correspondence of the proposed scheme with the partial photoionization differential oscillator strengths (fig. 5.33) is reasonably good in terms of both shape and magnitude. Fig. 5.34 shows the presently proposed dipole induced breakdown scheme for CF_2Cl_2. A

more detailed analysis of the dipole induced breakdown scheme of CF_2Cl_2 may be obtained from photoelectron-photoion coincidence studies as a function of photon energy.

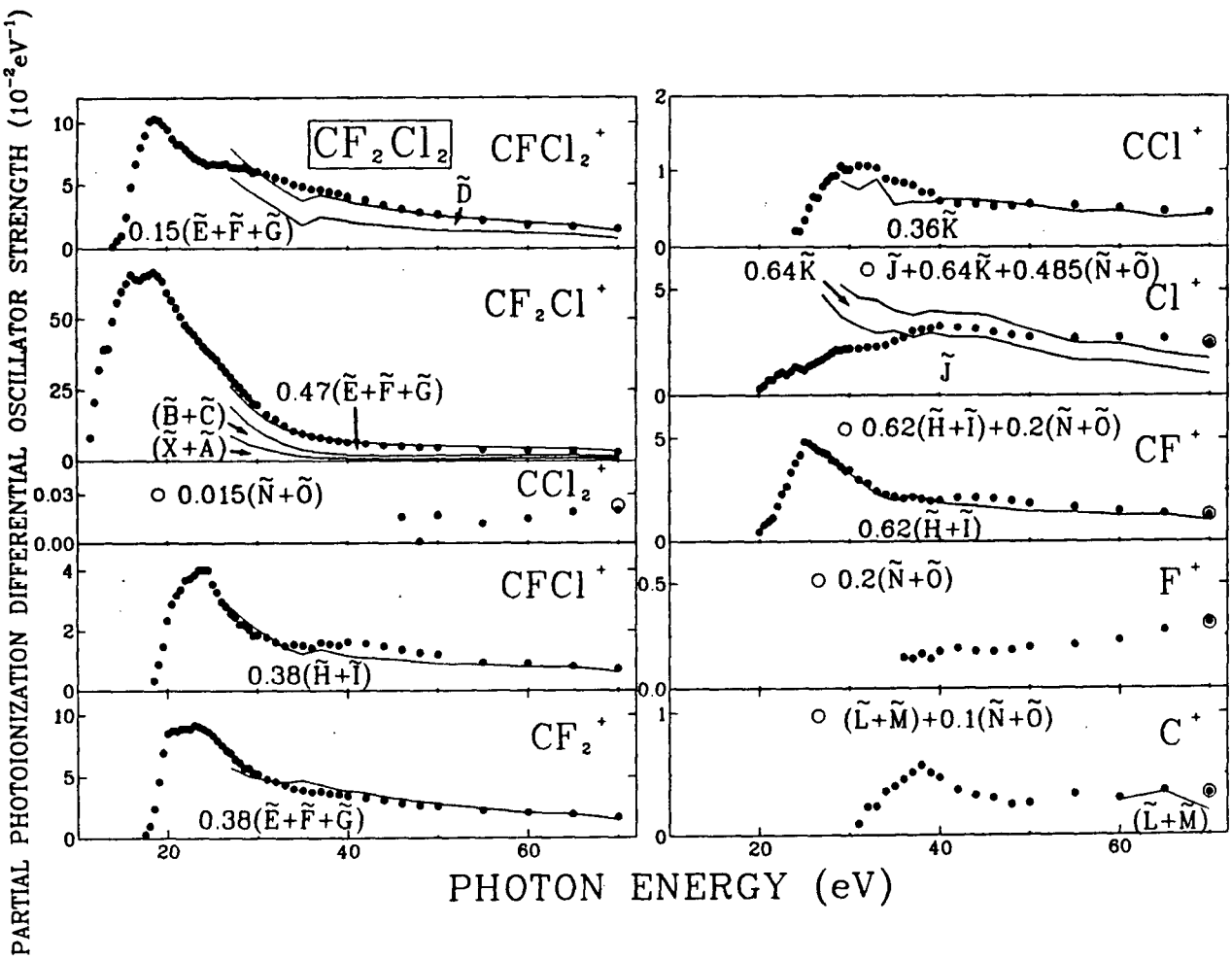

Figure 5.33: Absolute differential oscillator strengths for the proposed dipole induced breakdown scheme of CF_2Cl_2. Solid circles—present dipole (e,e+ion) experimental data. Solid lines—sums of electronic state partial differential oscillator strengths using the presently determined photoabsorption differential oscillator strengths and PES branching ratio data in the 27–41 eV [151] and 41–70 eV (chapter 6) regions. See section 5.6.3 for details.

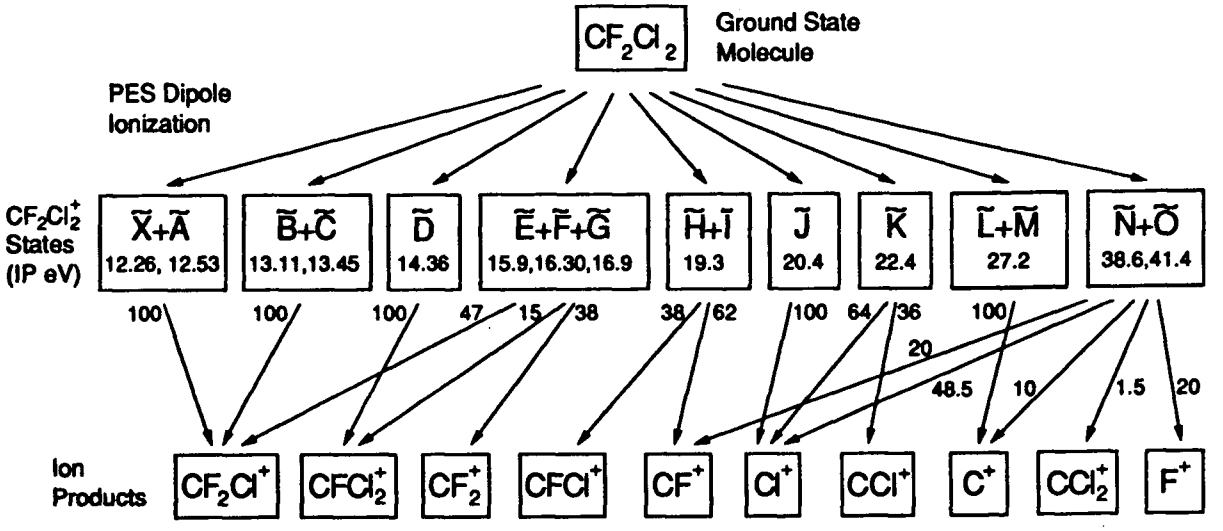

Figure 5.34: Proposed dipole induced breakdown scheme for the ionic photoionization of CF_2Cl_2. See text for details.

Chapter 6

Photoelectron Spectroscopy and the Electronic State Partial Differential Oscillator Strengths of the Freon Molecules CF_3Cl, CF_2Cl_2 and $CFCl_3$ Using Synchrotron Radiation from 41 to 160 eV

The presently reported PES spectra for CF_3Cl, CF_2Cl_2 and $CFCl_3$ were measured by Dr. G. Cooper at the Canadian Synchrotron Radiation Facility (CSRF) located at the ALADDIN facility at The University of Wisconsin [152]. The measurement method and apparatus have been described previously [121,153,154,155,156]. Briefly, a 1200 line/mm holographic grating in a Grasshopper Monochromator is used to monochromate synchrotron radiation from the Aladdin storage ring in Stoughton, Wisconsin. The grating has useful output at photon energies above 40 eV. The sample is photoionized in a free gas jet and the photoelectrons are energy analyzed at the pseudo magic angle using a Leybold Heraeus LHS-11 hemispherical photoelectron spectrometer. The spectrometer is isolated from the optical elements of the beam line by two stages of differential pumping. The overall resolution of the monochromator/spectrometer apparatus in the present experiments was in the range 0.2–0.3 eV FWHM, depending upon the photon energy (since $\Delta\lambda \propto \Delta E/E^2$ is constant, where E is photon energy) and the pass energy (typically 12.5 or 25 eV) used in the electron analyzer. The transmission efficiency of the photoelectron spectrometer has been found to be effectively constant over the range of photoelectron kinetic energy used in the present work.

6.1 Photoelectron Spectra

Photoelectron spectra of $CFCl_3$ and CF_2Cl_2 obtained with synchrotron radiation at 80 eV energy are shown in figs. 6.35a and 6.35b respectively, while the spectrum of $CFCl_3$ at $h\nu = 90$ eV is shown in fig. 6.35c. The assignments of the photoelectron bands up to 30 eV ionization energy indicated in the figures follow those given by Cvitaš *et al.* [100], while the assignments of the higher energy bands are the same as those of Potts *et al.* [157]. Green's function calculations within the two particle-hole Tam-Dankoff approximation (2ph TDA) method performed by Cambi *et al.* [158] indicate that the one electron description of ionization is not adequate to describe ionization of the inner-valence orbitals of freon molecules (the orbitals with predominantly Cl 3*s* and F 2*s* character), and that each inner-valence orbital will give rise to a number of many-body photoelectron states. Therefore the molecular orbital labels for the bands > 25 eV ionization energy in fig. 6.35 are an approximation and give only the major one electron configuration involved in the ion states. Unlike Potts *et al.* [157] we do not observe clear separations between the F 2*s* $1b_1^{-1}$ and $1a_1^{-1}$ states in CF_2Cl_2 or the F 2*s* $1e^{-1}$ and $1a_1^{-1}$ states in CF_3Cl. The reason for this is unclear since the electron energy resolution of the presently reported measurements should be adequate to observe the splittings seen by the authors of ref. [157]. The estimated vertical ionization energies for the inner valence states obtained in the present work are given in table 6.26.

The features in the $CFCl_3$ and CF_2Cl_2 spectra (see fig. 6.35) at apparent ionization energies of 46.8 and 48.7 eV ($CFCl_3$) and 47.1 and 48.8 eV (CF_2Cl_2) are in fact due to Cl $2p_{3/2}^{-1}$ and $2p_{1/2}^{-1}$ states respectively produced by third order radiation from the monochromator. The kinetic energies of these peaks match those expected on the basis of the reported ionization energies of the Cl $2p^{-1}$ states of $CFCl_3$ (207.20 eV ($2p_{3/2}^{-1}$),

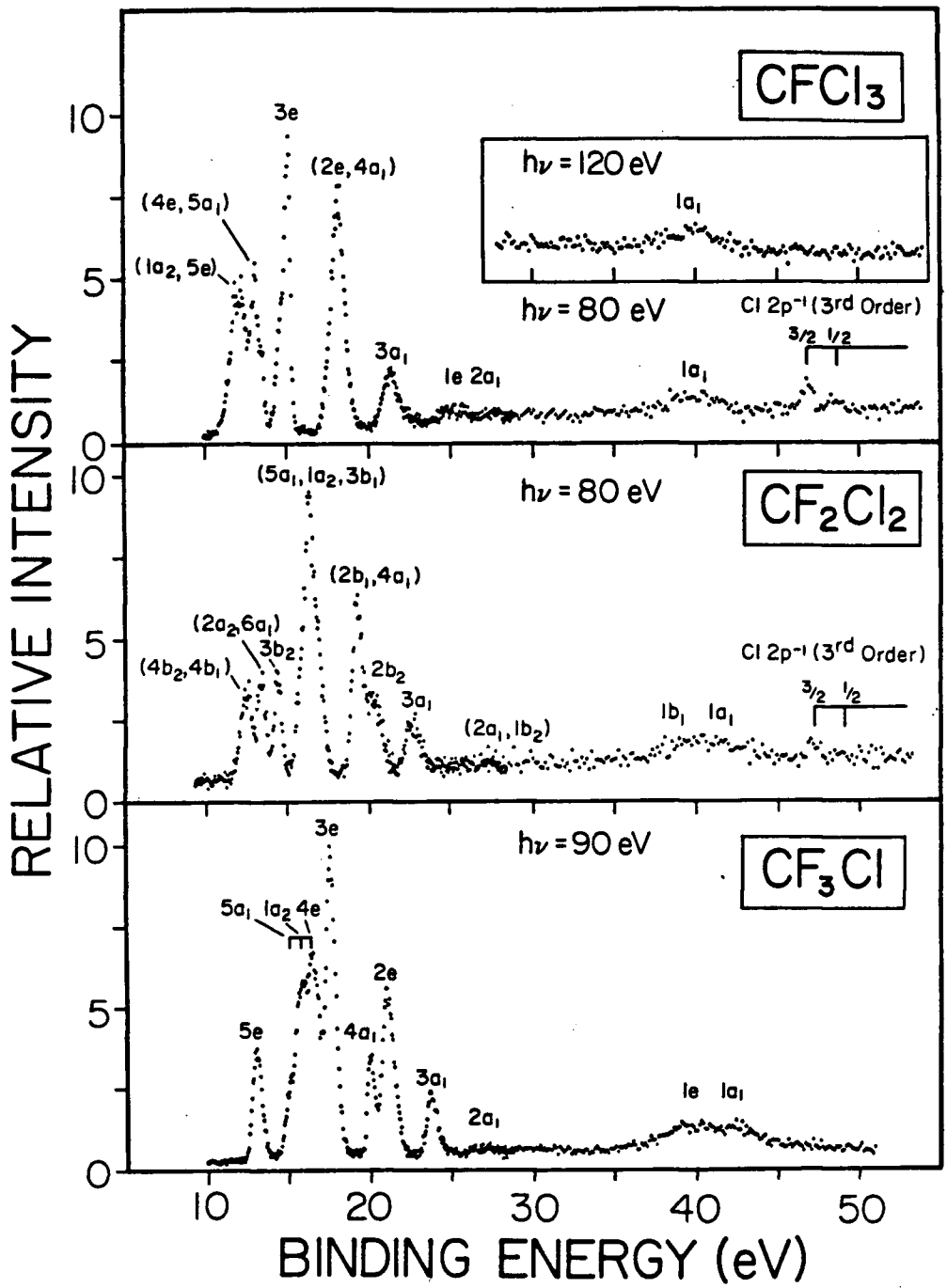

Figure 6.35: Photoelectron spectra of: a) $CFCl_3$ at $h\nu = 80$ eV (Insert shows $h\nu = 120$ eV); b) CF_2Cl_2 at $h\nu = 80$ eV; c) CF_3Cl at $h\nu$ =90 eV. The assignments shown on the spectra follow those given in refs. [100] and [157] (see section 6.1 for details). The peaks above 45 eV in a) and b) are spin-orbit doublets from Cl $2p$ ionization by third order radiation (see text).

Table 6.26: Vertical ionization energies for the inner valence regions of CF_3Cl, CF_2Cl_2 and $CFCl_3$

Molecule	Ionization energy (eV)					
	this work[a]			ref. [157]		
CF_3Cl	$2a_1$	$1e$	$1a_1$	$2a_1$	$1e$	$1a_1$
	26.9	40.0	42.5	26.3	40.0b	42.8 [b]
CF_2Cl_2	$(2a_1, 1b_2)$	$1b_1$	$1a_1$	$(2a_1, 1b_2)$	$1b_1$	$1a_1$
	27.0	38.6	41.4	—	39	41
$CFCl_3$	$1e$	$2a_1$	$1a_1$	$1e$	$2a_1$	$1a_1$
	25.3	27.6	40.0	25.5	27.6	39.5

[a] $\pm$ 1.0 eV.

[b] The ionization energies for the $1e$ and $1a_1$ orbitals of CF_3Cl given in the text of ref. [157] are 42.8 and 44 eV respectively, however the spectrum shown in fig. 2c of ref. [157] is not consistent with these values. The numbers given in the table therefore have been estimated from fig. 2c of Potts *et al.* [157].

208.81 eV ($2p_{1/2}^{-1}$) [159]) and CF_2Cl_2 (207.47 eV ($2p_{3/2}^{-1}$), 209.10 eV ($2p_{1/2}^{-1}$) [159]) for $h\nu$ = 240 eV. The assignment as spin-orbit doublets is supported by the relative intensities and spacing of the two peaks in each case. Further support is gained from the fact that no such spin-orbit doublets appear within the same spectral range of the (first order) spectra at other photon energies (for example see the insert to fig. 6.35a which shows the spectrum of $CFCl_3$ at $h\nu$ = 120 eV). Fig. 6.35c shows the spectrum of CF_3Cl at $h\nu$ = 90 eV.

6.2 Photoelectron Branching Ratios and Partial Photoionization Differential Oscillator Strengths

The photoelectron spectra were analyzed by least squares fitting the data to Gaussian peak shapes plus a linear background function. For some molecular orbitals individual photoelectron branching ratios could not be obtained since the photoelectron bands were too heavily overlapping each other at the resolution used in the present experiments. In these cases branching ratios for groupings of peaks are presented below. Photoelectron branching ratios of CF_3Cl, CF_2Cl_2 and $CFCl_3$ are presented in tables 6.27–6.29 and in figs. 6.36–6.38 respectively. Where the separate contributions from overlapping peaks could not be adequately determined from the curve fitting procedure, a combined branching ratio is presented. In fig. 6.36 are also plotted the branching ratios reported by Bozek *et al.* [153] for CF_3Cl from 41 to 70 eV. Above 70 eV the branching ratios of the F 2*s* 1*e* and $1a_1$ orbitals begin to become significant so that comparison of the presently reported results with those of ref. [153] is no longer appropriate since Bozek *et al.* [153] did not make measurements in the inner valence region. Novak *et al.* [151] did not directly report their measured photoelectron branching ratios for CF_3Cl and CF_2Cl_2, instead they quoted partial photoionization cross-sections which they derived from the

Table 6.27: Photoelectron branching ratios of CF_3Cl

Photon Energy (eV)	Branching Ratio (%)									
	$5e$	$5a_1$	$1a_2$	$4e$	$3e$	$4a_1$	$2e$	$3a_1$	$2a_1$	$(1e+1a_1)$
41	4.4	10.4	14.1	31.2	21.1	4.0	13.2	1.6		
45	4.0	10.7	12.0	27.1	21.0	4.6	15.7	4.7	0.3	
50	3.9	10.1	9.7	26.9	19.3	5.6	17.1	7.2	0.4	
55	4.2	10.1	8.9	24.1	18.2	5.8	17.2	9.5	1.9	
60	5.4	11.3	6.9	25.3	18.0	6.5	17.0	8.5	1.0	
65	5.9	9.1	{	52.4	}	8.3	15.8	7.3	1.4	
70	6.5	8.8	8.2	24.1	21.8	6.0	16.7	6.4	1.4	
75	7.4	8.3	7.6	23.3	21.0	5.4	16.6	5.7	0.8	3.8
80	6.5	7.9	6.3	21.9	19.0	5.5	16.0	5.6	0.8	10.5
85	7.0	7.9	4.6	26.0	16.0	5.6	15.0	5.0	0.4	12.5
90	7.5	5.2	9.4	17.0	22.0	5.1	14.4	4.5	0.4	14.6
95	7.5	6.7	8.3	18.5	18.7	5.1	13.6	4.6	0.5	16.6
100	7.9	6.2	9.7	18.5	19.9	5.0	14.1	4.4	0.6	13.5
105	7.9	6.6	7.5	21.1	15.9	4.0	12.7	4.8	0.4	19.0
110	9.1	8.9	6.9	21.1	15.1	5.6	12.5	5.2	0.5	15.2
115	8.6	7.4	8.9	19.2	16.9	4.4	12.4	5.1	1.0	16.2
120	8.8	8.3	8.8	21.0	17.1	4.5	13.2	4.8	0.9	12.7
130	9.4	8.5	8.6	20.8	16.8	4.8	12.1	4.8	0.4	13.8
140	9.5	8.0	8.5	18.0	15.1	4.5	11.5	4.4	1.0	19.8
150	10.5	8.0	8.1	16.6	15.2	5.3	11.8	5.6	1.1	17.9
160	10.1	7.9	8.1	16.5	17.2	4.6	13.0	6.1	1.4	15.0

Table 6.28: Photoelectron branching ratios of CF_2Cl_2

Photon Energy (eV)	Branching Ratio (%)								
	$(4b_2+4b_1)$	$(2a_1+6a_1)$	$3b_2$	$(5a_1+1a_2+3b_1)$	$(2b_1+4a_1)$	$2b_2$	$3a_1$	$(2a_1+1b_2)$	$(1b_1+1a_1)$
41	3.9	5.4	9.4	46.6	13.8	12.9	8.0		
45	3.3	6.5	9.1	44.1	14.4	14.2	8.6		
50	4.2	7.5	8.5	43.8	14.1	12.9	8.9		
55	5.5	8.2	9.1	42.0	15.4	11.1	8.5		
60	7.5	7.2	8.9	38.8	14.9	11.6	9.3	2.0	
65	7.4	8.0	8.4	39.4	16.0	10.0	8.1	2.7	
70	7.0	6.9	6.6	33.0	13.8	8.2	9.9	1.6	13.1
75	8.5	7.0	6.0	34.5	15.2	8.2	6.3	1.5	12.9
80	8.7	6.6	6.5	34.8	14.7	9.2	6.3	2.1	11.2
85	8.7	6.9	6.2	32.7	14.4	7.9	6.2	2.2	14.7
90	10.0	8.1	5.2	32.5	15.2	6.5	6.7	3.8	12.1
95	10.6	9.3	6.2	31.5	14.9	7.2	6.0	3.5	10.8
100	11.1	9.6	7.0	32.6	13.5	8.6	5.8	1.4	10.6
105	11.7	9.5	7.4	32.2	13.0	8.1	5.8	2.5	9.7
110	12.3	10.6	6.7	31.9	13.1	7.5	5.4	2.1	10.2
120	12.2	11.1	7.4	30.6	11.1	7.6	5.1	2.6	12.5
130	11.7	10.2	8.4	30.1	11.1	8.5	5.4	4.5	10.2
140	12.8	11.1	8.3	29.2	11.4	7.2	5.5	3.0	11.6
150	12.2	12.9	7.9	27.5	12.1	6.4	6.2	2.8	12.0
160	13.2	9.1	8.8	26.5	12.2	6.5	6.4	2.8	14.4

Table 6.29: Photoelectron branching ratios of $CFCl_3$

Photon Energy (eV)	Branching Ratio (%)					
	$(1a_2 + 5e + 4e + 5a_1)$	$3e$	$(2e + 4a_1)$	$3a_1$	$(1e + 2a_1)$	$1a_1$
41	20.7	29.0	33.8	10.6	5.8	
45	20.8	27.9	35.2	10.2	6.0	
50	22.8	27.7	31.5	10.7	7.4	
55	28.3	27.3	29.8	10.0	4.6	
60	28.4	25.5	30.0	10.1	6.0	
65	31.0	26.4	30.1	8.7	3.8	
70	28.3	24.0	29.7	6.4	6.5	5.2
75	28.9	21.8	28.3	9.1	7.3	4.6
80	32.4	21.4	27.8	7.5	4.4	6.4
90	32.6	18.1	25.2	7.5	7.7	9.0
100	36.2	18.2	23.2	7.6	6.8	8.1
110	39.2	17.9	22.5	7.4	6.4	6.7
115	41.6	17.8	22.4	7.0	5.7	5.5
120	40.6	18.3	21.2	6.7	6.6	6.7
130	41.4	17.4	20.4	7.0	6.4	7.6
140	42.1	17.2	20.7	7.3	7.4	5.4
150	41.8	17.0	21.8	6.7	4.7	7.9

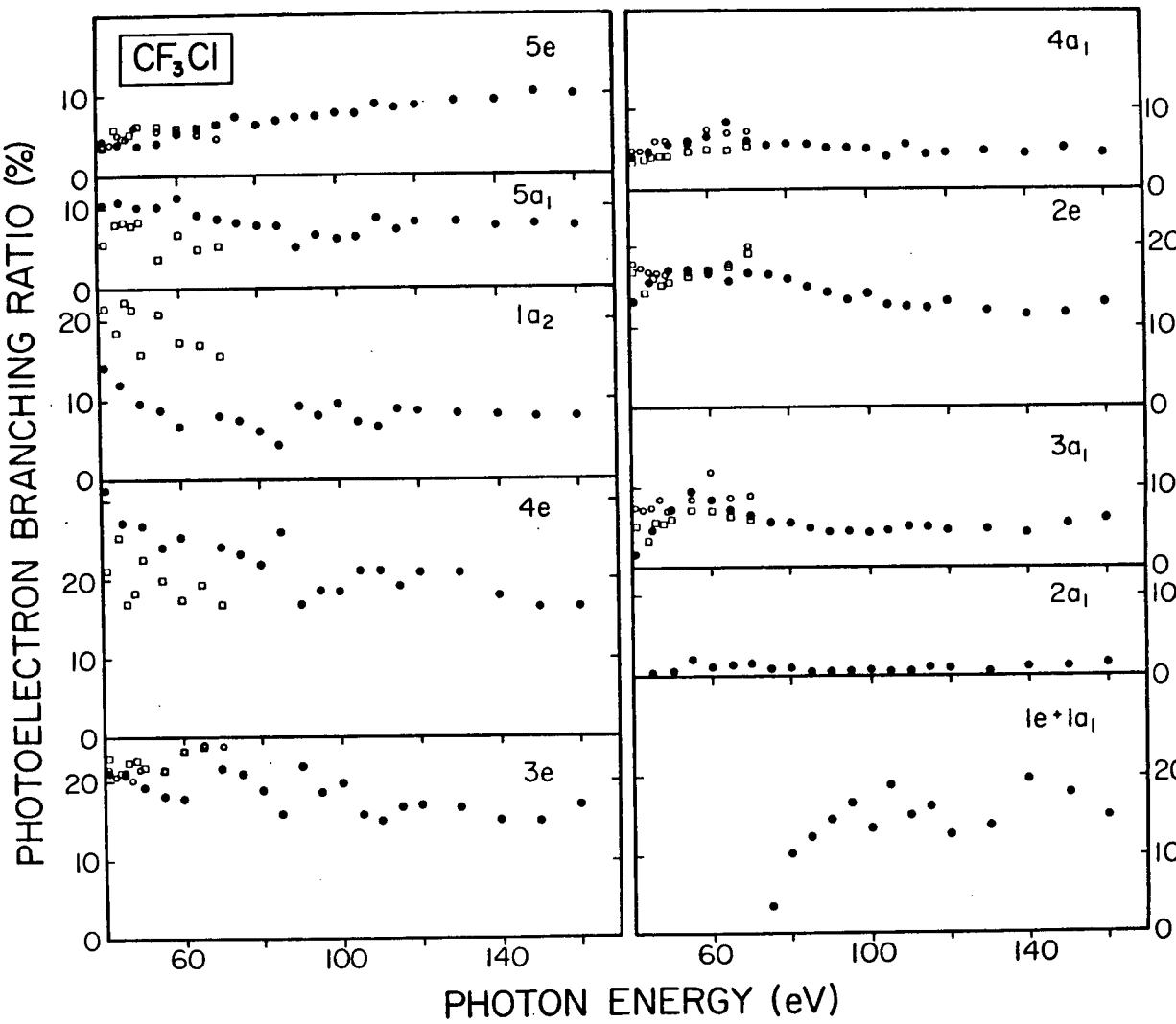

Figure 6.36: Photoelectron branching ratios for CF_3Cl. Solid circles–this work; open circles–ref. [151]; open squares–ref. [153].

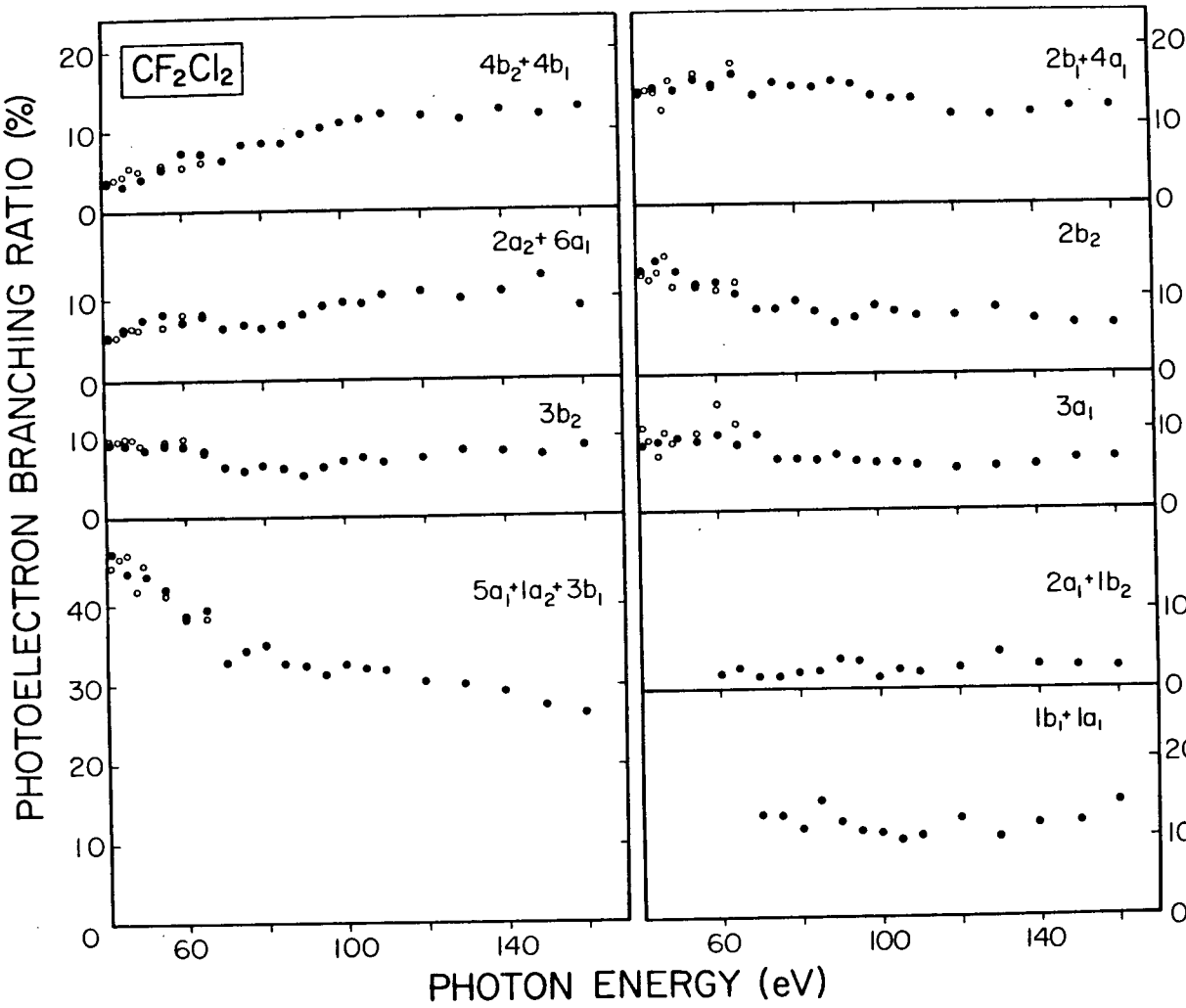

Figure 6.37: Photoelectron branching ratios for CF_2Cl_2. Solid circles–this work; open circles–ref. [151].

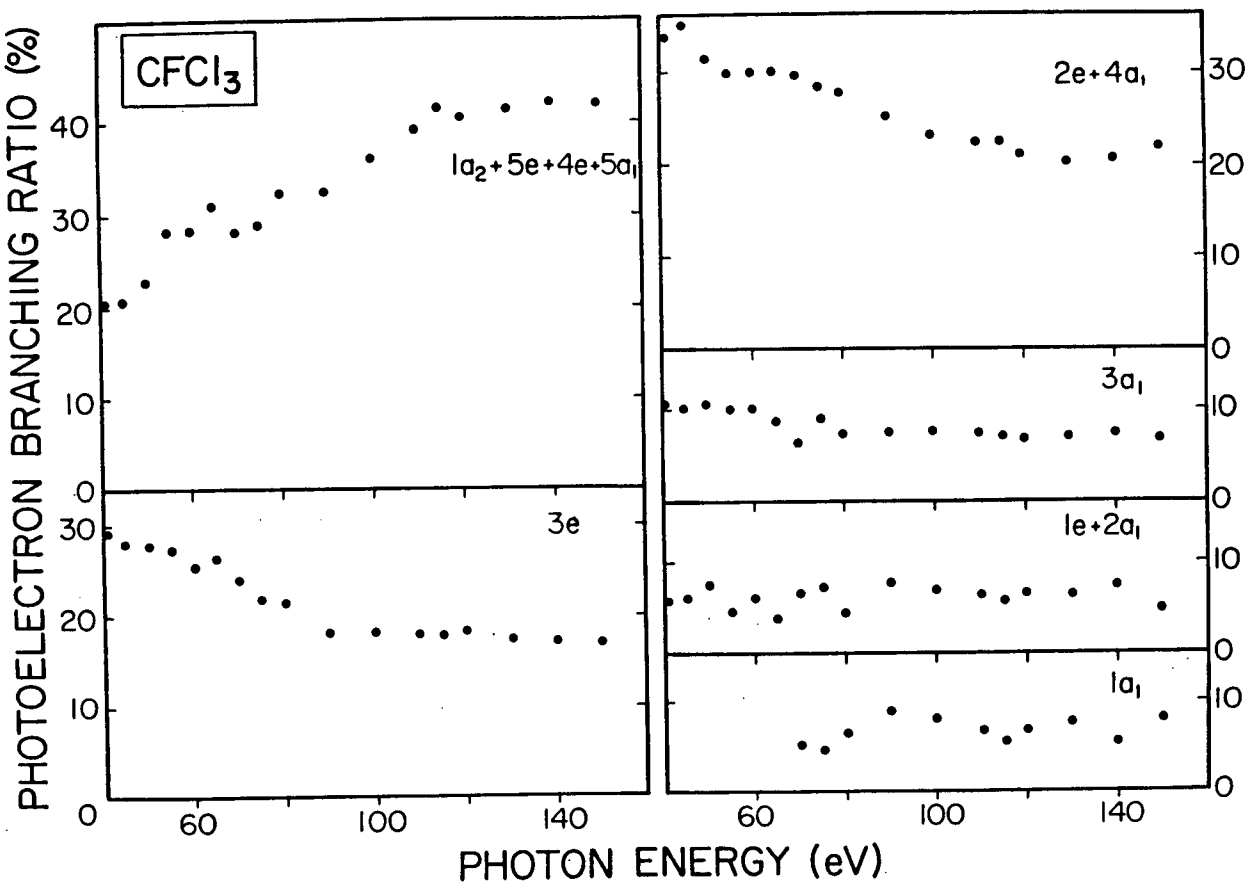

Figure 6.38: Photoelectron branching ratios for $CFCl_3$.

product of their branching ratios and previously published photoabsorption cross-sections for CF_3Cl [101] and CF_2Cl_2 [110]. We have therefore recalculated photoelectron branching ratios from their published tables of cross-sections [151] in order to facilitate valid comparisons with the present work. The so obtained photoelectron branching ratios of Novak *et al.* [151] are plotted in figs. 6.36 and 6.37. Note that unlike in the present work and that of ref. [153], Novak *et al.* [151] did not obtain separate branching ratios for the $5a_1$, $1a_2$ and $4e$ orbitals of CF_3Cl and instead presented combined values for these bands. Thus in these cases their data [151] is not represented in fig. 6.36.

Fig. 6.36 shows that in general there is good agreement between the presently reported photoelectron branching ratios and the two previously published data sets [151,153] for CF_3Cl from 41 to 70 eV. The agreement seen in fig. 6.37 between the present data for CF_2Cl_2 and that of ref. [151] from 41 to 70 eV is equally good. Some significant and systematic differences between the presently reported results and those of Bozek *et al.* [153] do exist however, for the $5a_1$, $1a_2$, $4e$ and $3e$ orbitals of CF_3Cl. While the combined branching ratio sum ($5a_1$+$1a_2$+$4e$+$3e$) of ref. [153] is very similar to that of the present work (not plotted in fig. 6.36), their branching ratios for the $5a_1$ and $4e$ orbitals are smaller than those presented here, while those for the $1a_2$ and $3e$ are larger. These differences are due largely, if not entirely, to aspects of the respective curve fitting procedures used. It appears that Bozek *et al.* [153] fitted the overlapping band system comprised of ionization from the $5a_1$, $1a_2$, $4e$ and $3e$ orbitals with peaks of equal width, which is not necessarily valid. Therefore in the present work we have allowed the fitting program to determine individual widths for each peak in the spectrum. The major difference in the two procedures is that the $1a_2^{-1}$ band is determined to be substantially narrower and the $4e^{-1}$ band wider in the present work than in ref. [153]. The He II spectrum of CF_3Cl reported by Cvitaš *et al.* [100] clearly shows a narrower

profile of the $1a_2^{-1}$ band and a wider $4e^{-1}$ band, supporting the presently employed curve fitting strategy. We therefore believe the presently reported branching ratios for the $5a_1$, $1a_2$, $4e$ and $3e$ orbitals of CF_3Cl to be more accurate than those of Bozek *et al.* [153]. The photoelectron branching ratio sum ($5a_1$+$1a_2$+$4e$+$3e$) reported by Novak *et al.* [151] agrees very well with the equivalent summation performed on the presently reported data and that of ref. [153] (not shown in fig. 6.36).

Using total photoabsorption differential oscillator strengths for CF_3Cl, CF_2Cl_2 and $CFCl_3$ presented in sections 5.2.2–5.2.4 along with the presently reported photoelectron branching ratios, we have derived partial photoionization differential oscillator strengths for each of the electronic ion states of the three molecules. These are given numerically in tables 6.30–6.32 and are shown graphically in figs. 6.39–6.41. Bozek *et al.* [153] and Novak *et al.* [151] used previously published photoabsorption cross-sections for CF_3Cl [101] and CF_2Cl_2 [110] in order to derive partial photoionization differential oscillator strengths from their electronic state branching ratios. Since their branching ratio data is very similar to the presently reported values except where noted above, any differences in the shapes of the electronic state partial photoionization differential oscillator strengths between the values reported in refs. [151,153] and the present values shown in figs. 6.39 and 6.40 from 41 to 70 eV are caused solely by differences in the total photoabsorption differential oscillator strengths presented in sections 5.2.2, 5.2.3 and reported in refs. [101,110]. These differences are discussed in sections 5.2.2 and 5.2.3. However, Cauletti *et al.* [160] used a method of internal calibration in order to directly measure partial photoionization cross-sections (differential oscillator strengths) at 40.81 eV for the outermost $5e$ orbitals of CF_3Cl and the ($4b_2$+$4b_1$), ($2a_2$+$6a_1$) and $3b_2$ orbitals of CF_2Cl_2. We therefore compare the present data with that of ref. [160] in figs. 6.39 and 6.40. The partial photoionization differential oscillator strength for the $5e$ orbitals of CF_3Cl at

Table 6.30: Electronic state partial photoionization differential oscillator strengths for CF_3Cl

Photon Energy (eV)	Differential oscillator Strength ($10^{-2}eV^{-1}$) [a]									
	$5e$	$5a_1$	$1a_2$	$4e$	$3e$	$4a_1$	$2e$	$3a_1$	$2a_1$	$(1e+1a_1)$
41	1.24	2.95	3.99	8.83	5.97	1.12	3.73	0.44		
45	0.95	2.53	2.85	6.42	4.96	1.08	3.71	1.10	0.07	
50	0.78	2.04	1.95	5.41	3.88	1.12	3.44	1.45	0.08	
55	0.76	1.83	1.60	4.35	3.27	1.05	3.10	1.72	0.35	
60	0.89	1.86	1.14	4.16	2.96	1.07	2.79	1.39	0.17	
65	0.87	1.34	{	7.72	}	1.22	2.32	1.07	0.20	
70	0.86	1.17	1.10	3.22	2.90	0.80	2.23	0.86	0.19	
75	0.89	0.99	0.91	2.79	2.53	0.65	2.00	0.68	0.10	0.46
80	0.72	0.88	0.71	2.44	2.11	0.61	1.78	0.63	0.09	1.17
85	0.72	0.81	0.48	2.69	1.65	0.58	1.55	0.52	0.04	1.29
90	0.67	0.47	0.85	1.54	1.99	0.46	1.30	0.41	0.03	1.32
95	0.62	0.56	0.69	1.54	1.56	0.42	1.13	0.38	0.04	1.38
100	0.64	0.50	0.78	1.49	1.60	0.40	1.13	0.36	0.05	1.09
105	0.57	0.48	0.54	1.52	1.15	0.29	0.92	0.34	0.03	1.37
110	0.60	0.59	0.46	1.39	1.00	0.37	0.83	0.34	0.04	1.01
115	0.53	0.46	0.55	1.19	1.04	0.27	0.77	0.31	0.06	1.00
120	0.50	0.47	0.50	1.19	0.97	0.25	0.75	0.27	0.05	0.72
130	0.48	0.43	0.44	1.06	0.86	0.24	0.61	0.25	0.02	0.70
140	0.41	0.34	0.37	0.78	0.65	0.19	0.50	0.19	0.04	0.86
150	0.41	0.31	0.31	0.64	0.59	0.20	0.45	0.22	0.04	0.69
160	0.36	0.28	0.29	0.59	0.62	0.16	0.47	0.22	0.05	0.54

[a] $\sigma(\text{Mb}) = 1.0975 \times 10^2 (df/dE)(\text{eV}^{-1})$.

Table 6.31: Electronic state partial photoionization differential oscillator strengths for CF_2Cl_2

Photon Energy	Differential oscillator strength $(10^{-2}eV^{-1})$ [a]								
(eV)	$(4b_2+4b_1)$	$(2a_1+6a_1)$	$3b_2$	$(5a_1+1a_2+3b_1)$	$(2b_1+4a_1)$	$2b_2$	$3a_1$	$(2a_1+1b_2)$	$(1b_1+1a_1)$
41	0.84	1.15	2.02	9.99	2.96	2.76	1.70		
45	0.63	1.24	1.74	8.48	2.76	2.72	1.64		
50	0.71	1.26	1.43	7.33	2.37	2.16	1.49		
55	0.81	1.22	1.36	6.27	2.30	1.67	1.27		
60	1.03	0.99	1.23	5.36	2.05	1.60	1.29	0.28	
65	0.95	1.04	1.09	5.11	2.07	1.30	1.05	0.35	
70	0.79	0.77	0.74	3.69	1.54	0.92	1.11	0.18	2.02
75	0.89	0.74	0.63	3.63	1.59	0.86	0.66	0.16	1.36
80	0.86	0.65	0.65	3.46	1.46	0.91	0.63	0.20	1.11
85	0.77	0.61	0.55	2.92	1.29	0.71	0.56	0.20	1.31
90	0.83	0.68	0.44	2.70	1.26	0.54	0.56	0.32	1.00
95	0.82	0.71	0.48	2.43	1.15	0.55	0.46	0.27	0.83
100	0.77	0.66	0.48	2.25	0.93	0.60	0.40	0.10	0.73
105	0.77	0.62	0.49	2.12	0.86	0.53	0.38	0.16	0.64
110	0.76	0.66	0.43	1.98	0.81	0.46	0.34	0.13	0.64
120	0.66	0.60	0.40	1.65	0.60	0.41	0.28	0.14	0.67
130	0.55	0.48	0.39	1.41	0.52	0.40	0.25	0.21	0.48
140	0.52	0.45	0.34	1.19	0.47	0.29	0.22	0.12	0.47
150	0.44	0.46	0.28	0.99	0.43	0.23	0.22	0.10	0.43
160	0.43	0.29	0.29	0.86	0.40	0.21	0.21	0.09	0.47

[a] $\sigma(\text{Mb}) = 1.0975 \times 10^2 (df/dE)(\text{eV}^{-1})$.

Table 6.32: Electronic state partial photoionization differential oscillator strengths for $CFCl_3$

Photon Energy (eV)	Differential oscillator strength $(10^{-2}eV^{-1})$ [a]					
	$(1a_2 + 5e + 4e + 5a_1)$	$3e$	$(2e + 4a_1)$	$3a_1$	$(1e + 2a_1)$	$1a_1$
41	2.93	4.14	4.81	1.51	0.83	
45	2.69	3.61	4.55	1.31	0.77	
50	2.68	3.26	3.70	1.25	0.87	
55	3.03	2.93	3.20	1.07	0.49	
60	2.88	2.59	3.05	1.03	0.61	
65	2.94	2.50	2.86	0.83	0.36	
70	2.62	2.22	2.75	0.59	0.60	0.48
75	2.45	1.85	2.40	0.77	0.61	0.39
80	2.51	1.66	2.15	0.58	0.34	0.50
90	2.28	1.26	1.76	0.53	0.54	0.63
100	2.18	1.10	1.40	0.46	0.41	0.49
110	2.01	0.92	1.16	0.38	0.33	0.34
115	2.06	0.89	1.12	0.35	0.29	0.27
120	1.89	0.85	0.99	0.31	0.31	0.31
130	1.68	0.71	0.83	0.28	0.26	0.31
140	1.49	0.61	0.73	0.26	0.26	0.19
150	1.30	0.53	0.68	0.21	0.15	0.25

[a] $\sigma(\text{Mb}) = 1.0975 \times 10^2 (df/dE)(\text{eV}^{-1})$.

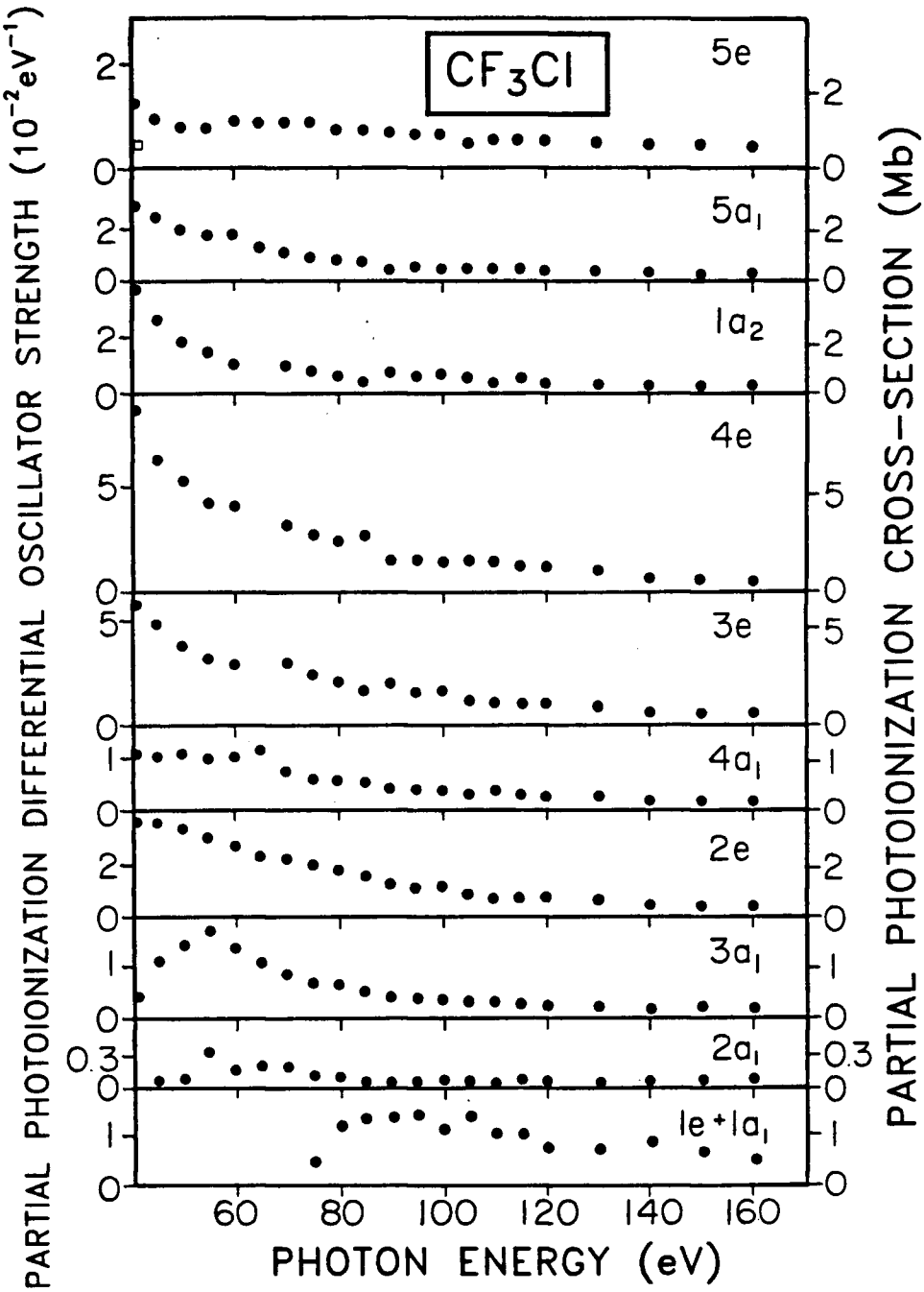

Figure 6.39: Electronic state partial photoionization differential oscillator strengths (cross-sections) of CF_3Cl. Solid circles–this work; open square on the 5*e* data set–ref. [160].

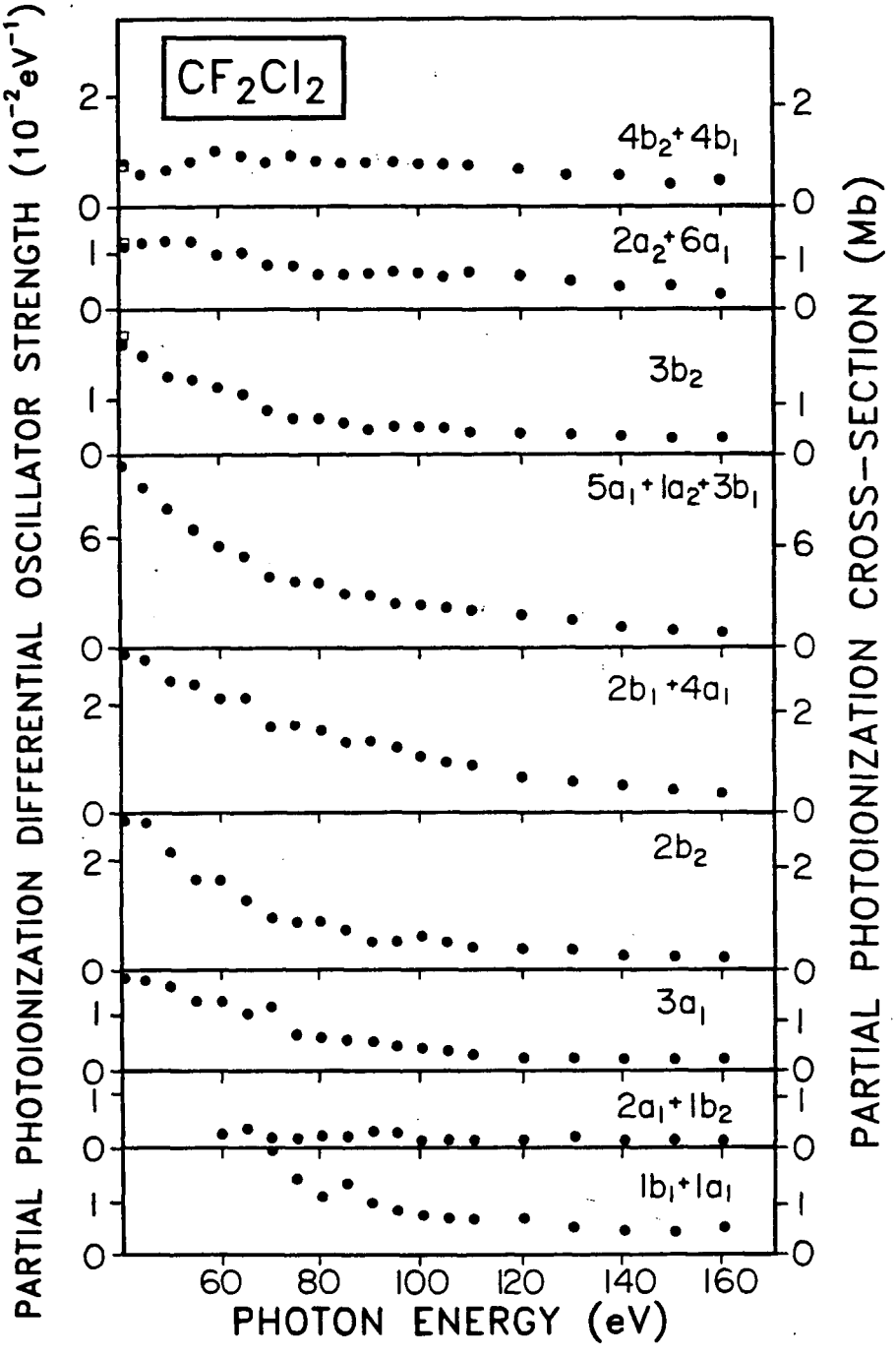

Figure 6.40: Electronic state partial photoionization differential oscillator strengths (cross-sections) of CF_2Cl_2. Solid circles–this work; open squares at 41 eV on the $4b_2$+$4b_1$, $2a_1$+$6a_1$ and $3b_2$ data sets—ref. [160].

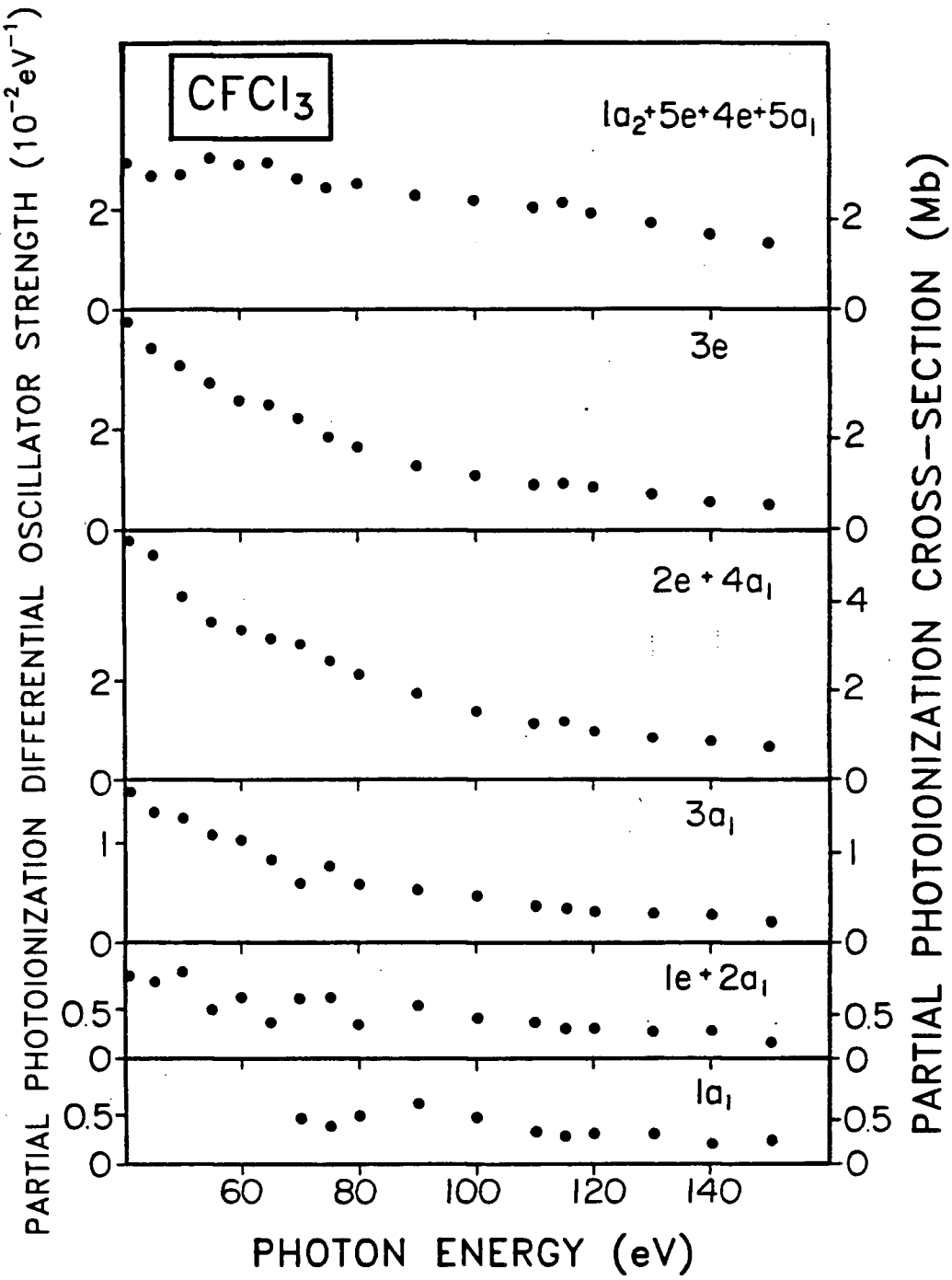

Figure 6.41: Electronic state partial photoionization differential oscillator strengths (cross-sections) of $CFCl_3$.

40.81 eV reported by Cauletti *et al.* [160] is much lower ($\sim$ 50%) than that measured in the present work (see fig. 6.39), but the results for CF_2Cl_2 (see fig. 6.40) are in good agreement. The fact that Cauletti *et al.* [160] used an internal standard and in addition did not make their measurements at the magic angle, but attempted to correct for this using approximate theoretical values of the photoelectron asymmetry parameter β, may account for the large discrepancy for the $5e$ orbitals of CF_3Cl.

MS-Xα calculations of the outer valence photoelectron branching ratios and partial photoionization differential oscillator strengths of CF_3Cl were reported by Bozek *et al.* [153]. These proved to be in generally good agreement with their experimental values. The presently reported branching ratios and partial photoionization differential oscillator strengths, especially those for the $5a_1$, $1a_2$ and $4e$ orbitals, further improve the agreement between theory and experiment from 41 to 160 eV. The theoretical results [153] predict weak resonances at high photon energies (>100 eV) in the partial photoionization cross-sections of all the valence orbitals of CF_3Cl caused by scattering of the photoelectrons. These resonances should also be visible in the photoelectron branching ratios. While the presently reported branching ratios and differential oscillator strengths for CF_3Cl shown in figs. 6.36 and 6.39 suggest the possibility of such weak resonances for various orbitals (e.g. the $3a_1$ and $2e$), the data do not unequivocally corroborate their existence.

The general features of the photoelectron branching ratios and electronic state partial photoionization differential oscillator strengths for CF_3Cl, CF_2Cl_2 and $CFCl_3$ shown in figs. 6.36–6.41 may be understood qualitatively in terms of the atomic orbital characters of the molecular orbitals from which the photoelectron bands are derived. Of course, this discussion implicitly invokes the independent particle and the frozen orbital approximations, and ignores molecular effects such as shape resonances. Such a model was formulated by Gelius [161] in a quantitative way and should increase in validity as

the photoelectron energy increases. It can be used quantitatively in X-ray photoelectron spectroscopy but is only qualitatively useful at the photoelectron energies involved in the present work. Therefore, we may understand shapes of the molecular orbital branching ratios and partial photoionization differential oscillator strengths shown in figs. 6.36–6.41 by reference to the C $2p$, C $2s$, F $2p$, F $2s$, Cl $3p$ and Cl $3s$ atomic orbital differential oscillator strength curves [68]. For example, the "lone pair" molecular orbitals that have predominantly Cl $3p$ atomic character (the $5e$ in CF_3Cl, the $4b_2$, $4b_1$, $6a_1$ and $3b_2$ in CF_2Cl_2 and the $1a_2$, $5e$, $4e$ and $5a_1$ in $CFCl_3$) increase in branching ratio from 50 to 160 eV. This is because there is a Cooper minimum [25,127] in the Cl $3p$ atomic orbital photoionization cross-sections at 35–40 eV [68], so that above this energy they first increase in intensity then decrease very slowly with increasing photon energy. Similarly the branching ratio and partial differential oscillator strength characteristics of the molecular orbitals of essentially fluorine lone pair character (the $1a_2$, $4e$ and $3e$ in CF_3Cl and the 3b1 and $1a_2$ in CF_2Cl_2), are very much like those of F $2p$ atomic orbitals [68]. The molecular orbitals having C-F and C-Cl bonding character exhibit differential oscillator strength and branching ratio curves which are generally consistent with mixed C/F and C/Cl character.

The inner valence molecular orbitals of CF_3Cl, CF_2Cl_2 and $CFCl_3$ (the $3a_1$ orbitals and all lower lying levels) may be expected to show partial photoionization differential oscillator strengths more consistent with atomic-like behaviour than the outer valence orbitals since they exist closer to the atomic centres and thus will be less influenced by molecular bonding and symmetry effects. Electron correlation will, however, be more important for ionization of the inner valence orbitals [158], leading to several many-body ion states for ionization of a given molecular orbital. The $3a_1$ orbitals of all three molecules have predominantly C $2s$ character and exhibit very similar photoionization

differential oscillator strengths from 65 to 160 eV. These differential oscillator strengths are also in semi-quantitative agreement with Hartree-Slater theoretical calculations of the C 2*s* atomic orbital differential oscillator strengths [68] (within 20%). In addition, however, the $3a_1$ differential oscillator strengths of CF_3Cl show different behaviour from those of CF_2Cl_2 and $CFCl_3$ below 60 eV. For the latter two molecules the $3a_1$ differential oscillator strengths continue to rise to lower energy, whereas those for CF_3Cl show a maximum at 55 eV photon energy. These types of differences can arise near threshold due to the influence of the molecular field on low energy (slow moving) photoelectrons; in fact this maximum is predicted by the MS-Xα calculations for CF_3Cl [153]. The inner valence orbitals of Cl 3*s* character (the $2a_1$ for CF_3Cl, the $2a_1$ and $1b_2$ for CF_2Cl_2 and the $1e$ and $2a_1$ for $CFCl_3$) have very low photoionization differential oscillator strengths from 41 to 160 eV, with magnitudes approximately in proportion to the number of Cl atoms in the molecule. Comparison with the Hartree-Slater calculations [68] for Cl 3*s* atomic orbitals reveals that the presently reported differential oscillator strengths for these molecular orbitals (per chlorine atom) are substantially lower (40–75%) than those expected on the basis of the Gelius model [161]. The inner valence orbitals of predominantly F 2*s* character (the $1e$ and $1a_1$ for CF_3Cl, the $1b_1$ and $1a_1$ for CF_2Cl_2 and the $1a_1$ for $CFCl_3$) show similar behaviour, i.e. the differential oscillator strengths are approximately proportional to the number of F atoms in the molecules, but are significantly (10–40%) less than predicted using the Gelius model [161] and the atomic F 2*s* differential oscillator strengths given in ref. [68]. One possible reason for this is that electron correlation effects cause the inner valence Cl 3*s* and F 2*s* orbitals to lead to a large number of many-body final ion states [158], many of which may not be readily visible in the photoelectron spectra above what is assumed to be the (non-spectral) background. Such intensity will not be included in the data analysis procedure, and this will result

in branching ratios and partial photoionization differential oscillator strengths for these orbitals which are too low.

The present work clearly demonstrates that the partial photoionization differential oscillator strengths (cross-sections) of inner valence orbitals of C 2*s* and especially F 2*s* character are quite substantial in the freon molecules and certainly cannot be ignored when attempting to use photoelectron branching ratios and total photoabsorption differential oscillator strengths to calculate partial photoionization differential oscillator strengths for valence level electronic ion states. In the absence of direct experimental measurements of the branching ratios or differential oscillator strengths of the inner valence orbitals, it may be possible to use estimates based on atomic data. Although the inner valence partial photoionization differential oscillator strengths determined in the present work are substantially lower than would have been estimated from atomic data, it is uncertain whether this is a real effect or a consequence of the many-body nature of the inner valence electronic ion states, leading to underestimates of their true intensities. Photoelectron spectra with much higher signal/noise ratio and possibly higher resolution and/or photoelectron/photoion coincidence measurements will be required to answer this question with greater certainty.

Chapter 7

Absolute Dipole Differential Oscillator Strengths for Inner Shell Spectra from High Resolution Electron Energy Loss Studies of the Freon Molecules CF_4, CF_3Cl, CF_2Cl_2, $CFCl_3$ and CCl_4

The CF_3Cl, CF_2Cl_2 and $CFCl_3$ inner shell EELS spectra used to derive absolute differential oscillator strengths were measured using the high resolution dipole(e,e) spectrometer described in section 3.2. The CF_4 inner shell EELS spectra are from refs. [130,162] and those for CCl_4 are from ref. [163].

7.1 Absolute Differential Oscillator Strengths

Absolute photoabsorption differential oscillator strength (cross section) spectra have been obtained from the presently measured inner shell electron energy loss spectra. The procedures used in the present chapter for obtaining absolute inner shell differential oscillator strength spectra were as follows (Similar types of investigation have previously been reported by Mclaren *et al.* [44] and also in section 5.3 above). Firstly, the underlying continuum due to valence and less tightly bound inner shells plus any non-spectral background was fitted to a function of the form $a(E-b)^c+d$ in the energy region just before the inner shell edge of interest (E is the energy loss and a, b, c and d are constants). This fitted function was then extrapolated to higher energy and subtracted from the particular inner shell electron energy loss spectrum. The resulting spectrum which should be due to the particular inner shell excitation alone was then converted to an approximate

relative optical spectrum using a kinematic Bethe-Born factor estimated to be proportional to $E^{2.5}$ (see section 2.2 and equations 2.37 and 2.38). The absolute scale was then obtained by normalizing the relative optical spectrum at a sufficiently high photoelectron energy (typically ~25–35 eV above the IP) to the sum of the corresponding atomic subshell optical differential oscillator strengths for the appropriate constituent atoms at that photoelectron energy. The principles underlying this normalization method have been discussed in sections 2.3.4.3 and 2.3.8. For this procedure semi-empirical total atomic cross sections [57] were used to obtain relevant subshell atomic cross sections (differential oscillator strengths) by subtracting estimated contributions from shells with lower excitation energies from the total.

The accuracy of the background subtraction procedures used to obtained the subshell molecular differential oscillator strength spectrum was considerably improved by further constraining the fitting of the background region such that the resulting differential oscillator strength spectrum in the higher (photoelectron) energy continuum region matched the *shape* of the appropriate summed (i.e. C 1s, F 1s, Cl 2p and Cl (2p+2s)) atomic oscillator strength distributions (see, for example, figure 7 below which illustrates the results of such constrained procedures for Cl 2p, 2s spectra). As discussed in section 2.3.4.3, molecular effects, such as EXAFS, are of low amplitude relative to the direct ionization continuum and will thus have little adverse effect on these procedures as long as the energy range used for matching molecular and atomic spectra is sufficiently large.

As discussed in section 2.3.4.3 at sufficiently high photoelectron energy, the molecular photoionization differential oscillator strength *contributed by each atom in a molecule* can be considered, to a first approximation, to be equal to the corresponding atomic photoionization differential oscillator strength. Therefore the integrated oscillator strengths for the molecule and for the constituent atom above a sufficiently high photoelectron

Table 7.33: Estimations of integrated atomic oscillator strengths (OS) for inner shell excitations in C, F, and Cl atoms

	$E_0 - IP^a$	OS above $E_0{}^b$	OS transferred^c	OS below $E_0{}^d$
C 1s	38.7	1.393	0.0913	0.5157
F 1s	48.0	1.5	0.275	0.225
Cl 2p	60.2^e	4.8	-0.9026	2.1026

[a] E_0 is the photon energy below which the integrated oscillator strength for the given inner shell excitation is to be estimated. $E_0 - IP$ is thus the photoelectron energy.
[b] The integrated oscillator strength from E_0 to 1.5×10^6 eV (effectively infinity) as estimated from calculation [69]. See text for details.
[c] oscillator strength transferred to other shells due to the Pauli excluded transitions from the present sub-shell to the already occupied orbitals [112].
[d] Using the partial TRK sum-rule: the sub-shell oscillator strength below E_0 = (number of electrons in the inner shell) – (OS above E_0) – (OS transferred).
[e] with reference to the Cl $2p_{1/2}$ IP.

Table 7.34: Integrated sub-shell oscillator strengths per atom for CF_4, CF_3Cl, CF_2Cl_2, $CFCl_3$ and CCl_4 below E_0

Excited shell	$E_0 - IP^a$	Atom^b	CF_4	CF_3Cl	CF_2Cl_2	$CFCl_3$	CCl_4
C 1s	38.7	0.52	0.57	0.57	0.57	0.54	0.53
F 1s	48.0	0.23	0.23	0.23	0.23	0.22	
Cl 2p	60.2^c	2.10		1.99	1.92	1.90	1.84

[a] $E_0 - IP$ is the photoelectron energy below which oscillator strength for a given sub-shell is to be integrated.
[b] from table 7.33.
[c] with reference to the Cl $2p_{1/2}$ IP.

energy should be approximately equal. Therefore, assuming that the oscillator strength transfer due to Pauli excluded transitions [38] to already occupied orbitals is similar for both the molecule and summed atomic situation, the integrated molecular oscillator strength per atom is expected (on the basis of the partial TRK sum-rule considerations, see sections 2.3.4.3 and 2.3.8) to be comparable to the corresponding atomic oscillator strength integral up to the same photoelectron energy. The integrated sub-shell oscillator strengths for C ($1s$), F ($1s$) and Cl ($2p$) atoms have been estimated using the partial TRK sum-rule considerations and are shown in table 7.33. The integrated oscillator strength above the photon energy E_0 was obtained by integrating the calculated photoionization differential oscillator strength [68,69] from E_0 to infinity (actually to the limit of the relativistic Hartree-Slater calculation at 1.5×10^6 eV [69]. The contribution to the oscillator strength above 1.5×10^6 eV is estimated to be less than 2×10^{-6}). The oscillator strength transfer due to Pauli excluded transitions is taken from Hartree-Slater calculations [112]. The adequacy of the presently employed background subtraction and normalization procedures is evident from table 7.34 from which it can be seen that the presently obtained integrated molecular oscillator strength per atom is very close to the corresponding integrated atomic oscillator strength.

7.2 Electronic Configurations and Spectral Assignments

The CF_3Cl and $CFCl_3$ molecules are of C_{3v} symmetry, CF_2Cl_2 has C_{2v} symmetry and CF_4 and CCl_4 have T_d symmetry. The ground state electron configurations may be written as in table 7.35. The valence shell electronic configurations of CF_3Cl, CF_2Cl_2, $CFCl_3$ and CF_4 are as reported in the earlier PES studies in references [99,100,117,157] and in this thesis work (chapter 6). The inner shell electronic configuration for CF_4 is as reported in XPS measurements [86]. Gaussian 76 calculations were carried out for CF_4,

Table 7.35: Electronic configurations for the CF_4, CF_3Cl, CF_2Cl_2, $CFCl_3$ and CCl_4 molecules[a]

Molecule	Cl 1*s*	F 1*s*	C 1*s*	Cl 2*s*	Cl 2*p*
CF_4 [b]		$1t_2^6 1a_1^2$	$2a_1^2$		
CF_3Cl	$1a_1^2$	$2a_1^2 1e^4$	$3a_1^2$	$4a_1^2$	$5a_1^2 2e^4$
CF_2Cl_2	$1b_2^2 1a_1^2$	$2a_1^2 1b_1^2$	$3a_1^2$	$2b_2^2 4a_1^2$	$5a_1^2 3b_2^2 4b_2^2 2b_1^2 1a_2^2 6a_1^2$
$CFCl_3$	$1a_1^2 1e^4$	$2a_1^2$	$3a_1^2$	$2e^4 4a_1^2$	$5a_1^2 3e^4 1a_2^2 4e^4 6a_1^2 5e^4$
CCl_4	$1t_2^6 1a_1^2$		$2a_1^2$	$2t_2^6 3a_1^2$	$3t_2^6 4a_1^2 1t_1^6 1e^4 4t_2^6$

Molecule	Valence orbitals[c]	Virtual valence orbitals (unoccupied)
CF_4	$3a_1^2 2t_2^6 4a_1^2 3t_2^6 1e^4 4t_2^6 1t_1^6$	$\underbrace{5a_1^0 5t_2^0}_{(C-F)^*}$
CF_3Cl	$6a_1^2 3e^4 7a_1^2 8a_1^2 4e^4 9a_1^2 5e^4 6e^4 1a_2^2 10a_1^2 7e^4$	$\underbrace{11a_1^0}_{(C-Cl)^*}\ \underbrace{8e^0 12a_1^0}_{(C-F)^*}$
CF_2Cl_2	$7a_1^2 3b_1^2 8a_1^2 5b_2^2 9a_1^2 6b_2^2 10a_1^2 4b_1^2 11a_1^2 2a_2^2 5b_1^2$ $7b_2^2 12a_1^2 3a_2^2 6b_1^2 8b_2^2$	$\underbrace{13a_1^0 9b_2^0}_{(C-Cl)^*}\ \underbrace{7b_1^0 14a_1^0}_{(C-F)^*}$
$CFCl_3$	$7a_1^2 8a_1^2 6e^4 9a_1^2 10a_1^2 7e^4 8e^4 11a_1^2 9e^4 10e^4 2a_2^2$	$\underbrace{12a_1^0 11e^0}_{(C-Cl)^*}\ \underbrace{13a_1^0}_{(C-F)^*}$
CCl_4	$5a_1^2 5t_2^6 6a_1^2 6t_2^6 2e^4 7t_2^6 2t_1^6$	$\underbrace{7a_1^0 8t_2^0}_{(C-Cl)^*}$

[a] See section 7.2 for details.
[b] from ref. [86].
[c] from chapter 6 and refs. [99,100,117,157].

Table 7.36: Dipole-allowed transitions between orbitals for C_{3v}, C_{2v} and T_d symmetries

	Initial state		Final state
C_{3v} (CF_3Cl and $CFCl_3$)	a_1	$\longrightarrow$	a_1, e
	a_2	$\longrightarrow$	e
	e	$\longrightarrow$	a_1, e
C_{2v} (CF_2Cl_2)	a_1	$\longrightarrow$	a_1, b_1, b_2
	a_2	$\longrightarrow$	b_1, b_2
	b_1	$\longrightarrow$	a_1, b_1
	b_2	$\longrightarrow$	a_1, b_2
T_d (CF_4 and CCl_4)	a_1	$\longrightarrow$	t_2
	t_2	$\longrightarrow$	t_2, t_1, e, a_1
	e	$\longrightarrow$	t_2, t_1
	t_1	$\longrightarrow$	t_2, t_1, e, a_2

CF_3Cl, CF_2Cl_2, $CFCl_3$ and CCl_4 to further aid in the analysis of the energy orderings of the orbitals and to establish the dominant orbital characters (i.e. (C-F)* or (C-Cl)*) of the unoccupied (virtual) valence antibonding orbitals as indicated in table 7.35.

The dipole-allowed transitions for T_d (CF_4 and CCl_4), C_{3v} (CF_3Cl and $CFCl_3$) and C_{2v} (CF_2Cl_2) symmetries are shown in table 7.36. The reported Cl $2p$, C $1s$ and F $1s$ inner shell electron ionization energies [164,165] for CF_4, CF_3Cl, CF_2Cl_2, $CFCl_3$ and CCl_4 are shown in tables 7.37–7.40 (see below). The transitions in the various inner shell spectra have been tentatively assigned using the information in table 7.35 and 7.36. Term values for transitions given Rydberg final orbitals are expected to be transferable between different inner shell spectra of the same molecule. In contrast term values for core to particular virtual valence orbital transitions are not in general transferable.

7.3 C $1s$ Spectra

Figs. 7.42 and 7.43 show the presently obtained high resolution (short energy range) and low resolution (long energy range) C $1s$ dipole differential oscillator strength spectra respectively for CF_3Cl, CF_2Cl_2 and $CFCl_3$, together with spectra determined from earlier reported EELS measurements for CF_4 [130] and CCl_4 [163]. We have Bethe-Born converted and normalized the high and low resolution EELS spectra of CCl_4, reported earlier by Hitchcock and Brion [163], to yield dipole differential oscillator strength spectra. In section 5.3 we have also presented a C $1s$ long range absolute differential oscillator strength spectrum for CF_4, derived from earlier obtained small angle EELS data [130], by approximate Bethe-Born conversion followed by single point normalization to the atomic differential oscillator strength. In the case of the C $1s$ of CF_4 the background was earlier estimated (section 5.3) using very approximate procedures. However the integrated oscillator strength and peak intensity of the CF_4 data are apparently too high and we

have therefore re-derived the CF_4 C 1*s* differential oscillator strength spectrum with the presently used more stringent and consistent procedures for accessing the background. The CF_4 C 1*s* short range EELS spectra reported in reference [162] have been also placed on an absolute differential oscillator strength scale in the present work. These newly normalized C 1*s* spectra for CF_4 and CCl_4 are also presented in figs. 7.42 and 7.43. The higher resolution C 1*s* spectrum of CF_4 [162] is shown on an expanded energy scale as an insert at the top right of fig. 7.42. The C atomic differential oscillator strength spectrum [57] was used to obtain the absolute scale for the C 1*s* molecular spectra by matching the overall shapes at high photoelectron energy over a wide energy range as discussed in section 7.1 above. The energy positions, term values and possible assignments of the observed features in the recently reported C 1*s* spectra of CF_3Cl, CF_2Cl_2 and $CFCl_3$ and are listed in tables 7.37–7.39 and those for CF_4 and CCl_4 are summarized in table 7.40. Also shown in the tables are the integrated oscillator strengths for selected transitions for CF_3Cl, CF_2Cl_2, $CFCl_3$ and CCl_4 obtained by fitting Gaussian peaks (not shown in the figures) to the spectral features. The integrated oscillator strength up to the C 1*s* IP for CF_4 is shown in table 7.40.

Strong chemical shift effects with increasing fluorination can be seen in fig. 7.42. It can also be seen that the "center of mass" of the pre-ionization edge oscillator strength distribution moves towards the respective IP as the number (degeneracy) of (C-F)* antibonding orbitals increases and that of (C-Cl)* decreases, in going from CCl_4 to CF_4. From the transition energies and IPs it is apparent that the term values for the more prominent peaks are in two energy ranges. Furthermore the changes in intensity distribution with successive fluorination suggest that the larger and smaller term value groups are associated with the (C-Cl)* and (C-F)* normally unoccupied orbitals respectively. With these considerations in mind the prominent pre-ionization edge spectral features

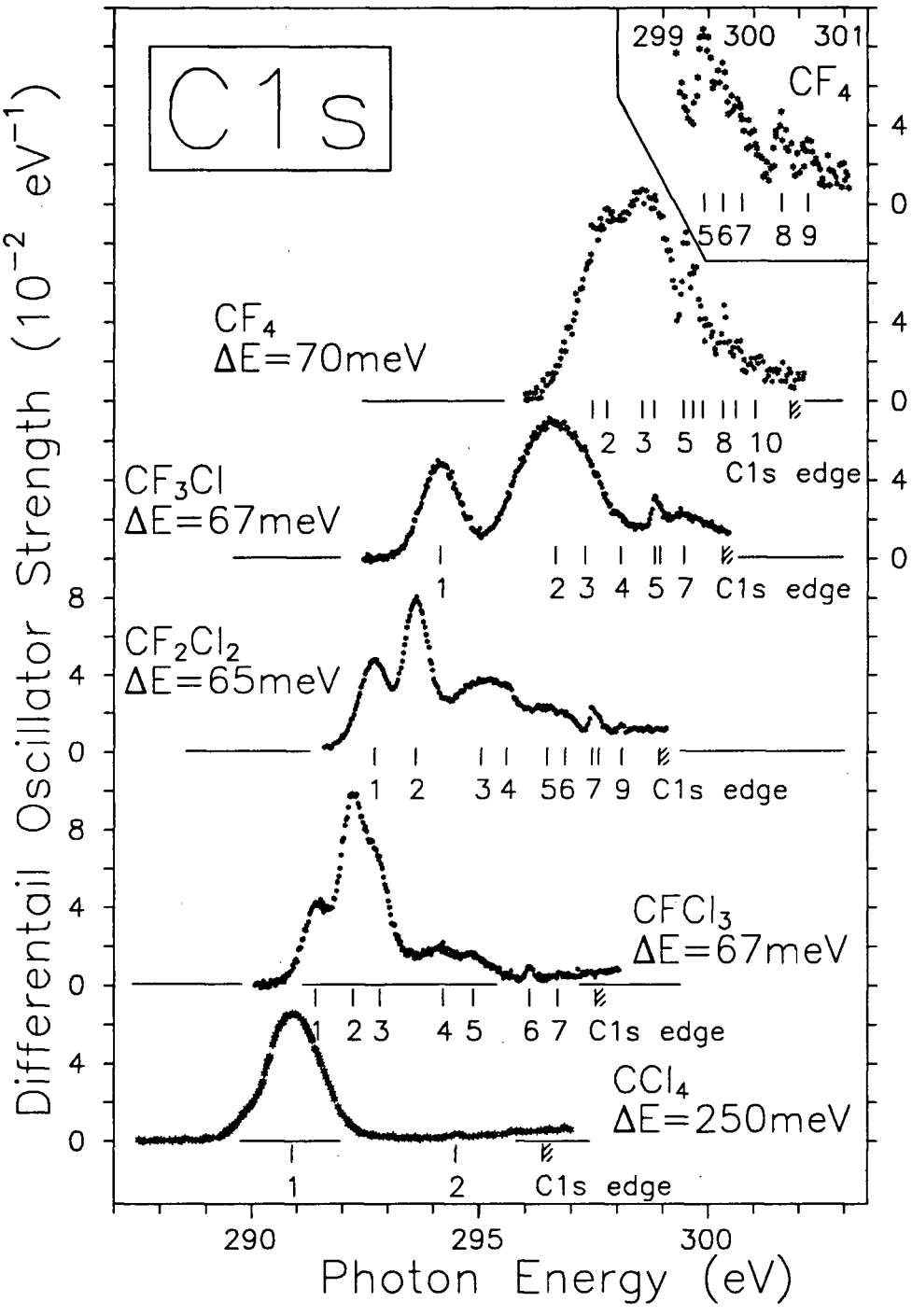

Figure 7.42: Differential oscillator strength spectra for C 1*s* excitation of CF_4, CF_3Cl, CF_2Cl_2, $CFCl_3$ and CCl_4 in the discrete region. The CF_4 and CCl_4 spectra were derived from EELS measurements in refs. [162,163] respectively. See section 7.3 and tables 7.37–7.40 for details.

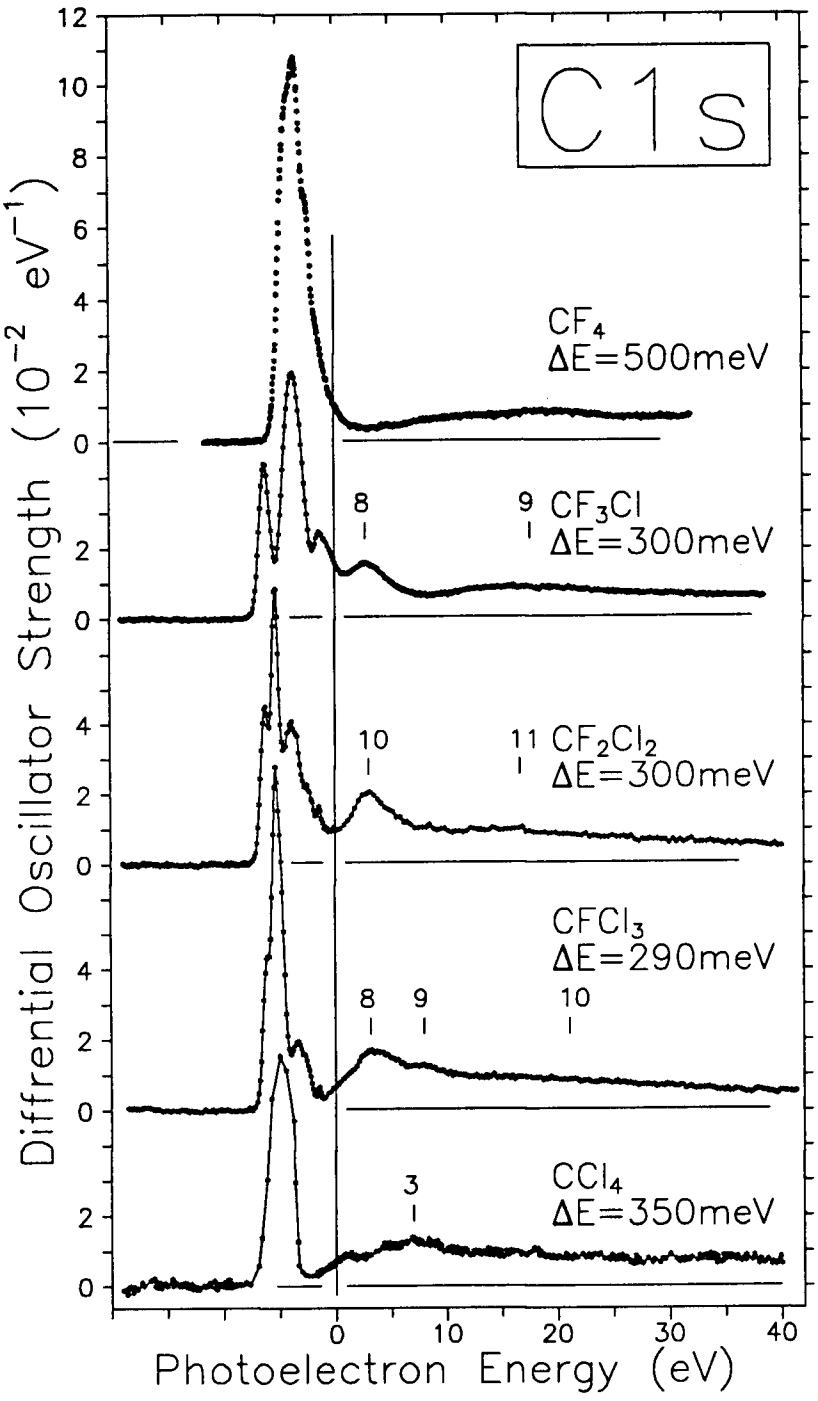

Figure 7.43: Differential oscillator strength spectra for C 1*s* excitation of CF_4, CF_3Cl, CF_2Cl_2, $CFCl_3$ and CCl_4 in the discrete and continuum regions. The CF_4 and CCl_4 spectra were derived from EELS measurements in refs. [130,163] respectively. See section 7.3 and tables 7.37–7.40 for details.

Table 7.37: Experimental data for C 1*s*, F 1*s* and Cl 2*s*, 2*p* excitations of CF_3Cl

	Feature[a]	Photon energy (eV)	Oscillator strength[b] ($\times 10^{-2}$)	Term value (eV)	Possible assignment (final orbital)
C 1*s*	1	294.16	4.8	6.15	$11a_1$
	2	296.66	16.4	3.65	$8e$
	3	297.3		3.0	$12a_1$
	4	298.07		2.24	$4p$
	5	298.82		1.49	$5s$
	6	298.93		1.37	$5p$
	7	299.46		0.85	$6s$
	IP	(300.31)[c]		0	
	8	303.12		-2.81	shape resonance
	9	~318.0		~-17.7	XANES
F 1*s*	1	690.51		4.53	$11a_1$
	2	692.60	15.5	2.44	$8e$+$12a_1$
	3	694.5		0.5	?
	IP	(695.04)[c]		0	
	4	720		-25	XANES
Cl 1*s*	D	2823.5		6.7	$11a_1$
	E	2827.4		2.8	$12a_1$+$8e$
	F	2827.3		2.4	$4p$
	IP	2830.2		0	
Cl 2*s*	9	271.5		7.3	virtual valence
	IP	(278.84)[c]		0	

				Cl $2p_{3/2}$	Cl $2p_{1/2}$	Cl $2p_{3/2}$	Cl $2p_{1/2}$
Cl 2*p*	1	201.13	1.6	6.70		$11a_1$	
	1′	202.71	1.1		6.73		$11a_1$
	2	204.31	0.6	3.52	5.13	$8e$+$12a_1$	
	3,2′	205.74		2.09	3.7	$4p$	$8e$+$12a_1$
	4	206.26		1.57		$5s$	
	5	206.56		1.27		$5p$	
	3′	207.32			2.12		$4p$
	$2p_{3/2}$ IP	(207.83)[d]		0			
	4′	208.0			1.44		$5s$
	5′	208.26			1.18		$5p$
	$2p_{1/2}$ IP	(209.44)[d]		0			
	6	214.8		-7	-5.4		
	7	219.6		-11.8	-10.2	XANES	
	8	228.0		-20.2	-18.6		

[a]For features, see figs. 1 and 2 for C 1*s*, figs. 3 and 4 for F 1*s*, figs. 5 and 6 for Cl 2*s* and 2*p* and ref. [166] for Cl 1*s*.

[b]Integrated oscillator strengths. See sections 7.3–7.5 for details.

[c]from XPS measurement [165].

[d]from XPS measurement [164].

Table 7.38: Experimental data for C 1*s*, F 1*s* and Cl 2*s*, 2*p* excitations of CF_2Cl_2

	Feature[a]	Photon energy (eV)	Oscillator strength[b] ($\times 10^{-2}$)	Term value (eV)	Possible assignment (final orbital)
C 1*s*	1	292.73	3.7	6.22	$13a_1$
	2	293.62	6.2	5.31	$9b_2$
	3	295.05		3.88	$7b_1$
	4	295.60		3.33	$14a_1$
	5	296.48		2.46	$4p$
	6	296.87		2.06	$4p'$
	7	297.46		1.47	$5s$
	8	297.6		1.33	$5p$
	9	298.10		0.83	$6s$
	IP	(298.93)[c]		0	
	10	301.93		-3	shape resonance
	11	315.6		-16.7	XANES
F 1*s*	1	689.40		5.26	$13a_1+9b_2$
	2	691.90	9.6	2.78	$7b_1+14a_1$
	3	693.37		1.31	$5p$
	IP	(694.68)[c]		0	
	4	697.54		-2.86	shape resonance
	5	717.92		-23.24	XANES
Cl 1*s*	D	2823.0		6.6	$13a_1+9b_2$ [d]
	E	2826.4		3.2	$14a_1+7b_1$ [d]
	F	2827.2		2.4	$4p$
	IP	(2829.6)		0	
Cl 2*s*	11	271.3		7.3	virtual valence
	IP	(278.63)[c]		0	

				Cl $2p_{3/2}$	Cl $2p_{1/2}$	Cl $2p_{3/2}$	Cl $2p_{1/2}$
Cl 2*p*	1	200.73	2.1	6.74		$13a_1$	
	2	201.39	0.7	6.08		$9b_2$	
	1′	202.32	1.2		6.78		$13a_1$
	2′	203.01	0.4		6.09		$9b_2$
	3	204.04	1.7	3.43		$7b_1$	
	4	204.40		3.07		$14a_1$	
	5	205.17		2.3		$4p$	
	6	205.38		2.09		$4p'$	
	7,3′	205.80		1.67	3.3	$5s$	$7b_1$
	4′	206.02			3.08		$14a_1$
	5′	206.76			2.34		$4p$
	6′	207.02			2.08		$4p'$
	$2p_{3/2}$ IP	(207.47)[e]		0			
	7′	207.78			1.32		$5s$
	$2p_{1/2}$ IP	(209.10)[e]			0		
	8	216.3		-8.8	-7.2		
	9	222.8		-15.3	-13.7	XANES	
	10	230.6		-23.1	-21.5		

[a] For features, see figs. 1 and 2 for C 1*s*, figs. 3 and 4 for F 1*s*, figs. 5 and 6 for Cl 2*s* and 2*p* and ref. [166] for Cl 1*s*.

[b] Integrated oscillator strengths. See sections 7.3–7.5 for details.

[c] from XPS measurement [165].

[d] $9b_2$ and $7b_1$ have been mistakenly denoted as $10b_2$ and $6b_1$ in ref. [166].

[e] from XPS measurement [164].

Table 7.39: Experimental data for C 1*s*, F 1*s* and Cl 2*s*, 2*p* excitations of $CFCl_3$

	Feature[a]	Photon energy (eV)	Oscillator strength[b] ($\times 10^{-2}$)	Term value (eV)		Possible assignment (final orbital)	
C 1*s*	1	291.42	3.3	6.12		$12a_1$	
	2	292.24	9.7	5.30		$11e(1)$	
	3	292.83		4.71		$11e(2)$	
	4	294.22		3.32		$13a_1$	
	5	294.87		2.67		$4p$	
	6	296.10		1.44		$5s$	
	7	296.71		0.83		$6s$	
	IP	(297.54)[c]		0			
	8	300.7		-3.16		shape resonance	
	9	305.51		-7.97			
	10	318.60		-21.1		XANES	
F 1*s*	1	688.7		5.63		$12a_1$+$11e$	
	2	690.42	3.8	3.91		$13a_1$	
	IP	(694.33)[c]		0			
	2	697.80		-3.47		shape resonance	
	3	720.0		-25.67		XANES	
Cl 1*s*	D	2822.8		6.5		$12a_1$	
	E	2825.7		3.6		$11e$+$13a_1$	
	F	2827.1		2.2		$4p$	
	IP	(2829.3)		0			
Cl 2*s*	8	270.9		7.3		virtual valence	
	IP	(278.24)[c]		0			
				Cl $2p_{3/2}$	Cl $2p_{1/2}$	Cl $2p_{3/2}$	Cl $2p_{1/2}$
Cl 2*p*	1	200.65	3.6	6.55		$12a_1$	
	2	201.79	0.5	5.41		$11e(1)$	
	1′	202.33	1.4		6.48		$12a_1$
	3,2′	203.15	0.9	4.05	5.66	$11e(2)$	$11e(1)$
	4	203.96	2.9	3.24		$13a_1$	
	3′	205.11			3.70		$11e(2)$
	4′	205.62			3.19		$13a_1$
	$2p_{3/2}$ IP	(207.20)[d]		0			
	$2p_{1/2}$ IP	(208.81)[d]			0		
	5	216.6		-9.4	-7.8		
	6	222.7		-15.5	-13.9	XANES	
	7	233.7		-26.5	-24.9		

[a]For features, see figs, 1 and 2 for C 1*s*, figs. 3 and 4 for F 1*s*, figs. 5 and 6 for Cl 2*s* and 2*p* and ref. [166] for Cl 1*s*.

[b]Integrated oscillator strengths. See text sections 7.3–7.5 for details.

[c]from XPS measurement [165].

[d]from XPS measurement [164].

Table 7.40: Experimental data for C 1*s*, F 1*s* and Cl 2*s*, 2*p* excitations of CF_4 and CCl_4

		Feature[a]	Photon energy[b] (eV)	Oscillator strength[c] ($\times 10^{-2}$)	Term value (eV)	Possible assignment (final orbital)
CF_4	C 1*s*	1	297.45		4.35	
		2	297.77		4.03	$5t_2$ plus
		3	298.54		3.26	outer well states
		4	298.81		2.99	
		5	299.45		2.35	3p
		6	299.66	29	2.14	?
		7	299.87		1.93	?
		8	300.31		1.49	4s
		9	300.60		1.20	4p
		10	301.03		0.77	5s
		IP	(301.8)[d]		0	
	F 1*s*	1	~690.5		~ 5	$5a_1$
		2	692.9	25.4	2.6	$5t_2(1)$
		2	~ 694		1.2	$5t_2(2)$
		IP	(695.52)[d]		0	
CCl_4	C 1*s*	1	290.9	9.9	5.5	$8t_2$
		2	294.5		1.8	5s
		IP	(296.38)[d]		0	
		3	~303		~7	shape resonance
	Cl 2*s*	4	271.8		6.2	virtual valence
		IP	(278.04)[d]		0	
					Cl $2p_{3/2}$ Cl $2p_{1/2}$	Cl $2p_{3/2}$ Cl $2p_{1/2}$
	Cl 2*p*	$2p_{3/2}$IP	(207.04) [e]		0	
		$2p_{1/2}$IP	(208.73)[e]		0	
		1	-217.7		-10.7 -9	
		2	-224.7		-17.7 -16	XANES
		3	-235.2		-28.2 -26.5	

[a] See figs. 1 and 2 for C 1*s* features, figs. 3 and 4 for F 1*s* features, and figs. 5 and 6 for Cl 2*s* and 2*p* features.
[b] experimental results for CF_4 are from [162] and those for CCl_4 are from [163]
[c] Integrated oscillator strengths. See text sections 7.3–7.5 for details.
[d] from XPS measurement [165].
[e] from XPS measurement [164].

have been assigned assuming that the term values for a particular type (i.e. (C-Cl)* and (C-F)*) of antibonding orbital have similar values in the different molecules. The oscillator strength concentrated within a broad band (feature 1) in the CCl_4 spectrum which corresponds to the dipole allowed transition to the $8t_2$ C-Cl antibonding orbital [163] is redistributed (see fig. 7.42 and tables 7.37–7.40) upon successive fluorination among the transitions to $12a_1$ ((C-Cl)*, feature 1) $11e$ ((C-Cl)*, feature 2 and 3, see discussion below) and $13a_1$ ((C-F)*, feature 4) for $CFCl_3$ (see table 7.39); to $13a_1$ ((C-Cl)*, feature 1), $9b_2$ ((C-Cl)*, feature 2), $7b_1$ ((C-F)*, feature 3) and $14a_1$ ((C-F)*, feature 4) for CF_2Cl_2 (see table 7.38); to $11a_1$ ((C-Cl)*, feature 1), $8e$ ((C-F)*, feature 2) and $12a_1$ ((C-F)*, feature 3) for CF_3Cl (see table 7.37); and finally concentrates in a single broad band again in CF_4 (see table 7.40), corresponding to the transition to the $5t_2$ (C-F)* antibonding orbital [150]. Under the present assignment, the term values for transitions from the C $1s$ orbitals to (C-Cl)* antibonding orbitals are found to be between 5.4–6.2 eV while those to (C-F)* antibonding orbitals are between 3.3–3.9 eV. In the $CFCl_3$ spectrum the feature 2 and the shoulder shown as feature 3 are ~0.6 eV apart and they are probably the two Jahn-Teller components of the transition to the $11e$ virtual orbital. A Jahn-Teller splitting of ~0.8 eV has been observed in PES studies [167].

It is interesting to note from fig. 7.43 that a minimum followed by an above IP maximum is observed near the ionization edge in the C $1s$ spectra of CF_3Cl, CF_2Cl_2, $CFCl_3$ and CCl_4. In proceeding from CCl_4 to CF_3Cl, the minimum shifts towards the IP and finally moves above the IP in CF_3Cl. In the case of CF_4, there is no localized near-edge maximum above IP. A potential barrier due to the presence of the halogen ligands in the freon molecules is expected to affect the absorption spectra as discussed in section 2.3.6. CCl_4 and CF_4 belong to the same symmetry point group T_d with the same central atom (C) and they each have similar a_1 and t_2 manifolds of unoccupied valence

orbitals (see table 7.35). Theoretical calculations on the LiF_6^+ system [168] with varying Li-F distance have shown that the longer the Li-F distance, the stronger the inner well strength, i.e. the lower the energy of state supported by the potential, with respect to the ionization limit (i.e. a larger term value). Consistent observations on spectra for the molecular series $SiBr_4$, $SiCl_4$ and SiF_4 [169], BBr_3, BCl_3 and BF_3 [170], and PBr_3, PCl_3 and PF_3 [171] have also shown that the corresponding virtual valence feature and/or shape resonance feature shifts to higher energy with respect to the IP of the central atom as the ligand changes from Br to Cl to F. In the present situation, the fact that the term value of the prominent C $1s \rightarrow t_2$ transition in CCl_4 (5.4 eV) [163] is larger than that in CF_4 (~3.4 eV) [130,162] illustrates that the inner well potential of CCl_4 is stronger and this is consistent with the C-Cl bond length (1.77 Å) for CCl_4 being greater than the C-F bond length (1.32 Å) for CF_4 [172]. Moreover, the presence and the absence of the above IP near edge spectral maximum in the CCl_4 and CF_4 spectra respectively is consistent with the CF_4 inner well strength being so small that an above IP shape resonance is not seen. We assign the maxima features above the IP to transitions to shape resonance states (see fig. 7.43 and tables 7.37–7.40). These shape resonances may be associated with virtual orbitals involving Cl $3d$ components. Such an interpretation is consistent with the absence of such resonances in the case of CF_4. The weak structures superimposed on the broad band at ~298 eV in CF_4 are probably due to transitions to outer well states which are not Rydberg in character.

The remainder of the pre-ionization edge features in all molecules are interpreted as transitions to Rydberg states. The Rydberg transition features are usually sharp in shape as discussed in section 2.3.2. The narrow shapes and similar term values of features 8 for CF_4, 5 for CF_3Cl, 7 for CF_2Cl_2, 6 for $CFCl_3$ and 2 for CCl_4 (fig. 7.42) suggest that they are associated with Rydberg orbitals of the same type (s). Other Rydberg transitions are

similarly identified. The fact that feature 9 is well resolved from feature 8 for CF_4 suggests that the corresponding Rydberg transitions (p) are associated with the shoulders 6 for CF_3Cl and 8 for CF_2Cl_2. Similarly features 10 for CF_4, 7 for CF_3Cl, 9 for CF_2Cl_2 and 7 for $CFCl_3$ are all of the same type (s), and also features 5, 6 and 7 for CF_4, 4 for CF_3Cl, 5 and 6 for CF_2Cl_2, and 5 for $CFCl_3$ are of the same type (p). It is interesting to note that the very weak $6s$ Rydberg transition (feature 2) in the CCl_4 spectrum increases in intensity with successive fluorination so that it is much more intense for CF_3Cl than for CCl_4. When the series proceeds to CF_4, the Rydberg feature merges with the single band.

7.4 F 1s Spectra

Figs. 7.44 and 7.45 show the presently obtained high resolution (short range) and low resolution (long range) F 1s differential oscillator strength spectra for CF_3Cl, CF_2Cl_2 and $CFCl_3$ along with that for CF_4 presented in section 5.3. The spectra in fig. 7.45 are presented with photoelectron energy as the x axis. Energies, term values, integrated oscillator strengths up to IPs and possible assignments for transitions in the F 1s spectra are presented in tables 7.37–7.40.

It has recently been demonstrated from X-ray absorption experiments for CF_3Cl, CF_2Cl_2 and $CFCl_3$ that transitions from Cl 1s to C-F antibonding orbitals have appreciable intensities [166] in addition to those to (C-Cl)* antibonding orbitals, even though the Cl 1s orbital is localized in a very small spatial region at the Cl atomic sites in the molecule. In keeping with this observation [166] transitions to both C-F and C-Cl antibonding orbitals are used to interpret the F 1s spectra obtained in the present work. The strong band (feature 2) below the F 1s IP in the $CFCl_3$ spectrum (fig. 7.44) can therefore be attributed to the transition to the $13a_1$ (C-F)* antibonding orbital. Since

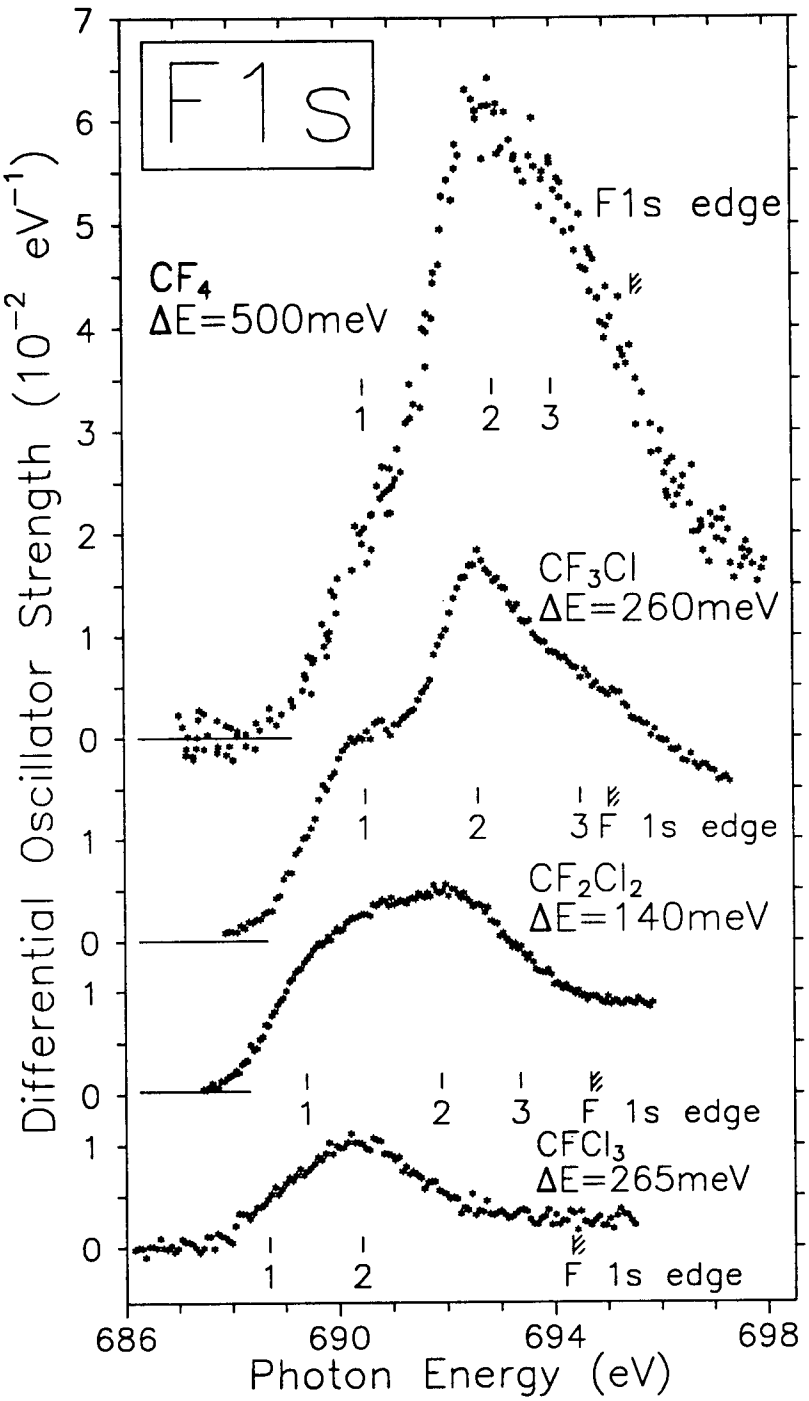

Figure 7.44: Differential oscillator strength spectra for F 1*s* excitation of CF_4, CF_3Cl, CF_2Cl_2 and $CFCl_3$ in the in discrete region. The CF_4 spectrum was obtained from section 5.3. See section 7.4 and tables 7.37–7.40 for details.

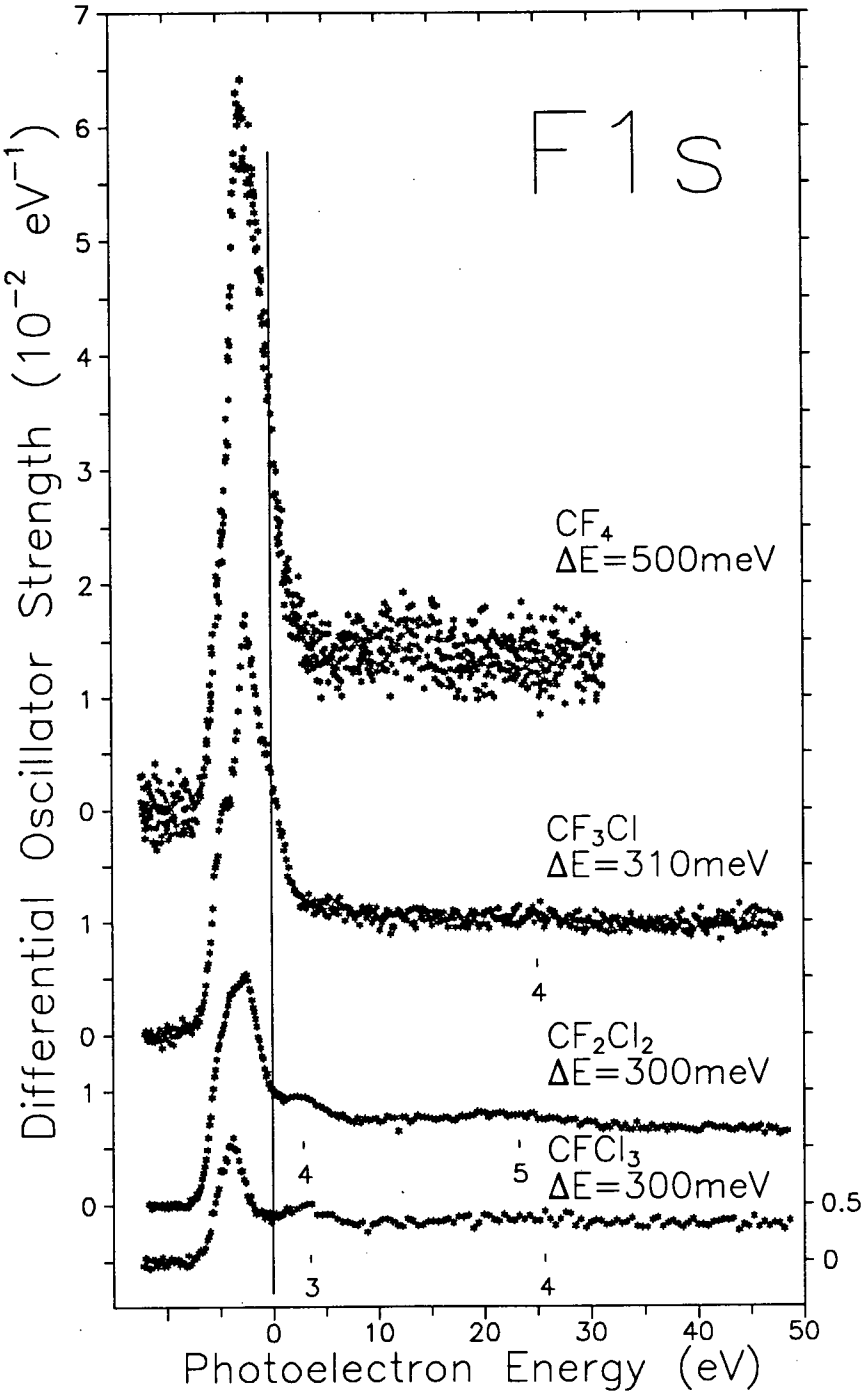

Figure 7.45: Differential oscillator strength spectra for F 1*s* excitation of CF_4, CF_3Cl, CF_2Cl_2 and $CFCl_3$ in the discrete and continuum regions. The CF_4 spectrum was obtained from section 5.3. See section 7.4 and tables 7.37–7.40 for details.

the overall band is asymmetric, the expected weaker transitions to the (C-Cl)* antibonding orbitals ($12a_1$,$11e$) here therefore been assigned to the lower energy shower (feature 1). Similarly transitions to the ($13a_1$+$9b_2$,(C-Cl)*) and ($7b_1$+$14a_1$,(C-F)*) are assigned to features 1 and 2 in the F 1s spectrum of CF_2Cl_2. Likewise, the $11a_1$ ((C-Cl)*) and ($8e$+$12a_1$) ((C-F)*) final orbitals have been assigned to the two features 1 and 2 in the CF_3Cl spectrum. The broad CF_4 pre-ionization edge band has been attributed to the transitions to the t_2 and a_1 states [150]. The shoulder 1 in the CF_4 spectrum may correspond to the transition to the $5a_1$ orbital. The partially resolved features 2 and 3 may be due to transitions to the $5t_2$ orbital where the degeneracy is removed by the Jahn-Teller effect.

In the long range F 1s spectra (fig. 7.45) a minimum followed by a maximum is observed near the edge in the spectra of $CFCl_3$, CF_2Cl_2 and possibly CF_3Cl as in the C 1s spectra. The minimum shifts from below the IP for $CFCl_3$ to above the IP for CF_2Cl_2 and CF_3Cl. The above IP spectral maxima, like those in the C 1s spectra are probably due to transitions to virtual orbitals involving Cl 3d participation (shape resonances), since the structure is not present in the CF_4 spectrum. The fact that these above edge resonances are relatively more intense in the C 1s spectra than in the F 1s spectra (compare figs. 7.43 and 7.45) is consistent with spatial overlap considerations for the respective initial and final states if the later have Cl 3d character.

7.5 Cl 2s and 2p Spectra

The presently obtained high resolution Cl 2p differential oscillator strength spectra for CF_3Cl, CF_2Cl_2 and $CFCl_3$ are shown in fig. 7.46. Gaussian peaks were fitted to the pre-ionization edge spectra in the low energy region. Three peaks for CF_3Cl and five peaks

for CF_2Cl_2 and $CFCl_3$ were fitted as shown in fig. 7.46. Long energy range, low resolution Cl $2p$, Cl $2s$ and C $1s$ spectra of CF_3Cl, CF_2Cl_2, $CFCl_3$ and CCl_4 are shown in fig. 7.47 on a common photoelectron energy scale (respective to Cl $2p_{1/2}$). The CCl_4 differential oscillator strength spectrum was obtained by converting the previously reported EELS spectrum [163] using the method outlined in section 7.1. It should be noted that the CCl_4 EELS spectrum had to be digitized from the figure in ref. [163] and therefore the resulting "noise level" on the spectrum in fig. 7.47 is greater than for the other spectra shown. In fig. 7.48 the molecular spectra are shown as differential oscillator strength per Cl atom in the molecule in order to facilitate comparison. The Cl atomic spectrum (also shown in fig. 7.48) for Cl $2p$ and Cl $2s$ excitations [57] was used to normalize the Cl $2p$ molecular spectra (see section 7.1 for details). Energies, term values, integrated oscillator strengths and possible assignments for various transitions in the Cl $2s$, $2p$ spectra of CF_3Cl, CF_2Cl_2, $CFCl_3$ and CCl_4 are presented in tables 7.37–7.40. Also shown in tables 7.37–7.39 are results from Cl $1s$ X-ray absorption spectra for CF_3Cl, CF_2Cl_2 and $CFCl_3$ recently reported by Perera *et al.* [166].

Two series of structures related to the Cl $2p_{3/2}$ and Cl $2p_{1/2}$ ionization potentials respectively are observed in the Cl $2p$ spectra of CF_3Cl, CF_2Cl_2 and $CFCl_3$ (fig. 7.46). The intensities of the series related to the Cl $2p_{3/2}$ IP are greater than those for Cl $2p_{1/2}$ as expected. The present assignment of the lower energy structures is based on the transitions to the normally unoccupied virtual valence molecular orbitals. Only two peaks (1 and 1′) are observed at low energy in the CF_3Cl spectrum (fig. 7.46) and they assigned to transitions to the $11a_1$ C-Cl antibonding orbital. The less intense peaks 2 and 2′ can then be attributed to transitions to the C-F antibonding orbitals, $8e$ and $12a_1$. In the CF_2Cl_2 spectrum two pairs of peaks (1 and 1′, 2 and 2′) have been fitted to the

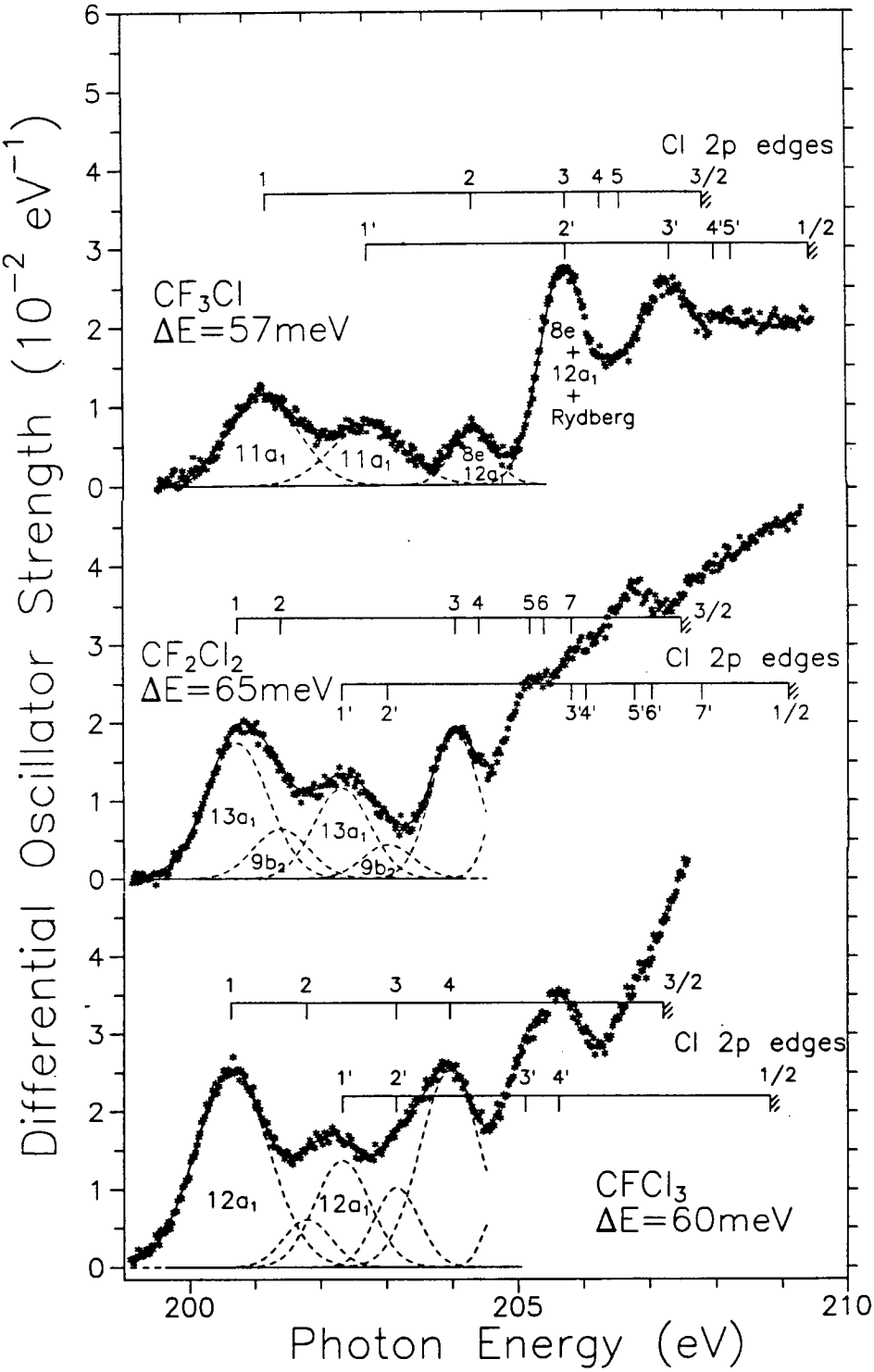

Figure 7.46: Differential oscillator strength spectra for Cl 2*p* excitation of CF_3Cl, CF_2Cl_2 and $CFCl_3$ in the discrete region. See section 7.5 for details.

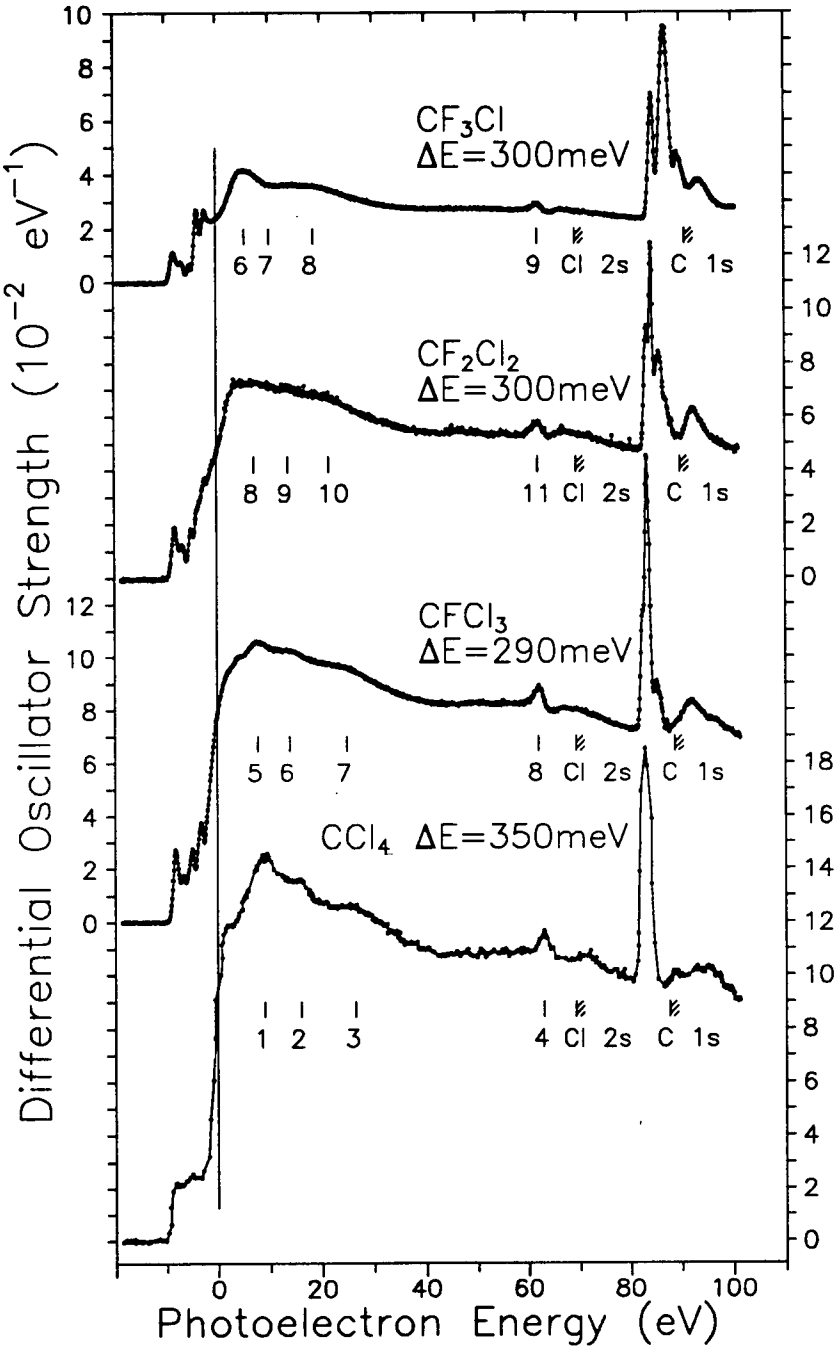

Figure 7.47: Differential oscillator strength spectra for Cl 2*p*, Cl 2*s* and C 1*s* excitations of CF_3Cl, CF_2Cl_2, $CFCl_3$ and CCl_4 in the discrete and continuum regions. The CCl_4 spectrum was derived from EELS measurements in refs [163]. See section 7.5 and tables 7.37–7.40 for details.

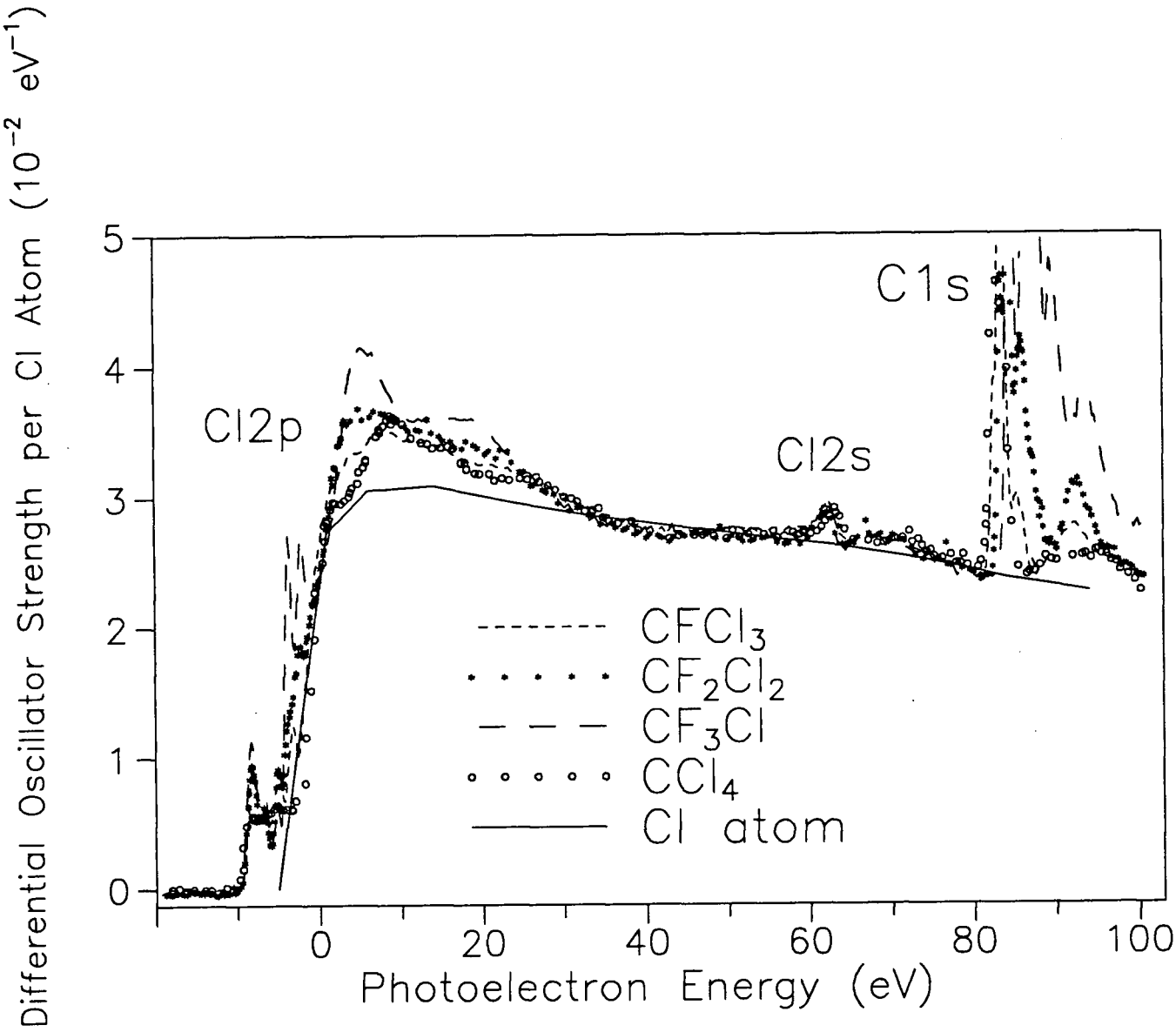

Figure 7.48: Differential oscillator strength spectra per Cl atom for Cl $2p$, Cl $2s$ and C $1s$ excitations of CF_3Cl, CF_2Cl_2, $CFCl_3$ and CCl_4 (measured, this work and ref. [163]) and for Cl $2p$ and Cl $2s$ excitations of the Cl atom (ref. [57]). See section 7.5 for details.

spectrum at low energy and we interpret these as being due to transitions to the $13a_1$ and $9b_2$ C-Cl antibonding orbitals. Notice that the fitted peak 2, related to the Cl $2p_{3/2}$ hole state, is more intense than peak 2′ associated with the Cl $2p_{1/2}$ hole. Peaks (3 and 3′, 4 and 4′) are assigned as transitions to the C-F antibonding orbitals $7b_1$ and $14a_1$. In the $CFCl_3$ spectrum peaks 1 and 1′ can be attributed to transitions to the $12a_1$ C-Cl antibonding orbital. Considering the term values and of peaks 4 and 4′, it is likely that they are due to transitions to the $13a_1$ C-F antibonding orbital. The two pairs of peaks (2 and 2′, 3 and 3′) can then assigned to transitions to the two components of the $11e$ antibonding orbital whose degeneracy is removed due to the broken symmetry of $CFCl_3$ when an electron in the Cl inner shell is promoted. Since 2′ and 3 share the same fitted Gaussian peak in the spectrum, the fact that peak 2 has lower intensity is not inconsistent with the above observation that the series related to Cl $2p_{3/2}$ exhibits larger intensities.

In the present assignments 7.37–7.39 the term values for transitions to C-F antibonding orbitals are in the region 4–7 eV, while those for C-Cl antibonding orbitals are in the region 3–3.5 eV, similar to the observation on the C $1s$ spectra (section 7.3). Rydberg structures are heavily overlapped and are superimposed on the rising ionization edge. Tables 7.37–7.40 list the tentative assignments.

The long energy range spectra in figs. 7.47 and 7.48 show delayed onsets (see section 2.3.4.1) which resemble the Cl atomic situation [25]. In the spectra *per Cl atom* shown in fig. 7.48, all four molecular spectra are very similar in overall shape at photoelectron energies above ~25 eV. It should be noted that in this higher energy region all molecular spectra exhibit rather similar low amplitude EXAFS modulations on the photoionization continuum (see sections 2.3.4.2 and 2.3.4.3) with respect to the situation in the smooth atomic Cl spectrum [57] indicated by the solid line in fig. 7.48. The

similar modulations in this region are due to the fact that EXAFS is the result of *single* scattering processes in which the high energy photoelectron is scattered by only one neighboring atom as discussed in section 2.3.4.2. In the present situation the neighboring electron scatterers are C, F and Cl atoms, each of which is at a similar distance (i.e. Cl-C (~1.75 Å), Cl-F (~2.53 Å) and Cl-Cl (~2.88 Å)) from the ionized Cl atom in each of the different molecules [172]. Similar types of EXAFS modulation pattern have been seen in the Cl $2p$ spectra of CH_2Cl_2, $CHCl_3$ and CCl_4 [163].

From fig. 7.47 it can be seen that there are also additional structures in the spectra for CF_3Cl (features 6 and 8), CF_2Cl_2 (features 8, 9 and 10) and $CFCl_3$ (features 5,6 and 7) and CCl_4 (features 1, 2 and 3) in the near edge region below ~25 eV photoelectron energy. The term values and magnitudes of these XANES structures are different in the various molecules (see fig. 7.48), since XANES is the the effect of *multiple* scattering of the outgoing photoelectron by the neighboring atoms as discussed in section 2.3.4.2.

The Cl $2s$ spectra are broadened due to the short lifetime of the excited states with respect to autoionizing decay to the underlying Cl $2p$ continuum. The energies and possible assignments of these features are shown in tables 7.37–7.40.

Chapter 8

Conclusions

This work has presented dipole (e,e) and dipole (e,e+ion) experimental results including the total and partial (photoion) absolute optical differential oscillator strength spectra of CF_4, CF_3Cl, CF_2Cl_2 and $CFCl_3$ in the valence shell excitation region; the high resolution absolute optical differential oscillator strength spectra for Cl $2p$, Cl $2s$, C $1s$ and F $1s$ inner shell excitation of CF_3Cl, CF_2Cl_2, and $CFCl_3$ and for N $1s$ and O $1s$ inner shell excitation of NO_2. This work has also reported the absolute photoionization partial (electronic state) differential oscillator strength spectra for CF_3Cl, CF_2Cl_2 and $CFCl_3$ and proposed dipole induced breakdown pathways for CF_4, CF_3Cl and CF_2Cl_2 by combining the results from the dipole (e,e) and dipole (e,e+ion) measurements and previously published synchrotron radiation measurements.

The good agreement between the differential oscillator strength spectra obtained in the present work using the dipole (e,e) technique and previously measured spectra using synchrotron radiation where available, plus the good agreement between the dipole (e,e) experimental and the MCQD theoretical results has demonstrated that the EELS technique is a useful alternative to experiments utilizing synchrotron radiation for studying photoabsorption and photoionization processes. The present measurements have considerably extended the available oscillator strength data base for photoabsorption and photoionization processes in NO_2 and the freon molecules CF_4, CF_3Cl, CF_2Cl_2 and $CFCl_3$ in the vacuum UV and soft X-ray regions.

Bibliography

[1] J. Heicklein. *Atmospheric Chemistry* (Academic, New York, 1978).

[2] Jr. L. Spitzer. *Physical Processes in the Interstellar Medium* (Wiley, New York, 1978).

[3] J.W. Chamberlain. *Theory of Planetary Atmospheres* (Academic, New York, 1978).

[4] M. Inokuti (ed.). *Proceedings of the Workshop on Electronic and Ionic Collision Cross Sections Needed in the Modeling of Radiation Interaction with Matter* 6—8 December 1983 (Argonne National Lab. Report No. ANL 84-28, Argonne, IL, 1984).

[5] U. Becker and D.A. Shirley. *Physica Scripta* **T31** (1990) 56.

[6] H. Winick and S. Doniach. *Synchrotron Radiation Research* (Plenum, New York, 1980).

[7] E. Koch (ed.). *Handbook on Synchrotron Radiation* Vol. I, (North Holland, 1983).

[8] J.W. Gallagher, C.E. Brion, J.A.R. Samson, and P.W. Langhoff. *J. Phys. Chem. Ref. Data* **17** (1988) 9.

[9] J. Frank and G. Hertz. *Verhandl. Deut. Physik. Ges.* **16** (1914) 457 and 512.

[10] H. Bethe. *Ann. Physik.* **5** (1930) 325.

[11] E.N. Lassettre and S.A. Francis. *J. Chem. Phys.* **40** (1964) 1208.

[12] J. Geiger. *Z. Phys.* **181** (1964) 413.

[13] M.J. Van der Wiel. *Physica* **49** (1970) 411.

[14] M.J. Van der Wiel and G. Wiebes. *Physica* **54** (1971) 411.

[15] M.J. Van der Wiel and G. Wiebes. *Physica* **53** (1971) 225.

[16] G. Cooper, T. Ibuki, Y. Iida, and C.E. Brion. *Chem. Phys.* **125** (1988) 307.

[17] W. Zhang, G. Cooper, T. Ibuki, and C.E. Brion. *Chem. Phys.* **137** (1989) 391.

[18] E.B. Zarate, G. Cooper, and C.E. Brion. *Chem. Phys.* **148** (1990) 277.

[19] E.B. Zarate, G. Cooper, and C.E. Brion. *Chem. Phys.* **148** (1990) 289.

[20] C.E. Brion and A. Hamnett. *Advan. Chem. Phys.* **45** (1981) 1.

[21] C.E. Brion. *Comments At. Mol. Phys.* **16** (1985) 249.

[22] C. Backx and M.J. Van der Wiel. in: *Proceedings of the IV International Conference on Vacuum Ultraviolet Radiation Physics,* edited by E.-E. Koch, R. Haensel and C. Kunz Hamberg, July 1974.

[23] E.N. Lassettre and A. Skerbele. in:*Methods of Experimental Physics,* 3B, edited by D. Williams (Academic Press, New York, 1974).

[24] E.N. Lassettre. in:*Chemical Spectroscopy in the Vacuum Ultraviolet,* edited by C. Sandorfy and M.B. Robin (Reidel, Boston, 1974) p. 43.

[25] U. Fano and J.W. Cooper. *Rev. Mod. Phys.* **40** (1968) 441.

[26] M. Inokuti. *Rev. Mod. Phys.* **43** (1971) 297.

[27] J.W. Chamberlain and D.M. Hunter. *Theory of Planetary Atmospheres,* 2nd Ed. (Academic Press, New York, 1987) pp. 122–140.

[28] R.S. Stolarski. *Sci. Am.* **258** (1988) 30.

[29] H.I. Schiff. *Nature* **305** (1983) 471.

[30] D.J. Wuebbles. *J. Geophys. Res.* **88C** (1983) 1433.

[31] G. Brasseur, A. De Rudder, and C. Tricot. *J. Atmos. Chem.* **3** (1985) 261.

[32] Y. Susumu. *Kogai* **23** (1988) 1.

[33] M.J. Molin and F.S. Rowland. *Rev. Geophys. Space Phys.* **13** (1975) 1.

[34] H. Massey and A.E. Potten. *Royal Institute of Chemistry, Lecture Series, No 1. Atmospheric Chemistry* (Roy. Inst. Chem., London, 1961) pp. 1–27, fig. 1.

[35] R. Eisberg and R. Resnick. *Quantum Physics of Atoms, Molecules, Solids, Nuclei, and Particles* (John Wiley & Sons, New York, 1974) pp. 53–54.

[36] P.W. Milonni and J.H. Eberly. *Lasers* (John Wiley & Sons, New York,1988) p. 222, p. 226.

[37] H.A. Bethe and E.E. Salpeter. *Quantum Mechanics of One- and Two-Electron Atoms* (Springer-Verlag, Berlin, 1957) p. 256.

[38] J.A. Wheeler and J.A.Bearden. *Phys. Rev.* **46** (1934) 755.

[39] L.D. Landau and E.M. Lifshitz. *Quantum Mechanics. Non-relativistic Theory* translated by J.B. Sykes and J.S. Bell (Pergamon, London, 1965), 2nd ed.

[40] R.A. Bonham and M. Fink. *High Energy Electron Scattering,* ACS Monograph 16.9 (Van Nostrand, New York, 1974).

[41] I.V. Hertel and K.J. Ross. *J. Phys. B* **1** (1968) 697.

[42] I.V. Hertel and K.J. Ross. *J. Phys. B* **2** (1969) 285.

[43] A.P. Hitchcock, G.R.J. Williams, C.E. Brion, and P.W. Langhoff. *Chem. Phys.* **88** (1984) 65.

[44] R. McLaren, S.A.C. Clark, I. Ishii, and A.P. Hitchcock. *Phys. Rev. A* **36** (1987) 1683.

[45] R.P. Feynman, R.B. Leighton, and M. Sands. *The Feynman Lectures in Physics* Vol. I (Addison-Wesley, Reading, Massachusetts, 1963) p. 43-4.

[46] M.J. Seaton. *Phys. Soc. London* **88** (1966) 801.

[47] M.B. Robin. *Higher Excited States of Polyatomic Molecules* Vol. I (Academic Press., New York, 1974).

[48] M.B. Robin. *Higher Excited States of Polyatomic Molecules* Vol. II (Academic Press., New York, 1975).

[49] M.B. Robin. *Higher Excited States of Polyatomic Molecules* Vol. III (Academic Press., New York, 1985).

[50] J.S. Binkley, R. Whiteside, P.C. Hariharan, , R. Seeger, W.J. Hehre, M.D. Newton, and J.A. Pople. GAUSSIAN76, Program no. 368, Quantum Chemistry Program Exchange, Indiana University, Bloomington, IN, U.S.A.

[51] R.N.S. Sodhi and C.E. Brion. *J. Electron Spectrosc. Relat. Phenom.* **34** (1984) 363.

[52] R.N.S. Sodhi and C.E. Brion. *J. Electron Spectrosc. Relat. Phenom.* **37** (1985) 97;125;145.

[53] K.H. Sze, C.E. Brion, X.M. Tong, and J.M. Li. *Chem. Phys.* **115** (1987) 433.

[54] G. Herzberg. *Molecular Spectra and Molecular Structure,* Vol. I (D. Van Nostrand Company, Inc, Princeton, 1950).

[55] C. Fabre and S. Haroche. in: *Rydberg State of atoms and molecules,* edited by R.F. Stebbings and F.B. Dunning, (Cambridge University Press, London, 1983).

[56] J. Berkowitz. *Photoabsorption, Photoionization and Photoelectron Spectroscopy* (Academic Press, New York, 1979).

[57] E.B. Saloman, J.H. Hubbell, and J.H. Scofield. *At. Data and Nucl. Data Tables* **38** (1988) 1.

[58] A. Bianconi. in: *EXAFS and Near Edge Structure,* Springer Series in Chemical Physics, edited by A. Bianconi, L. Incouia and S. Striprich, Vol. **27** (Springer, Berlin, 1983) p. 118.

[59] J.L. Dehmer and D. Dill. *J. Chem. Phys.* **65** (1976) 5327.

[60] G. Cooper, T. Ibuki, and C.E. Brion. *Chem. Phys.* **140** (1990) 147.

[61] V.I. Nefedov. *J. Struct. Chem.* **9** (1968) 217.

[62] J.L. Dehmer. *J. Chem. Phys.* **56** (1972) 4496.

[63] K.H. Sze and C.E. Brion. *Chem. Phys.* **137** (1989) 353.

[64] K.H. Sze and C.E. Brion. *Chem. Phys.* **140** (1990) 439.

[65] J.L. Dehmer. in: *Photophysics and Photochemistry in the Vacuum Ultraviolet,* edited by S.P. McGlynn, G.L. Findley and R.H. Hueber (Reidel, Dordrecht, 1985) p34.

[66] G.R. Wight, C.E. Brion, and M.J. Van der Wiel. *J. Electron Spectrosc. Relat. Phenom.* **1** (1972/73) 457.

[67] G.R. Wight and C.E. Brion. *J. Electron Spectrosc. Relat. Phenom.* **3** (1974) 191.

[68] J.J. Yeh and I. Lindau. *Atomic Data and Nucl. Data Tables* **32** (1985) 1.

[69] J.H. Scofield. *Theoretical Photoionization Cross Sections from 1 to 1500 keV,* Lawrence Livermore Laboratory Report No. UCRL-51326 (1973).

[70] B.L. Henke, P. Lee, T.J. Tanaka, R.L. Shimabukuro, and B.K. Fujikawa. *Atomic Data and Nucl. Data Tables* **27** (1982) 1.

[71] M.J. Van der Wiel, Th.M. El-Sherbini, and L. Vriens. *Physica* **42** (1969) 411.

[72] C. Backx, Th.M. El-Sherbini, and M.J. Van der Wiel. *Chem. Phys. Lett.* **20** (1973) 100.

[73] C. Backx and M.J. Van der Wiel. *J. Phys. B* **8** (1975) 3020.

[74] C. Backx, G.R. Wight, R.R. Tol, and M.J. Van der Wiel. *J. Phys. B* **8** (1975) 3007.

[75] C. Backx, R.R. Tol, G.R. Wight, and M.J. Van der Wiel. *J. Phys. B* **8** (1975) 2050.

[76] F. Carnovale, A.P. Hitchcock, J.P.D. Cook, and C.E. Brion. *Chem. Phys.* **66** (1982) 249.

[77] F. Carnovale and C.E. Brion. *Chem. Phys.* **74** (1983) 253, and references therein.

[78] S. Daviel, C.E. Brion, and A.P. Hitchcock. *Rev. Sci. Instr.* **55** (1984) 182.

[79] T. Yamazaki and K. Kimura. *Chem. Phys. Letters* **43** (1976) 502.

[80] W. Zhang, K.H. Sze, C.E. Brion, X.M. Tong, and J.M. Li. *Chem. Phys.* **140** (1990) 265.

[81] O. Edqvist, E. Lindholm, L.E. Selin, L. Åsbrink, C.E. Kuyatt, S.R. Mielczarek, J.A. Simpson, and I. Fischer-Hjalmars. *Physica Scripta* **1** (1970) 172.

[82] W.H.E. Schwarz, T.C. Chang, and J.P. Connerade. *Chem. Phys. Letters* **49** (1977) 207.

[83] C.R. Brundle, D. Neumann, W.C. Price, D. Evans, A.W. Potts, and D.G. Streets. *J. Chem. Phys.* **53** (1970) 705.

[84] D.W. Davis, R.L. Martin, M.S. Banna, and D.A. Shirley. *J. Chem. Phys.* **59** (1973) 4235.

[85] P. Finn, R.K. Pearson, J.M. Hollander, and W.L. Jolly. *Inorg. Chem.* **10** (1971) 378.

[86] K. Siegbahn, C. Nordling, G. Johansson, J. Hedman, P.F. Heden, K. Hamrin, U. Gelius and T. Bergmark, L.O. Werme, R. Manne, and Y. Baer. *ESCA Applied to Free Molecules* (North-Holland, Amsterdam, 1969).

[87] G.R. Wight and C.E Brion. *J. Electron Spectrosc. Relat. Phenom.* **4** (1974) 313.

[88] G.C. King, M. Tronc and F.H. Read. *J. Phys. B* **13** (1980) 999.

[89] A.P. Hitchcock and C.E. Brion. *J. Electron Spectrosc. Relat. Phenom.* **18** (1980) 1.

[90] G.C. King, F.H. Read, and M. Tronc. *Chem. Phys. Letters* **52** (1977) 50.

[91] G.R. Wight and C.E. Brion. *J. Electron Spectrosc. Relat. Phenom.* **4** (1974) 25.

[92] J.C. Slater. *Phys. Rev.* **38** (1931) 1109.

[93] L. Pauling and E.B. Wilson. *Introduction to Quantum Mechanics* (McGraw-Hill, New York, 1935).

[94] P.A. Cox. *Struct. Bonding* **24** (1975) 59.

[95] C.E. Brion and K.H. Tan. *Chem. Phys.* **34** (1978) 141.

[96] D.A. Outka and J. Stöhr. *J. Chem. Phys.* **88** (1988) 3539.

[97] D. Arvanitis, H. Rabus, L. Wenzel, and K. Baberschke. *Z. Physik D* **11** (1989) 219.

[98] P.S. Connell. *Energy Res. Abstr.* **12** No. 9891 (1987)

[99] C.R. Brundle, M.B. Robin, and H. Basch. *J. Chem. Phys* **53** (1970) 2196.

[100] T. Cvitaš, H. Güsten, and L. Klasinc. *J. Chem. Phys.* **67** (1977) 2687.

[101] L.C. Lee, E. Phillips, and D.L. Judge. *J. Chem. Phys.* **67** (1977) 1237.

[102] L.C. Lee, X. Wang, and M. Suto. *J. Chem. Phys.* **85** (1986) 6294.

[103] G.R. Cook and B.K. Ching. *J. Chem. Phys.* **43** (1965) 1794.

[104] G.C. King and J.W. McConkey. *J. Phys. B* **11** (1978) 1861.

[105] T.A. Carlson, A. Fahlman, W.A. Svensson, M.O. Krause, T.A. Whitleyr, F.A. Grimm and M.N. Piancastelli, and J.W. Taylor. *J. Chem. Phys.* **81** (1984) 3828.

[106] R. Gilbert, P. Sauvageau, and C. Sandorfy. *J. Chem. Phys.* **60** (1974) 4820.

[107] H.W. Jochims, W. Lohr, and H. Baumgärtel. *Ber. Bunsenges. Phys. Chem.* **80** (1976) 130.

[108] R.E. Rebbert and P. Ausloos. *J. Res. Natl. Bur. Std.* **75A** (1971) 481.

[109] B.E. Cole and R.N. Dexter. *J. Quant. Spectrosc. Radiat. Transfer* **19** (1978) 303.

[110] C.Y.R. Wu, L.C. Lee, and D.L. Judge. *J. Chem. Phys.* **71** (1979) 5221.

[111] J.C. Person, D.E. Fowler, and P.P. Nicole. *Argonne National Laboratory Report* ANL-75-60 Part I.

[112] M. Inokuti. Private communication (1985).

[113] M.A. Dillon and M. Inokuti. *J. Chem. Phys.* **82** (1985) 4415.

[114] Y. Iida, F. Carnovale, S. Daviel, and C.E. Brion. *Chem. Phys.* **105** (1986) 211.

[115] T. Ibuki, G. Cooper, and C.E. Brion. *Chem. Phys.* **129** (1989) 295.

[116] W.R. Harshbarger, M.B. Robin, and E.N. Lassettre. *J. Electron Spectrosc. Relat. Phenom.* **1** (1972/1973) 319.

[117] I. Novak, A.W. Potts, F. Quinn, G.V. Marr, B. Dobson, I.H. Hillier, and J.B. West. *J. Phys. B* **18** (1985) 1581.

[118] C.E. Brion, Y. Iida, F. Carnovale, and J.P. Thomson. *Chem. Phys.* **98** (1985) 327.

[119] W. Zhang, T. Ibuki, and C.E. Brion. *Chem. Phys.* , manuscript in preparation.

[120] A.W. Potts, I. Novak, F. Quinn, G.V. Marr, B.R. Dobson, and I.H. Hillier and J.B. West. *J. Phys. B* **18** (1985) 3177.

[121] G.M. Bancroft, J.D. Bozek, J.N. Cutler, and K.H. Tan. *J. Electron Spectrosc. Relat. Phenom.* **47** (1988) 187.

[122] J.S. Tse. *J. Chem. Phys.* **89** (1988) 920.

[123] B.M. Addison-Jones, K.H. Tan, B.W. Yates, J.N. Culter, and G.M. Bancroft and J.S. Tse. *J. Electron Spectrosc. Relat. Phenom.* **48** (1989) 155.

[124] C.R. Natoli. in: *EXAFS and Near Edge Structure,* Springer Series in Chemical Physics, edited by A. Bianconi, L. Incouia and S. Striprich, Vol. **27** (Springer, Berlin, 1983) p. 43.

[125] A. Bianconi, M. Dell'Ariccia, A. Gargano, and C.R. Natoli. in: *EXAFS and Near Edge Structure,* Springer Series in Chemical Physics, edited by A. Bianconi, L. Incouia and S. Striprich, Vol. **27** (Springer, Berlin, 1983) p. 57.

[126] R.H. Huebner, D.L. Bushnell, R.J. Celotta, S.R. Mielzarek, and C.E. Kuyatt. *Argonne National Laboratory Report* ANL-75-60 Part I.

[127] J.W. Cooper. *Phys. Rev.* **128** (1962) 681.

[128] V.N. Sivkov, V.N. Akimov, A.S. Vinogradov, and T.M. Zimkina. *Opt. Spectrosc. (USSR)* **60** (1986) 194.

[129] R.E. LaVilla. *J. Chem. Phys.* **58** (1973) 3841.

[130] G.R. Wight and C.E. Brion. *J. Electron Spectrosc. Relat. Phenom.* **4** (1974) 327.

[131] R.D. Hudson. *Rev. Geophys. and Space Phys.* **9** (1971) 305.

[132] H.M. Rosenstock, K. Draxl, B.W. Steiner, and J.T. Herron. *J. Phys. Chem. Ref. Data* **6** Suppl. 1 (1977).

[133] S.G. Lias, J.E. Bartmess, J.F. Liebman, J.L. Holmes, and R.D. Levin and W.G. Mallard. *J. Phys. Chem. Ref. Data* **17** No. 1 (1988).

[134] D.D. Wagman, W.H. Evans, V.B. Parker, I. Halow, S.M. Bailey, and R.H. Schumm. *NBS Tech. Note 270-3* (U.S. Government Printing office, Washington, 1968).

[135] M.M. Bibby, B.J. Toubelis, and G. Carter. *Electron. Letters* **1** (1965) 50.

[136] R.I. Reed and W. Snedden. *Trans. Faraday. Soc.* **54** (1958) 301.

[137] V.H. Dibeler, R.M. Reese, and F.L. Mohler. *J. Res. NBS* **57** (1956) 113.

[138] C. Lifshitz and F.A. Long. *J. Phys. Chem.* **69** (1965) 3731.

[139] T.A. Walter, C. Lifshitz, W.A. Chupka, and J. Berkowitz. *J. Chem. Phys.* **51** (1969) 3531.

[140] C.J. Noutary. *J. Res. Natl. Bur. Std.* **72A** (1968) 479.

[141] J.W. Warren and J.D. Craggs. *Mass Spectrometry* (The Institute of Petroleum, London, 1952) p. 36.

[142] J.M. Ajello, W.T. Huntress, Jr., and P. Rayermann. *J. Chem. Phys.* **64** (1976) 4746.

[143] K. Watanabe, T. Nakayama, and J. Mottl. *J. Quant. Spectrosc. Radiative Transfer* **2** (1962) 369.

[144] L.M. Leyland, J.R. Majer, and J.C. Robb. *Trans. Faraday Soc.* **66** (1970) 898.

[145] J.B. Farmer, I.H.S. Henderson, F.P. Lossing, and D.G.H. Marsden. *J. Chem. Phys.* **24** (1956) 348.

[146] F.C.Y. Wang and G.E. Leroi. *Ann. Isr. Phys. Soc.* **6** (1984) 210.

[147] H. Schenk, H. Oertel, and H. Baumgärtel. *Ber. Bunsenges. Phys. Chem.* **83** (1979) 683.

[148] R.K. Curran. *J. Chem. Phys.* **34** (1961) 2007.

[149] B.W. Yates, K.H. Tan, G.M. Bancroft, L.L. Coatsworth, and J.S. Tse. *J. Chem. Phys.* **83** (1985) 4906.

[150] J.A. Stephens, D. Dill, and J.L. Dehmer. *J. Chem. Phys.* **84** (1986) 3638.

[151] I. Novak, J.M. Benson, and A.W. Potts. *J. Electron Spectrosc. Relat. Phenom.* **41** (1986) 175.

[152] G. Cooper, W. Zhang, and C.E. Brion. *Chem. Phys.* **145** (1990) 117.

[153] J.D. Bozek, G.M. Bancroft, J.N. Cutler, K.H. Tan, and B.W. Yates. *Chem. Phys.* **132** (1989) 257.

[154] K.H. Tan, G.M. Bancroft, L.L. Coatsworth, and B.W. Yates. *Can. J. Phys.* **60** (1982) 131.

[155] B.W. Yates, K.H. Tan, L.L. Coatsworth, and G.M. Bancroft. *Phys. Rev. A* **31** (1985) 1529.

[156] K.H. Tan, P.C. Cheng, G.M. Bancroft, and J.Wm. McGowan. *Can. J. Spectrosc.* **29** (1984) 1381.

[157] A.W. Potts, I. Novak, F. Quinn, G.V. Marr, B. Dobson, I.H. Hillier, and J.B. West. *J. Phys. B* **18** (1985) 3177.

[158] R. Cambi, G. Ciullo, A. Sgamelotti, F. Tarantelli, R. Fantoni, A. Giardini-Guidoni, M. Rosi, and R. Tiribelli. *Chem. Phys. Lett.* **90** (1982) 445.

[159] E.J. Aitken, M.K. Bahl, K.D. Bomben, J.K. Gimzewski, and G.S. Nolan and T.D. Thomas. *J. Am. Chem. Soc.* **102** (1980) 4873.

[160] C. Cauletti, C. Furlani, C. Puliti, V.I. Nefedov, and V.G. Yarzhenski. *J. Electron Spectrosc. Relat. Phenom.* **31** (1983) 275.

[161] U. Gelius. *J. Electron Spectrosc. Relat. Phenom.* **5** (1974) 985.

[162] M. Tronc, G.C. King, and F.H. Read. *J. Phys. B* **12** (1979) 137.

[163] A.P. Hitchcock and C.E. Brion. *J. Electron Spectrosc. Relat. Phenom.* **14** (1978) 417.

[164] E.J. Aitken, M.K. Bahl, K.D. J.K. Gimzewski, G.S. Nolan, and T.D. Thomas. *J. Am. Chem. Soc.* **102** (1980) 4873.

[165] S.A. Holmes. M.S. Thesis (Oregon State University, Oct 1974).

[166] R.C.C. Perera, P.L. Cowan, D.W. Lindle, R.E. LaVilla, T. Jach, and R.D. Deslattes. *Phys. Rev. A* **43** (1991) 3609.

[167] J.H.D. Eland. *Photoelectron Spectroscopy* 2nd Ed. (Butterworths, London, 1984) p. 176.

[168] A.A. Pavlychev, A.S. Vinogradov, and I.V. Kondrat'eva. *Sov. Phys. Solid State* **26** (1984) 2214.

[169] A.A. Pavlychev, A.S. Vinogradov, T.M. Zimkina, D.E. Onopko, and S.A. Titov. *Opt. Spectrosc. (USSR)* **47** (1979) 40.

[170] E.I. Ishiguro, S. Iwata, Y. Suzuki, A. Mikuni, and T. Sasaki. *J. Phys. B* **15** (1982) 1841.

[171] E.I. Ishiguro, S. Iwata, Y. Suzuki, A. Mikuni, H. Kanamori, and T. Sasaki. *J. Phys. B* **20** (1987) 4725.

[172] A.D. Mitchell and L.C. Cross. (eds.) *Tables of Interatomic Distances and Configuration in Molecules and Ions* Special publication No. 11 (Chemical Society, London, 1958).